NOTTINGHAM TRENT UNIVERSITY

Computer Vision-Based Structural Health Monitoring and Condition Assessment for Small to Medium-Span Bridges

Chidiebere Brendan Obiechefu

A thesis update submitted to Nottingham Trent University for the degree of Doctor of Philosophy in the School of Architecture, Design and the Built Environment

December 2022

COPYRIGHTS DECLARATION

This thesis has been submitted to Nottingham Trent University (NTU) for the degree of PhD. I declare that the work in this thesis was carried out following the regulations of NTU. I certify that all material in this thesis which is not my own work has been referenced and that no material has previously been submitted and approved for the award of a degree by this or any other University. The research reported in this thesis was conducted at Nottingham Trent University between October 2017 and December 2022. Any views expressed in this thesis are those of the author and in no way represents the university.

ABSTRACT

Many UK bridges are currently nearing the end of their life cycles, and therefore their maintenance and inspection routines assume a higher priority, since they become more likely to fail. Bridge maintenance routines are still predominantly based on visual inspections which are expensive, time and labour consuming and prone to human error. Structural Health Monitoring (SHM) systems, mostly utilising contact sensors have been introduced to some larger structures such as the Humber and Severn bridges to complement visual inspections. Contact sensing, however, requires access to the structure, involves working at height and is expensive. More importantly, while many larger structures have received the aid of SHM, older assets, especially small bridges with small traffic volumes still rely solely on visual inspections due to high costs associated with such SHM systems. These challenges can be circumvented by employing the fast-emerging computer-vision based structural health monitoring systems (CV-SHM), which are much more affordable, can be set up to not require working at height, nor require direct access to the structure, and which do not cause traffic disruptions.

This thesis proposes an affordable and accurate CV-SHM and damage detection system to complement conventional bridge inspection routines for small to medium-size bridges. The framework comprises firstly, a computer vision (CV)-based sensing system which consist of a consumer-grade image acquisition device such as a GoPro or smartphone camera, a computer, and an image processing algorithm. This system obtains structural response without access to the structure by using image processing and feature detection techniques to analyse images of a structure captured during loading and obtain its structural response. The second part of this framework is the response analysis for damage detection and characterisation. Here, a set of data-based techniques are developed based on response information such as displacements, curvatures, inclination angles, and strains. Displacements serve as primary response obtained from the monitoring process. Others (strain, curvatures, and inclination angles) are secondary responses obtained by manipulating the primary. In this approach, response from any section of the structure can be analysed, without the requirement for further structural information, such as flexural rigidity (EI), or distance to support, unlike similar studies in literature. The condition of a structure can then be determined by comparing response measurements collected at a first inspection (R_0) – i.e., when the structure is assumed to be in a healthy state, with those collected at a latter inspection (R_i) – where i can be an inspection number, and the relative state of the structure can be determined.

The feasibility of the approach is theoretically validated on a numerical model of a concrete bridge girder under a slowly moving 25 tonnes rigid truck. Multiple damage scenarios are simulated. Damage detection is carried out on the four types of computed response. The robustness of vision measurement approach is validated at different levels of added measurement noise. Noise is expressed as the pixel resolution achievable with the image processing algorithm at multiple camera fields of view. Damage detection and location accuracies are influenced by damage severity, added measurement noise and type of response. A laboratory experiment follows theoretical/numerical validation. A simply supported, C-16 timber platform with attached circular targets serves as a bridge deck. A moving vehicle rides along the 2.2m test span to simulate vehicular traffic. Varying weights of 15kg, 20kg, and 25kg are loaded on the vehicle. Target displacements are collected with a FOV (field of view) covering 1.7m of the test span. Damage is simulated by a 20% cross-sectional stiffness reduction achieved by loosening attached steel plates. Damage is detected and localised on all load cases, and is influenced by load intensity, assuming a constant FOV. A full-scale field deployment is achieved on a timber footbridge in Leicester. Deflection, strains, inclination angles, and curvatures are obtained for the 2m span monitored, but measurement noise is expectedly much higher due to environmental conditions. Damage detection cannot be carried out at this stage in real-life structures since damage cannot be introduced. Response performance in damage detection is consistent for all case studies. Target displacements are much less sensitive to noise, but then also to damage; they appear to change very slowly, without clear spikes or shifts as with others, hence cannot be relied upon for damage localisation. Strains are most robust to noise and provide very good damage detection and location results at high measurement resolutions. Curvatures are more susceptible to noise than strains but perform slightly worse. Inclination angles are very susceptible to noise and are more likely to give false damage detection due to the nature of its curve profile.

The key factors ensuring accurate CV-based deformation monitoring are measurement resolution, camera FOV, and subpixel resolution of the image processing algorithm. If the latter can be increased with manageable demand in computing resources, then FOVs can get larger while maintaining the required measurement accuracy. The upper limit to this achievement is that the technology can be conveniently and confidently deployed to real life bridges where environmental conditions introduce more challenges. To achieve this, a multi-camera approach is proposed and discussed. CV-SHM has the potential to gain the trust of asset managers in complementing visual inspections for small-scale, short to medium-span bridges.

ACKNOWLEDGEMENTS

I would like to firstly express my profound gratitude to Dr Rolands Kromanis who not only gave me this wonderful opportunity to study for a PhD, but also closely guided me, especially in those early years, trusting me, and exposing me to this beautiful world of structural health monitoring.

To Dr Fouad Mohammad, who became my first supervisor after Dr Kromanis left, and who guided me in the latter stages of my program, I say a heartfelt 'thank you'. Your fatherly advices couldn't have come at a better time.

I would like to thank Dr Zakwan Arab, and Prof Amin Al-Habaibeh for all the help and guidance I got on my work. From Prof Amin, I learned to sometimes look at problems from different, sometimes even complementary perspectives. I am in deed, immensely grateful.

I thank the Leicestershire County Council for providing me with the As-built drawings for the footbridge which became my third case study. I thank all the laboratory staff who helped make the experimental phase a reality.

I am grateful to all my colleagues and friends I made during this journey. Some of them will remain friends for much longer. Florence Nwankwo, Kevin Naik, Sushmita Borah, and others. You made this journey fun; the memories will linger, and I wish you guys the best in all your endeavours.

At the latter part of this journey, the COVID pandemic hit. I was stuck in my little studio flat, unable to do much – especially my laboratory work, running out of money – and all the associated worries, and so on. It was a dark time to say the least. But as fate would have it, when life seemed most gloomy, out of nowhere I met an angel. In her was that candle light which suddenly flickers on in the midst of darkness and hopelessness, and which has eventually led me away from my gloom. I am getting married to her on the 22nd of July. Glory, I love you!

To my parents, Chief Basil and Lolo Dorothy Obiechefu, you sacrificed so much for me to be here, I owe you everything. Thank you for your unconditional love and support. To my siblings – Ijeoma, Chigozie, and Kelechi; thank you for being there for me. God bless us all.

TABLE OF CONTENTS

LIST OF FIGURES

LIST OF TABLES

LIST OF ACRONYMS

1D	One Dimensional
2D	Two Dimensional
3D	Three Dimensional
CCD	Charge Coupled Device
CHT	Circular Hough Transform
COMAC	Coordinate Modal Assurance Criterion
CV	Computer Vision
CV-SHM	Computer Vision-based Structural Health Monitoring
DAD	Deformation Area Difference
DIC	Digital Image Correlation
DOF	Degree of Freedom
DSLR	Digital Single-lens Reflex
FAST	Features from Accelerated Segment Test
FBG	Fibre Bragg Grating
FE	Finite Element
FoV	Field of view
FREAK	Fast Retina Keypoint Descriptor
GPR	Ground-penetrating Radar
HCP	Half-cell Potential
IE	Impact Echo
KLT	Kanade-lucas-tomasi
LED	Light Emitting Diode
LK	Lukas & Kanade
MAC	Modal Assurance Criterion
MEMS	Micro-electro-mechanical System
MLESAC	Maximum Likelihood Estimation Sample Consensus
MSER	Maximally Stable Extremal Regions
NDE	Non-destructive Evaluation
NDT	Non-destructive Testing
OCM	Orientation Code Matching
OOI	Object(s) of Interest
ORB	Oriented FAST And Rotated BRIEF
Orion-CC	Orion Cloud Cell
PR	Pixel resolution

RAC	Royal Automotive Club
RANSAC	Random Sample Consensus
RCS	Robotic Camera System
ROI	Region(s) Of Interest
SIFT	Scale Invariant Feature Transform
St-Id	Structural Identification
SURF	Speeded Up Robust Features
USW	Ultrasonic Surface Waves
WASHM	Wind And Structural Health Monitoring
ZNSSD	Zero-mean Normalised Sum Of Squared Differences

CHAPTER 1 | INTRODUCTION AND SCOPE OF THESIS

This chapter introduces the main subjects addressed in this work – which is the static condition assessment and SHM of beam-like civil structures (such as bridges or other horizontal structures) using CV-based technology. The general conceptual and historical background, theory and concepts behind the subjects investigated in this research are first presented. The aims, contribution to knowledge, and thesis outline then follow. Each chapter afterwards will have a more subject-specific introduction appropriate for its content.

1.1 SHM of Constructed Facilities

The construction, or otherwise provision of civil infrastructure is as old as civilisation itself; from the basics such as shelters of any form, water infrastructure, etc., to massive public works such as roads, bridges, sewerage systems, and dams, etc. Of course, the complexities, magnitude, and efficiency of these structures increased with advancements in technology and civilisation. But the need however, to maintain these structures and ensure their utmost performance seems to be increasing with the increasing sophistication of today's structures. The reason for this is quite simple – today's structures are daring, threading the fine line between efficiency (cost and otherwise) and performance. The origins of this phenomenon can be traced to the scientific and mathematical breakthroughs of the 17^{th} to 18^{th} centuries starting from Galileo's articulation of the science of strength of materials and object motion (Favaro et al., 1954), to other breakthroughs in elasticity, laws of motion, beam equations, and virtual work which followed almost in quick succession. These signalled the beginnings of mathematical analysis and design of building structures, and radically expanded the possibilities in analysis, and design of even more sophisticated structures. Structural engineers, to a larger extent, started basing designs especially larger ones such as bridges on mathematical rigour. Structural response therefore can now be predicted even before the structure is built, and thus have become measurable using mathematical calculations and aided by mechanical/electronic devices – themselves an outcome of rapid advances in their field.

Since structural performance can now be predicted even before the structures are built, - and designs based off these predictions, structures can now be monitored, and cost efficiency can be increasingly achieved, with huge savings in materials possible as compared to ancient structures. But clearly one can infer an increasing approach to the fine line between material/cost savings and efficiency, and so it becomes even more imperative that these structures are evaluated periodically to ensure agreement between predicted and

actual behaviour. These evaluations inform engineers in their lifecycle management and operations.

Structural health monitoring can be thought of as a range of systems implemented on full-scale civil infrastructures whose purposes are to assist and inform operators about continued fitness for purpose of those structures under gradual or sudden changes to their state, and to learn about either or both their load and response mechanisms (Brownjohn, 2007). The modern origins of SHM can be traced to the aerospace industry (Elber, 1971) from where it has spread to other engineering branches albeit with varying degrees of success. SHM is common practise in electrical and mechanical fields where most systems have well-developed sensing and anomaly detection systems that inform users of the state of the device when the need arises. An example of this can be experienced in a car, when it indicates that the engines need servicing, or is over-heated, or even the parking sensor systems fitted in them. For constructed systems however, SHM remains in its infancy relatively, but is making tremendous progress, nonetheless.

The very essence of building or developing a system is the satisfactory performance of that system defined by meeting certain criteria set for its particular domain of operations. Thus, monitoring the behaviour and performance of any built system is of fundamental importance to all known disciplines to humanity. In engineering, especially civil and mechanical, the systems developed can be manufactured – as in the mechanical (also electrical, etc.) engineering disciplines, or constructed – as in the civil engineering disciplines. These systems however, regardless of whether they are manufactured or constructed, must be monitored for performance evaluation, and ultimately for user safety.

1.2 SHM of bridges [Motivation]

Bridges are vital elements of civil infrastructure. Bridge operation and safety are very important for their users to avoid long delays and detours due to bridge repairs and closures or, in the worst case, loss of their lives. The recent bridge failure in Genoa, Italy, took lives of about 43 people (Osborne, 2018). The bridge collapse was another reminder since the collapse of I-35W Bridge over the Mississippi River in the USA in 2007 (Harlow, 2018) that asset owners should take better care of their assets. Many bridges in the UK are under weight restrictions and require special care. The Royal Automotive Club (RAC) Foundation reported in 2017 that 3,203 (4.4%) of UK bridges are structurally unfit (defined as inability to carry the heaviest vehicles on UK roads, including vehicles up to and above 44 tonnes), and the current bridge maintenance backlog is £3.9 billion (RAC Foundation, 2017). As at 2020 however, the proportion of unfit bridges has only marginally improved to 4.3% (RAC Foundation, 2020). The safety of many bridges relies solely on bridge inspections, which are time and labour consuming and subjected to human error, which can cause disruptions.

Delays in structural fault or damage recognitions can be expected, especially when considering that principal inspections which comprise close examinations within touching distance of inspectable parts are usually carried out every six years (Design Manual for Roads and Bridges, 2007). For example, the London's Hammersmith flyover was suddenly shut for emergency repairs in December 2011 following an inspection in which a substantial cable corrosion and weakening caused by water ingress was discovered (Transport for London, 2011).

To compliment visual inspections and provide load-response information, many large bridges are equipped with SHM systems. Examples of such large bridges are the Humber bridge (Brownjohn *et al.*, 1994), and the Wind and Structural Health Monitoring System (WASHM) on the Tsing Ma (suspension bridge), Kap Shui Mun (cable-stayed bridge), and Ting Kau (cable-stayed) Bridge in Hong Kong (Wong et al., 2000). The majority of SHM systems employ contact sensors such as fibre optic sensors, wireless sensor nodes, global positioning systems and traditional wired tilt, displacement and strain sensors. SHM systems have also been frequently installed in more recently built, large bridges, examples are the Queensferry Crossing in Scotland (Saul, 2017), and the new I35W bridge in Minneapolis, USA which uses fibre-optic sensors(Patterson, 2010). The condition assessment of older assets however, especially those with a small volume of traffic, still rely solely on visual inspections due to high costs associated with the installation, operation and maintenance of these SHM systems. For example, the installation cost of the SHM system on the new I35W bridge in Minneapolis, which included 323 fibre-optic sensors, wire connections and power sources, was about $1 million (Patterson, 2010). Factors influencing the cost of an SHM system and its operation are number and type of sensors, access requirements to the structure, system maintenance and data interpretation software/tools/experts. These prohibitive costs therefore present a need for affordable, low-cost systems that can be used to assess the condition of bridge structures.

Installations of contact sensing systems require access to the structure, involve working at height and can cause traffic disruptions and delays. All these can be circumvented by employing the fast-emerging CV-based systems, which in most general cases do not require working at height, traffic disruptions, nor even direct access to the structure. They are also much more affordable. CV-based systems have recently experienced vast interest from asset owners and bridge inspectors. Typically, a CV-based system consists of an image acquisition device, a computer, and an image processing package. The image acquisition device is used to acquire images or videos. This can be in a form of a professional camera with an adequate lens, camcorder or smartphone (Brownjohn et al., 2017; Fukuda et al., 2013; Kromanis and Liang, 2018; Zaurin and Catbas, 2010). The CV-

based monitoring process involves recording images of videos of a structure subjected to loading. which are then analysed with image processing software to obtain structural response of the structure. These responses could be displacements, curvatures, strains, inclination angles etc.

Various image processing techniques for extracting information from images or videos are now readily available such as two-dimensional (2D) and three-dimensional (3D) digital image correlation (DIC) (Pan et al., 2009a; Sutton et al., 2009; Yoneyama et al., 2007), template and pattern matching techniques (D. Feng et al., 2015b; Ye et al., 2013), feature detection using well-known techniques such as edge detection (Brownjohn et al., 2017), corner detection (Chang et al., 2010), and blob detection (Ferrer et al., 2015), etc.

This study focuses on CV-based condition assessment of bridges and other horizontal structures such as beams. Thus, an affordable CV-based condition assessment framework for small to medium scale bridges is proposed. The framework utilises consumer grade cameras for measurement collection, image processing for measurement extraction, and a suite of developed techniques for damage assessment and localisation from measured response.

1.3 Aims and objectives

The main aim of the research is to develop a CV-based bridge condition assessment and monitoring framework for small to medium span bridges based on structural response measurements. This aim is hinged on analysing the load response mechanism of horizontal structures under moving loads. This framework practically involves firstly obtaining structural response measurements using affordable CV-based sensing, and then applying developed damage detection techniques using measured response to give accurate structural performance assessment of horizontal structures.

To achieve the stated aim, the following objectives have been identified:

1. To extensively review existing literature, focussing on CV-based structural deformation monitoring, and damage detection/localisation techniques in horizontal structures.
2. To articulate and describe a simple and affordable CV-SHM and condition assessment framework that can be deployed on small to medium scale bridge structures.
3. To define a logical sequence of image processing activities suitable for the CV-SHM approach.
4. To derive and articulate mathematical response analysis techniques capable of damage detection and localisation using CV-SHM data.

5. To evaluate the practicability of the proposed approach using numerical and laboratory structure examples.
6. To deploy the proposed approach to a full-scale small-sized structure and assess for robustness and limitations under real-life scenarios, especially with regards to measurement accuracy.
7. To analyse the strengths and limitations of the proposed approach based on results obtained, and discuss the prospects and idea of an affordable, convenient, and accurate CV-SHM framework, that could be trusted to complement visual inspections.

1.4 Methodology

Figure 1-1 below is a diagrammatic overview of the methodology in which the thesis is conducted.

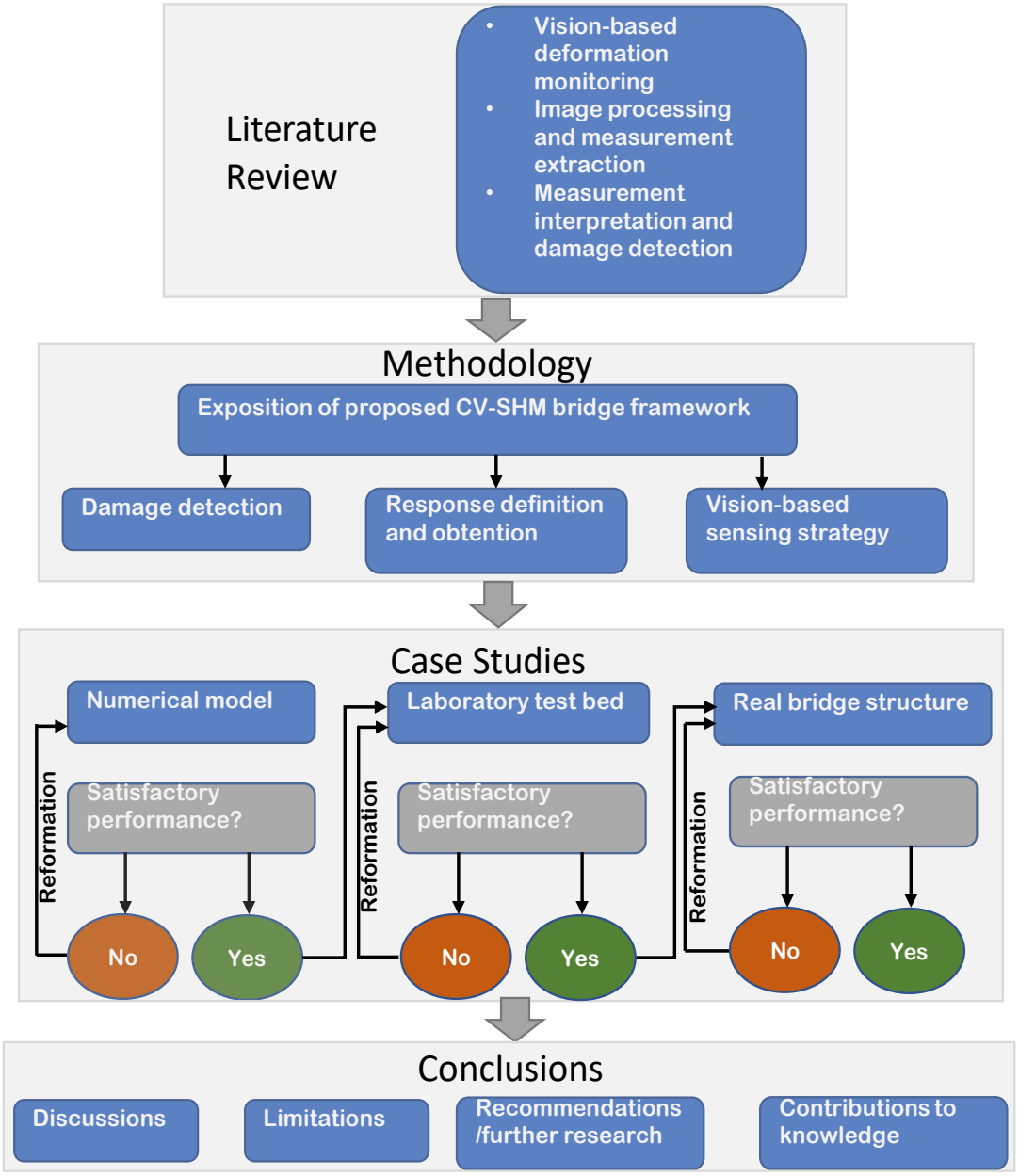

Figure 1-1: Methodology flow chart

The research is purely quantitative and seeks to develop anomaly detection techniques that can analyse structural response measurements obtained using affordable CV-based sensors.

A thorough review of existing literature is carried out identifying gaps in the process. The methodology chapter begins with an articulation of the proposed CV-based condition assessment framework, using written as well as diagrammatic descriptions. Going a step into more detail, the damage detection techniques are described and derived theoretically and mathematically. An analysis focussing on the scope, applicability, and limitations of the CV-based sensing strategy is then carried out.

The developed techniques are put to the test with carefully selected case studies. First, a numerical girder model with a truck load applied in varying ways. Secondly, a laboratory test bed with a moving load. And thirdly, the techniques are tested on a real bridge structure. At each case study, the results are evaluated, concerns are dealt with, before carrying on to the next.

The performance of the developed techniques is then discussed, establishing their scope and limitations, and also expressing how they can be improved with further research.

1.5 Contribution to knowledge

Limited body of work exist using curvatures, inclination angles, and strains for static damage detection and characterization. Most available literature on vision-sensor response acquisition applications have utilised high-grade professional camera photogrammetry for accurate response obtention and damage detection purposes.

The uniqueness of this research is two-fold. Firstly, that the fast-improving features of consumer-grade camera devices are exploited for response acquisition, and especially damage detection and characterisation, as opposed to high-grade video cameras, which improves the affordability of the process. Secondly and most importantly, in the definition of obtained responses for the purpose of damage detection. Most damage detection applications (reviewed thoroughly in Chapter 2) that rely on analysing structural response along the length of a structure involve differentiating the elastic curve to obtain derivative measurements, and as such, require much information about the structure (e.g., material properties, boundary conditions, geometry) and load on it (e.g., load location, amount, distribution) (Abdo, 2012; Erdenebat et al., 2018). A data-driven condition assessment approach requiring as little information as possible, but being accurate and reliable, is therefore sought after and fulfilled by this research [Also see: Obiechefu and Kromanis, (2021)]. The research fulfils this by the method of calculating inclination angles and strains, and a unique definition of curvature. Inclination angles and strains are calculated from two distributed targets on the structure. Curvature is defined as the quadratic coefficient of the curve formed by the deflection of three targets on a structure under loading. The desired usefulness of the response obtention and definition approach simply becomes that response can be obtained between any specified distances (x) between targets anywhere along the structure, with no further information (as aforementioned) required. For example, curvature from some load on the structure can be found for a 2m length at the middle of the structure, without any need for knowing or specifying boundary conditions, etc, which would be required when obtaining derivatives of the deflection curve. The thesis thus presents a more data-driven approach to damage detection in structures. This is a pragmatic approach

that increases the chances of successful and robust on-field applications. The entire approach including its theory and rationalisations is elucidated in the methodology chapter.

1.6 Outline of thesis

The contents of this thesis are outlined as follows:

Chapter One: Here, the reader is introduced to the idea and motivations for the structural health monitoring of constructed civil facilities. The big idea is then narrowed down to bridge structures where the argument for affordable CV-based sensing technologies for is laid out. The aims and objectives then follow.

Chapter Two: This chapter extensively reviews existing literature and is divided into two sections laid out in the following order:

- In the first section, CV-based deformation monitoring in reviewed. This includes the earliest applications of CV-based technologies in the UK, camera calibration, measurement extraction techniques, structural displacement computation. A comprehensive general state of the art in structural deformation monitoring is then reviewed with emphasis on applications and field deployments.
- The second section focuses on measurement interpretation with regards to damage detection and localisation techniques. Several methods such as vibration-based techniques, and techniques based on static measurements are also reviewed, such as curvatures, inclination angles, and strains. Lastly, CV-based applications are reviewed.

Chapter three: This chapter lays out the methodology employed in this research. It begins with a short introduction to structural performance evaluation, and reviews different kinds of loadings on bridges. The general theory for the methodology is then explained, followed by an articulation of the proposed condition assessment framework, as well as the CV-based sensing strategy. The damage detection and localisation techniques that make up the framework are then articulated and expressed mathematically.

Chapter four: This chapter describes the applications of proposed methodology to case studies including a numerical model, a laboratory test bed, and a full-scale bridge deployment.

Chapter five: This chapter discusses and summarises the findings of the research, analysing strengths and limitations of the proposed approach, and discussing the potential for trusted CV-SHM approach for small to medium scale structures.

Chapter six: Conclusions and further work.

CHAPTER 2 | LITERATURE REVIEW

SHM as a term in engineering generally refers to any of the numerous processes in implementing a damage detection and characterisation scheme for a structure. Now damage, as defined by Farrar and Worden (Farrar and Worden, 2007), refers to changes that are introduced into a system, either intentionally or unintentionally, that will affect its current or future performance. Damage can entail changes to the material and/or geometric properties of a structural system which affects its performance adversely. Damage detection procedures are implemented for civil, aerospace, or mechanical engineering structures.

Later on, in the chapter (section 2.2.2), the subtle difference between structural health monitoring and condition assessment will be described (even though they are regularly used interchangeably). Numerous damage detection strategies exist. Many of these can be based on dynamic (vibration) or static structural responses. For full-scale horizontal structures like bridges, deformation monitoring is central to many of their SHM strategies. This is also central to the methodology introduced in this thesis.

The rest of the chapter reviews historical and contemporary practices in CV-based deformation monitoring as well as detection and characterisation techniques and methods.

2.1 CV-based deformation monitoring

A CV-based sensing system typically consist of an image acquisition device, a computer and an image-processing package. Image acquisition devices can be in the form of a professional camera with an adequate lens, camcorder, smartphones, Go-pros or other consumer-grade cameras. The image-processing package is usually contained in the computer and can be any software or computer program capable of extracting some form of response information from recorded images or videos.

2.1.1 Early CV-based methods for monitoring bridge infrastructure

Some of the earliest known applications of optics, or CV-based methods for monitoring civil structures are at the Tacoma Narrows bridge in the USA (Farquharson and Vincent, 1949), and the Tagus River suspension bridge in Portugal (Marecos et al., 1969). In the UK, the earliest full scale continuous bridge deformation monitoring applications were at the Humber and Severn Bridges in the 1990s (Macdonald et al., 1997; Stephen et al., 1993).

In the Humber Bridge expedition, optometers (Zasso et al., 1993), utilising a charge coupled device (CCD) array to detect sharp contrasts in images of large moving targets were used.

2m focal length reflecting telescopes were employed by the optometers to focus on mid-span targets. Some draw-backs in the application were large vertical and horizontal drifts which led to respective targets moving out of the lens' field-of-view, and poor image quality due to poor illumination. A measurement extraction system based on template-matching for displacement measurements was developed also in this expedition. This was the first known application of such technology on a large scale in the UK.

In the Severn Bridge monitoring, a CV-based system was developed for dynamic response measurements. Using lenses with a focal length of 800 mm, a displacement measurement accuracy of 0·5 mm was achieved at a distance of over 200m based on a mid-span target. Other significant improvements it made on the earlier Humber bridge expedition included a synchronised multi-camera approach, and three-dimensional tracking. In the multi-camera approach, video signals from up to three cameras, trained on specific targets (either side of midspan and top of pylon) were recorded onto one video tape by multiplexing alternate image fields from each camera.

Seemingly inspired by these early successful expeditions, several other CV-based systems have since been developed, evaluated, and deployed for deformation monitoring of both short span (Busca et al., 2014; D. Feng et al., 2015c; Kim and Kim, 2011), and long span bridges (Xu et al., 2016; Ye et al., 2013)

Another optics-based method that has found application in structural deformation monitoring is photogrammetry. Photogrammetry and its application in SHM has been extended from mere topographic mapping (C. Chen *et al.*, 2015) to deformation monitoring in bridges (Jiang et al., 2008).

2.1.2 Target vs non-target CV-based monitoring

The two monitoring expeditions discussed in the preceding section have involved some contact with the structure itself, part of which is for the installation of some forms of an artificial marker that can serve as a target. This target becomes the focus point of the camera lens, and its movements during monitoring tracked, recorded, and interpreted as structural displacements. Access to, and the installation of artificial targets, or sensors etc., may be difficult to achieve, impracticable, or involve higher risks in certain conditions; for example, working at heights, and permits which may be required.

Non-target, or in a more puritanical sense, non-artificial target tracking systems aim to have no contact with the structure. Here, feature detection and tracking algorithms may be used to detect and track natural features on the structure such as bolts and joints on a steel bridge during monitoring. This eliminates the difficulties and potential risks involved in contact monitoring, although this may be more difficult to achieve in certain scenarios.

Full-scale dynamic monitoring of long-span bridges to date have mostly involved artificial targets or markers. In the earlier expeditions, measurements were obtained by target tracking of an artificial target installed at the bridge's midpoint (Macdonald et al., 1997; Stephen et al., 1993). However, the necessity for distributed sensing and contactless monitoring grew side-by-side and led to the development of techniques for obtaining measurements at several selectable locations. One of the earliest outcomes of this endeavour was the method proposed by Wahbeh et al., (2003) using targets consisting of high-resolution low-power light emitting diodes (LEDs), this was validated at Vincent Thomas Bridge in Los Angeles USA. Since the 2000s, some non-contact, target-less applications have been reported such as in (Ye et al., 2013).

2.1.3 Single-point vs multi-point tracking

Single and multi-point (or single target and multi target) tracking are terms that make sense only relative to each other. Single-point tracking denotes that just one target or feature or point in the structure is tracked. Of course, within the context of this research such target/feature must be small enough such that measurements obtained from its tracking can be considered to be from one point in the structure. Multi-point tracking denotes tracking of several targets at the same time (Kim et al., 2006; Yan Xu et al., 2018). Single-point tracking is utilised mainly in ascertaining dynamic properties of a structure as higher accuracy is ensured since the entire resolution of the CV-based monitoring device is focused on one target. Accuracy is traded off as more targets or area of the structure are fit into the same device's FOV. Multi-point tracking therefore has the disadvantage of a reduced accuracy, but the advantage that a response profile of a wider length of the structure can be obtained since measurements can be obtained from multiple targets along the structure (Busca et al., 2014). Multi-point tracking, both target and target-less, have become sufficiently experimentally validated and is now witnessing a vast amount of field applications especially in deformation monitoring of short-span bridges (Busca et al., 2014; D. Feng et al., 2015c; Kim and Kim, 2011).

2.1.4 Video processing and measurement extraction

A CV-based system's working application involves firstly, setting up one or more cameras in a suitable and stable location, focussing at a 'target' contained in, or at a portion of the structure; and secondly, deriving structural displacement measurements by video processing, which involves recording or 'tracking' target movements through the video/images of the structure. The target could be either artificial (e.g. a preinstalled marker, LED lamp or checkerboards etc.) or an existing structural feature (e.g. bolts or joints in a truss bridge). Figure 2-1 shows a typical CV-based set-up with GoPro camera focusing on pre-installed midpoint target.

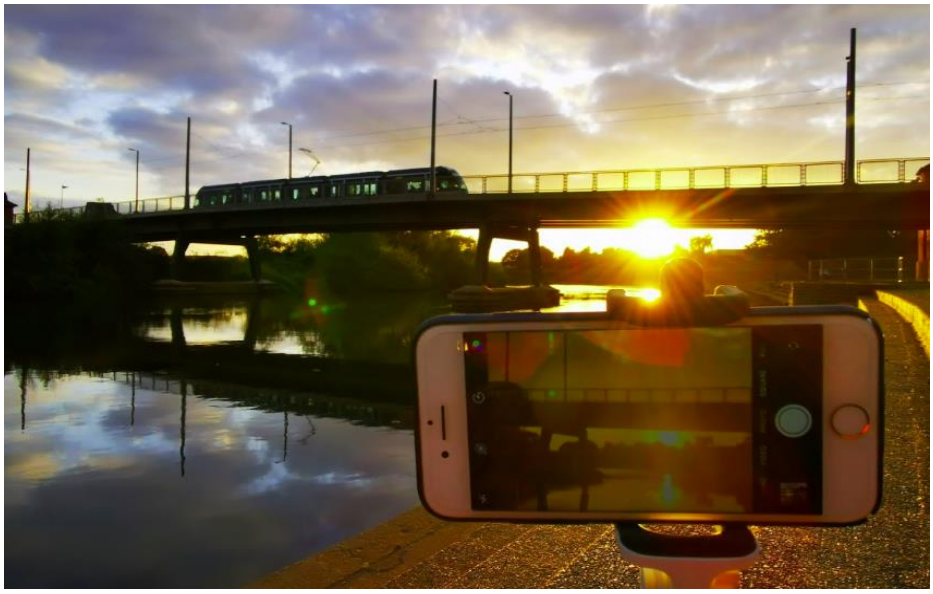

Figure 2-1: Nottingham Trent University (NTU)'s CV-based SHM set-up with camera focusing on a target section of the Wilford toll bridge in Nottingham

Apart from the broad target vs non-target classification, CV-based systems can be characterised also based on their image/video processing approaches. Any video processing method must include camera calibration, measurement extraction, and structural response estimation. The video processing phase involves calibrating the camera, and then from pictures/videos of the section of the structure containing the target, tracking the location(s) of said target(s) through the image sequence, and finally transforming these target locations to a time history of structural displacements. A brief theory and review of these phases and their applications in SHM is summarised in the subsequent sections.

Camera calibration

Camera calibration defines the relationship between structural points in the 3D structural coordinate system and the matching points in the 2D image plane. This makes it possible to accurately determine location of targets in the structure when its location in the image is known. In other words, this relationship between structural points in the 3D structural coordinate system and the matching points in the 2D image plane (expressed as coefficients, parameters, etc.) are used to convert displacements from image processing in pixels to real world engineering units (say in mm) at the end of the process. Three categories of project transformation are common: the full projection matrix, planar homography and scale factor method.

Full projection matrix:

This is the general projection transformation form from three dimensional (3D) structural axes to the two dimensional (2D) image plane. It requires no constraint on neither camera

orientation nor structural displacement plane. Generally, the projection transformation relationship is given by a point $P_S(X_W = [X, Y, Z, 1]^T)$ in structural coordinates mapping on to a 2D image plane to become $P_1(u = [u, v, 1]^T)$, thus:

$$\propto \{u\} = [H]_{3\times4}\{X_W\} \qquad 2.1$$

Where:

$[H]_{3\times4}$ is a full projection matrix with coefficient $\propto$ (see Figure 2-2)

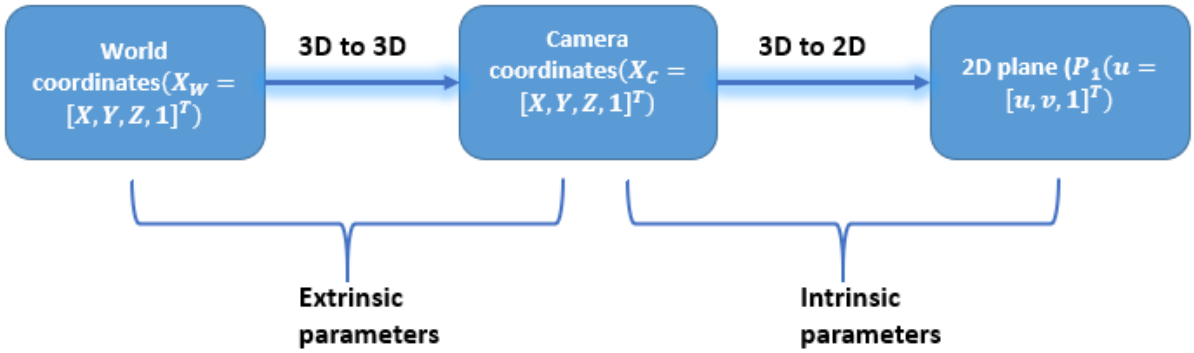

Figure 2-2: Full projection matrix

The calibration process involves estimating camera intrinsic and extrinsic parameters. The intrinsic parameters can be practically estimated using a calibration object by taking a set of images of the object from various angles (Zhang, 2000a). The calibration object is typically a flat object with grid patterns of known dimensions and spacing such as a checkerboard. At least two views are required for calibration by the Vision System Toolbox of MATLAB (The MathWorks Inc., 2013; Zhang, 2000a), three views are advised by Xu and BrownJohn (Xu and Brownjohn, 2018), and at least ten by Bradski and Kaehler for more robust estimates (Gary and Kaehler, 2009). Lens functions such as autofocus are turned off after calibration as they may lead to changes in intrinsic camera parameters. Lens distortion parameters could also be estimated in this process. This could be necessary when consumer-grade and smartphone cameras which employ short focal length, wide field-of-view (FOV) lenses that have significant distortion near the edges (Yoon et al., 2016) are used. This step is not needed when lens producing no apparent distortion are attached to cameras (Xu and Brownjohn, 2018). Obviously, target regions should ideally be as centrally located as practicable as central regions suffer less lens distortion.

The extrinsic parameters are estimated using point correspondences between 3D structural coordinates of control points and their projections on the 2D image plane. It consists of a rotation, *R*, and a translation, *t*. The least-squares optimisation finds the optimal camera extrinsic matrix in terms of minimalizing total re-projection error between image and image projection points. A handy and straightforward full projection matrix calibration algorithm, as

well as guidance and examples towards its laboratory application can be assessed at the Vision System Toolbox of MATLAB (The MathWorks Inc., 2013).

Full projection matrix has been used for camera calibration in many laboratory and field monitoring expeditions: Kim et al. described both laboratory and site calibrations in their field monitoring of a three-span bridge in Korea (Kim et al., 2006), while Martins et al. (Lages Martins et al., 2015) applied it in their mid-span displacement measurements on a long span bridge.

The full projection matrix provides a flexible (as it can be used with any camera configuration and 3D structural displacements), accurate, and easy-to-implement (thanks to packages such as MATLAB and OpenCV) way of calibrating cameras for reliable measurement obtention both in the laboratory and on the field.

Planar homography:

When the structural target's displacement is mainly two-dimensional, planar homography can simplify the projection matrix by mapping a 2D structural plane $(X_P = [X, Y, 1]^T)$ to a 2D image plane $(u = [u, v, 1]^T)$. It also incorporates geometric distortion in the projection and so no constraint is imposed on camera positioning.

$$\propto \{u\} = [P]_{3\times4}\{X_P\} \qquad 2.2$$

Where:

$[P]_{3\times4}$ is the planar homography matrix with coefficient $\propto$

The method was utilised by Xu et al. in the mid-span deformation monitoring of Humber bridge where three or more coplanar line correspondences from an attached planar target was used assuming negligible out-of-plane motion (Xu et al., 2016).

Planar homography method, just like the full projection matrix requires a planar target with known dimensions and can be employed with a necessary precondition or assumption of negligible third axis displacements

Scale factor

This is the simplest of the projection transformation methods. It assumes an equal depth-of-field for projected points (Xu and Brownjohn, 2018) and/or that the optical axis of the camera is perpendicular to one of the structural planes (Wu et al., 2014). The transformation therefore maps a 1D structural plane to a 1D image plane. Thus, the scale factor (F) is obtained by a one-dimensional real-world distance to pixel units ratio given by:

$$F = \frac{p}{d} \qquad 2.3$$

Where:

p is the length in pixels in the projection image of a known physical dimension d

Or

$$F = \frac{f_{pix}}{D} \qquad 2.4$$

Where:

$f_{pix}$is focal length of the camera in pixels, and D is distance from the structural surface plane to the camera's optical centre.

The scale factor method, especially using dimension correspondences with an artificial target has been relatively widely utilised in many monitoring campaigns (D. Feng et al., 2015c; Fukuda et al., 2010; Kim and Kim, 2011; Lee et al., 2006; Lee and Shinozuka, 2006; Ribeiro et al., 2014; Sładek et al., 2013; Stephen et al., 1993; Wahbeh et al., 2003; Ye et al., 2013; Yoneyama and Ueda, 2012; Yoon et al., 2016). If 2D displacement measurements are required then the scale factor can be calculated separately using p and d for each axis as used in (Fukuda et al., 2010; Lee et al., 2006; Lee and Shinozuka, 2006). Yoon et al. applied the method using known dimensions on the structure thus eliminating the need for artificial targets (Yoon et al., 2016). It is noteworthy that they also used the method in conjunction with the full projection calibration for lens' distortion correction. The camera-to-target plane distance was used by Khuc and Catbas in (Khuc and Catbas, 2016).

The scale factor is a simple projection transformation for 1D or 2D structural displacements with or without artificial target. The method is fairly flexible when using dimension correspondences as camera positioning is not critical (D. Feng et al., 2015c). For 2D displacements, care must be taken to apply the two different scale factors to their respective axes. When using camera-to-target distance however, short distance laboratory validation tests have suggested a camera optical axis tilt angle to be less than 10° (Choi et al., 2016).

2.1.5 Measurement extraction

A system or algorithm, capable of extracting metric information from targets in images is required to obtain structural measurements during monitoring. These systems already exist across various fields are readily employed prominently in CV-based deformation monitoring. Some of these systems include several feature detection and tracking systems, which are reviewed in the next sections.

Feature detection and tracking

Feature detection and tracking techniques fall into four main categories based on the nature of target (Xu and Brownjohn, 2018). These are:

- Template matching: A rectangular subset of pixels from image frame as target.

- Feature point matching: Sparse points with salient features given by descriptors as target.
- Optical flow estimation: Every pixel tracked within a selected target region
- Shape-based tracking: Tracking specific shapes e.g., Circles, lines, or custom-made targets

Template Matching

This technique tracks a target by searching, and finding in a new image a pixel subset, or area which has been specified in a previous – or reference image, known as the template. The correlation of the 'found' pixel subset to the template is computed by robust matching criteria such as zero-mean normalised cross correlation (ZNCC) and zero-mean normalised sum of squared differences (ZNSSD) which have been reported to show no sensitivity to offset and linear scale in illumination (Pan et al., 2009b). A more recent similarity coefficient called the orientation code matching (OCM) based on orientation code, was developed and validated on a long span bridge (Fukuda et al., 2013). Interpolation techniques such as bi-cubic interpolation (Choi et al., 2011), second-order polynomial interpolation (Sładek et al., 2013), and zero-padding interpolations (D. Feng et al., 2015c) in spatial and frequency domains respectively have been used to approximate results, which are accurate only to the pixel level by default, to sub-pixel accuracy.

Template matching is widely applied in monitoring of various civil structures. It featured in some of the earliest CV-based monitoring campaigns like the Humber bridge (Stephen et al., 1993), and the Severn crossing (Macdonald et al., 1997). It has also been utilised in more recent campaigns like a railway bridge (Fukuda et al., 2013), and a long-span bridge (Ye et al., 2013).

Digital Image Correlation (DIC):

DIC is direct derivation of template matching methodology, but also considers shape distortion under large structural deformations (Baker and Matthews, 2004; Lucas and Kanade, 1981). DIC has become widely used in structural deformation monitoring but has long been used in experimental solid mechanics for surface deformation and strain measurements (Pan et al., 2009b; Sutton et al., 2009). In simple terms, DIC provides displacements and strains by comparing digital images of a specimen surface in its un-deformed (or reference image) and deformed states. In its typical application in structural deformation monitoring, a subset from the reference image – such as 30 by 30 pixels is selected and its location on a subsequent image is found, and displacements computed. The correlation of the set of pixels to the reference image is then determined by defining a normalised cross-correlation coefficient, S (Yoneyama and Ueda, 2012)(Kim and Kim, 2011). S is defined as (Bruck et al., 1989):

$$S\left(x, y, u_x, u_y, \frac{\delta u_x}{\delta x}, \frac{\delta u_x}{\delta y}, \frac{\delta u_y}{\delta x}, \frac{\delta u_y}{\delta y}\right) = 1 - \frac{\sum I_u(x,y) I_d(x',y')}{\sqrt{\sum I_u(x,y)^2 \sum I_d(x',y')^2}} \quad 2.5$$

Where:

u_x and u_y are the displacement components at the center of the subset, I_u and I_d represent the gray levels of the undeformed and deformed images, respectively, and (x, y) and (x', y') are the coordinates of a point on the subset before and after deformation, respectively. The coordinate (x', y') after deformation is related to the coordinate (x, y) before deformation as

$$x' = x + u_x + \frac{\delta u_x}{\delta x}\Delta x + \frac{\delta u_x}{\delta y}\Delta y \quad 2.6$$

$$y' = y + u_y + \frac{\delta u_y}{\delta x}\Delta x + \frac{\delta u_y}{\delta y}\Delta y \quad 2.7$$

Where:

Δx and Δy are the x and y directional components of the distance from the centre of the subset to the point (x, y), respectively. Displacements are determined by searching for a set of displacements and gradients that minimalize S. The Newton-Raphson method is used to search for the displacements and gradients after the first estimation. An interpolation scheme reconstructs the discrete intensity pattern into a continuous one. More details on DIC, including the algorithm for its sub-pixel approximation with the Newton-Raphson method is given in (Bruck et al., 1989).

DIC has been used extensively for non-contact monitoring applications. Yoneyama et al. used DIC for deformation measurements of a short span steel girder bridge (Yoneyama and Ueda, 2012). The DIC measurements were also reported to correlate with approximate elastic deflection values by a standard deviation of 0.31mm or 0.06pixels. Kim and Kim (Kim and Kim, 2011) verified their multi-point displacement measurement algorithms with a shaking table test and a vehicle load test on a bridge using DIC. Dworakowski et al. proposed a damage detection and localisation method using DIC (Dworakowski et al., 2015). Dynamic characteristics of suspension bridge hangers were examined using DIC (Kim and Kim, 2013), as well as fatigue behaviour of concrete (Mahal et al., 2015).

As a whole, template matching is relatively easy to use. It is flexible in the sense that no distinct requirements are required of targets. For example, it has been used in conjunction, and performed well with artificial planar targets (Macdonald et al., 1997; Stephen et al., 1993), LED lamps (Ye et al., 2013), as well as feature targets (D. Feng et al., 2015c). Template matching is known to be sensitive to changes in brightness (Brownjohn et al., 2017), as well as background conditions (Guo and Zhu, 2016), which makes it unsuitable for monitoring slender components such as cables, as the template might include

background lighting. The sensitivity to illumination has been reported to be reduced by adjusting camera auto-exposure (Brownjohn et al., 2017).

Feature point matching and shape-based tracking

Feature point matching algorithms detect sparse key or special points within a target region of an image, independently detecting the same points across other images, and finding their correspondences based on their local positions. Key points have to be stable, distinctive, and reasonably invariant to translations and illumination changes, such as shape corners and connection bolts. Key points are extracted and described using a feature detector and matching criteria according to the appearance and properties of a small window around the key point (Szeliski, 2011). The feature point matching process is illustrated in Figure 2-3.

Figure 2-3: Feature point matching procedure

The Harris corner detector (Harris and Stephens, 1988) is a popular key point detector, and its efficiency has been demonstrated in many applications such as in (Chang et al., 2010; Khuc and Catbas, 2017a; Yoon et al., 2016). Some of the most common key point descriptors are given in Table 2-1. The scale invariant feature transform (SIFT) corresponds the region of interests across frames (Lowe, 1999), the Kanade-Lucas-Tomasi (KLT) method uses the spatial intensity information as guide for the search for the position that yields the best match between successive images (Lucas and Kanade, 1981) etc. Some algorithms (such as SIFT (Lowe, 2004)) have both detector and descriptor capabilities that can be used independently, i.e., key points can be computed by SIFT detector without descriptors, and descriptions of custom key points can be compiled without detectors. Descriptors summarise some characteristics of the key points. Float point-based descriptors are represented using float vectors. They reflect local intensity gradients around a key point. Binary string-based descriptors are represented using binary vectors which basically compare image intensities over a special pattern surrounding the key point. Matching criterion between descriptors is usually Hamming distance (Calonder et al., 2010), and outliers discarded using Random Sample Consensus (RANSAC) (Martin A. Fischler and Bolles, 1981). Several of these are available (see (Xu and Brownjohn, 2018)), and a thorough review of these techniques and their applications for CV-SHM is given in (Brownjohn et al., 2017; Dong and Catbas, 2020a). Some of these have also been incorporated into proprietary software such as Video Gauge™ (Imetrum, 2020)), or open

source software such as QUBDIsp (Lydon et al., 2019) and DeforMonit (Kromanis and Al-Habaibeh, 2017)).

Table 2-1: Feature descriptors

Categories	Descriptor
Float point based	SIFT (Lowe, 2004)
	Speeded up robust features (SURF) (Bay et al., 2008)
Binary string based	Binary robust independent elementary features (BRIEF)
	Oriented FAST and Rotated BRIEF (ORB) (Rublee et al., 2011)
	Fast retina Keypoint descriptor (FREAK) (Alahi et al., 2012)

Geometric alignment is used to verify matched key points and remove outliers in step 3 after the image has gone through a geometric transformation. The random sample consensus (RANSAC) (Martin A Fischler and Bolles, 1981) and least median of squares (Rousseeuw, 1984) are common techniques for discarding outliers. Tracking is the average movement of key points and intrinsically has sub-pixel resolution.

Feature point matching and shape-based tracking use sparse key points described by local descriptors, as opposed to pure image intensities of template matching and DIC. Hence it is less sensitive to illumination and scale variations (Xu and Brownjohn, 2018). Targets however, need to have rich textures and highly distinctive features to apply this method. More user intervention is required in the process as parameters such as contrast threshold for outlier removal may have to be adjusted depending on environmental changes (Khuc and Catbas, 2016).

Several target-tracking methods detect special shape-like features of targets such as edges of squares, thick lines, and circles etc. These shapes may be found in artificial targets or structural features such as bolts and joints. They can be detected and tracked the same way as feature point matching. This is known as shape-based tracking and it has been applied has been widely applied in deformation monitoring tests.

Choice of feature detection algorithms and descriptions of a selected few

Depending on the requirements of application, several local feature detection algorithms can be utilized such as Features from Accelerated Segment Test (FAST) (Rosten and Drummond, 2006), Harris, and Shi & Tomasi corner detectors (Harris and Stephens, 1988), Circular Hough Transform (CHT) (Duda and Hart, 1972), Maximally Stable Extremal Regions (MSER) blob detectors (Matas et al., 2004) etc. The feature-detection algorithm to

be selected must take into consideration the properties such as geometrical shape of the feature to be detected, illumination, brightness and colour contrast, etc.

The MSER blob detector (Matas et al., 2004), for example, is suitable for detecting whole regions which differ from surrounding regions in intensity and/or colour and works well with spherical objects. A blob is a spherical region in an image with (relatively to surrounding regions) similar or constant properties. The CHT, which specialises in detecting circular objects is also known for its robustness in the presence of noise, occlusion and varying illumination (Yue*n et al*, 1990). The aim of the CHT is to find circular formations of a specified radius R, in an image. A diagrammatic description is given in Figure 2-4. A set of high gradient edge pixels within an image are designated as candidate pixels that cast 'votes' in an accumulator array. There are several candidate pixels in the set forming a sphere indicated by the black circle. The candidate pixels vote around themselves in a circular pattern of a fixed radius (See Figure 2-4). By voting, each candidate pixel contributes a circular accumulator array of radius R shown by the grey broken-lines circles. The accumulator circles have a peak where they all overlap which is at the centre of the original circle. The original circle centres are then estimated by detecting the peaks in the accumulator array.

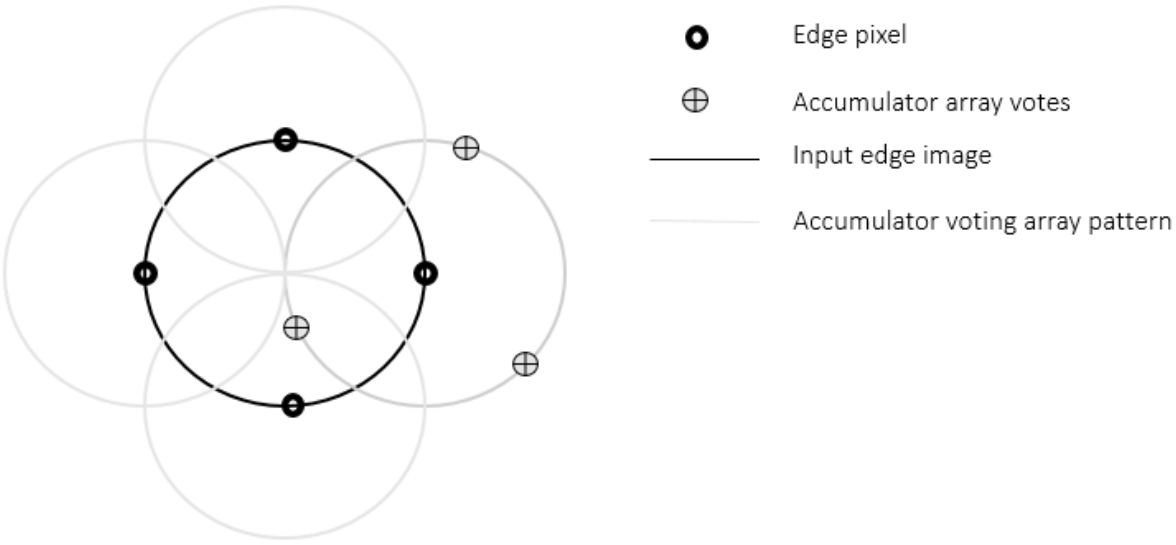

Figure 2-4: Circular Hough Transform (CHT)'s circle detection mechanism

Two CHT algorithms are used in MATLAB '*imfindcircles*' function – the two stage, and the phase coding methods (MathWorks, 2018). Both have the same computational steps but differ in the method of computing circle radii. In the two stage algorithm, radii are estimated using the estimated circle centres along with image information, based on computing radial histograms (Davies, 2012; Yuen et al., 1990). The key idea of phase coding is the use of

complex values in the accumulator array with the radius information encoded in the phase of the array entries such that radius can be estimated by simply decoding the phase information from the estimated centre location in the accumulator array (Atherton and Kerbyson, 1999).

Feature point Matching Applications review

Ji and Chang (Khuc and Catbas, 2016) used edge detection method in measuring the displacement response and modal characteristics of line-like structures such as a steel cantilever beam and cable vibrations of a cable-stayed bridge.

Circle detection of circular-shaped targets has been widely applied through intensity gradients or brightness thresholding and computing centroid coordinates (C.-C. Chen et al., 2015; Song et al., 2014; Wahbeh et al., 2003). Shan et al. (Shan et al., 2015) however, used a combination of the Canny operator method and Zernike orthonormal moment to detect circular edges to sub-pixel accuracy in their vibration response experiment. Detection of square edges have also been reported (Ribeiro et al., 2014), as well as the classic grid dots detection using Harris corner method for camera extrinsic matrix determination (Chang et al., 2010).

A laboratory system identification application was carried out on a cantilever steel beam using a target (markers) tracking method based on the circular Hough transform (CHT) (Song et al., 2014). The FREAK and SIFT methods were utilised in the deformation measurement of a stadium and railway bridge (Khuc and Catbas, 2017a, 2016), and Ehrhart and Lienhart applied the ORB method for a short span bridge deformation measurement (Khuc and Catbas, 2017a).

Shape-based tracking

This refers to the application of known tracking algorithms in such a way that depends on the shape of the target. In other words, target tracking here depends on the detection of special shapes or patterns which could be artificial or natural to the structure. Any of the already reviewed tracking techniques and algorithms can be applied here. For example, in tracking circular targets edge detection algorithms (Shan et al., 2015), or even improved brightness thresholding methods such as in (Park et al., 2014). Other examples are found in detecting line edges as in (Ji and Chang, 2008), and in the use of Harris corner detector (Harris and Stephens, 1988) to find and detect grid corners when estimating camera extrinsic matrix parameters in the full projection matrix calibration as in (Chang and Xiao, 2010). Camera calibration is described in detail in 2.1.4.

Optical flow estimation

Optical flow estimation detects the flow or motion of pixels within a target region by detecting the brightness pattern shift (Beauchemin and Barron, 1995). The optical flow function estimates the flow velocity for each pixel and reflects two basic assumptions: 1 – the image intensity remains constant for the same pattern over time, and 2 – coherent flow in adjacent pixels (Song et al., 2014). The method has several variants, but the Lucas and Kanade (LK) differential technique (Tomasi and Kanade, 1991) and the phase-based technique (Fleet and Jepson, 1990) are widely used in deformation monitoring applications. Their theories and algorithms are briefly summarized here. Mathematical details can be found in (Tomasi and Kanade, 1991) and (J. G. Chen et al., 2015) respectively.

In the LK differential technique, the brightness intensity at a point is assumed to be constant across all frames. Sparse estimation, as opposed to computation at every pixel, is applied by detecting key points in the reference image frame usually using the Shi-Tomasi corner detector (Shi and Tomasi, 1994). Image motion is then computed for each detected Keypoint across all image frames using the LK algorithm. Outlier detection can be performed using RANSAC or LMS, and image motion is estimated. In the phase-based technique, image motion at each pixel is estimated from variations of the local phase for each filtered image (Xu and Brownjohn, 2018)

Application of the LK optical flow estimation was reported in the vibration monitoring of a footbridge (Fukuda et al., 2013), and cable-stay bridge (Caetano et al., 2011). Phase-based optical flow estimation has been used in system identification, extracting dynamic characteristics in the laboratory (J. G. Chen et al., 2015; Yang et al., 2017)

Overall, optical flow estimation is a flexible and easy method that enables a complete non-target tracking. Inherently, the method works better with robust features. An 'aperture problem' means that edges are not suitable for tracking (Xu and Brownjohn, 2018), except when edge motion is one-dimensional translation where direction is known e.g. vibration of stay cables (Yoon et al., 2016). The phase-based technique is also intrinsically sensitive to illumination (Chen et al., 2017), while a sensitivity to choice of pixel location has also been reported (Diamond et al., 2017).

General summary of feature detection and target tracking methods

Accuracy:

The most accurate methods as reported in literature are based on DIC. Reported accuracies in practical applications range from 0.5 to 0.01 pixels (D. Feng, Maria Q Feng, *et al*, 2015). However, the patented algorithm by Potter and Setchell (Potter and Setchell, 2014), based on DIC, can get measurements to 1/200th of a pixel. The algorithm is assigned to and used

exclusively by iMETRUM Ltd, a company offering non-contact precision measurements of structures.

Need for user intervention:

In template matching, only the initial selection of a set of pixels is required. Others may require threshold values dependent on structural (physical) or environmental factors. For example, contrast threshold for feature detector in feature matching, and size adjustments when using circle detectors to detect specific circles.

Busca et al. (2014) compared three techniques (template matching, edge detection and digital image correlation) by applying them on a steel truss railway bridge and reported similar tracking performance between them, they also found similar performance between camera and laser interferometer measurements with a maximum discrepancy of 0.4mm. Ehrhart and Lienhart (Ehrhart and Lienhart, 2015) compared optical flow, template matching, and feature point matching by tracking features on a foot bridge; they reported a robustness to environmental conditions (snowfall) by feature point matching, and observed a drifting of measurements over time by optical flow and template matching techniques.

2.1.6 Structural displacement computation

Structural displacement is derived from the change of target coordinates on an image and the projection relationship. Projection transformation could be a fixed matrix or value throughout the monitoring tests, without any updates; or it could be based on the variation of real-time camera extrinsic matrix. In the latter option, since the camera is in one position throughout the test, variation of camera extrinsic matrix is estimated from the target – its change of position and orientation during recording. This method could estimate target motions in six degrees of freedom (6DOF). Projection transformation can be categorized as 'offline', and 'online'.

Offline projection transformation

In single camera applications, this projection transforms the target locations in the image to 2D structural coordinates using a projection transformation value or matrix. Projection transformation used is scale factor or planar homography. For two or more cameras whose views are overlapped, 3D displacements can be obtained using a triangulation method (Hartley and Zisserman, 2003). This was applied in (Chang and Ji, 2007; Jáuregui et al., 2003). A multi-camera approach provides more reliable results than a single view approach (Xu and Brownjohn, 2018). The method is however dependent on time synchronisation of the cameras.

Online pose estimation

Fixed projection transformations support only 2D structural displacement estimation. Therefore, the camera extrinsic matrix is estimated for every image frame and 3D target motions derived by comparing camera extrinsic matrix to that of the initial image frame. Applications include Chang and Xiao (Chang et al., 2010) who attached artificial planar targets with square grid patterns to a bridge for 6DOF measurements and Martins et al. (Lages Martins et al., 2015) who derived 3D structural displacements in a long-span bridge by tracking non-coplanar LED targets.

The ability to measure 6DOF structural displacements from a single camera is the biggest advantage of online pose estimation, but it requires that tracked targets should consist of at least four non-collinear points of known geometry, with rigid motions and visible during the entire monitoring period (Xu and Brownjohn, 2018). Chang and Xiao (Chang et al., 2010) reported that the technique cannot measure translation along the optical axis of the camera.

A diagrammatic summary of the entire image processing and measurement extraction procedures, with their associated techniques, are summarised below in Figure 2-5.

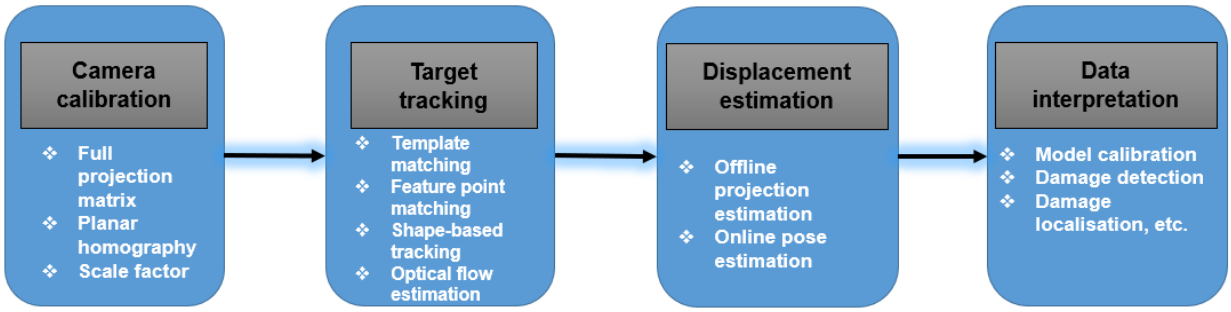

Figure 2-5: Image processing procedure and associated techniques for each step

2.1.7 State of the art in CV-based deformation monitoring

Following the preceding sections of this chapter, this section summarises the trends in contemporary techniques, practice and applications of computer vision to general structural health monitoring (including structures other than bridges) in both laboratory and field applications.

A major theme in the current state of the art of VB SHM is the significant growth in low-cost computer vision systems, which is the emphasis of this thesis. With the tremendous growth in consumer-grade camera specifications and image analysis over the past few decades, robust and practical condition assessment of structures can be performed remotely and on-site. Digital single-lens reflex (DSLR) cameras and medium to high-end phone cameras etc., are capable of speedy data acquisition, while readily-available image processing

algorithms are used for image processing to derive structural responses. For example, an iPhone 8 offers 4K resolution at 60fps, same as the GoPro Hero 6. These can easily be fitted with zoom lens if needed, for efficient monitoring, for example in (Kromanis and Al-Habaibeh, 2017) where full scale bridge deformation monitoring is carried out. For smartphones, their camera specifications and general capabilities such as ease of mobility, storage capacities, easily accessible and updateable software, and significant computational power keep improving tremendously. Therefore, they have the potential for incorporation into affordable CV-based condition assessment systems.

Earlier in Section 2.1.3, the distinction was made between single and multipoint (or multi target) tracking – the distinction technically being the length of area of the structure covered by the camera (or simply its FOV). The majority of studies have focussed on displacement measurement of a single target (i.e., localised sensing) on a bridge (Ribeiro et al., 2014). For example, Khuc and Catbas (2017a) employed fast retina key-point algorithm to match detected key points at a nut on a steel girder. Brownjohn et al., (2017) used the Dynamic Monitoring System with a template matching and super resolution image-based patented algorithm (Imetrum, 2020; Potter and Setchell, 2014) to measure mid-span deflections of the Humber and Tamar bridges. However, one of the main strengths of CV-based monitoring is the ability to collect track multiple targets offering distributed sensing (Kromanis and Forbes, 2019; Yan Xu et al., 2018). There are, however, limitations in achievable measurement resolution in the vision measurement, which can depend on, but are not limited to, the image processing algorithm and camera field-of-view. A scenario when the entire length of the bridge is fitted in the FOV of a single camera (or a few cameras) while achieving a desired measurement accuracy is possible only for short-span bridges with relatively high deflections, considering the specifications of currently available consumer-grade cameras (Chu et al., 2019; Kromanis, 2020; Yan Xu et al., 2018). The collection of accurate measurement along a length of the bridge is desirable because a structural response profile of the bridge can be generated, from which the condition of the structure can be assessed. This can be especially applicable in short-span bridges governed by static response and analysis.

2.1.8 State of the art in dynamic monitoring (including with vision and non-vision-based sensors)

This section aims to briefly review the development and state of the art in dynamic monitoring specifically. Static and dynamic CV-SHM applications rely largely on similar or related equipment and technology, for example the smartphone and its technical specifications such as frame rate and resolution. They also make use of the same

responses – example, displacements. And therefore, improvements and innovations happen synchronously. Since the thesis focusses on static applications (derived from dynamic measurements), it becomes imperative to highlight the incredible developments that have also taken place here.

Dynamic measurements often also employ the use of other sensors apart from vision, for example accelerometers. It all started with the first attempt in using mobile embedded 3D accelerometers for human movement recognition using supervised learning methods (Lau and David, 2010). A maximum sampling rate of about 60 – 70 Hz, capable of human motion capture was achieved in this study. Since then, there has been an increasing trend of smartphone applications in SHM, both in laboratory and full-scale structure scenarios. This is due to much-improved general capabilities, not limited to camera, but also to their embedded accelerometers and other sensors etc., and also due to their much-increased affordability.

Use of accelerometers

Morgenthal and Höpfner, (2012) in an early application, used an android OS smartphone for obtaining dynamic displacements and natural frequencies. The smartphone's limited range of measurable acceleration was reported to hinder full SHM utilization. They also reported temperature fluctuations and component calibrations as sources of inaccuracy in the study. The possibility of using multiple smartphones in vibration monitoring was explored in (Shrestha et al., 2018). The methodology involved the use of micro-electromechanical systems (MEMS) in place of conventional wireless sensors, which transfers information through an infrastructure network that includes phone applications responsible for acquiring, analysing, storing, and transferring useful data to the cloud. Measurements were validated on laboratory and field studies. In (Kong *et al*, 2018), sensors inside smartphones were used in monitoring a full-scale building. Recordings from the smartphones during the shaking test displayed high correlation with those from a reference sensor in the building. Crack assessment applications have also been reported such as in (Oraczewski et al., 2016). In (M. Feng et al., 2015), smartphone accelerometers are utilised for structural vibration monitoring, from which post-event damage can be diagnosed. Three different smartphones – iPhone 3GS, iPhone 5, and Samsung Galaxy 4 were utilised. Laboratory shaking tests were performed, and a field study was carried out on a dynamically loaded prestressed reinforced concrete pedestrian bridge. Observed error was less than 1% when results were compared to conventional sensors. Zhao *et al.*, (2015) developed as Orion Cloud Cell (Orion-CC) – an iOS based (7.0 or higher) software for cable force measurement. Calculated error here (between conventional wireless sensors and smartphone) was 0.54% for frequency, and for cable force measurement it was 1.09%. Zhao, Han, *et al.*, (2016)

developed a mobile application that works with multiple phones working simultaneously in obtaining vibration and geo-spatial information. Their proposed method was validated by obtaining cable force measurements from a cable-stay bridge. Other earlier CV-based crack detection systems and applications have been reported such as in (Ju L*ee et al*, 2011) which was a more advanced CV-based robotic system employing a digital camera for image acquisition.

Use of other sensors and applications

In (Zhao et al., 2017), laser-projection technology for real-time displacement monitoring was evaluated. A specimen structure with a laser device installed on it, had the laser spot projected onto a projection plate. A smartphone (iPhone 6) recognised and captured the laser spot movements and structural displacements were derived from image processing (D-viewer and Orion-CC). in (Zhao et al., 2016b), Samsung A5 and Meizu MX4 were used for measuring static and dynamic displacements. The results from the experiment showed a 0.85% error in displacement measurement, but for the suspension bridge model, the error was observed to be 6.33%. The authors also noted that the smartphone used in the study had short monitoring range and low acquisition frame rate but could be improved in subsequent studies. Kromanis and Al-Habaibeh, (2017) used smartphones to monitor structural movements by tracking blob-like features. The method was applied to laboratory structures and the Wilford Bridge in Nottingham, UK. Using a camcorder and image processing software installed in a computer, Fukuda, Feng and Shinozuka, (2010) developed an early cost-effective system and used it to monitor large infrastructure by capturing displacements of a target and movement and also included dynamic analysis. Xu *et al.*, (2018) used a technique called the Boltzmann machine in training deep learning network for crack detection in steel box girder bridges using images captured by consumer-grade camera (Nikon D7000). Zhao *et al.*, (2017) obtained bridge displacement response by photogrammetry using the “D-viewer” mobile application. Displacements were obtained using the laser projection method by tracking the changes in pixel positions using iPhone 6 and 6+. It was also validated on a medium span bridge using both static and dynamic measurements.

The use of smartphones in SHM has come a long way and shows much potential. It however requires competence in software and/or programming as these are required heavily in post-processing.

Dynamic measurements for modal identification

Non-contact monitoring systems using consumer-grade cameras offer some promise with modal identification. Feng and Feng, (2017a) , using measurements obtained with a camera (Point Grey/FL3-U3-13Y3M-C), linked measured displacement data to the quantification of

the structural health condition, by validating the feasibility of simultaneous identification of structural stiffness and unknown excitation forces in time domain using output-only CV-based displacement measurement. Xu, Brownjohn and Kong, (2018) evaluated modal frequencies of a cable-stayed bridge using consumer-grade cameras (GoPro Hero 4 Black).

Dynamic measurements for multi-point displacement monitoring

Multi-point displacement monitoring applications have also become popular, and they are important in many cases especially with larger structures. Feng and Feng, (2015) obtained multipoint displacements from a three-story framed structure and evaluated these measurements using orientation code matching (OCM) and unsampled cross-correlation – two advanced techniques in template matching. They also compared the results from a single camera, laser, and accelerometers. *InnoVision*, an image/video processing application was developed by (Luo et al., 2018). This application addressed the challenges of limited lighting, multipoint displacement, and camera-vibration in CV-based sensing systems. DeforMonit, an app developed at Nottingham Trent University by Dr Rolands Kromanis (Kromanis and Al-Habaibeh, 2017) is capable of analysing both images and videos by tracking blob-like surface features which could either be structural surface features or put on the structure by the user. In (Xu, Brownjohn and Kong, 2018), distributed sensing was used in evaluating modal frequencies using images from a GoPro Hero 4. When carrying out multi-point monitoring, adequate consideration should be given to the trade-off between resolution/accuracy and a wider object field.

Target-less tracking

Efforts have also been made to achieve target-less/non-contact structural monitoring with remarkable success. Non-contact monitoring has the intrinsic value of not requiring contact with the specimen structure, and this can potentially reduce cost and time involved in the monitoring process. The idea of non-contact monitoring is hinged on not needing an artificial target placed on the specimen structure whose movements are to be tracked by the computer-vision algorithm. This is practically realised by employing some computer-vision algorithms capable of detecting and tracking salient intrinsic features or selected pixel subsets on the structure across the range of collated image frames. These could be structural features such as bolts and joints. A review of these image processing techniques relevant in SHM has been done in 2.1.4. These techniques are just applied in this case in non-contact SHM scenarios.

Yoon et al., (2016b) proposed a target-free approach utilising consumer-grade camera in structural displacement measurement. In the absence of targets, three algorithms were utilised: the KLT for feature detection and pixel coordinates determination, the Maximum Likelihood Estimation Sample Consensus (MLESAC) for image geometry estimation, and

Eigen system realisation for St-Id. The author also outlined the procedure including – region of interest (ROI) selection, feature detection, feature tracking, and outlier removal. In the deformation measurement of a stadium and railway bridge (Khuc and Catbas, 2017a, 2016), the FREAK and SIFT methods were utilised to select key points defined as localized points that describe textures of specific locations in images, such as object corners, maxima peaks of bright- ness, or colour on the images. The motion of the key points is then tracked over time and translated to structural displacements after calibration. In (Kromanis and Al-Habaibeh, 2017) smartphones achieved contactless monitoring of both laboratory and real-life structures, by tracking blob-like features.

Challenges

Lighting, and other problems associated with weather conditions were evaluated using pattern matching and subpixel estimation image processing techniques, only 1% variation was found in the camera as compared to accelerometer measurements *(Kim et al*, 2016). However, despite the surge in use of CV-based sensors in structural monitoring applications, several challenges remain, some of which include weather conditions such as rain, fog, or wind etc., and surrounding vibrations on sensor measurements (Sony et al., 2019).

2.2 Measurement interpretation and damage detection

Civil engineering structures are constructed with longevity in mind, hence the logical need for monitoring their performance. This section builds on the previous and is charted to achieve a twofold aim. Firstly, it takes the reader on a journey briefly through the historical development and literature, then through to the contemporary practises in structural performance evaluation and damage detection. Secondly, the chapter introduces the reader to, and reviews the current practise of employing advances in video technology and CV-SHM outlined in Section 2.1 to contemporary damage detection and condition assessment in horizontal civil structures.

2.2.1 Why monitor structural performance?

Usually, a design life is stipulated on structures as part of the design process. During the design life of any structure, its response to loads are expected to not exceed calculated thresholds stipulated by the design. But this has not always been the case. Civil engineering, well at least in the various forms in which it existed, either as part of the age-long '*military engineering'* or otherwise, had been taught and learnt as a craft or art. Prior to the eighteenth century in Europe, most civil engineers were nurtured through pupillage systems where they learnt their craft from more established figures.

The foundations of today's structural engineering can be attributed to the works of the great 17th century pioneers, amongst them Galileo Galilei, Robert Hooke and Sir Isaac Newton. In 1631, Galileo had published his paper where he articulated to a large extent the sciences of strength of materials and object motion (Favaro et al., 1954). This was to a large extent, the first detailed scientific and mathematical approach to structural engineering including also one of the first attempts at developing the beam theory. It signalled the beginnings of mathematical analysis and design of building structures. Other mathematical breakthroughs in elasticity, laws of motion, beam equations, and virtual work theory followed in quick succession in the same century and the next. These tools became fundamental, and radically expanded the possibilities in analysis, and design of even more sophisticated structures. Thus, structural engineers started basing designs, especially larger ones such as bridges, to a larger extent on mathematical rigour; and documentation; and quality control became a reality. Structural response of structures thus became measurable using mathematical calculations. Mechanical/electrical advances also meant that these structural responses could be conveniently physically measured.

With the possibilities created by mathematical and technological advancements, engineers have become concerned with quality control and structural performance. Since structural performance can be predicted even before the structures are built, - and designs based off these predictions, it becomes logically imperative that they are evaluated periodically to ensure agreement between predicted and actual behaviour. These evaluations inform engineers in the lifecycle management and operation of structures: - they help to ensure that the structure is performing as expected, and if not, anomalous behaviour can be detected, analysed, and possible interventions provided. These evaluations are also very essential especially since many structures in use today have achieved, or are near to achieving their design lifespans. They also serve those interested in research, as performance data are studied, and learnt from.

The premise here is that from analysing measurements obtained from monitoring, the condition and performance of the structure can be assessed, and possible damages detected.

2.2.2 Condition assessment vs structural health monitoring

Condition assessment and structural performance (or health) monitoring are two types of investigations used in the lifecycle management and operation of bridges. Condition assessments are relatively routine, and are predominantly visual inspections with desk-based studies and assessments using appropriate guidance documents (Design Manual for Roads and Bridges, 2007). On special occasions, condition assessments could also involve non-destructive evaluation (NDE) technologies such as impact echo (IE), ultrasonic

surface waves (USW), ground-penetrating radar (GPR), half-cell potential (HCP), and electrical resistivity (ER) (Shokouhi et al., 2006), and even advanced sensing systems. These exhaustive campaigns are used in the short-term to assess the condition of a bridge at any instance in time. NDE technologies have a vast usage in bridge condition assessments, for example, reinforced concrete structures like bridge decks usually experience degradations over time for many reasons including chemically-induced (alkali–silica reaction, carbonation, corrosion, leaching, salt and acid action, etc.), physically-induced (creep, fatigue, shrinkage, etc.), and even initial quality of the deck; these can be ameliorated using a suite of NDE technologies, for example, HCP testing provides information regarding the likelihood of active corrosion, and IE enables detection and characterization of delaminated areas on a concrete deck, and GPR has shown the ability to detect severely delaminated areas (Gucunski et al., 2010).

Of all these, the IE method (see Figure 2-6) perhaps has had the longest history. Generally, acoustic methods, in their raw form – striking an object and listening to the sound to detect the presence of voids, is the oldest form of Non-Destructive Testing (NDT) apart from visual inspections (Sansalone and Carino, 1986). Technologies have over the years, combined these raw practises with sound analysis techniques to identify and quantify these damages (Zhang et al., 2016), of which the IE method, introduced by Carino and Sansalone (Sansalone and Carino, 1986) is a prime example. Condition of structures can also be assessed by controlled load testing with heavy vehicles, for example direct evaluation of load capacity (Bakht and G. Jaeger, 1990), or dynamic testing for modal flexibility evaluation (Mark *et al*, 2001; Catbas, Brown and Aktan, 2006) which leads to model calibration and indirectly to capacity estimation. These, however are labour-intensive operations and are heavily manned.

Structural Health Monitoring, on the other hand, insinuates continuous measurement collation of load/response data over time that can vary from days to a lifetime, in the form of time series, the primary aim being to establish statistical properties and performance bounds of loading and response, and characterise their relationships (Brownjohn et al., 2014). Having established these relationships, variations in, and deviations from them can be attributed to an anomalous behaviour or performance problems. Many technologies such as strain and deflection measurement equipment have shared usage between both monitoring and assessment exercises. The more sophisticated monitoring systems also perform a continuous condition assessment due to density, comprehensive coverage of the instrumentation and direct links to ‘physics-based’ analytical models (Brownjohn et al., 2014).

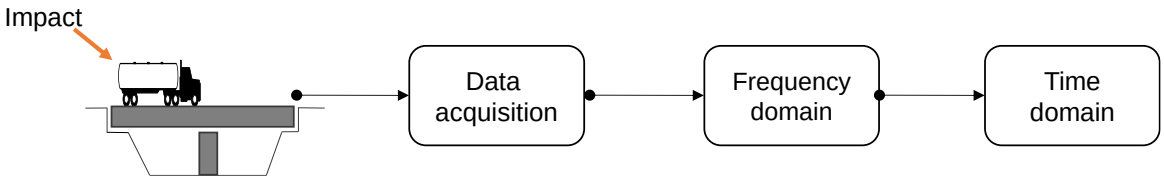

Figure 2-6: Impact echo method

Many large bridges are equipped with Structural Health Monitoring (SHM) systems, such as the Humber bridge (Brownjohn et al., 1994), and the Wind and Structural Health Monitoring System (WASHMS) system on the Tsing Ma (suspension bridge), Kap Shui Mun (cable-stayed bridge), and Ting Kau (cable-stayed) Bridge in Hong Kong (Wong et al., 2000). The majority of SHM systems employ contact sensors such as fibre optic sensors, wireless sensor nodes, global positioning systems and traditional wired tilt, displacement and strain sensors. Factors influencing the cost of an SHM system and its operation are number and type of sensors, access requirements to the structure, system maintenance and data interpretation software/tools/experts. Due to increasing popularity, SHM systems are frequently installed in newly built, large bridges, examples are the Queensferry Crossing in Scotland whose array of 2300 sensors monitor strain, acceleration, displacement and environment (JFTS, 2019) using tri-axial strain gauges and accelerometers, load cells, temperature sensors, displacement transducers; and the new I35W bridge in Minneapolis, USA which has fibre-optic sensors installed (Patterson, 2010). The condition assessment of older assets however, especially those with a small volume of traffic, still rely solely on visual inspections due to high costs associated with the installation, operation and maintenance of such SHM systems.

But in practice both terms – structural health monitoring and condition assessment, are sometimes used interchangeably. Indeed, regular condition assessments, measurement obtention events, or even inspections could form part of an SHM campaign that could last for as long as required. What seems vital are that the inspection, condition assessment, or measurement obtention techniques are consistent and reliable. This thesis proposes such an arrangement of regular scheduled measurement collection events, where obtained are analysed each time for anomalies or damages in the structure.

Figure 2-7: Queensferry crossing (Brownlie, 2017)
Note: Shutterstock Standard Image License

2.2.3 Damage detection in beam type structures including with CV-based sensing

Contemporary condition assessment methods – visual inspections and local NDE techniques practically need an a priori global location of a damage in a structure, as well as easy and unhindered access to the damaged region for effective assessment (See Section 2.2.2). Thus, any damage detection techniques capable of a global analysis is desired by all stakeholders in the industry. Global analysis here refers to a non-local damage assessment, for example when a whole bridge can be monitored such that damage at any location can be detected. A global damage detection technique is expected to at least:

- Detect if a structure is damaged.
- Locate the damage if any.
- Estimate the damage severity.

Vibration-based techniques

Most, as well as the earliest of damage detection techniques were often based on the dynamic properties of the structures. Vibration-based damage identification (VBDI) techniques are usually applied in the SHM of bridges subjected to considerable dynamic

load. These methods are sometimes classified into acceleration-based and strain-based methods.

Acceleration-based techniques

The premise of acceleration-based methods is that changes in the vibration modes of structures are usually as a result of the presence of structural damages, and these changes manifest as modifications in modal parameters such as natural frequencies, mode shapes and modal damping values (Salawu, 1997). These parameters are easily obtainable from vibration testing. An abnormal stiffness loss can be detected when resonant frequencies are significantly lower than expected. The reverse can also be detected and indicate that supports are stiffer than expected (Morgan and Oesterle, 1994). A thorough review of early dynamic-based damage detection methods and principles was carried out by Salawu, (1997).

The fact that cracking in beam structures cause but small changes in natural frequencies reduces the efficiency of these methods (Salgado et al., 2006). Thus, other related techniques became commonplace. The Modal Assurance Criterion (MAC) is one of the earliest methods used for comparing mode shapes. The MAC is a statistical indicator, based on the least squares form of linear regression analysis and yields an indicator that is most sensitive to the largest difference between comparative values and results in modal assurance criterion that is insensitive to small changes or small magnitudes (Pastor et al., 2012). The coordinate modal assurance criterion (COMAC) compares the change of the mode shapes at various points on the structure. Building on these early techniques, Pandey, Biswas and Samman, (1991) found that curvatures (defined as the second derivative of mode shapes) is more damage-sensitive than ordinary mode shapes. The damage index method, based on the curvature method, was proposed by (Stubbs et al., 1995). Wavelet analysis is another promising technique for damage detection. It was first applied in civil engineering structures considering the mode shapes of a cracked simply supported beam obtained from modifying its stiffness matrix (Liew and Wang, 1998). Chang and Sun, (2005), proposed a method that involves decomposing the dynamic response into wavelet packet components; a given component's energy and level of decomposition is obtained for all the measuring points, and finally, these energies' curvatures are calculated and the damage is said to be a local disturbance along the beam. An extensive review of damage detection methods based on frequency domain modal property changes, including natural frequencies, mode shapes, mode shape curvatures, modal strain energy, etc., are presented in (Carden and Fanning, 2004).

Strain-based techniques

A review of strain-based, vibration damage detection strategies, oriented mainly towards civil infrastructure was carried out in (Ren and Zhou, 2013). Strain-based, vibration techniques have the inherent advantage of a relatively global testing of the entire structure, but also the limitation that a large enough damage needs be present to alter modal shapes. In (Li, 2010), the authors, concluded that at least for beam-like and truss structures, strain modal shapes are a more damage-sensitive feature than modal displacements. The accuracy however of these strategies for damage quantification are yet to be verified (Güemes et al., 2018).

Static response techniques

The static equilibrium equation is related only to structural stiffness. This makes static structural assessment/damage detection/structural identification (St-Id) inherently easier and less prone to error. In St-Id, even though vibration testing is much more common and developed, using static response still maintains the advantage that it requires only stiffness properties, as opposed to the use of mass, stiffness, and damping properties in dynamic testing. Also, adequate control of excitation for precise mode-shape estimation could be difficult in field applications. Thus the structural response measured in static tests is more precise than the structural response measured in modal testing and are expected to yield more reliable results (Bakhtiari-Nejad et al., 2005).

Since the static response is related only to structural stiffness, accurate static responses such as displacement, strain data, inclination angles, and displacement curvatures can be obtained or derived relatively rapidly and easily. Hjelmstad and Shin, (1997) proposed a damage detection and assessment algorithm based on a parameter estimation and an adaptive parameter grouping scheme that with known baseline parameter values, localises damage in a structural system with sparse measured data. Using a numerical simulation study on a planar bowstring truss structure, the algorithm can assess the sensitivity of each member parameters simultaneously with the damage detection procedure, but due to the number of perturbation trials used in the study, requires too much computation.

Static response (such as displacements, strains, tilt angles and curvatures) thus forms the basis for several damage detection techniques that may be applied to such short-span structures (Abdo, 2012; Chen et al., 2005; Gauthier et al., 2008; Kromanis and Liang, 2018). Responses such as curvatures and tilts are derivatives of the deflection curve, so are directly related to bending moment and flexural rigidity, and therefore will be affected by any change in the latter, and which is the premise on which much of the literature here is built (Abdo, 2012; Chen et al., 2005; Erdenebat et al., 2018). More recently, Erdenebat et al., (2018) used the deflection curve to derive curvatures and tilts for damage detection. The

method resolves the problem of unknown initial structural conditions by using numerical or theoretical models with known initial conditions as a reference system, and the method was validated using CV-based sensing. One advantage of static testing over dynamic methods is that it is possible to exploit mainly stiffness properties of the structure, which can be obtained easily and may yield more reliable results for damage detection than dynamic testing (Bakhtiari-Nejad et al., 2005). Damage detection here may then be classified according to the response used – for example displacements, or inclination angles.

The use of derivatives of the deflection curve in these studies above require much structural information such as on loading type, material properties, boundary conditions, as well as geometry (e.g., distance from support to region(s) of interest), or even initial conditions. This has led to the development of a wholly data-driven response obtention approach in CHAPTER 3 (also see (Obiechefu and Kromanis, 2021)) where displacements, strains, tilts, and curvatures can be obtained from a structure in its present state, and requiring no contact, and no previous structural information nor differentiation of the deflection curve. Based on this, a damage detection technique was also established in the same chapter where response collated at a first measurement collection event forms a baseline condition with which subsequent response is compared to infer the presence or otherwise of damage. The particular techniques in static damage detection are reviewed next.

Curvature techniques

In static structural damage detection literature, the use of some form of structural curvature technique to detect and localise damages features prominently. In mathematics, curvature as a term, is associated with a band of inter-related concepts in different areas of geometry/differential geometry that describe the degree by which a geometric object such as a surface or curve deviates from a flat plane or line respectively. For a circle, the curvature (k) is given as a reciprocal of its radius of curvature (R):

$$k = \frac{1}{R} \qquad 2.8$$

In beam theory, this relationship holds true and is related to the moment equation. In general, the moment/curvature relation or the basic differential equation that governs beam deflection can be expressed as follows and can determine curvature at any point of the deflection curve:

$$k = \frac{1}{R} = \frac{\delta^2 y}{\delta x^2} = \frac{M}{EI} \qquad 2.9$$

Thus, curvature values at any point(s) on a deflected beam from one or more scenarios can be obtained and compared to one another. This is the basis of static curvature-based damage detection literature till date.

Application review

One of the earliest applications of this theory in damage localisation was in (Pandey et al., 1991). Chen, Hong-ping and Chuan-yao, (2005), proposed a damage localisation and St-Id technique that utilises the grey relation coefficient to define and detect outliers in nodal displacement curvatures along the beam. The cantilever beam numerical model validation showed that the method can localise even slight damages of 7% stiffness loss and can quantify damage magnitude by minimising the output error vector using the quadratic programming technique with high accuracy. Grey's coefficient was used also in (Abdo, 2012), which was a parametric study using displacement curvatures in structural damage localisation. The robustness of the method was tested with added measurement noise. The methods, however, were not tested on laboratory structures with a seeing system, which may produce measurement errors, neither has there been any full structure application of the technique despite promising numerical results. Gauthier et al., (2008) proposed a higher order derivative discontinuity (HODD) technique which requires no reference to an intact structure. In the technique, it is shown that localised damage causes large discontinuities in the magnitude of the fourth derivative, and stiffnesses losses as low as 0.15% can be detected. In (Helfrick et al., 2009), curvature changes in an aluminium cantilever beam obtained using DIC were investigated for damage detection, where damage was inflicted as cracks in the beam.

Dworakowski *et al.*, (2015) developed two algorithms for CV-based applications – line segments method (LS), and the voting methods, and also utilised a third one – the second derivative (SD) method. These algorithms are applied to data obtained using two canon EOS 5D MKII cameras and DIC and are designed for damage detection in cantilever beams when damage is inflicted as a crack or single cut out. The algorithms adopt a global approach by utilising the whole deflection curve which reduces noise sensitivity and increases damage detectability. (S*un et al*, 2017) proposed a method in which static displacements of a bridge are obtained by decomposing the dynamic displacements. Curvatures are then calculated using static displacements. Perhaps one of the most interesting and recent applications is found Erdenebat et al., (2018) which proposed the deformation area difference method (DAD) using deflections, inclination angles and curvatures for condition assessment of concrete structures. The method uses numerical or theoretical models with known initial conditions as a reference system. The method was validated using both numerical and laboratory models with CV-based measurement at

severe damages (i.e., 60% reduction of bending stiffness for a part of a beam section). The method did not include strain measurements as a damage sensitive feature. More applications of this technique from the same author is found here: (Erdenebat et al., 2019; Erdenebat and Waldmann, 2020).

Use of strains and inclination angle measurements

The use of tilt sensors for inclination measurement finds utility in several engineering and research domains. Fiber Bragg grating (FBG) based tilt sensors are popular in geotechnical operations where they are used to monitor ground movement (Peng et al., 2006; Wang et al., 2015). Ground movements and landslide monitoring are also achieved typically using grouted inclinometer casings where the related strain change along the casing can be used in calculating cumulative lateral displacement of surrounding soils (Ho et al., 2005; Pei et al., 2011; Wang et al., 2015). A thorough review of FBG sensors for geotechnical health monitoring can be found in (Hong et al., 2016).

In Bremer *et al.*, (2016), the application of FBG tilt sensors for tunnel SHM was reported; here tilt sensors were specifically used to detect tunnel misalignment. In (Dong *et al*, 2018), the use of a micro-electro-mechanical system (MEMS)-based three-axis acceleration sensor is described; the sensor measures the tilt angle of a tower body by employing a method based on the difference between the acceleration due to combination of gravity and other stresses and the acceleration due to gravity alone. The angle which is generated between the two accelerations corresponds to the slope of the sensor and the tile angle of the tower body. In Kromanis and Kripakaran, (2014), measurements from tilt sensors are utilised in validating the proposed regression-based anomaly detection methodology for structural response, from distributed measurements. In Xiao, Hulsey and Balasubramanian, (2017), tilt sensors were used to monitor rotation at bridge supports. A railway anomaly detection patent partly utilising tilt sensors was filed in the USA (Bryan, 2000). Till date only a few studies (Erdenebat et al., 2019, 2018)have used CV (Computer Vision) based sensing to validate inclination angles as damage sensitive response. As can be inferred from above, tilt measurements, have been employed in general condition assessment of several civil structures, and have yielded good results.

Accurately measuring strain is becoming more critical in the monitoring of modern structures. With the difficulties posed by contact strain gauges, obtaining strain from multiple locations along a horizontal structure becomes difficult. An increasingly current trend however, is the calculation of strain from displacement data obtained from CV-based sensing. Apart from a handful of especially laboratory and few field applications, there is not yet much done in this regard, and it is still very much a new but rapidly developing sphere of CV-SHM; but however, all tests done so far show agreement between strain

measurements from CV-sensing and contact sensors, thereby promising reliability. For example in Kromanis and Forbes's (2019) paper, strain was calculated from displacements obtained from two devices – the low-cost robotic camera system (RCS) and a smartphone camera. Strain measurements agreed with contact measurements, and with a minimum accuracy of $^{1}/_{50^{th}}$ of a pixel or $10\mu rad$. Though this is ten times less than patented algorithms like imetrums' (Imetrum, 2020; Potter and Setchell, 2014), it is still of reasonably high precision, bearing in mind its affordability.

Damage detection from CV-based derived static response

The application of CV-based SHM entails that response measurements as described in the previous section (0) can be obtained using CV-based techniques. Damage detection, localisation, severity, and other parametric studies can then be carried out. A thorough review of CV-based deformation monitoring, through which structural condition assessments can be carried out has been done already in sections 2.1 and 2.1.4. However, there is still not enough literature on its applications in damage localisation and estimation of damage severity, but there has recently (say in the past decade) been an exponential increase in peer-reviewed, published research in the area, and even real-life field applications. But this area is still in infancy – relatively speaking, and most research is still laboratory-based.

Clearly, the degree to which damage detection is possible or effective is contingent on the degree of accuracy of obtained measurements. The accuracy of measurements depends on the specifications of the image acquisition device, and the pixel resolution achievable from image processing (Obiechefu and Kromanis, 2021). The author suspects that this is why it seems the CV-based damage detection frontier lags behind the damage detection frontier. It makes logical sense that damage detection techniques are developed based on the most accurate (and maybe practical) measurements achievable, which may then be adopted for use with CV-based sensing only if and when its accuracy (the CV-based sensing) matches that on which the damage detection technique was based. Therefore, the search for applications in literature focuses on what damage detection techniques have been validated using CV-based sensing as opposed to techniques made for CV-based sensing alone. Also worthy of note is that CV-based damage detection from dynamic response and modal analyses still dominate this field, applications from mainly static response remains scarce. Some of these applications have already been reviewed in the preceding section but are highlighted here for emphasis. In Helfrick et al., (2009), curvature changes in an aluminium cantilever beam obtained using DIC were investigated for damage detection, where damage was inflicted as cracks in the beam. Dworakowski *et al.*, (2015) developed two algorithms for CV-based applications (using two canon EOS 5D MKII

cameras and DIC) – line segments method (LS), and the voting methods, and also utilised a third one – the second derivative (SD) method. Also noteworthy is that the algorithms adopt a global approach by utilising the whole deflection curve which reduces noise sensitivity and increases damage detectability. Perhaps one of the most interesting and recent applications is found Erdenebat et al., (2018) which proposed the deformation area difference method (DAD) using deflections, inclination angles and curvatures for condition assessment of concrete structures and was validated using both numerical and laboratory models with CV-based measurement at severe damages (i.e., 60% reduction of bending stiffness for a part of a beam section). The DAD method uses numerical or theoretical models as a reference system and is able to detect local stiffness reductions of as little as 1% in theoretical models, and 23.8% in laboratory models, with CV measurement (Erdenebat et al, 2018; Erdenebat, Waldmann and Teferle, 2019). The method has also shown to be suitable for measurement collection on real structures with stationary loads only (Erdenebat and Waldmann, 2020).

CV-based sensing strategy

The practical utilities of a bridge condition assessment framework based on affordable CV-based sensing systems is clearly desirable. This has been discussed in the introduction. The practicability of a CV-based sensing strategy is dependent on the ability of the image acquisition device (with help from image processing algorithm) to accurately capture and detect changes in measurement response, which are sometimes very small. For example, for strains as small as 1μ to be calculated, displacements in the order of $1/50^{th}$ of a millimetre must be captured. The capability of the image acquisition device to accurately capture these changes in turn depends on its specifications, for example its resolution, as well as the pixel resolution of the image processing algorithm. This subject is important particularly as the proposed methodology is based on the use of affordable consumer-grade cameras, and require multi-point displacement estimation.

Ensuring accuracy if several images from different devices have to be stitched together had been a relatively unexplored territory. This may now be done with the use of one of several third-party software. For example, Kromanis and Forbes, (2019) introduced a low-cost robotic camera system (RCS) for accurate measurement collection of structural response. The RCS automatically captures images of multiple (successive) portions of the structure using a robotic mechanism for camera rotation and open-source software for wireless communication. Images are high pixel density and measurements more accurate, as pixels are concentrated on each captured portion, as opposed to capturing entire structure with a single camera. Results from a statically loaded laboratory beam test bed show that the accuracy of measurements collected with the robotic camera system are in a good

agreement with the contact sensors and much higher than those obtained with a smartphone camera. Another major challenge to the entire framework itself is how to ensure that the cameras are placed at exactly the same location when the structure is to be inspected at another time after a first inspection. With regard to this, a multi-epoch imaging approach was introduced (Kromanis and Liang, 2018), which transforms feature locations captured from devices at different positions to a reference coordinate system as derived from one phone. This can be applied to this framework by setting the reference coordinate system to the device used in a first inspection.

2.3 Conclusions and gaps in literature

Figure 2-8 below is a comprehensive flow chart of the main topics and sub-topics that have been treated thus far in the review of literature.

This chapter was divided into two sections:

- Section 1 – Review of CV-based deformation monitoring: here, the history, development, and state of the art in CV-based deformation monitoring was reviewed. The procedures involved in the entire CV-based deformation monitoring process including measurement obtention and response extraction were also reviewed alongside their applications in both the laboratory and field. These processes include camera calibration, image processing and feature tracking, and structural displacement computation.
- Measurement interpretation/damage detection: this section reviewed techniques that have been used in condition assessment and SHM of civil structures; from dynamic methods, then more specifically to static damage detection and localisation techniques. Use of static responses such as displacements, curvatures, inclination angles, and strains for damage detection and localisation were also reviewed. Discussions on the compatibility of such techniques with a CV-based sensing system were also provided.

From reviewed literature, gaps were identified within the scope of the thesis. These are the themes that would be investigated in the research.

The research is focused on the obtention and interpretation of structural response measurements using CV-based systems. Applications of deformation monitoring and other forms of SHM abound and have been covered in this chapter. Damage detection techniques also abound and have been covered. But the gap starts to appear when searching for damage detection methodologies evaluated using CV-based sensing. In other words, there is a lot more focus on response obtention or monitoring using vision- based sensing, since damage detection requires high measurement accuracy and specialised measurement

analysis or damage detection techniques. This research hopes to add to this field by evaluating formulated damage detection methodologies with response measurement obtained using particularly affordable CV-based sensors such as smartphones, so as to ascertain their effectiveness, efficiency, and accuracy. As earlier mentioned, this depends to the achievable accuracy obtainable from affordable camera devices, with help from sub-pixelling image processing algorithms.

The second area exploited in the research lies in the formulation of the damage detection techniques themselves. The use of derivatives of the deflection curve in damage detection and measurement response analysis is found to be prevalent in literature. As discussed earlier in this chapter, their use requires much structural information. For example, to obtain '*curvature*' as defined in literature on a bridge structure, information such as loading type, material properties, boundary conditions, as well as geometry (e.g., distance from support to targets), etc, must be known. This is evident in literature on use of curvature in static load-based damage detection, both for numerical models and laboratory validations including with the use of CV-based photogrammetry for response obtention (Abdo, 2012; Erdenebat et al., 2018; Helfrick et al., 2009; Jáuregui et al., 2003; Lee and Eun, 2008; Sun et al., 2017). Therefore, the opportunity for development of a more data-driven response obtention and damage detection approach is addressed in this thesis. Based on this, a damage detection technique is also established in the next chapter where response collated at a first measurement collection event forms a baseline condition with which subsequent response is compared to infer the presence or otherwise of damage. This novelty is discussed in more detail in section 3.5 where the contribution to knowledge has been explicated.

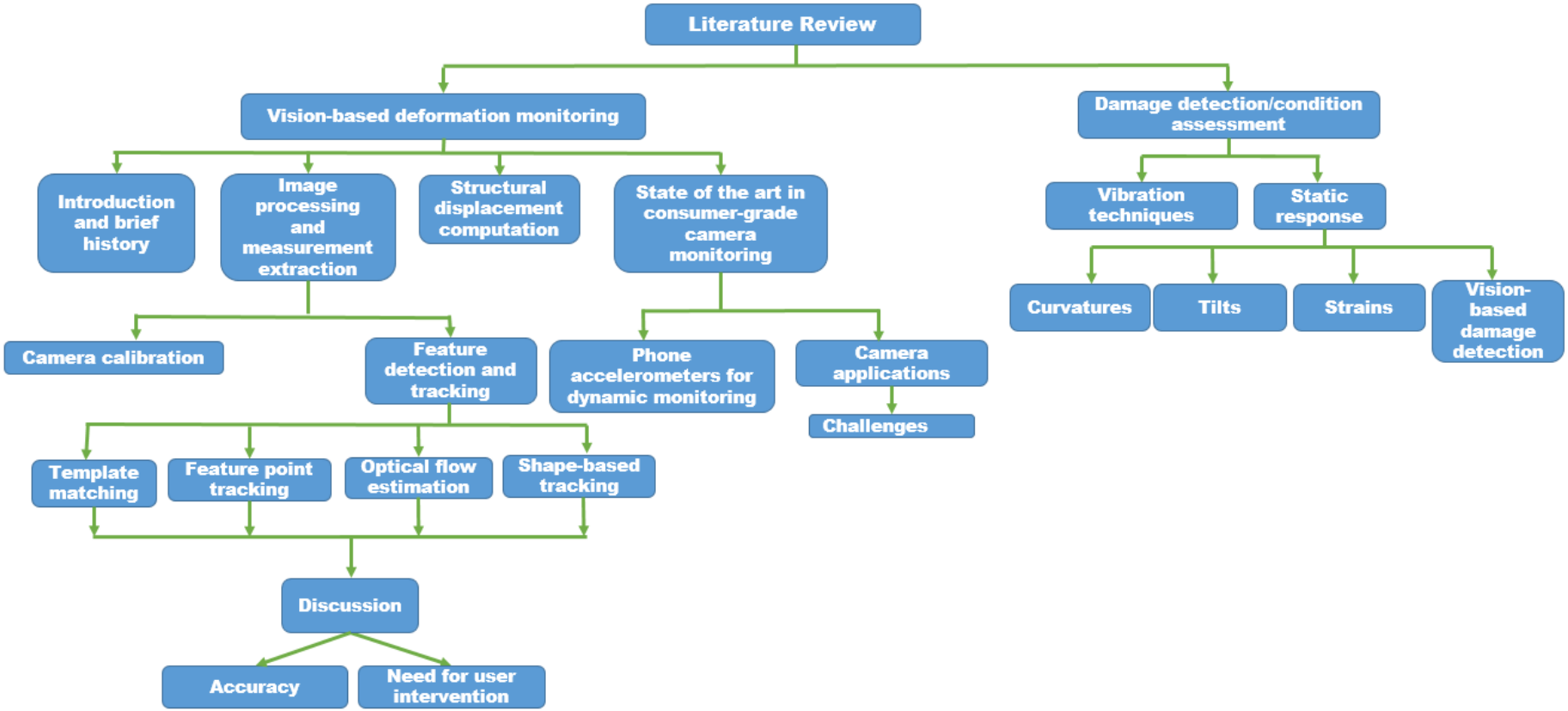

Figure 2-8: Chart of reviewed literature

CHAPTER 3 | METHODOLOGY – COMPUTER VISION-BASED SHM AND DAMAGE DETECTION IN HORIZONTAL STRUCTURES

Bridges are designed to safely carry and resist a range of loads, from cyclic thermal to human and vehicle loads which have both static and dynamic components. This chapter makes the case for a simple, and affordable CV-based condition assessment of bridge structures, and describes in detail, techniques that can be used in analysing the static response of bridges, establishing an *'intact'* or *'undamaged'* state, which is used in defining a *'damaged'* state, and then accurately locating the presence of damage.

The chapter starts with a general introduction to the idea of structural performance evaluation by way of analysing the load/response chain, as well as a brief overview of static and dynamic loads on bridges.

Structural response using affordable CV-based system is described in detail in the body of this chapter. The procedure broadly consists of a measurement collection phase, and an image processing phase, at the end of which structural response is obtained.

The damage detection techniques are based on the premise that the presence of some form of damage on a structure alters its stiffness properties, thereby causing changes to its response to applied load. This variation in structural response is analysed and interpreted using the techniques developed in this chapter.

3.1 Structural performance evaluation and prediction

During the design life of a structure, its measured responses to loads are expected to not exceed calculated thresholds stipulated by the design codes which govern the structure's design and construction. However, this is not always the case as several other metrics for example, design flaws can cause progressive or rapid deterioration or collapse of a bridge well within its design life. The bridge failure in Genoa, Italy, in 2018 took lives of about 43 people (Osborne, 2018). That of the I-35W Bridge over the Mississippi River in the USA in 2007 killed 13 and injured another 145 (Harlow, 2018). These serve as painful reminders of the real possibilities of bridge collapses. Older assets also, especially those with a small volume of traffic, and which still rely solely on visual inspections due to high costs of monitoring systems, require frequent structural performance evaluations, as they are nearer to or about the end of their design lives. Many of these bridges are already on weight restrictions as reported by the RAC Foundation (RAC Foundation, 2020, 2017). Asides the

prevention of collapse and early detection of anomalous behaviour, structural performance evaluations are of high importance for researchers, as it gives new insights and understanding of structural behaviour. Many larger structures all over the world have been equipped with expensive and complex monitoring systems. An example would be the Wind and Structural Health Monitoring System (WASHMS) on the Tsing Ma (suspension bridge), Kap Shui Mun (cable-stayed bridge), and Ting Kau (cable-stayed) Bridge in Hong Kong (Wong et al., 2000).

To explore and predict structural behaviour, a systems approach consisting of inputs and outputs is appropriate and is typical. Inputs can be considered as loads on the system, either static, dynamic, or ambient; while outputs can be considered as response parameters obtainable due to inputs (e.g., displacements, inclination angles, strains, curvatures etc.). For this to be the case, the structure will have to be modelled either as physics-based or data-driven, as described in Chapter 1. Physics-based models such as those modelled with the use of Finite Element (FE) software are very popular and effectual in most industry and academic based applications. The pieces of software are based on design assumptions and mathematical computations which may be linear or non-linear, and based on design parameters, material properties etc. For SHM applications, data-driven models have been acknowledged for being more effective, especially with the deluge of data that comes with monitoring campaigns. Data-driven models deal directly with measured response and uses this in its predictions. A hybrid of both models has been utilised however, for example in (Bakhtiari-Nejad et al., 2005; Beauchemin and Barron, 1995; D. Feng et al., 2015; Hong et al., 2015; Mark et al., 2001) where physics-based models are used to calibrate data-driven models.

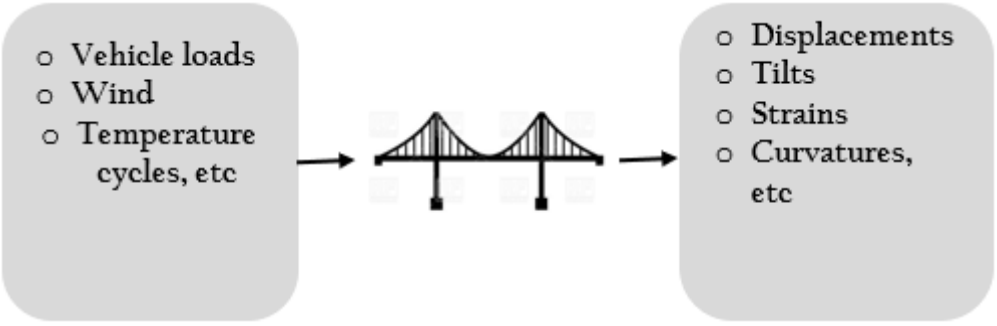

Figure 3-1: Predicting structural behaviour with system inputs and outputs

3.2 Static and dynamic loads on bridges

Inputs used in structural performance evaluations are basically loads. And all bridge structures are subjected to multiple loading configurations and scenarios, mainly from dead, vehicular, wind, and thermal loads. For design purposes in especially for short span bridges,

static analyses are mainly used. They are deemed enough for analyses purposes as the dead load from the structure itself outweighs by orders of magnitude, any other loadings that may be considered; thus, simple dynamic load allowances are made to accommodate dynamic effects. Nonlinear Static Analysis (Pushover Analysis) may also be used to determine displacement capacity of a bridge structure by incrementally increasing load until the structure reaches collapse.

In free vibration analysis, vehicles like trains and cars crossing a bridge at a given speed generate dynamic effects. Parameters on which the dynamic response of the bridge to a moving load depends on include – the impact factor of the vehicle which decreases as bridge span decreases, surface roughness, mass, damping characteristics of the bridge, spring stiffness, speed, damping characteristics of the vehicle, etc. vibration analyses would be crucial for long span bridges subject to wind loads.

The techniques developed in this work would be mainly concerned with analyses of static response from small to medium size bridges, especially those for whom dynamic properties dominate less. A review on applications of deformation monitoring and damage detection using static load components/response can be found in Chapter 2. In this chapter, static deformations of moving loads are obtained using CV-based sensing methods described next. Techniques including curvatures, strains, and inclination angles are then used to analyse the displacement response measurements for damage detection and localization.

3.3 A CV-based condition assessment framework for bridge management

3.3.1 Overview

The premise of the methodology is this: – the presence of damage in a structure will alter its stiffness properties, and consequently its structural response. Thus, by comparing response measurements collected at a first inspection (R_0) – i.e., when the structure is assumed to be in a healthy state, with those collected at a latter inspection (R_i) – where i can be an inspection schedule number, the relative state of the structure can be determined. Mathematically, we can say that:

$$\Delta R_i = R_0 - R_i \qquad 3.1$$

Where ΔR_i is difference between a baseline and subsequent response. In a no-damage condition, ΔR_i should be very close to 0, i.e., $\Delta R_i \approx 0$.

Many technologies and equipment can be used in structural response obtention as has been laid out in previous chapters of this thesis. The methods presented herein however, explore affordable CV-based sensing for response collection. The application of affordable

CV-based sensing systems is hinged on their ability to detect ΔR_i, which could be really small changes in measurement response. The proposed methodology forms a simple condition assessment framework that can support inspection routines with a cost-effective CV-based monitoring and damage detection system employing affordable camera devices such as smartphones and/or Go Pros. The set-up of the CV-based system is depicted diagrammatically in Figure 3-2.

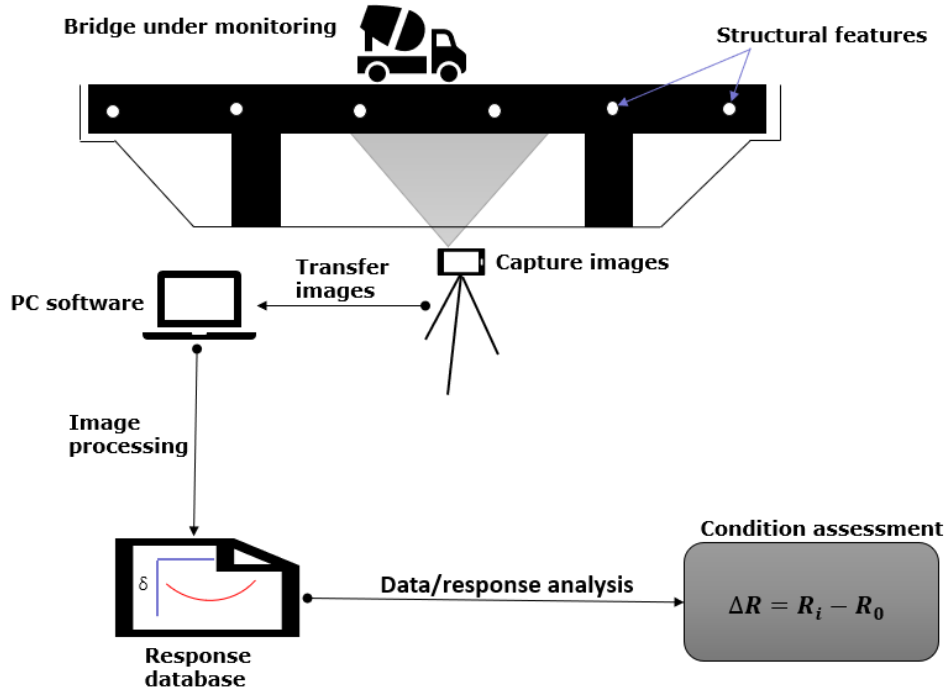

Figure 3-2: CV-based monitoring set up

3.3.2 Framework

A CV-based monitoring system simply consists of a fixed image acquisition device(s) and image processing software. The set-up stage begins with setting up a tripod in a remote and stable location within clear view of the structure. During a measurement collection event, a camera acquires images or videos when the structure is loaded, for example when a tram crosses a bridge. Cameras are focused on either the entire bridge or at selected part(s) of it. These images are then analysed using image processing algorithms which track targets on the structure and extract required structural response information such as displacements, curvatures, strains, and inclination angles. Targets may be artificial such as markers, aruco codes or checkerboard targets etc. Structural response such as deflection and curvature from targets along the bridge's length is computed from each image frame. When response from all image frames have been calculated, absolute maximum response values from time histories of each target location are extracted. These form a response profile along the bridge's length, from here on referred to as bridge response profile. The bridge response at the first inspection is assumed to represent baseline conditions of the

bridge. In each new monitoring or measurement collection event, bridge response is obtained and compared to baseline bridge response to assess the condition of the bridge. Derived structural response measurements are stored in a data bank where authorised personnel and researchers have access to. Results from structural response assessments using afore-mentioned techniques will help inform authorities of any needed interventions. A general condition assessment framework for a bridge is shown in Figure 3-3.

Information extracted during image processing is the primary response – which is displacement. Three further responses (called secondary responses as they are calculated from primary response) are developed from displacement data – curvature, strains, and inclination angles. With any response, absolute maximum response values from each target location's measurement histories are extracted. These, collected from each target along the structure, form a bridge response profile. Altogether, these various responses make up the damage detection and localisation suite developed in this thesis for condition assessment of structures. The damage detection suite is incorporated into the CV-based bridge monitoring and condition assessment framework being discussed.

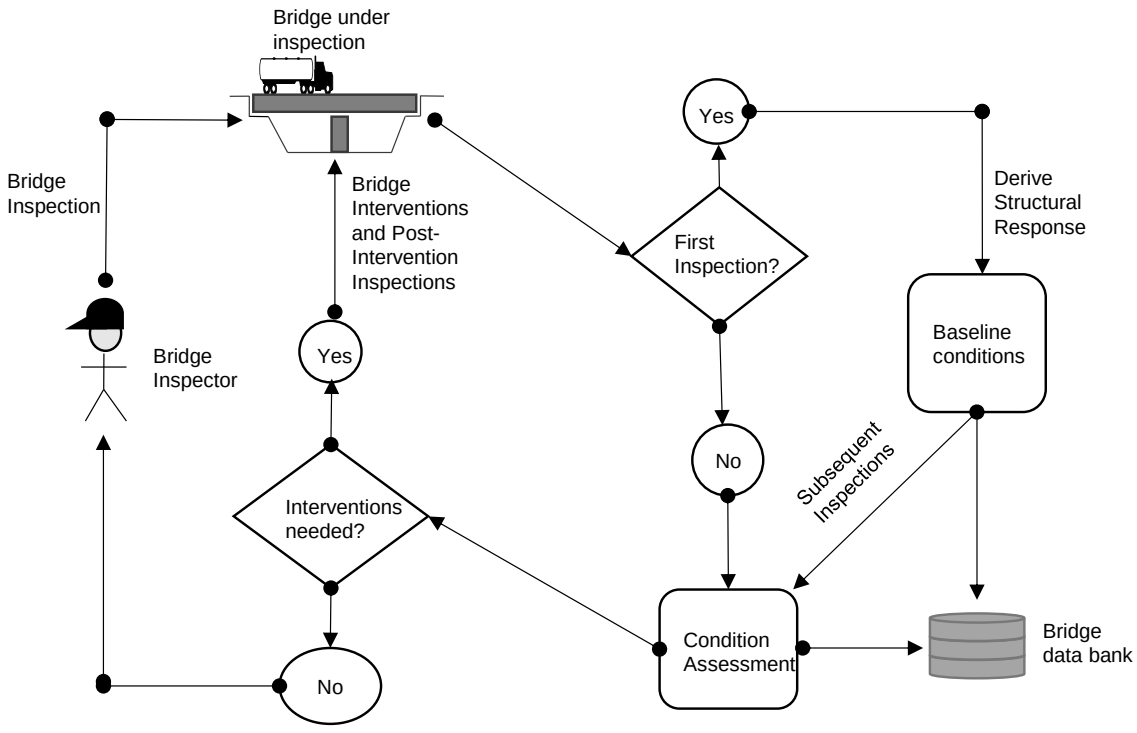

Figure 3-3: Bridge condition assessment and interventions framework

Figure 3-3 describes a general condition assessment framework in which monitoring can be accomplished by any technology (i.e., not restricted to CV-based sensing). It must be said here again that CV-based sensing is the focus of this thesis. For bridge inspection/monitoring campaigns using CV-based monitoring, Figure 3-4 can represent diagrammatically, the condition assessment framework.

From Figure 3-3, it must be stated that the outcome of condition assessments may indicate the need for interventions. This research aims only for a diagnosis and does not cover the interventions aspect.

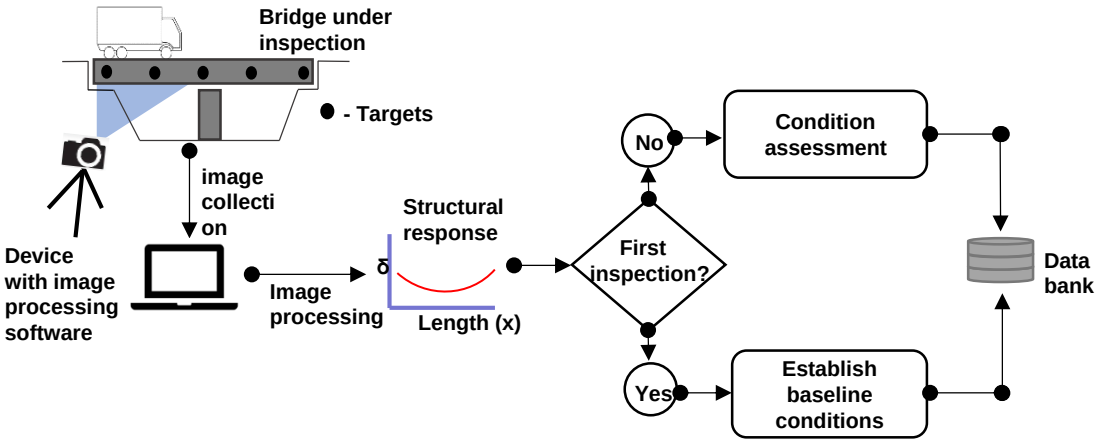

Figure 3-4: Computer CV-based condition assessment of bridges (Obiechefu and Kromanis, 2021)

Obtained responses may undergo preliminary analyses or pre-processing and this depends on the amount and condition of data, as well as computing power. Pre-processed response data can then be fed into the damage detection computer program developed in MATLAB for use within this framework. The program analyses the response data with reference to the baseline data, and advises on the possible presence of damage, as well as its locality if it indeed exists. Results from the analyses can then be the basis of a report or presented through any suitable interface or means, so that engineers and asset managers can plan and prioritize structural interventions or other asset management schedules.

For any measurement collection or monitoring event, the complete list of processes involved can be summarised into:

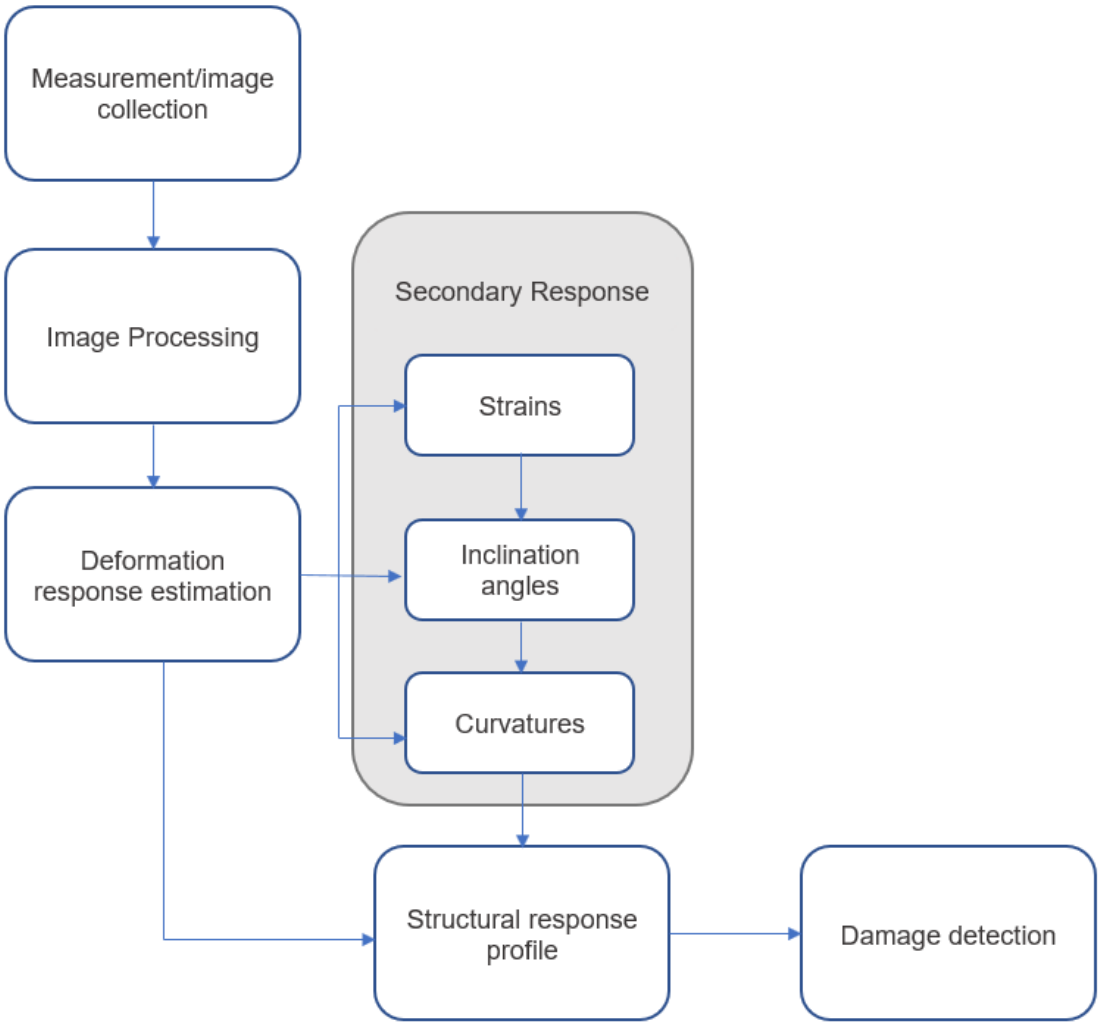

Figure 3-5: Processes involved in Computer CV-based condition assessment of bridges

3.3.3 Image processing

The image processing stage typically begins after the measurement collection event. The images/videos collated are transferred to a computer with image processing software and capability. The primary purpose of image processing in CV-SHM is to extract structural information from collected image frames by tracking a target (or object) or an area from the structure. Image processing employs a variety of feature detection, template matching, and target tracking algorithms, including digital image correlation (DIC) feature point matching, optical flow estimation, and shape-based tracking, among others. The whole process can be done on the MATLAB interface. A thorough literature review of these techniques and algorithms have already been given in CHAPTER 2. Steps may vary slightly depending on what algorithm is used. This in turn will depend on a number of factors including the nature of targets. For example, circular targets would be best served by shape-based tracking algorithms such as blob detectors like MSER, etc. Further practical descriptions of how some of these algorithms are used is given as used in the two case studies in CHAPTER

4. However, a general overview of this phase using feature point or shape-based tracking can be given. The fundamental steps involved in the image processing phase using most object tracking algorithms are:

1. Selection of reference image: A reference image from the measurement collection event (videos/images), most likely the first image frame in the sequence, is selected as a reference image to which others are compared.
2. Specification of region(s) of interest (ROI): ROIs are specified as fixed rectangular regions of known coordinates and dimensions immediately surrounding individual targets to be monitored. They are here described as 'fixed' because their coordinates and dimensions are rigidly applied to all subsequent image frames after the reference image. ROIs are specified such that they would accommodate target movements due to loading, across image frames.
3. Selection/identification of object(s) of interest (OOI) within ROIs: Targets within each ROI are specified as OOIs. In object tracking, OOIs, compared to their immediate surroundings in the ROI must be robust, distinct, and invariant to image transformation and illumination variations. This is because they have to be detected as mathematical features by an appropriate feature/shape detection/tracking algorithm. The choice of tracking algorithm depends on the characteristics of the OOI (see Section 2.1.5). Depending on the algorithm to be used, ROI images may need to be transformed to grayscale images, and then to binary via binarization — a method that assigns image pixels to one of two categories: black or white based on pixel intensity values. This is surely the case for MSER blob detector. The user must check the requirements for their preferred feature detection and tracking algorithm.
4. Detection and tracking of OOIs: Mathematical features of the OOIs are detected in the reference image and recorded. The tracking process involves detecting the OOIs in subsequent images and recording their positions also, till the end of the sequence. This results in a displacement time series of OOI pixel positions based on their local ROI coordinates.
5. Transformation from local to global coordinate system: OOI displacements are local to the ROI, i.e., each OOI's displacement time series originates from its ROI. These must then be transformed such that the whole image frame (global, as opposed to local in ROI) serves as new reference with origin at its bottom corner.
6. Deformation estimation: This involves conversion of pixel displacements to engineering units such as millimetres using either a scale factor, planar homography, or full projection matrix method.

The entire process is shown diagrammatically in Figure 3-6 below.

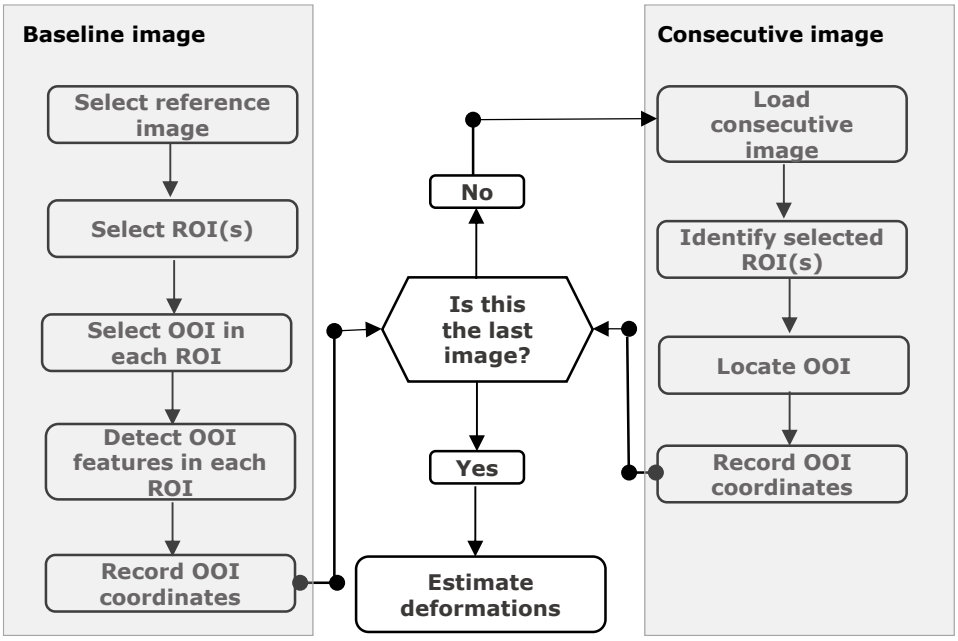

Figure 3-6: Fundamental Image processing with feature point or shape-based tracking

3.3.4 Deformation estimation, secondary response, and camera calibration

Pixel displacements obtained from image processing would have to be converted to engineering units such as millimetres. This can be termed the deformation estimation process. The deformation could be determined from a scale factor using a known object dimension from the image frame as in (D. Feng et al., 2015a; Ji et al., 2020; Yoon et al., 2016), or using at least four 2D control points with known structural coordinates (Lee et al., 2015; Xu et al., 2016), or from a full projection matrix (Oh et al., 2015; Park et al., 2015). To use a scale factor, a one-dimensional real-world distance to pixel unit ratio is required as given in Equation 2.3. A full projection matrix calibration can be done at the beginning to estimate camera parameters, both intrinsic and extrinsic, as well as distortion coefficients that help remove lens distortion, which may be necessary with wide angle lens cameras. Camera parameters can be estimated in the laboratory by analysing a set of calibration images taken from different viewpoints (Zhang, 2000). The calibration object is usually a plane object with grid pattern or dot with known dimensions. At least three views of the calibration object are required, but at least ten images are advised to obtain more accurate estimates (Bradsky and Kaehler, 2008). A full literature review on calibration has been done in CHAPTER 2. Calibration algorithms are available in MATLAB (The MathWorks Inc., 2021). The final output of this process is a set of displacement time series for each target. Secondary response is then calculated from displacements.

3.3.5 Structural Response Profile

Target measurement series from image processing are transformed into a structural response profile (r_δ) for the structure by extracting maximum response (r_{max}) from each target's displacement history (see Figure 3-7). This exercise is applied also to other secondary response types to obtain their own structural profiles.

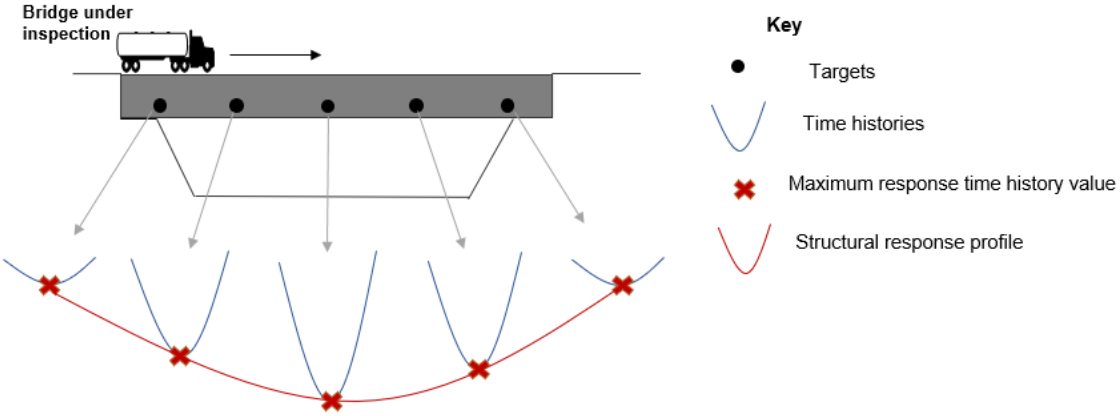

Figure 3-7: Structural response profile obtention

3.3.6 Damage detection and condition assessment

Damage detection is assessed by comparing subsequent response from a structure to that collected at its first inspection – when the bridge is considered to be in a healthy, intact, or undamaged state. Measurements collected at a first inspection are used to establish the bridge's baseline conditions. Subsequent measurements are compared to baseline measurements to estimate the bridge's condition. This comparison between both sets of responses are expressed in two ways:

First, the change in response (Δr) simply is the difference between response from subsequent inspection (r_i), and baseline response (r_0) as given in Equation 3.1.

Secondly, a damage sensitive feature ($e_{r,i}$) can be calculated at any location from structural response. It is defined as the ratio of the change in bridge response (Δr_i) to baseline response (r_0). The variable subscript *'r'* in $e_{r,i}$ indicates the types of response, i.e., r becomes (δ) for displacements, (c) for curvature, (θ) for inclination angles, and (ε) for strains. These are also added as a subscript to r_0 for the same purpose, for example r_0 becomes $r_{\delta,0}$ for displacements, etc. Therefore, the formula is to be adapted for all response types – primary and secondary. $e_{r,i}$ is given by Equation 3.2.

$$e_{r,i} = \frac{\Delta r_i}{r_0} = \frac{r_i - r_0}{r_0} \qquad 3.2$$

3.3.7 Structural response obtention

Primary and secondary response

The suite of damage detection techniques proposed in this methodology is based on four response measurements – displacement, curvature, tilt, and strain. Structural response begins with the obtention of the primary response which is displacement. Displacements can be obtained using any appropriate technique or apparatus, for example, LVDTs, other sensors, and not just CV-based sensing systems, even though this thesis is based on them. Displacements are the product of image processing and deformation estimation phases. Secondary responses on the other hand, are derived from primary response. They are those structural responses derived mathematically from displacement data or the deflection curve. They include curvatures, inclination angles, and strains.

The deflection curve, in structural analysis, relates directly to the stiffness of the structure, and for this reason is considered by some a superior structural index for damage detection (Feng and Feng, 2017). For any structure however, it is influenced by many indices including local stiffness, boundary, and environmental conditions such as temperature. Local stiffness is the index exploited in this study to detect, localise, and quantify damage, and can be applied in condition monitoring of civil infrastructure. The theory behind these techniques is described hereafter, and a number of case studies used to validate the theory.

Notes for application in contact sensing

For contact sensing, targets could also be defined as sensors installed on the structure. This will work exactly as trackable targets in a CV-based application, but of course there would be no image processing as response is logged by the sensors. The sensors record displacements at their locations resulting in time series. These may be converted to secondary responses, and then maximum responses obtained, and response profile derived.

3.3.8 Deflection (Vertical displacements)

This is the primary response obtained from the monitoring process. Vertical displacements are the outcome of the image processing and deformation estimation process (see Section 3.3.2). Image frames collected of the bridge are analysed frame-by-frame using any of the measurement extracting (image processing) techniques reviewed in CHAPTER 2 (with their procedures shown in Section 3.3.2 above). A target displacement technically speaking, is the movement that a target makes between time steps $t = 0$ and $t = n$. This can also be expressed in terms of image frames (collected in time at a certain frequency), e.g., movement of T between two frames – say f_1 and f_n, where f_1 is the first or baseline image and f_n a subsequent one. Target displacements are collected at all image frames and response profile obtained as in Section 3.3.5.

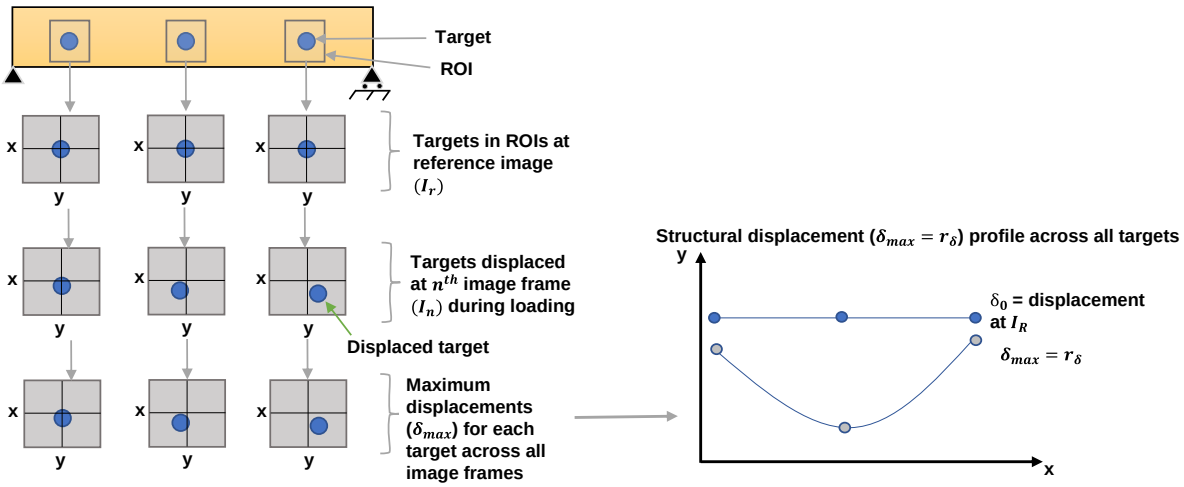

Figure 3-8: Target displacements obtention and response profile

Damage detection and location

If the structure's flexural rigidity is compromised by introducing damage at a small section (See Figure 3-9), then hypothetically the beam should bend differently. This entails amongst other things, a change in δ. If r_δ can be obtained for the structure in both a baseline condition and in this new damaged state, then the condition of the structure can be calculated using Equation 3.1. But since $r = r_\delta$ in this case, the Equation becomes:

$$\Delta r_\delta = r_{\delta,i} - r_{\delta,0} \qquad 3.3$$

Where $r_{\delta,0}$ is the displacement response profile at a first inspection – when the structure is assumed to be in a healthy condition, and $r_{\delta,i}$ – displacement response profile at any subsequent inspection. If $\Delta r_\delta \approx 0$ the structure's performance can be considered to not have changed. If $\Delta r_\delta \gg 0$ the structure's performance can be considered to have changed, in which case further analyses must be carried out to ascertain damage location.

A displacement damage sensitive feature ($e_{\delta,i}$) which is the ratio of the change in bridge displacement response ($\Delta r_{\delta,i}$) to baseline displacement response ($r_{\delta,0}$) and can be calculated at any location from displacement response. Here, $e_{\delta,i}$ is the damage sensitive feature derived from deflection (δ) at the i^{th} measurement collection event. $e \approx 0$ indicates that the performance of the structure has not changed. $e \gg 0$ indicates that the structure is damaged. Damage threshold(s) (γ) are defined to help detect and locate damage. They can be case-specific. In the case studies described in latter sections, a $\gamma > 5\%$ threshold is adopted. Damage is located where e spikes. For displacements:

$$e_{\delta,i} = \frac{\Delta r_{\delta,i}}{r_{\delta,0}} = \frac{r_{\delta,i} - r_{\delta,0}}{r_{\delta.0}} \qquad 3.4$$

3.3.9 Curvature technique

The '*curvature*' technique outlined in this section differs definitively from its various applications found in reviewed literature (See section 2.2.3). A novel curvature technique is hereby proposed where the curvature (c) along a defined length of a horizontal structure is the quadratic coefficient of the curve that best approximates its position in a two – dimensional Euclidean plane. Consider the simply supported beam in Figure 3-9. Initially the beam has no deflection; when a point load is applied through the middle the beam deflects; this deflection increases with the introduction of a damaged element. The point load acts as a force which bends the beam. If the beam can be positioned on a two-dimensional plane, a quadratic fit can be defined for the displacements along its length, or along any portion of its length for that matter, for both damaged and undamaged states.

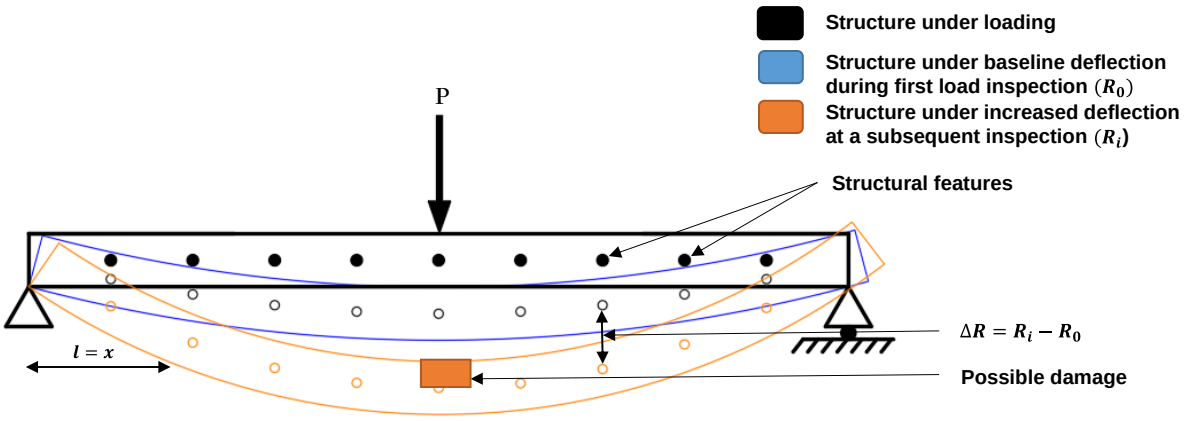

Figure 3-9: Simple beam under point load

The general form for a quadratic equation can be written for the deflection curve along a select portion of the beam in Figure 3-9, say – from $l = 0$, to $l = x$.

$$f(x) = ax^2 + bx + d \qquad 3.5$$

x can be the position of a target, which could be a node in the numerical model, an artificial target placed on a real structure, or a feature such as bolts or joints used as a target on a real-life structure.

The curvature technique thus involves fitting a second-degree polynomial curve on a set of coordinate points from at least three targets altogether called a target set (T). The univariate quadratic function that results (see Equation 3.5), is suitable for deriving the quadratic coefficient (a), linear coefficient (b) and the constant or Y intercept (d) representing a curve fitted on these three points of interest (or targets). a determines the degree of curvature of the quadratic fit, and therefore it becomes a damage-sensitive feature. The curvature (c) at an i^{th} time step then becomes the residual of quadratic coefficients between the first and i^{th} time step (see Equation 3.6).

$$c_i = a_i - a_0 \qquad 3.6$$

When a target set is fit with a curve, the quadratic coefficient (a) of that curve, is related to and determines the degree of curvature of the resultant quadratic fit. A larger a value denotes an increased curvature which would be obtainable in smaller circles or sharper bends, and a smaller a value indicates the opposite. To obtain a curvature response profile, c must be derived along the entire length of the structure. This can be achieved by analysing c, target set by target set, from one end of the beam to the other, omitting a pre-defined number of targets (most preferably one) each time, i.e., a moving window (See Figure 3-10). At each target set, c can be assumed to act through the centre or middle target. This is a necessary approximation as curvature cannot be found for each target as just discussed, but with a set of three targets. It is important to note that this is different from displacements where maximum response can be taken from every single target since the response itself (displacements) is primary and can be obtained from each of them. So, in this way a curvature response time series is derived for each target set along the entire length of the structure, from which a curvature response profile (r_c) can be (T) by extracting maximum curvature response (c_{max}) from them as described in Section 3.3.5.

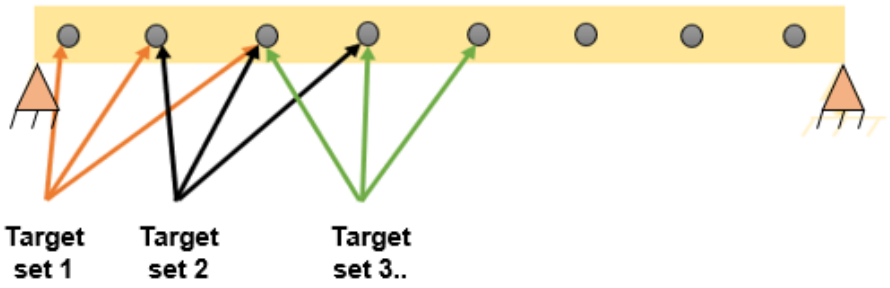

Figure 3-10: Node or target set selection for curvature response

It is important to comment on the flexibility with which targets can be selected. They can be selected as desired. Some factors that may affect how they are selected include the level of localisation required, as well as the distance between the features themselves. For example, the user may decide to skip targets if there are too many of them too close to each other, if they prefer not to have a very high localisation; or the user may decide to use all of them if they prefer that much localisation or are deemed appropriately spaced. This all depends on the spacing between targets and the degree of localisation required. Mathematically, a set of targets (T) for the beam in Figure 3-10 may be defined as:

$$T_i = \{t_k, t_{k+1}, t_{k+2}, \dots t_n\} \qquad 3.7$$

Where T_i is a target set, and k is the first target's number.

Procedure to obtain curvature

Having described the theory and idea of curvature as defined in this thesis, the next stage is how to practically obtain this using some programming or computational interface. The steps to practically obtain curvature is described diagrammatically in Figure 3-12. All computation used to achieve this has been done on MATLAB interface (The Mathworks Inc., 2016). The steps are as follows:

1. Identify targets and define target sets (T).
2. Compute target coordinates.
3. Calculate inclination (or rotation) angles (α) using a straight line connecting the first and last targets in each target set. This forms a right-angled triangle of which α, from basic trigonometric ratios, is the inverse tangent relationship between vertical and horizontal components (see Inclination angles in Section 3.3.10).
4. Define a rotation matrix using R obtained for each target set (T) (see Equation 3.11).
5. Multiply each target's coordinates by the rotation matrix (R) of its target set (T) defined by its obtained α. This rotates each target set such that the first and last targets are at the same y coordinate, e.g., $y = 0$.
6. Fit a quadratic curve on targets in each target set (T).
7. Obtain the quadratic coefficient for each quadratic curve.
8. Repeat ad nauseum for all time steps or image frames.

The rotation matrix is given by:

$$r = \begin{bmatrix} \cos\theta & -sin\theta \\ \sin\theta & cos\theta \end{bmatrix} \qquad 3.8$$

Where θ is the angle subtended by the straight line between the coordinates of the first and last targets, as illustrated in Figure 3-11 below.

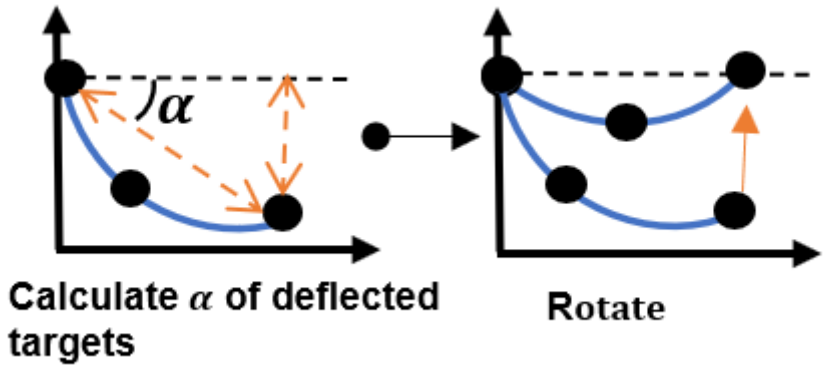

Figure 3-11: Multiplying target coordinates by rotation matrix (R) to rotate target sets (T)

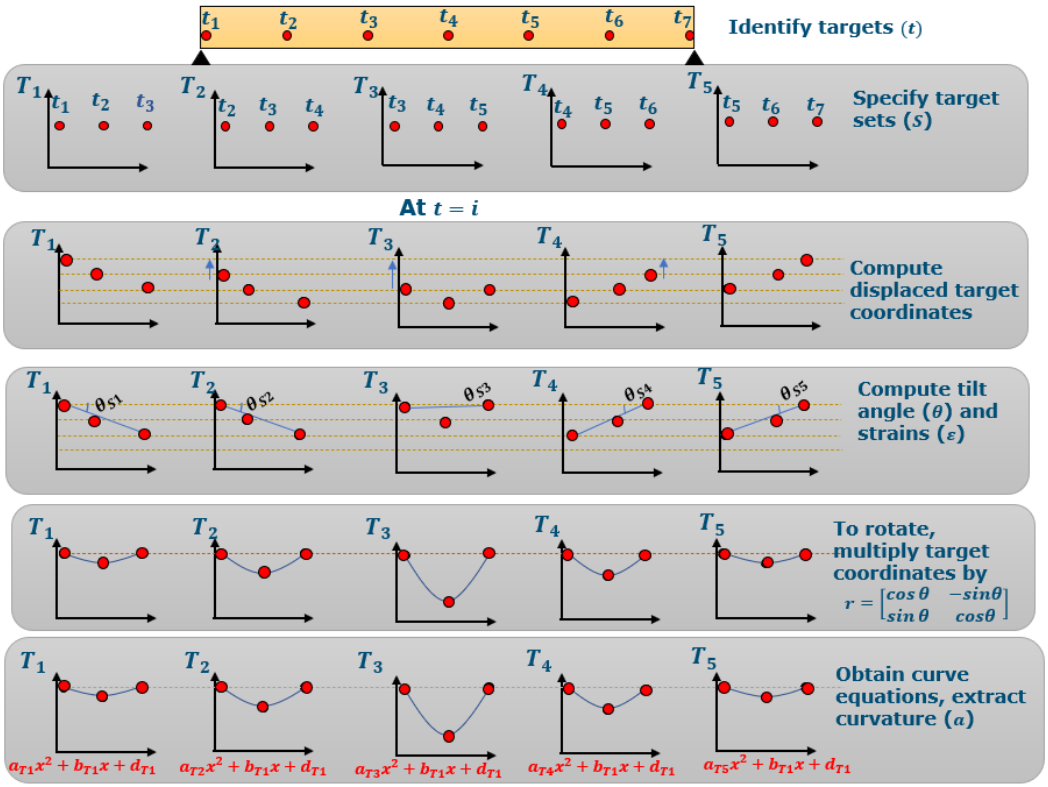

Figure 3-12: Curvature response obtention process

Damage detection and location

If the structure's flexural rigidity is compromised by introducing damage at a small section (See Figure 3-9), then hypothetically the beam should bend differently. This entails amongst other things, a change in r_c. If r_c can be obtained for the structure in both a baseline condition and in this new damaged state, then the condition of the structure can be approximated using Equation 3.1 since $R = r_c$ in this case, and so the Equation becomes:

$$\Delta r_c = r_{c,i} - r_{c,0} \qquad 3.9$$

Where $r_{c,0}$ is the curvature response profile at a first inspection – when the structure is assumed to be in a healthy condition, and $r_{c,i}$ – curvature response profile at any subsequent inspection. If $\Delta r_c \approx 0$ the structure's performance can be considered to not have changed. If $\Delta r_c \gg 0$ the structure's performance can be considered to have changed, in which case further analyses must be carried out to ascertain damage location.

A curvature damage sensitive feature ($e_{c,i}$) which is the ratio of the change in bridge curvature response ($\Delta r_{c,i}$) to baseline curvature response ($r_{c.0}$) and can be calculated at any location from displacement response. Here, $e_{c,i}$ is the damage sensitive feature derived from curvature (δ) at the i^{th} measurement collection event. $e \approx 0$ indicates that the performance of the structure has not changed. $e \gg 0$ indicates that the structure is damaged. Damage threshold(s) (γ) are defined to help detect and locate damage. They can

be case-specific. In the case studies described in latter sections, a $\gamma > 5\%$ threshold is adopted. Damage is located where e spikes. For curvature:

$$\mathrm{e}_{c,i} = \frac{\Delta r_{c,i}}{r_{c,0}} = \frac{r_{c,i} - r_{c,0}}{r_{c.0}} \qquad 3.10$$

3.3.10 Inclination angles

If a horizontal structure deflects, it is expected that an angle subtended to the horizontal forms between any two targets on the structure selected – say t_k and t_m . t_k and t_m can be said to form a target set (T) whose angle between them (α) is given by its tangent relationship, i.e., from basic trigonometric ratios, the inverse tangent of the ratio of its vertical to its horizontal components. α between t_k and t_m can be computed using Equation 3.11 where y and x represents their vertical and horizontal coordinates respectively (see Figure 3-13). Inclination angles (θ_i) therefore becomes the residual of α at an i^{th} time step, with reference to α at the first image frame. This is shown described by Equation 3.12.

$$\alpha = \tan^{-1}\left(\frac{y_{Tk} - y_{Tm}}{x_{Tk} - x_{Tm}}\right) \qquad 3.11$$

$$\theta_i = \alpha_i - \alpha_0 \qquad 3.12$$

θ is collated for all image frames. θ_{max} is the maximum inclination angle at any target set and is referred to as the structural response r_θ at that set (consistent with all other response types). θ_{max} collated for all target sets gives the response profile of the whole structure and is considered the inclination angle response (r_θ).

Target set selections for inclination angles is similar to that for curvature, but with target pairs instead. This is because only two targets (or points) are required to compute inclination angles. Having collected displacement responses from targets using image processing, the inclinations between any pair of features can then be calculated. Inclination angles in literature is usually measured in degrees, radians, and in mm/m. The latter two are particularly mostly used in SHM and condition assessment applications. These units are convenient considering the usually low ratios of vertical to horizontal measurements, for example 1mm:1000mm vertical displacement to horizontal distance between two points can simply be written in mm/m as 1mm/1m. A larger angle means higher vertical displacements, and this generally occurs towards the midspan.

Procedure for calculating inclination angles

Calculation of inclination angles is achieved at the third step of the curvature obtention process described in Section 3.3.10 above, and can also be seen in the diagrammatic

description of Figure 3-12 in the same section. However, one must remember that only two targets need be selected here for calculation of inclination angles. The tangent relationship α for a pair (or set) of targets is more particularly described in Figure 3-13 below. At the first image targets are in the original position. At any other image frame the targets may have moved relative to each other due to loading imposed on the structure.

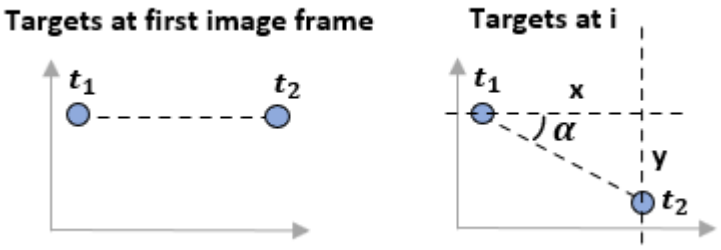

Figure 3-13: Demonstrating the change in inclination between targets due to loading

Damage detection

If the structure's flexural rigidity is compromised by introducing damage at a small section (See Figure 3-9), then hypothetically the beam should bend differently. This entails amongst other things, a change in r_θ. If r_θ can be obtained for the structure in both a baseline condition and in this new damaged state, then the condition of the structure can be approximated using Equation 3.1 since $R = r_\theta$ in this case, and so the Equation becomes:

$$\Delta r_\theta = r_{\theta,i} - r_{\theta,0} \qquad 3.13$$

Where $r_{\theta,0}$ is the inclination angle response profile at a first inspection – when the structure is assumed to be in a healthy condition, and $r_{\theta,i}$ – inclination angle response profile at any subsequent inspection. If $\Delta r_\theta \approx 0$ the structure's performance can be considered to not have changed. If $\Delta r_\theta \gg 0$ the structure's performance can be considered to have changed, in which case further analyses must be carried out to ascertain damage location.

A curvature damage sensitive feature ($\mathrm{e}_{\theta,i}$) which is the ratio of the change in bridge inclination angles response ($\Delta r_{c,i}$) to baseline inclination angle response ($r_{\theta.0}$) and can be calculated at any location from displacement response. Here, $\mathrm{e}_{\theta,i}$ is the damage sensitive feature derived from inclination angle (θ) at the i^{th} measurement collection event. $e \approx 0$ indicates that the performance of the structure has not changed. $e \gg 0$ indicates that the structure is damaged. Damage threshold(s) (γ) are defined to help detect and locate damage. They can be case-specific. In the case studies described in latter sections, a $\gamma > 5\%$ threshold is adopted. Damage is located where e spikes. For inclination angles:

$$\mathrm{e}_{\theta,i} = \frac{\Delta r_{\theta,i}}{r_{\theta,0}} = \frac{r_{\theta,i} - r_{\theta,0}}{r_{\theta.0}} \qquad 3.14$$

A case-specific derivation of e_θ

A case-specific derivation of e_θ is proposed here due to inaccurate damage detectability observed with the case studies in CHAPTER 4. But before explaining this case-specific derivation, it is important to conceptualise the problem.

r_θ is the maximum inclination angle value (r_{max}) from each target set's response time history, i.e., $r_\theta = r_{max}$. This r_θ is obtained from all target sets spread across the beam (see Figure 3-7). r_θ is therefore a response profile which ideally, theoretically, and in the absence of measurement noise should resemble Figure 3-14(a). It can be observed that somewhere near the beam's midpoint r_θ takes on negative values as it falls below zero. Let us call this point the "*changepoint"*. In other words, the inclination angle response profile is positive before the changepoint, and negative after. In other words, their maximum values become minimum values as they become negative. Now in practice the presence of random fluctuating measurement noise is guaranteed in each target set's time history. The implication of this noise is that the r_{max} value for each target set's response time history becomes inflated. This is true for all response types and some results from the numerical model are reproduced here in Figure 3-15 to explain this fact. Now since r_{max} is the maximum response from each target set's time history, and is inflated by noise, it follows that at any two target sets straddling both sides of the *changepoint* (which should be at about the girder's midpoint), the value of r_{max} for the target on the positive side must be a maximum positive θ value inflated by noise, and that at the negative side target must be its lowest negative θ value also inflated by noise. In other words – taking an extreme positive value on one side, and an extreme negative value on the other side of zero. This extremity caused by noise is what creates a measurement shift which increases in scale with increasing θ values. In summary, measurement noise inflates both positive r_{max} and negative r_{max} (or r_{min}) values for inclination angle time histories, causing a measurement shift at the changepoint in r_θ structural profiles (see Figure 3-14).

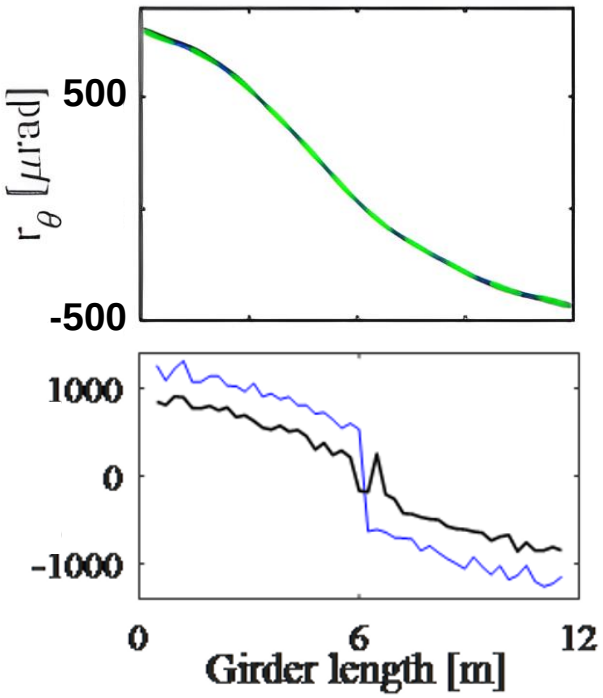

Figure 3-14: (top) Ideal r_θ shape with no noise, negligible damage (extracted from Figure 4-7), and (bottom) r_θ shape with high noise, no damage (extracted from Figure 4-11). Note the measurement shift at the middle, caused by inflated positive r_{max} and negative r_{max} (or r_{min}) time history values. This inflation is caused by noise, which in turn causes a measurement shift at the changepoint ($r_{max} = 0$) in r_θ response profiles

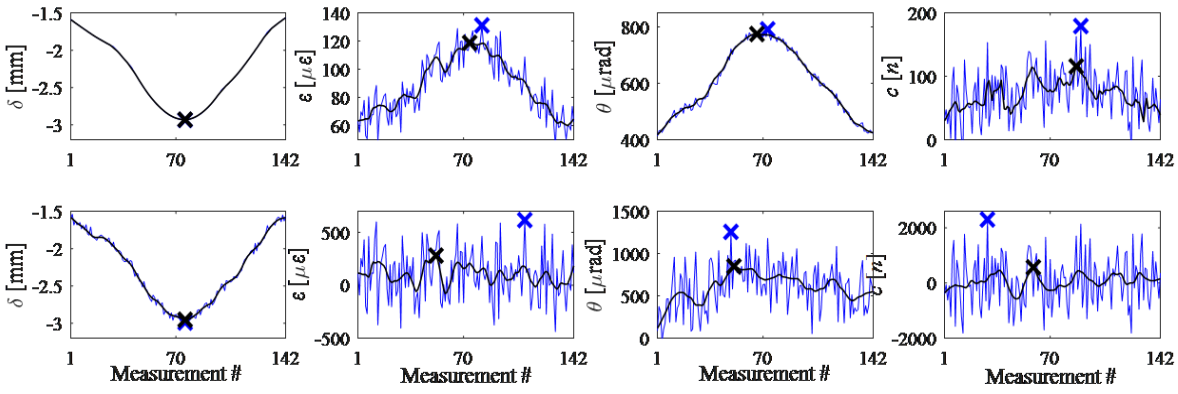

Figure 3-15: Showing response time histories at a girder midpoint (for δ, ε, c) and near support (for θ) with different noise levels. Black 'x' markers indicate maximum response value from pre-processed response; blue 'x' markers indicate the same for raw (un-pre-processed) data. Note here that noise serves also to inflate response values, apart from the inaccuracies which their presence alone brings.

The case-specific technique thus goes this way. A moving window is used to obtain $e_{\theta,g}$ at a g^{th} response measurement location along the length of the girder. e_θ is computed as the ratio of the range of Δr_θ (q_n) to the mean of r_θ ($\bar{r}_\theta$) for n number of consecutive response measurements. To compute e_θ at the g^{th} response location, values to its left and right are selected so that the g^{th} response location is always in the middle. Therefore n needs to be an odd integer, larger or equal to 3. Large n values round q_n and $\bar{r}_\theta$ hindering damage locations, thus damages close to supports may not be revealed. But small n values can also be sensitive to small, local changes to the response and provide e_θ values that frequently exceed the damage threshold. The selection of n therefore depends on the number of distributed targets (f) on the structure and distance between them. Larger distance between targets and a smaller n value can be selected, and vice versa. In this study n is set to 5. Also see Equations 3.18, 3.19, and 3.19.

$$e_{\theta,g} = \frac{q_{n,g}}{\bar{r}_{\theta,n,g}}, \begin{cases} \frac{(n-1)}{2} < g < f - \frac{(n-1)}{2} \\ n \geq 3 \\ n = \{2k+1 : k \in \mathbb{Z}\} \end{cases} \quad 3.15$$

$$q_{\theta,n,g} = \max_{l,m=1,\ldots,n} \left(\Delta r_{\theta,g-l-1} - \Delta r_{\theta,g-m-1}\right) \quad 3.16$$

$$\bar{r}_{\theta,n,g} = \frac{1}{n}\sum_{l=1}^{n} \left| r_{\theta,g-l-1} \right| \quad 3.17$$

3.3.11 Strain measurement response

We know from basic beam bending theory that a beam that deflects due to loading will stretch below the neutral axis and compress above it. Strain (ε) can be measured for a pair of targets (or target set (T)). It is important to clarify here that 'strain' here refers to global one-dimensional (1D) strain. 1D strain, from basic mechanics, is defined in terms of the relative displacement (u) of a point (l) to the original length of a line formed from an origin (o) to l. 1D strains, of course are not just easily calculated, but have proven a reliable damage-sensitive response, judging by their extensive use in bridge damage detection studies (see (Ferrer et al., 2015; Kromanis & Forbes, 2019; Obiechefu & Kromanis, 2021)). Equation 3.18 can be used to calculate ε at an i^{th} time step (ε_i), which is the change of the length (Δl) over the original length (l_0) between the two targets t_k and t_m. The distance between targets (or length l) is computed from their x and y coordinates at any image frame i (see Equation 3.19). Strain is unitless, therefore, x and y coordinates can be either in pixel or other measurement space.

$$\varepsilon_i = \frac{\Delta l_i}{l_0} = \frac{l_i - l_0}{l_0} \quad 3.18$$

$$l = \sqrt{(x_{Tk} - x_{Tm})^2 + (y_{Tk} - y_{Tm})^2} \quad 3.19$$

ε is collated for all image frames. ε_{max} is the maximum strain at any target set and is referred to as the structural response r_ε at that set (consistent with all other response types). ε_{max} collated for all target sets gives the response profile of the structure and is considered the strain response (r_ε).

Target set selections for strains is similar to that for curvature, but with target pairs instead. This is because only two targets are required to compute inclination angles. Having collected displacement responses from targets using image processing, the strains between any pair of features can then be calculated. Strains in literature is usually measured in micro strains (μ) which is strains multiplied by 10^{-6}. Larger strains would be expected near the midspan.

ε is collated for all image frames. ε_{max} is the maximum strain at any target set and is referred to as the structural response r_ε at that set (consistent with all other response types). ε_{max} collated for all target sets gives the response profile of the structure and is considered the strain response (r_θ).

Procedure for calculating strains

Calculation of strains can be achieved after displacements are obtained, at the third step of the curvature obtention process described in Section 3.3.10 above, and can also be seen in the diagrammatic description of Figure 3-12 in the same section. However, one must remember that only two targets need be selected here for calculation of strains. Strain obtention for a pair (or set) of targets is described in Figure 3-16 below. At the first image targets are in the original position. At any other image frame the targets may have moved relative to each other due to possible loading. The change in distance of the direct distance between both targets, which is the hypotenuse of the right-angled triangle, is used to calculate strains.

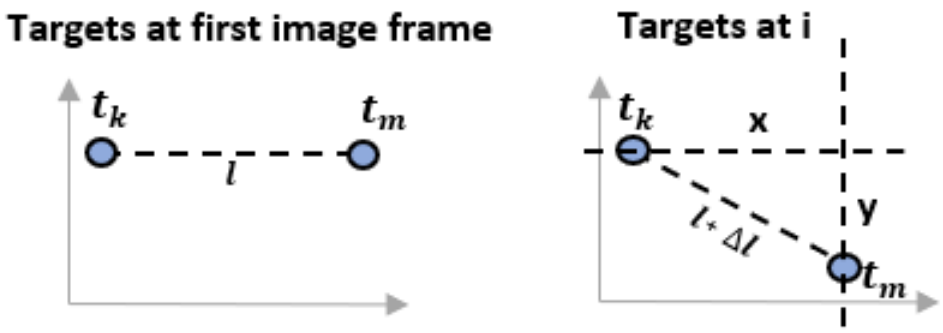

Figure 3-16: Demonstrating an initial length between targets, and the change in length occuring at another time step or image frame

Damage detection

If the structure's flexural rigidity is compromised by introducing damage at a small section (See Figure 3-9), then hypothetically the beam should bend differently. This entails amongst other things, a change in r_ε. If r_ε can be obtained for the structure in both a baseline condition and in this new damaged state, then the condition of the structure can be approximated using Equation 3.1 since $R = r_\varepsilon$ in this case, and so the Equation becomes:

$$\Delta r_\varepsilon = r_{\varepsilon,i} - r_{\varepsilon,0} \qquad 3.20$$

Where $r_{r_{\varepsilon,0}}$ is the strain response profile at a first inspection – when the structure is assumed to be in a healthy condition, and $r_{\varepsilon,i}$ – strain response profile at any subsequent inspection. If $\Delta r_\varepsilon \approx 0$ the structure's performance can be considered to not have changed. If $\Delta r_\varepsilon \gg 0$ the structure's performance can be considered to have changed, in which case further analyses must be carried out to ascertain damage location.

A strain damage sensitive feature ($\mathrm{e}_{\varepsilon,i}$) which is the ratio of the change in bridge strain response ($\Delta r_{\varepsilon,i}$) to baseline strain response ($r_{\varepsilon,0}$) and can be calculated at any location from displacement response. Here, $\mathrm{e}_{\varepsilon,i}$ is the damage sensitive feature derived from strain (ε) at the i^{th} measurement collection event. $e \approx 0$ indicates that the performance of the structure has not changed. $e \gg 0$ indicates that the structure is damaged. Damage threshold(s) (γ) are defined to help detect and locate damage. They can be case-specific. In the case studies described in latter sections, a $\gamma > 5\%$ threshold is adopted. Damage is located where e spikes. For strains:

$$\mathrm{e}_{\varepsilon,i} = \frac{\Delta r_{\varepsilon,i}}{r_{\varepsilon,0}} = \frac{r_{\varepsilon,i} - r_{\varepsilon,0}}{r_{\varepsilon.0}} \qquad 3.21$$

3.3.12 Summary

Figure 3-17 below gives an overview of the formulation of the responses so far developed in this Chapter. Displacements (or deflection), being the primary response are obtained from

the image processing phase. Secondary responses (strains, curvatures, and inclination angles) are then obtained using displacement data. All secondary response is obtainable at some point in the curvature obtention procedure of Section 3.3.10. Both strains and inclination angles can be obtained at the same Step 3 of the curvature procedure. Using the diagrammatic strain obtention description from Figure 3-16 to summarize this, we have:

$$(L + \Delta L)^2 = x^2 + y^2 \qquad 3.22$$

$$\alpha = \tan^{-1}\left(\frac{y}{x}\right) \qquad 3.23$$

Where Equation 3.22 gives the change in length required for strain calculation. And Equation 3.23 calculates the angle between both targets.

The point is to stress the ease with which the responses can be obtained almost simultaneously. Coming from the same primary response, strains and inclination angles are response metrics obtainable at some point in a process that culminates at curvature obtention.

This ends this important section where damage detection techniques have been formulated and explained. In CHAPTER 4 these are applied to case scenarios and their effectiveness tested.

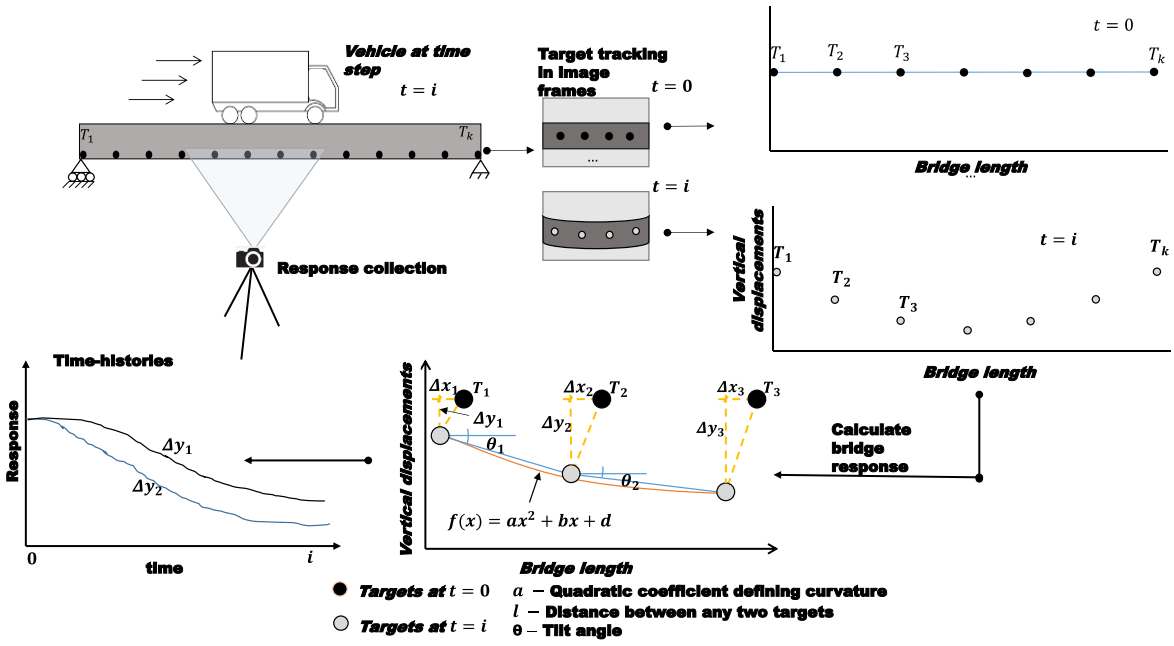

Figure 3-17: Generation of structural response.

3.4 CV-SHM sensing strategy and its Practicality

This section takes a brief hypothetical look at the possibility and practicality of a CV-based framework employing these damage detection techniques. More on this is in Chapter 5,

within a deeper context of the results and peculiarities from case studies given in CHAPTER 5.

The practicability of a CV-based sensing strategy is dependent on the ability of the image acquisition device to accurately capture and detect changes in measurement response which are usually very small. Camera specifications become very important to achieve this purpose. The important factors affecting the suitability of consumer-grade cameras for measurement extraction such as resolution, accuracy, FOV, etc., have been discussed in section 0.

In real world applications, noise from several sources are expected also to contaminate the measurements. Sources of noise contaminations include sources of vibrations such as wind, ground motion, camera drifts, operation of the image processing device (for example phone clicking to start recording), and even vibrations from the structure itself. Some of these can be readily mitigated. For example, the use of stationary targets on rigidly fixed surfaces within view of the camera helps reduce much background noise from obtained response when their responses are subtracted from the structure's response. Also, remote controllers are now available for phone and digital cameras to eliminate the vibrations from clicking on the phone.

3.4.1 Consumer-grade camera specifications

The specifications of affordable consumer-grade cameras have risen tremendously in the past two decades or so, which is a major reason that research of this kind is possible. As examples, the iPhone 8 camera offers 4K resolution videos at 60fps, which is the same as the GoPro Hero 6 camera. These can easily be fitted with zoom lens if needed, for efficient monitoring, for example in (Kromanis and Al-Habaibeh, 2017), and both cost under £900. By general comparison, most smartphones of the last few years have similar or slightly better specifications. The latest Samsung S10 phone with 4K resolution, has settings where the aspect ratio of the camera can be changed, for example – 4:3 (12MP, 4032 x 3024), 16:9 (9.1MP, 4032 x 2268), etc.

Perhaps it should be noted that these modern-day cameras also offer incredible wide-angle lens which while valuable in many general photography applications, may not be so helpful for CV-based monitoring due to radial distortions around the edges. These may have to be corrected by camera calibration (Yoon et al., 2016). However, lens with no apparent or significant radial distortion need no calibration (Xu and Brownjohn, 2018); this would be the case for wide angle lens cameras with focal length between 24mm and 35mm, and examples would be GoPros (which may also offer extra-wide angle lens options), and the iPhone brand from iPhone 7 upwards.

3.4.2 Optimal field-of-view and accuracy for measurement collection

As zoom level decreases, the FOV available increases, and it is possible to obtain images of a wider portion of the structure, and therefore, more measurements. The upper limits to this would be a single camera obtaining measurements from a very wide area with no targets (Bus*ca et al*, 2014). But this is not strictly the case. A wider field-of-view trades off some of the accuracy (as the same resolution covering – say a single point, is made to cover a wider area). This should be the major consideration in deciding field-of-view for multi-point displacement measurements methodologies such as this. As such, a reasonable portion of the structure is at least required, while retaining sufficient accuracy to detect changes in response. The physical accuracy of a camera is given as:

$$Accuracy = object\ field\ /\ camera\ resolution \qquad 3.24$$

While the Nyquist Limit is half the sampling frequency (number of pixels/mm) i.e.

$$N = \frac{1}{2}\left(\frac{pixels}{mm}\right) \qquad 3.25$$

Where N is the Nyquist limit.

Camera precision can be increased further by using image processing techniques with subpixel interpolations, such as DIC which is reported in literature as capable of subpixel accuracy ranging between $^1/_{2^{th}}$ to $^1/_{100^{th}}$ pixels (Feng *et al*, 2015), and even up to $^1/_{200^{th}}$ of a pixel (Potter and Setchell, 2014). For real world bridges, multiple high-resolution cameras can be employed to cover more length, the images may be stitched together using third party software if required.

Consider a road bridge under monitoring (Figure 3-18). A camera is set up to capture a specific portion of the entire bridge length (L). Any desired portion can be analysed. Since accuracy is determined largely by image resolution, it may be unlikely to detect structural response from multiple locations when capturing the entire structure (especially real-life structures like bridges). Thus, several cameras may be employed, with each camera's field-of-view focused on pre-determined portions of the structure (See Figure 3-18). Images from any portion can then analysed with known coordinates.

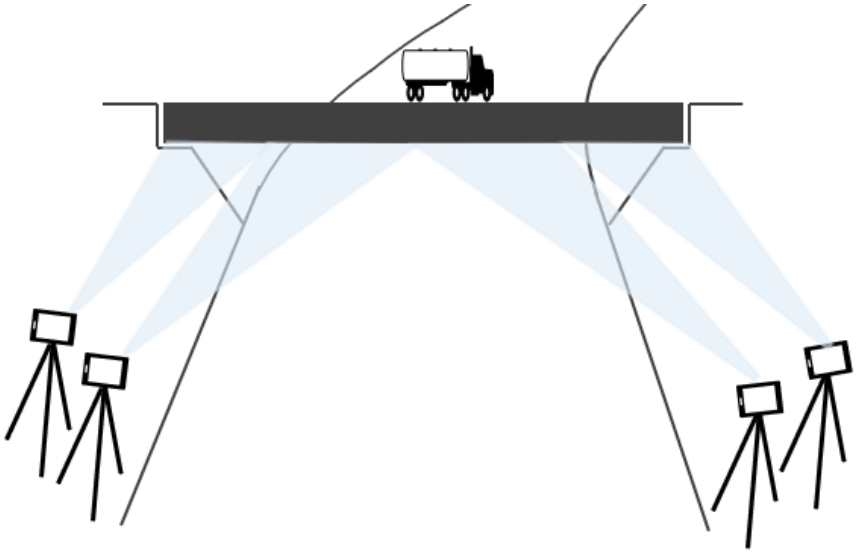

Figure 3-18 CV-based sensing (multiple devices)

As an analogy, assuming that the camera in Figure 3-18 is a GoPro Hero 7 camera with a screen resolution of 4096x3072 pixels, and its field-of-view covers a horizontal length of 2,400mm. The horizontal accuracy can be derived readily using Equation 3.24 as $2400mm/4096pixels = 0.59mm/pixel$. The vertical accuracy in this case can only be calculated during image processing phase as the pixel dimension of a known length has to be obtained. However, let us assume that it is similar to the horizontal accuracy in this case. The accuracy can be improved using methods such as sub-pixel sampling and DIC (Potter and Setchell, 2014; Feng et al, 2015). Assuming also a working accuracy of 1/50th of a pixel post-sub-pixel sampling, the image accuracy expected becomes 0.0117mm/pixel. Now, even without any sub-pixel techniques, regular bridge displacements can be detected. The uncertainty may start to appear when changes in displacements, curvatures, strains and inclination angles are to be calculated from measurements near supports, especially when the load is relatively light. This idea would become clearer with the case studies completed, and is thus more clearly discussed in CHAPTER 5.

Accuracy of measurements collated must be ensured from the image collection phase using the techniques described above. Accurately collated images can then be analysed using image processing and techniques from the damage detection suite described. These are tested in the next chapter.

3.5 Contributions to knowledge

From literature review (CHAPTER 2), it was clear from the literature gaps discovered that there is the opportunity for development of an easier but still accurate, and more data-driven response obtention and damage detection approach. Also, as discussed earlier in Chapter

2, the use of derivatives of the deflection curve in bridge monitoring and damage detection requires much information about the structure. To use the derivatives of a beam's deflection curve, information such as loading type, material properties, boundary conditions, as well as geometry (e.g., distance from support to targets), etc (Abdo, 2012; Erdenebat et al., 2018; Helfrick et al., 2009; Jáuregui et al., 2003; Lee and Eun, 2008; Sun et al., 2017). This chapter has laid down proposed techniques and approaches to fill this gap at least partly, with easy-to-use techniques requiring little or no prior structural information from the structure. The damage detection approach has been established using displacements, strains, inclination angles, and curvature responses. Response collated at a first measurement collection event forms a baseline condition with which subsequent response is compared to infer the presence or otherwise, of damage. These responses used have been uniquely formulated and implemented to fulfil the stated need for easier and more data driven approaches to bridge monitoring and damage detection.

Curvature in this research is unique in the sense that it has been redefined in such a way as to aid a relatively simple and flexible damage detection approach. To start with, several applications (already reviewed in chapter 2) of '*curvature'* techniques in static load-based structural monitoring and damage detection exist in literature, both for numerical models, real life bridges, and laboratory validations, some even including the use of CV-based photogrammetry for response obtention (Abdo, 2012; Erdenebat et al., 2018; Helfrick et al., 2009; Jáuregui et al., 2003; Lee and Eun, 2008; Sun et al., 2017). In all these studies, curvature has been defined in its classic sense – as a metric inversely proportional to radius of curvature (R), and closely related to the bending moment and flexural rigidity (EI), given as:

$$Curvature = \frac{1}{R} = \frac{M}{EI} \qquad 3.26$$

From Equation 3.26, this relationship is exploited for damage detection purposes, as any change in EI correspondingly affects curvature. The application of this technique in literature is limiting in a CV-based approach due to some reasons. To use the curvature formulae:

1. The distance to any point of interest on the structure, from its support is at least needed to estimate moment, which is even more practically unrealistic with a multi-span structure.
2. Secondly, the boundary conditions, and flexural rigidity (EI) of the structure needs to be known which may be difficult as material properties and geometry have to also be known.

3. Thirdly the vision sensor (camera) may be focused at only a portion of the structure – say the middle portion (see Figure 3-19) in which case, displacements outside the camera field-of-view are unknown and curvature estimation becomes difficult.

Summarily, estimating the parameters of classic curvature formulae is difficult and not always possible. Curvature as defined in this Chapter, makes use of the quadratic coefficient of curves, thereby eliminating the need for its classic definition, i.e., as one of the derivatives of the deflection curve. While effective in damage detection, practically, this means that curvature can be obtained at any point in the structure without recourse to other factors and information (e.g., material properties, boundary condition, etc.), if the target displacement data is present.

Strains and inclination angles, though not uniquely defined as with curvature, are prescribed to be used in the same way – i.e., can be obtained at any point in the structure without recourse to other factors (e.g., material properties, boundary condition, etc.).

The techniques proposed in this chapter are therefore very practical, easier to use, and unique in the sense of their being more computational or data-based. Structural response and damage detection are based completely on displacement data obtained from any portion of the bridge, without need for any further information from the structure, or other theoretical knowledge, like for example in the use of derivatives or models of the deflection curve. All that is needed with the proposed approach is to track and obtain target displacements of any selected section. It must be noted here that despite the focus on computer CV-based sensing, primary response can be obtained using any other form of contact or non-vision-based monitoring. Secondary response (curvatures, strains, inclination angles) may then be calculated from the displacement data between any desired targets within the structure. Damage detection is a comparison between response collected at any time, with that collected at a reference time or a first inspection. This is a pragmatic approach that has the potential to increase the chances of successful and robust on-field applications.

It is important to note here that the challenges remedied by this approach to response obtention would not exist in controlled, small-scale laboratory experiments where the full length of the structure is captured, or even in a small-scale bridge structure with super high-resolution devices capable of containing the whole structure at high resolution. For example, in a controlled, small scale laboratory experiment, boundary conditions, material properties, etc., and other required information would be known, and therefore the deflection curve can be used to derive responses. These sets of information may not be available in real world scenarios. This highlights the robustness of this approach as structural response can be obtained in the laboratory or on site, and at any part of the structure. These techniques (as

discussed in the chapter) are to be incorporated into the already-described CV-based condition assessment framework and have the potential to become an affordable and flexible bridge condition assessment method especially for small to medium-scale structures.

Figure 3-19: Camera focused on a portion of a structure

3.6 Conclusions

This chapter laid out the methodology of the research. It started by expressing the influence of static loads on bridges, justifying the overwhelming emphasis laid on it in practical design considerations especially for regular short-span and highway bridges. A robust framework for affordable CV-based condition assessment of small to medium-span structures was then introduced. The framework incorporates a computer vision sensor system for displacement response obtention, and a suite of secondary structural responses obtained from displacements, namely – curvatures, inclination angles, and strains. The techniques for damage detection based on these responses are also explicated in detail.

This framework would greatly benefit asset owners and managers, as it is intended to complement and reduce the need for visual inspections with its obvious limitations, and provide real-time, affordable condition assessment for short to medium-span bridge structures. The most important targets of this framework are the older assets nearing end of design life, with small traffic volumes, and unsustainable visual inspection routines due to cost and long intervals between principal inspections which is unsafe.

CHAPTER 4 NUMERICAL AND EXPERIMENTAL CASE STUDIES

This chapter seeks to validate and investigate the performance of the methodology and techniques introduced in CHAPTER 3 using case studies. The case studies include numerical models, a laboratory structure, and a real bridge structure. They are listed below:

1. A single-span numerical beam model with geometry similar to common highway bridge girders. This model serves to demonstrate, validate, and calibrate the damage detection techniques.
2. A laboratory beam structure. This laboratory structure serves to examine the applicability of the entire methodology and assess its readiness to be deployed for field applications. The laboratory structure is monitored using CV-based system, from where response measurements are derived to be used in damage detection. It is also instrumented with displacement and strain sensors for comparison purposes.
3. Small scale real structure where it is demonstrated that the responses introduced in this thesis can be obtained from a real structure, and a structural profile created. Damage detection is not possible here due to the obvious impracticality of recreating damage on a real structure.

4.1 Case Study 1: Numerical Validation

A numerical model of a highway road bridge girder is used to demonstrate the methodology, and to assess its robustness. It is set up to measure and assess a girder's response to static live loads expected on a regular bridge girder.

4.1.1 Bridge girder model and loading

The model is a simply supported beam structure representative of a typical reinforced concrete girder found in highway bridges. The hypothetical highway bridge carriageway is supported by three girders. A deck load analysis is not considered here as it is not vital to the overall philosophy or to prove the general idea behind the inquiry. What matters is that response from a structure can be obtained and analysed, and the extents to which this is possible. Thus, a simply working truck load value (P) is obtained by factoring a hypothetical test truck load (p) using the total number of girders (n) bearing its weight.

$$P = p/3 \qquad 4.1$$

The girder, one of three distributed across the carriageway, is subjected to load from a 25-ton, three axle rigid truck ($p = 8.3ton$) (Figure 4-2) slowly moving across it. The factored axle loads used are enough to yield significant deflections.

One may also question why all girders are not used instead of just one. Answer is this. If goal of computer CV-based structural response monitoring campaign is to obtain response either at a point, at multiple points, or the entire (global) bridge creating a response profile, then one response at each point along its length is enough, representing bridge response at that point, except if specifically required in any case, - for example if investigating cross-sectional torsional effects, etc. In this work the focus is on multi-point and global structural analyses of bridges, so response from a girder is taken along bridge length.

4.1.2 Numerical modelling

The model is created using eight-node plane stress Plane 183 elements in ANSYS (ANSYS Inc., 2019). Each element has the following dimension: 240mm by 300mm by 500mm ($length \times width \times thickness$). The model has a span length of 12m and 1.5m depth (See Figure 4-1). It has 250 elements – 50 on each level, five levels from bottom to top. Damages are simulated by stiffness reductions in select locations. Damage locations for the model (shown in Figure 4-1) are at the bottom of the beam, 3m, 6m, and 9m from left support. The bridge is subjected to a load from a slowly moving 25 tonne, three axle rigid truck. The load application is simulated as a series of sequentially applied load steps on nodes. As an example, axle loads on the modelled girder at 50th load step is shown in Figure 4-3.

Damage scenarios are created by reducing the value of Young's modulus (or stiffness) of an element (E) or a combination of elements. In Figure 4-3 the selected elements for damage ($E_i, i = 1,2,3$) as well as their locations are shown. Six damage location scenarios (Ds) are investigated and are listed in Table 4-1. Element stiffness reduction is done in levels - 10%, 50%, and 100%. These element stiffness reductions (or damage severity (S)) by 10%, 50%, and 100% are referred to as S_1, S_2, and S_3 for ease of analysis. These correspond to a calculated 2%, 10%, and 20% stiffness reduction of the entire girder cross-section, respectively. Damage scenario S_1D_4, for example, denotes 10% reduction of stiffness in E_1 and E_2, or a 2% cross-sectional stiffness reduction at locations E_1 and E_2. With six damage location scenarios and six damaged element combinations, a total of 18 damage scenarios are simulated.

Table 4-1: Damage location scenarios

Damage location scenarios	D_1	D_2	D_3	D_4	D_5	D_6
Damaged element (E)	E_1	E_2	E_3	E_1, E_2	E_1, E_3	E_1, E_2, E_3

4.1.3 Sensor selection

The model has 101 bottom nodes, which can be assumed to be sensors S-1 to S-101 replicating real life scenarios where sensors have to be installed along the bridge and

structural response obtained from them. In this model, response measurements are obtained from only the corner nodes of the eight-node elements. Mid-nodes are not considered. Their corner nodal displacements for damaged elements have strong evidence of damage, which is immediately discernible in the bridge response along the length of the girder and hence the reason why they are selected. The selected nodes are considered to be targets (S_1 to S_{51}) on the real structure. Node arrangement for response is guided by the response technique as described in sections 3.3.8, 3.3.9, 3.3.10, and 3.3.11.

Nodal displacements are collected at each time step. The axle loads are applied in time steps using ANSYS APDL steady state analysis. Nodal displacements are collected from all sensors at each time-step as the axle loads roll over the girder. Collated nodal displacements are stored in a convenient and easily accessible data structure first stored on ANSYS and then exported. Further analyses derive secondary response from displacements and all responses are then used for damage detection analyses. The measurements are then analysed for possible damages and their locations.

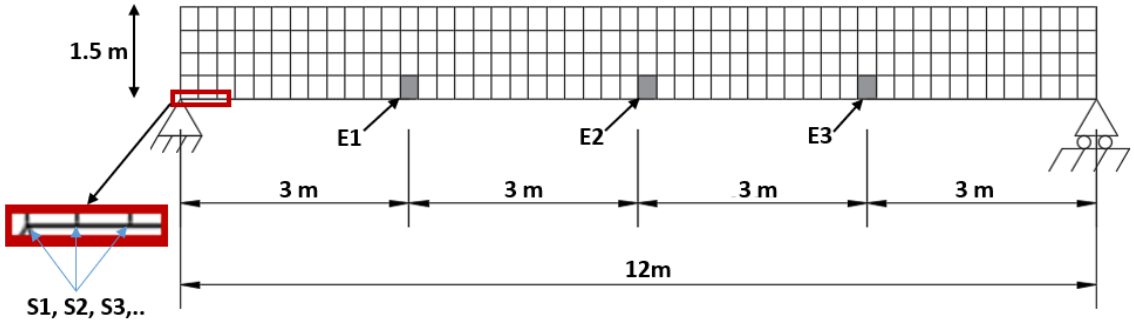

Figure 4-1: Numerical model girder

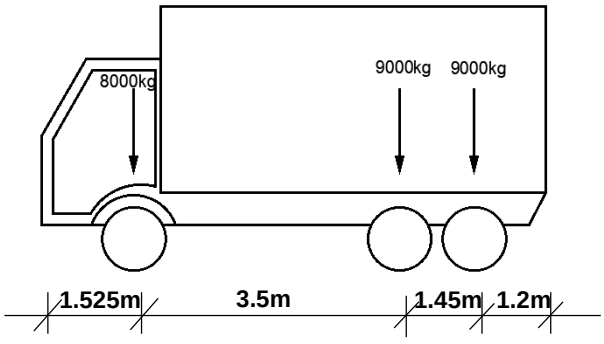

Figure 4-2: Vehicle and load model

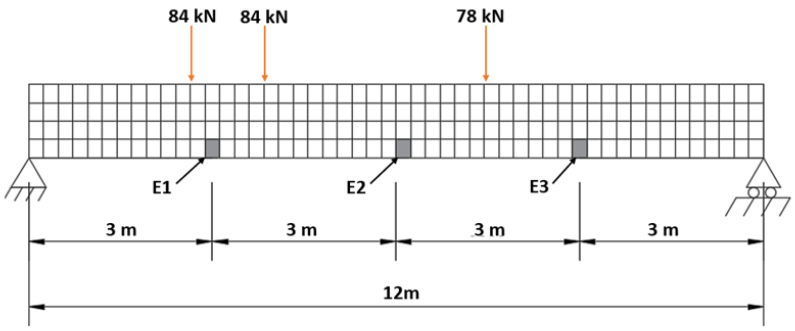

Figure 4-3: A sketch of the numerical model and load locations at 50th measurement step

4.1.4 Results

Results from the numerical study is presented in two main phases:

- Phase I: Response from main simulation, i.e., girder under a moving load from truck.
- Phase II: Parametric studies are conducted to investigate the robustness and sensitivity of the techniques – effects of damage locations, damage severities, and effects of noise, and finally effects of FoV.

Response time histories

Response time histories (or the influence line) derived from the target or a set of targets are shown in Figure 4-4. It is worth remembering here that whether targets or target sets are used depends on the response technique in use (see sections 3.3.8, 3.3.9, 3.3.10, and 3.3.11). Targets are used for displacements, target sets are used for secondary responses, - a pair of targets for inclination angles and strains, and three targets for curvature. From basic knowledge of structures, the largest deflections (in mm), strains (in $\mu\varepsilon$) and curvatures (unitless, therefore expressed in n or 10^{-9}) are expected at the mid-span of the girder (S_{25} at 6m), while the highest inclination angles (in $\mu\mathrm{rad}$) are expected close to the right support of the girder (S_{50}). These largest response histories are here reproduced in Figure 4-4, from which it is clear that maximum displacement, strain, inclination angle, and curvature are about 2.9mm, 120$\mu\varepsilon$, 800$\mu\mathrm{rad}$, and 100n respectively – relatively small values for a structure of its size.

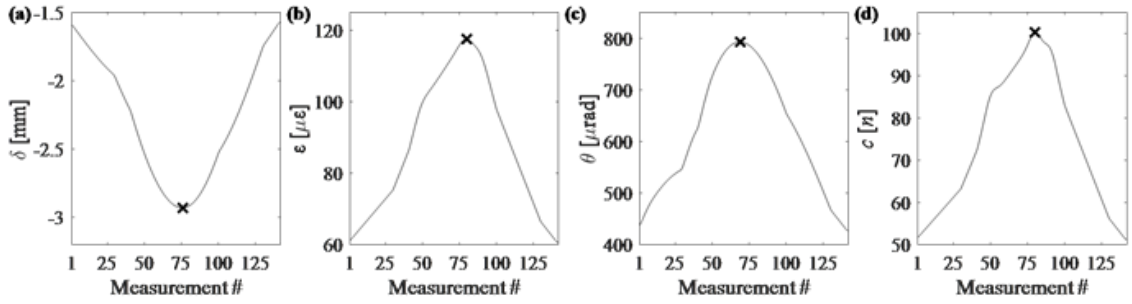

Figure 4-4: Response histories of (a) deflection, (b) strain and (d) curvature at the mid- span of the girder, and (c) inclination angle next to the left support derived from nodal displacements. 'x' marks the maximum absolute response value.

Brief numerical validation of response time histories

Primary response (displacements) are the obtained directly from the load-response process of the numerical model, as is obtainable in practice where displacements are the primary output of the image processing phase. Secondary responses (strains, curvatures, and inclination angles) are calculated using displacement data.

Since strains are also obtainable from the FE software (ANSYS), they are briefly checked against each other for the undamaged (in-tact) state of the girder. At the last measurement step (i.e., step 141, when the last axle of the truck is on the last node), the FE value is identical to the calculated value at $\approx 60\mu\varepsilon$.

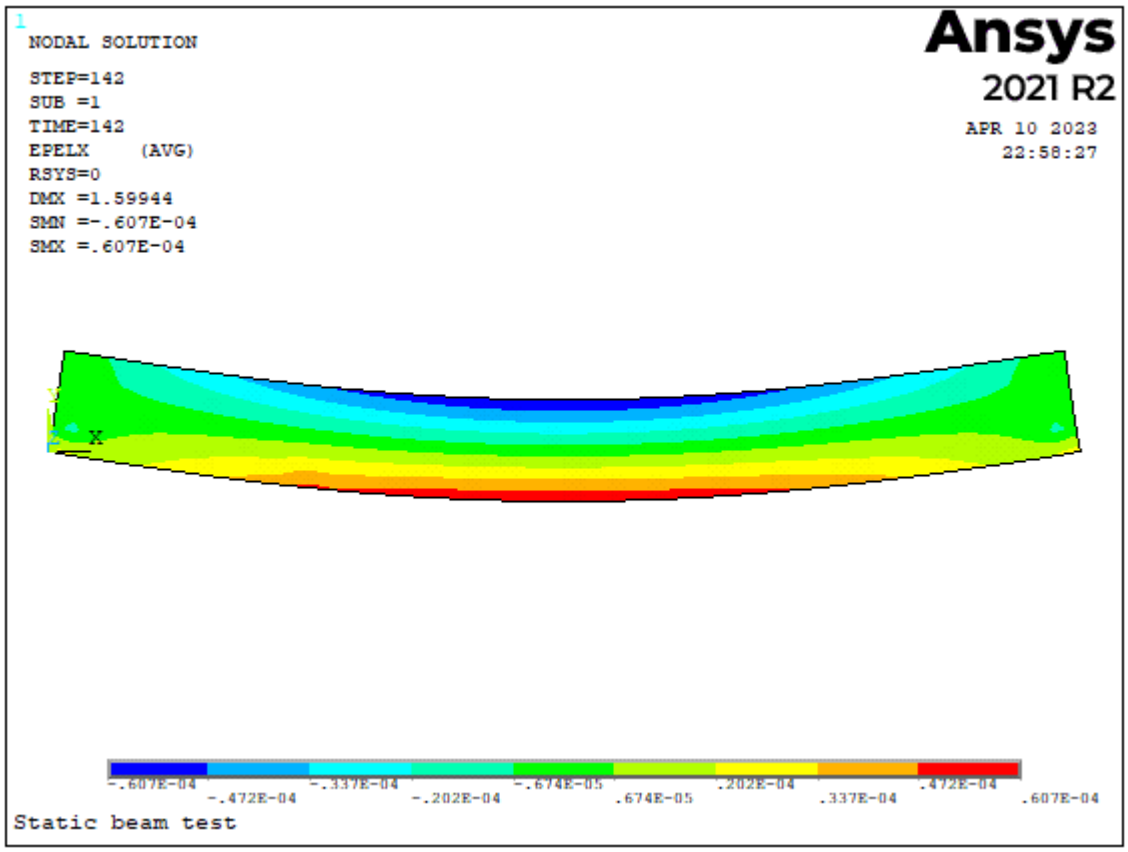

Figure 4-5: FE 1-D strain for last measurement step (strain at girder midpoint $\approx 60\mu\varepsilon$, same as calculated)

At maximum strain, which occurs when track is at girder midpoint, the FE vale is midpoint $\approx 120\mu\varepsilon$, similar to $\approx 117\mu\varepsilon$ from calculations, the difference attributed to the differences in engineering strain vs true strain used by the FE software.

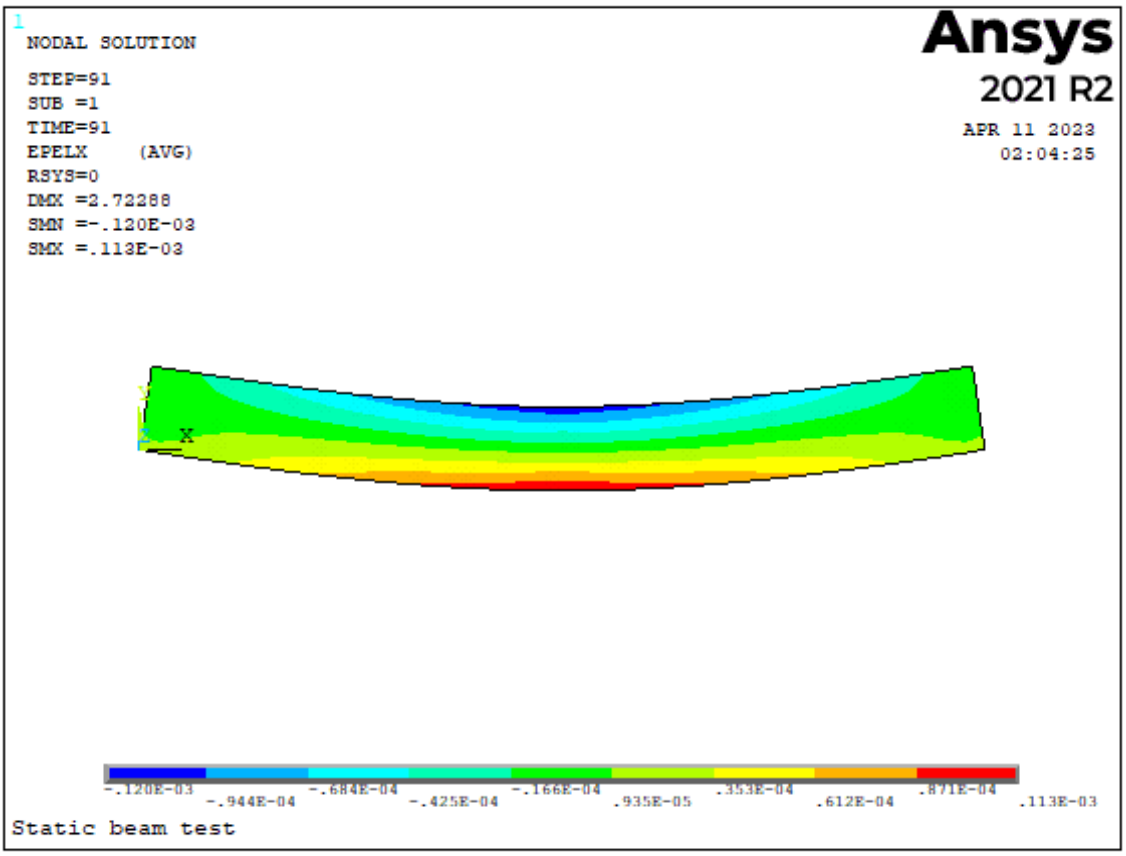

Figure 4-6: FE 1-D strain for measurement step 75 – when truck is near girder midpoint (strain at girder midpoint $\approx 120\mu\varepsilon$*, similar to* $\approx 117\mu\varepsilon$ *from calculations)*

Damage detection

As described in Chapter 3, the maximum response (r_{max}) for each target location(s) is extracted from their time histories. This is done for all response types (displacements, curvatures, strains, and inclination angles). r_{max} from each target location forms the girder response (r) along its length, - also known as response profile. Damage is then sought for by comparing response profiles obtained at different inspections or load cycles.

Damage detection is demonstrated on all four types of response: deflection (r_δ), strain (r_ε), inclination angles (r_θ) and curvature (r_c). Damage scenarios S_1D_2 and S_2D_5 are used as demonstrators, shown in Figure 4-7. In Figure 4-7, response profiles (r_δ) are shown in the top row, change in response (between baseline response and selected damage scenarios) (Δr_δ) are shown in the middle row, and damage sensitive features (e_δ) are shown in the last row, for deflections, strains, inclination angles and curvatures respectively (column wise). Also, the green dashed lines are response at no damage (only for response plots); blue and black lines are S_1D_2 and S_2D_5, respectively.

Plots for r_δ and r_θ for undamaged and damaged girder show no discernible differences. Plots for r_ε and r_c show spikes at damaged locations which indicates damages – at midpoint for blue lines (S_1D_2), and at 3m and 9m for black lines (S_2D_5). Since spikes can be observed in strains and curvatures even before subtracting responses, it then follows that they are more sensitive to local damages than deflections and inclination angles going by the spikes for the damaged structure. As expected, values of inclination angle along the length of the girder change from positive (clockwise inclination) to negative (anticlockwise inclination). strains at the left support are larger than at the right support. This can be explained with the load distribution (i.e., axel loads) on the girder, as shown in Figure 4-2.

Δr values along the length of the girder on the second row show changes in girder response, which suggest for damage(s) and its(their) location(s). It is worth recalling here that Δr values are derived by subtracting scenario response from the baseline, so as expected, responses that already show clear spikes in r_δ plots also show the largest spikes in damaged regions in Δr_δ plots. Also noteworthy is that clear differences also emerge in Δr_δ and Δr_θ. For inclination angles, these differences are not so much spikes as they may be described as response shifts at damaged locations at any case scenarios. So, what we know is that at damage locations a small shift in inclination angles occur. Primary structural response computed directly from target displacements (i.e. deflections/displacements) are much less sensitive to damage; they appear to change very slowly (see Δr_δ and e_δ plots), without clear spikes or shifts as with others, and hence cannot be relied upon for damage localisation. This is supported by similar studies using the deflection curve of horizontal structures, for example in (Erdenebat et al, 2018).

Changes in Δr_ε and Δr_c are significant for S_2D_5 due of course, to its higher damage severity. But for S_1D_2, the peak at the middle of the girder is small (although noticeable), which is due to scale (as they are plotted together with S_2D_5), as a larger scale will allow spikes to be more prominent. Δr_δ for S_1D_2 spikes, though with a small maximum value, at the mid-section of the girder, where the damage is located. Δr_δ indicates damage location for S_2D_5, when it peaks between 3 m and 9 m of the girder length. Δr_θ for both damage scenarios shifts abruptly at damage locations. This abrupt change however, is less visible with more damaged locations on the structure (say S_2D_6 which has three damaged elements. The trend of Δr_θ to shift at damage locations is different from the others, prompting a different technique for generating the damage sensitive feature (e_θ) for localising damages.

At the bottom plots of Figure 4-7 are values of the damage sensitive feature e_r along the length of the girder. e_r as explained in section 3.3, is a ratio of change in response to original response, expressed as a percentage. This makes it easy to calibrate and quantify change in response, and thus compare them. But to objectively claim that damage occurs at a

location, one must specify a threshold that must be surpassed before such claim can be made. As we will see in the following paragraphs, it is not easy to specify this threshold such that it applies to all calculated responses, therefore a threshold value (γ) of 5% is selected. The difficulty is due to differences in behaviour and sensitivity of the responses. For example, strain damage sensitive feature (e_ε) changes by about twice as much as that for curvature (e_c), for the same damage scenario; target displacements as already explained in preceding paragraphs change slowly and without spikes, and for the same damage scenario e_ε has its peak at 30 times its value, and never even reaches the set threshold. Tilts, as already explained in the preceding paragraph has shifts instead of spikes at damage locations and so a case-specific approach had to be developed for its damage sensitive feature (e_θ).

The case-specific derivation of e_θ is used here as proposed in Section 3.3.10 of Chapter 3.

e_θ peaks above 2% at damage locations for both scenarios, but the damage threshold is not breached for either of them.

For displacements, e_δ for S_1D_2 and S_2D_5 do not exceed 2%, which indicates that the damage sensitive feature does not exceed the confidence bound, even though e_δ peaks at damage locations. e_ε for both selected damage scenarios exceed γ at damage locations and the peaks correctly indicate damage locations. Damage in S_1D_2 is not significant enough for e_c to exceed γ (even though a spike is clearly seen at damaged location), however, for S_2D_5, e_c surpasses γ significantly at both damage locations.

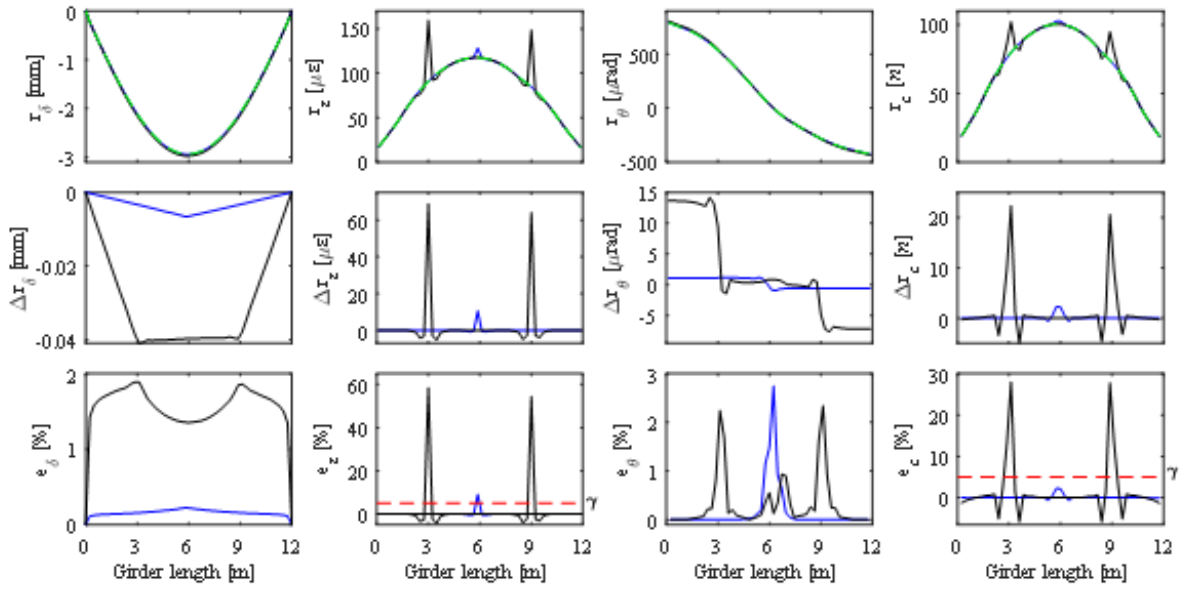

Figure 4-7: From left to right: deflection, strain, inclination angle and curvature along the length of the girder. From top to bottom: girder response (r), change in girder response (∆r) and damage sensitive feature (e). Green dashed lines are response at no damage (only for response plots); blue and black lines are S_1D_2 and S_2D_5, respectively.

The summary of damage detection performance is given in Table 4-2 for all responses. If e_r exceeds the damage threshold at the damage location(s), the damage is said to be detected, if this is not the case damage is said to be not detected, if e_r exceeds damage thresholds at both no damage locations and also at damage locations, damage is deemed to be partially detected.

Table 4-2: Damage detection performance summary

Damage feature	Damage severity	D_1	D_2	D_3	D_4	D_5	D_6
e_δ	$S_1/S_2/S_3$	N/N/Y	N/N/Y	N/N/Y	N/N/Y	N/N/Y	N/N/Y
e_ε	$S_1/S_2/S_3$	Y/Y/Y	Y/Y/Y	Y/Y/Y	Y/Y/Y	Y/Y/Y	Y/Y/Y
e_θ	$S_1/S_2/S_3$	N/N/Y	N/Y/P	N/N/P	N/P/Y	N/N/P	N/P/Y
e_c	$S_1/S_2/S_3$	N/Y/Y	N/Y/Y	N/Y/Y	N/Y/Y	N/Y/Y	N/Y/Y
Y – damage is detected; P – damage is partly detected; N – damage is not detected.							

Added measurement noise

One challenge with CV-SHM systems is to accurately capture sub-pixel movements of targets, to accurately obtain their structural responses. These are influenced by many factors some of which are (i) camera resolution, (ii) camera or ground motion, (iii) environmental conditions, and (iv) target tracking algorithm. Having a stationary reference target in a FOV has been used to remove noise induced by camera motion in (Luo et al., 2018). Camera specifications, FOV, and achievable pixel resolution are the major determinants of final measurement resolution achieved and are thus important for achieving accurate response measurements, compulsory for a reliable assessment of bridge conditions. Increase in FOV results in a decrease of the measurement resolution as a greater portion of the structure is captured with the same camera settings, i.e., increase of the measurement noise (η). The achievable pixel resolution from the image processing algorithm is also as important as the selection of the suitable FOV. Image processing algorithms have been reported to achieve resolutions anywhere between 1/2 and 1/100 pixels (further referred to as $\frac{1}{100}px$) (Feng et al, 2015). One patented algorithm has been claimed by its authors to reach even $\frac{1}{500}px$ resolution (Imetrum, 2020; Potter and Setchell, 2014).

In this section, an investigation is carried out on the influence of measurement error due to camera FOV and pixel resolution on final measurement resolution and consequently damage detection performance. This is in form of Gaussian noise (η) here given as the product of the scale factor (SF) and pixel resolution (PR) (Equation 4.2), and is added to horizontal and vertical displacements of each target which gives the structural response (i.e., nodal displacements of the numerical model), at each load step. SF captures the camera FOV as it is the quotient of image distance (d) and its known physical dimension (D), expressed in millimetres per pixel (mm/px) (see Equation 4.3).

$$\eta = SF \cdot PR \qquad 4.2$$

$$SF = \frac{D}{d} \qquad 4.3$$

For the purpose of this demonstration, it is assumed that a 12 MP camera(s) (4096×3072-pixel frame), set perpendicular to the girder mid-span is used for monitoring the bridge. SF for vertical and horizontal fields of view are also assumed to be the same. Two horizontal FOVs – $F_1 = 12m$ and $F_2 = 2.4m$ are selected.

First camera FOV (F_1): F_1 covers the entire length of the girder. From Equation 4.3, SF for F_1 is 2.93 mm/px. With an assumed 1/500 pixels resolution η is no larger than 5.9×10⁻³ mm. With a 240mm distance (D) between target nodes, maximum strain error is limited to $\frac{5.9\times10^{-3}mm}{240mm} \times 10^6 = 25\mu$. Such measurement accuracy is not sufficient for the detection of damages at S_1 as we would see. To improve measurement accuracy, a lesser FOV and/or a high pixel resolution image processing algorithm must be utilised.

Second camera FOV (F_2): F_2 covers only a fifth (2.4m) length of the girder. Its measurement accuracy is five times higher, giving SF = 0.6mm/px from Equation 4.3. $\eta \leq 1.2\times10^{-3}$ mm and maximum of 5μ error in strains is expected for the same 240mm distance. With F_2 at least five cameras are required to capture response of the entire girder.

A range of pixel resolutions are selected for the study to reflect both the current boundaries in industry, as well as practically achievable values for people without the cutting-edge technologies. $\frac{1}{500}px$ is the highest pixel resolution reported in the academic literature of this sub-field (Imetrum, 2020; Potter and Setchell, 2014). Achieving such high accuracy in-situ is of course challenging. Practically with limited technology, anywhere between $\frac{1}{20}$ to $\frac{1}{100}px$ could be achieved. Three PRs, $\frac{1}{500}px$, $\frac{1}{100}px$ and $\frac{1}{20}px$, are therefore included in the study. Using these in Equation 4.2, three measurement noise levels ($N_i, i = 1,2,3$) are computed for each FOV F_1 and F_2. These are added to displacements collected for each time step for both fields of view. Combinations of added measurement noise and fields of view are given in Table 4-3. The combinations are

written in terms of the noise level (N_i) and FOV (F_1 and F_2). For example, N_2F_1 corresponds to $\frac{1}{100}px$ resolution accuracy (or measurement error) derived from a horizontal FOV that captures 12m (i.e., the entire length) of the girder. N_2F_2 and N_3F_2 are the same as N_1F_1 and N_2F_1 respectively, as their (N_2F_2 and N_3F_2) pixel resolutions are five times more, while their fields of view are five times less than those of as N_1F_1 and N_2F_1 respectively. Equation 4.3 mathematically sets the limits of η, which follows random Gaussian distribution.

$$-0.5 \cdot (SF \cdot PR) < \eta < 0.5 \cdot (SF \cdot PR) \qquad (4.4)$$

Table 4-3: Combinations of added measurement noise and camera FOV

N_i	PR (px)	F_1 (the entire length of the girder)	F_2 (2.4 m of the girder)
N_1	$\frac{1}{500}$	$-\frac{5.9}{2} \cdot 10^{-3}mm < \eta < \frac{5.9}{2} \cdot 10^{-3}mm$	$-\frac{1.2}{2} \cdot 10^{-3}mm < \eta < \frac{1.2}{2} \cdot 10^{-3}mm$
N_2	$\frac{1}{100}$	$-\frac{29.3}{2} \cdot 10^{-3}mm < \eta < \frac{29.3}{2} \cdot 10^{-3}mm$	$-\frac{29.3}{2} \cdot 10^{-3}mm < \eta < \frac{29.3}{2} \cdot 10^{-3}mm$
N_3	$\frac{1}{20}$	$-\frac{146}{2} \cdot 10^{-3}mm < \eta < \frac{146}{2} \cdot 10^{-3}mm$	$-\frac{146}{2} \cdot 10^{-3}mm < \eta < \frac{146}{2} \cdot 10^{-3}mm$

Figure 4-8: L – R | Diagrammatical description of $F_1$and F_2

Response pre-processing

This is an important stage where raw, noisy response is cleaned up before performance assessment. Response pre-processing includes several signal de-noising and filtering techniques and approaches. The choice of which to use completely depends on the type and nature of data at hand. The best results for this study was achieved by implementing the response pre-processing in two stages.

1. Firstly, displacement time histories both vertical and horizontal for each target are smoothed with the moving average filter using a 10-measurement window.

2. Secondly, a conditional moving average filtering of the secondary response obtained from pre-processed displacement time histories, done if they are deemed to still be noisy after the first round of pre-processing.

After this, the change in response (Δr) is computed and damage sensitive feature (e_r) is derived.

As a demonstration of the pre-processing phase, Figure 4-9 displays midspan target vertical and horizontal displacements from the undamaged state at N_1F_1 and N_3F_1 scenarios. Displacements at N_1F_1, compared with those at N_3F_1, are expectedly much smoother with little visible measurement noise. This is true for both vertical and horizontal displacements. Visible noise contamination of course depends on the severity of noise combination (i.e. N_i).

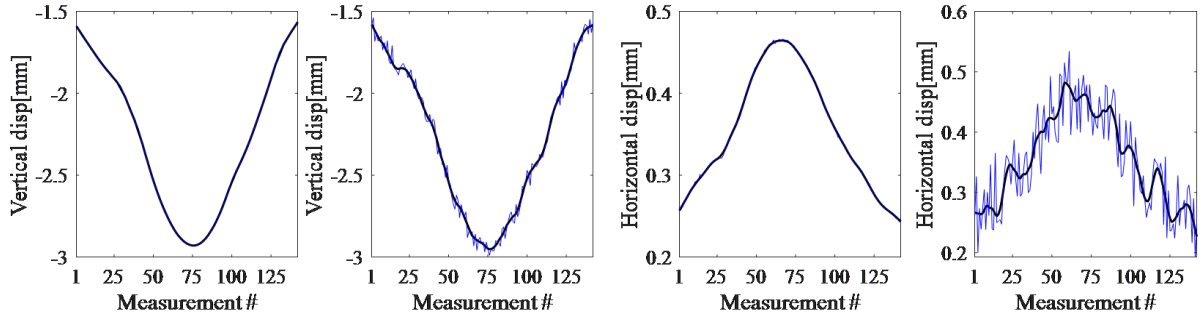

Figure 4-9: Raw (blue line) and pre-processed (black line) displacements of a target at the midspan of the girder. Left to right: Vertical displacements at N1F1, N3F1, and horizontal displacements at N1F1, N3F1

Pre-processed target displacements are used to derive the secondary responses of strain, inclination angles, and curvature. If raw, noisy displacements are used to derive secondary responses, they appear noisier, the degree to which is dictated by the noise levels (N_i) added to the original raw displacements. Essentially, derived secondary responses look much noisier than primary displacement responses for the same noise levels inflicted on the primary. Again, this is due to the relatively much increased sensitivity of derived responses. This is graphically explained in the plots in Figure. 4-10 which (from L – R) display raw and pre-processed deflection, strain, inclination angle and curvature histories at N_1F_1 and N_3F_1. Deflection with N_1F_1 combination added does not seem to differ much from that computed directly from nodal displacements (with no added measurement noise), (see Figure 4-4), but the noise combination as expected affects derived responses more as shown in strain, inclination angle, and curvature histories on the top row. On the bottom row, deflection with N_3F_1 combination appears noisier than with N_1F_1 (in top row), and this phenomenon is the same with the secondary responses with N_3F_1 (i.e., they are noisier than

their counterparts in the top row with N_1F_1). Curvatures, in particular require needs very accurate coordinates of targets, as even the slightest deviations from the accurate values cause large errors and a noisy data as evident in Figure. 4-10.

One more importance of the pre-processing phase that may be inferred from Figure. 4-10 is in the obtention of maximum response value from response histories. Noisy data tends to yield higher and inaccurate values for maximum response (and also lower for inclination angles). When this is replicated at all target time histories across the structure, the result is a significantly inaccurate structural response profile with values higher or lower than that obtained with pre-processed data. This is shown in the girder response plots in Figure 4-11.

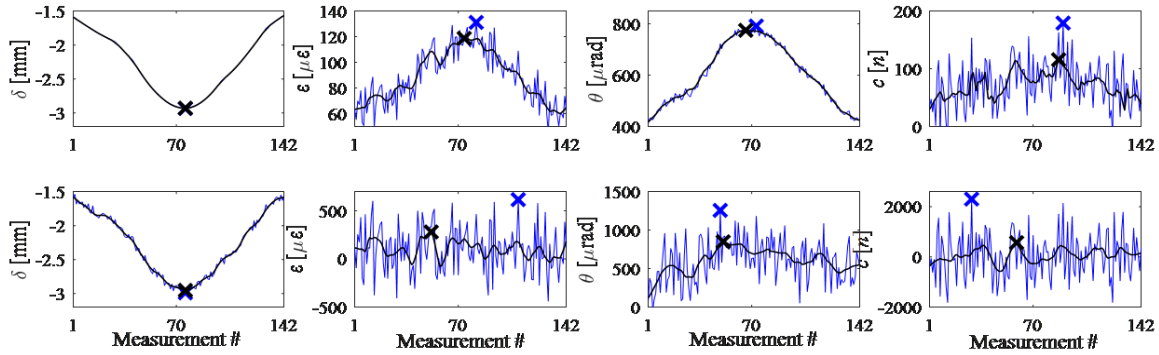

Figure. 4-10 From left to right: Measurement histories of raw (blue line) and pre-processed (black line) deflections, strains and curvatures at the mid-span of the girder, and inclination angles next to the left support derived from pre-processed target displacements at N_1F_1 (top) and N_3F_1 (bottom) combinations. 'x' indicates the absolute maximum response value.

Structural response

As described in Section 3.3, maximum response (r_{max}) values for each target location (or a set of targets) are extracted from target displacements after pre-processing, and this forms the bridge's response profile (r) along its length. For the purpose of comparison, maximum values are extracted here from both raw and pre-processed measurements.

In Figure 4-11 the girder response generated from both raw and pre-processed target displacements at N_1F_1 and N_3F_1 combinations are displayed. r_δ, at N_1F_1 is smooth with no visible measurement error, and only slightly distinguishable in N_3F_1. Both raw and pre-processed r_ε at N_3F_1 are noisy and, in contrast to N_1F_1, do not bear a resemblance to the expected strain distribution at the bottom side of the girder (as for example in Figure 4-7) due to the noise contamination. For r_c, only that at N_1F_1 vaguely resembles the expected girder curvature in the curvature. This can only suggest that curvature response is more sensitive to noise and highly contaminable to the extent that the chance of detecting

damage is relatively more compromised. The same approach is employed to compute girder response for all other damage scenarios at all combinations of measurement noise and camera FOV.

The condition of r_θ at N_1F_1 is similar to that of r_δ at same combination (i.e., very smooth with no visible measurement noise), but at N_3F_1 it appears noisier. A measurement shift at damaged locations (girder midpoint) is observed in both r_θ plots in same figure despite the noise. This shift may result in false damage detection so must be properly understood. To begin, we must observe that the measurement shift is absent in r_θ plot at the top row of Figure 4-7 (i.e., response derived before noise contamination). This can only mean that the noise contamination has something to do it. The measurement shift is due to a combination of r_{max} obtention process and the effect of noise contamination, diagrammatically described in Figure 3-14. It follows that since r_{max} is the maximum response from each target's time history, at any two targets straddling both sides of zero (which should be about the girder's midpoint), the value of r_{max} at the target on the positive side must be its maximum positive θ value, and that at the negative side target must be its lowest negative θ value. From here it must now be concluded that measurement noise inflates both positive r_{max} and negative r_{max} (or r_{min}) values for inclination angles. For all other responses, and as can be inferred from.

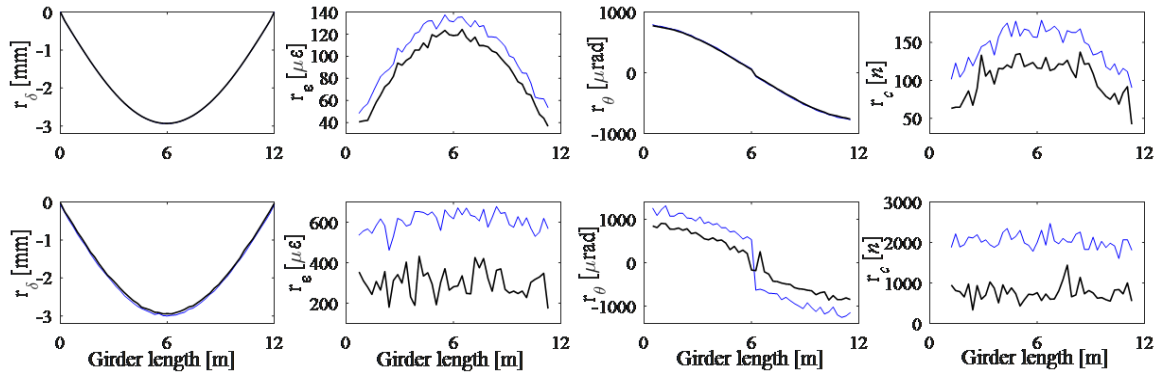

Figure 4-11: Girder response (r) from raw (blue line) and pre-processed (black line) r_{max} values at N_1F_1 (top) and N_3F_1 (bottom) combinations. From left to right: deflection (r_δ), strain (r_ε), inclination angle (r_θ) and curvature (r_c).

Damage detection from noisy response

Damage detection is performed on the pre-processed girder response (r). Using one scenario with the most damage severity, i.e., – S_3D_5 at N_1F_1 and N_3F_1 combinations as demonstrator, the damage detection procedure is carried out. Figure 4-12 shows plots of the change in girder response (Δr) and damage feature (e). Though with noisy appearance, Δr_ε, Δr_c, and Δr_θ plots show damage locations clearly (through spikes, or for inclination

angles, through shifts). In Δr_δ plots however, just as in Figure 4-7 (without noise), damage locations may be inferred from the corners in the curve. This remained clear at all noise levels at this phase. This method cannot be a fail-safe way of locating possible damages as corners are less sharp if there are more damage locations (e.g., three damage locations), especially if close to each other.

e_δ values for the selected scenarios exceed damage threshold and spike at damage locations. e_ε spikes at damage locations, however, measurement noise affects the reliability of damage detection as damage threshold is surpassed at most undamaged locations, especially at N_3F_1. e_θ at N_3F_1 is very strongly affected by measurement noise. The values exceed damage threshold across the entire length of the girder, including a false spike at midpoint. However, e_θ at N_1F_1 has less noise so its values seldom exceed the damage threshold, except at damage locations, which means the threshold rightly detects and locates damage for this response. The effect of added measurement noise is severely affecting damage detection using e_c at N_1F_1 and N_3F_1 as e_c values frequently exceed the damage threshold. Damage locations can still be inferred however from the spikes in the less noisy N_1F_1 response.

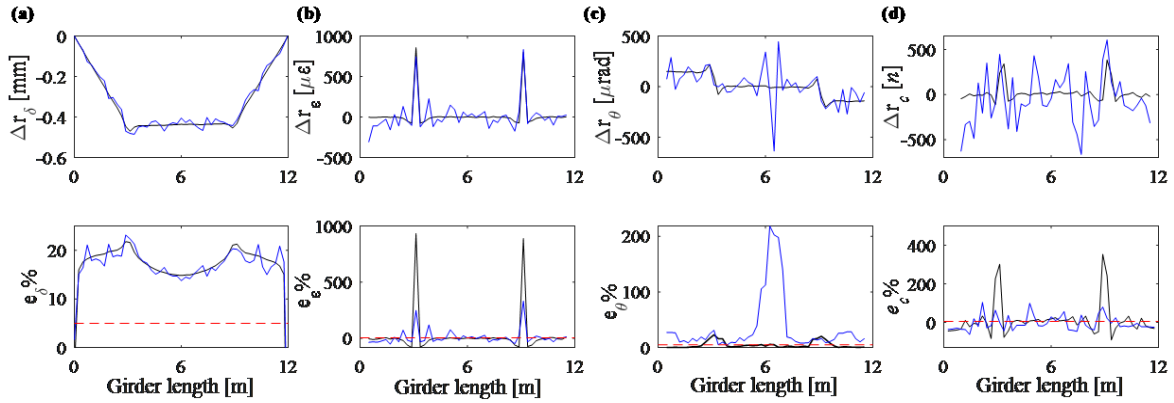

Figure 4-12: Δr and e for deflection, inclination, strain and curvature (from left to right) at damage scenarios S_3D_5 at N_1F_1 (black lines) and N_3F_1 (blue lines) combinations. Red dashed line is the damage threshold.

Damage detection performance for all damage scenarios at all combinations of added measurement noise and camera FOV are summarized in Table 4-4. Damage detection here means that either damage thresholds are surpassed at damage locations, or as often with noisy measurements where the threshold is breached at several locations, - clear distinguishable spikes at same damage locations. At the lowest damage severity (i.e., S_1), damages are detected and localised only with the lowest measurement noise (N_1F_1) in strain measurements. In S_2, robustness improves as they are detected and localised with N_1F_1 and N_1F_2. Damage and its location(s) are detected from strain and displacement

measurements at all combinations of measurement noise and camera FOV at damage severity S_3. Inclination angles and curvatures (e_θ and e_c) do not provide such good results as they are only detected with some degrees of added measurement noise and not others.

Table 4-4: Damage detection performance at added measurement noise

Damage severity	e	Noise and FOV combinations	$\boldsymbol{D_1}$	$\boldsymbol{D_2}$	$\boldsymbol{D_3}$	$\boldsymbol{D_4}$	$\boldsymbol{D_5}$	$\boldsymbol{D_6}$
S_1	e_ε	$N_1F_1/N_1F_2/N_2F_1/N_3F_1$	Y/N/N/N	Y/N/N/N	Y/N/N/N	Y/N/N/N	Y/N/N/N	Y/N/N/N
S_1, S_2	e_δ, e_θ, e_c	All	N	N	N	N	N	N
S_2	e_ε	$N_1F_1/N_1F_2/N_2F_1/N_3F_1$	Y/Y/N/N	Y/Y/N/N	Y/Y/N/N	Y/Y/N/N	Y/Y/N/N	Y/Y/N/N
S_3	e_δ, e_ε	All	Y	Y	Y	Y	Y	Y
S_3	e_θ	$N_1F_1/N_1F_2/N_2F_1/N_3F_1$	Y/Y/N/N	Y/Y/N/N	Y/Y/N/N	Y/Y/N/N	Y/Y/N/N	Y/Y/N/N
S_3	e_c	$N_1F_1/N_1F_2/N_2F_1/N_3F_1$	Y/N/Y/Y	Y/N/Y/Y	Y/N/Y/Y	Y/N/Y/Y	Y/N/Y/Y	Y/N/Y/Y
N – damage not detected; Y – damage detected;								

Figure 4-13 highlights the robustness of e_ε values for damage scenarios, as reported in Table 4-4. It displays several combinations of measurement noise and FOV at which damages and their location are detected, at the two lowest severities (i.e., S_1 and S_2). For no other response type were its damages detected and localised, at both S_1 and S_2. Even at N_1F_1 damages can be detected at S_2, although, at S_2D_4 e_ε values exceed the damage threshold slightly at no damage locations, but even at these, clear spikes are distinguishable at damage locations.

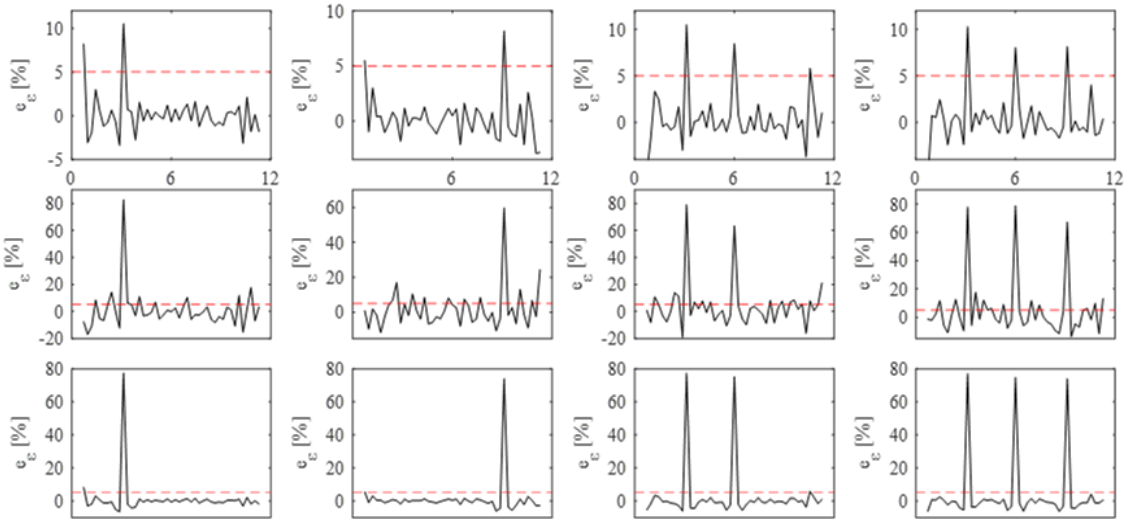

Figure 4-13: e_ε for damage location scenarios D_1, D_3, D_4, and D_6 (left to right) at damage severity S_1 at N_1F_2 (top), and S_2 at N_1F_1 (middle) and N_1F_2 (bottom).

4.1.5 Discussions and Summary of damage detection in numerical simulation

Here findings from the numerical study and considerations for field applications of cost-effective computer CV-based measurement are discussed.

Displacement time histories from selected targets (or nodes in numerical simulations) along the length of a structure are obtained while a truck passes over the structure in a simulated load-response test, when the structure is in healthy and damaged conditions. The displacement time histories can be seen as primary response from which secondary response of curvature, inclination angles, and strains are derived. For each response, its absolute maximum values from the time histories of each target are selected to form girder response profile along its length. Damage sensitive features, which are ratios expressing the current girder response increase with respect to the baseline response, are plotted along the length of the girder to also form a damage sensitive feature profile of the structure. In locations where damage features exceed the damage threshold, which in this study is set at 5%, damage is said to be detected and located. From Figure 4-7, damage locations are clearly discernible from damage feature plots, although they may not exceed the threshold in some cases, in which case they should be discerned from the spikes at damage locations. However, when the measurement noise is added to target displacements, damage detection is challenging, requiring pre-processing of primary target displacements before the derivation of response.

Damage features computed directly from target displacements (deflections) are less sensitive to low severity damages than features computed from secondary response which are derivatives of target displacements (inclination angles, strains and curvatures) and breach the damage threshold only when damage severity is high (see Table 4-4). Though damages can be clearly discernible from the plots of damage features from deflections (for example, see Figure 4-12), accurately localising the damage is not as straightforward as with other responses. As previously explained in Section 4.1.4, they appear to change very slowly, without clear spikes or shifts as with others, and hence cannot be relied upon for damage localisation. This is supported by similar studies using the deflection curve of horizontal structures, for example in (Erdenebat et al, 2018).

Damage features from strains are the most robust to noise, and small damages can be detected and accurately located even for some combinations in the least severe damage scenarios (see Figure 4-12 Figure 4-13). Although the girder response from inclination angles seems much smoother than that of curvatures, results in Table 4-4 show that damage features from curvatures detect more damage cases. This is related to the computation of damage feature from inclination angles. Damage features are computed to

detect shifts rather than spikes in inclination angles. Damage features are derived from their neighbouring response (inclination angle) values (see Equations 3.15, 3.16, and 3.17). Small values of neighbouring responses, especially when contaminated with measurement noise, result in high damage feature, leading to false damage localisations. Results from the girder with measurement noise can be summarised as follows:

- Achieving 1/500th pixel resolution (PR) with 2.4m FOV is required to detect damages of 2% stiffness loss using strain which is the best performing and most robust. For 10% loss, damage can be detected at same pixel resolution and full 12m FOV. At 20% loss, damage can be detected at all combinations, even at N_3F_1 (i.e., 1/20th pixel resolution and the entire girder).
- Other secondary response (inclination angles and curvatures) can only detect and locate damages from 20% stiffness loss, inclination angles from 1/500th at 12m FOV, and curvatures at all combinations except N_1F_1 and N_2F_2 which combined are the least measurement resolution.
- Displacements can only detect and locate damages from 20% stiffness loss, but cannot be relied upon for localisation, especially with multiple damage locations.

With damage thresholds there seems to be an issue of scale. The 5% threshold is casually surpassed all along the girder's length at higher noise combinations (please refer to Figure 4-12). On some of the plots clear spikes substantially higher than the damage threshold occur at damage locations, and it can be seen that at other points of the girder the threshold is breached simply because the increased noise scale which causes increased fluctuations on the response curve. An obvious solution to this issue is a corresponding increase in damage threshold as damage severity increases, but when one considers potential real-world applications, they can see the challenge with this idea – that damage severity will not be known beforehand.

To conclude, all that has been done in this section is to numerically explore the limits of a real-world application of this approach, recreating and incorporating field and environmental error factors as much as is possible. It is now pertinent to discuss the potential of such application before it is actually carried out.

4.1.6 CV-based measurement challenges in field applications

The success of an affordable CV-SHM system in the engineering community lies within its ability to offer accurate and cost-effective measurements of bridge response. Affordable cameras and open source image processing tools makes computer-vision measurement an attractive option for short term measurement collection (Dong and

Catbas, 2020b; Feng and Feng, 2016). But the challenge remains to accurately capture sub-pixel movements of targets, which are influenced by many factors such as

1. camera resolution,
2. camera or ground motion,
3. environmental conditions, and
4. target tracking algorithm.

Placing, or having a stationary reference target within a FOV may help removing measurement error induced by camera motion (Luo et al., 2018), by simply subtracting structural response from that of stationary target. Capturing response of a bridge may require multiple cameras that must cover the entire length of the bridge to maintain an adequately-high measurement resolution if this is required. A robotic camera system that can be programmed to capture pre-set FOVs at multiple truck crossings can be considered to achieve this (Kromanis and Forbes, 2019). When bridge dynamic response is collected, then cameras have to be time-synchronised (Lydon et al., 2018). But the approach proposed in this paper does not require this, and cameras do not need being placed in the same positions at each measurement event since a simple position-independent approach is used (Kromanis and Liang, 2018).

4.1.7 Summary and conclusions

The numerical validation that has been presented tests the limits of applicability and robustness for an affordable CV-SHM system which could potentially complement regular visual inspections of small to medium span bridges. With the aid of cameras and an increasing number of open source image processing techniques, measurement response can be obtained with confidence as to its accuracy. Developed data-driven techniques can then be applied to analyse measured response for anomalies indicating damages.

This study lays the foundation for data-driven damage detection for CV-SHM of bridges and evaluates its feasibility using numerical simulations. A concrete girder is modelled and load truck crossings are simulated for a range of damage scenarios. Nodal displacements, which are targets in real world CV-SHM of the girder are obtained during loading. Measurement noise, which is a product of the camera FOV and pixel resolution of image processing algorithms, is added to target displacements before the computation of the structure's response (deflection, strain, inclination angle and curvature) and its damage sensitive features. In addition to already established factors known to influence measurement resolution and consequently damage detection such as (i) response type, (ii)

damage intensity, (iii) measurement noise, and (iv) damage location, the following conclusions are drawn:

- High measurement resolution is crucial for CV-SHM of bridges. Even small damages of 2% stiffness loss can be detected in the absence of measurement noise, but this is not the case in real world applications. It is shown that if high PR can be achieved, for example 1/500th PR, then less cameras are required to cover a structure and obtain accurate response. Conversely, less PR will mean that more cameras are needed since FOV must also reduce, if an adequate measurement resolution is to be achieved.
- The proposed damage detection technique does require a synchronized measurement collection even if multiple cameras are employed, since only absolute maximum response values, which are extracted target measurement series, are needed to derive bridge response.
- Pre-processing target displacement histories is vital to obtain precise structural response data from which response profile and damage sensitive features are calculated.
- Damage sensitive features derived from strains perform better than other structural response types. At high enough PRs small damages can be detected. Strains are unitless and calculated from movements of two targets, therefore requiring no scale factor, and thus making them a good option for field applications, provided that high PR is attained.

The next phase of the research is a laboratory application. The setup will include a beam that will be tested in both undamaged and damaged states using a moving load and camera system.

4.2 Case study 2: Laboratory test bed

4.2.1 Description

A laboratory test bed is proposed to validate the proposed methodology. The structural and loading arrangements are similar to that of the numerical model previously reported, i.e., a simply supported beam with a moving load across it. A schematic outline of the proposed set-up is given in Figure 4-14 with the vehicle model given in Figure 4-15. The beam is 2200mm long at the test span, with 1000mm loading and exit spans. Its cross-sectional dimensions are 90mm x 45mm. It is made from C-16 timber, simply supported, with a roller support on one end and pinned at the other. Three 1mm steel plates are attached in front

at three locations within the test span as shown. The loosening of any of these plates from the timber beam simulate a 20% reduction in the stiffness of the region in which they were placed. To mimic a vehicle crossing a bridge, a moving load which essentially is a wheeled wooden platform on which weights can be attached. Therefore, several vehicle weights can be tested on the structure. The mechanism for moving the vehicle is an attached pulling string connected to a motor fixed at the end of the platform. The vehicle is guided along the platform by a guide rail that runs from one end of the platform to the other and propelled by the motor at one end of the platform. Pictures of the laboratory test rig are shown in Figure 4-17, Figure 4-18, and Figure 4-19.

A load scenario is defined as the crossing of the vehicle with a known mass across the test span of the structure. Damage at any load scenario is introduced by loosening the bond (by unscrewing the bolts) between steel plate and timber beam, creating a 20% reduction in stiffness of the affected region.

Aim: The experiment aims to validate the developed damage detection techniques using proposed CV-based sensing. To achieve stated aim, the following objectives were set:

- To detect and obtain structural displacement data due to loading, using CV-based sensing.
- To detect and obtain secondary response (curvature, inclination angles, and strains) from displacement data.
- To localise and quantify damage using both primary and secondary responses.
- To establish the accuracy of response obtained from vision-sensing, especially considering the sub-pixelling capacities of image processing algorithms used, and type of response.

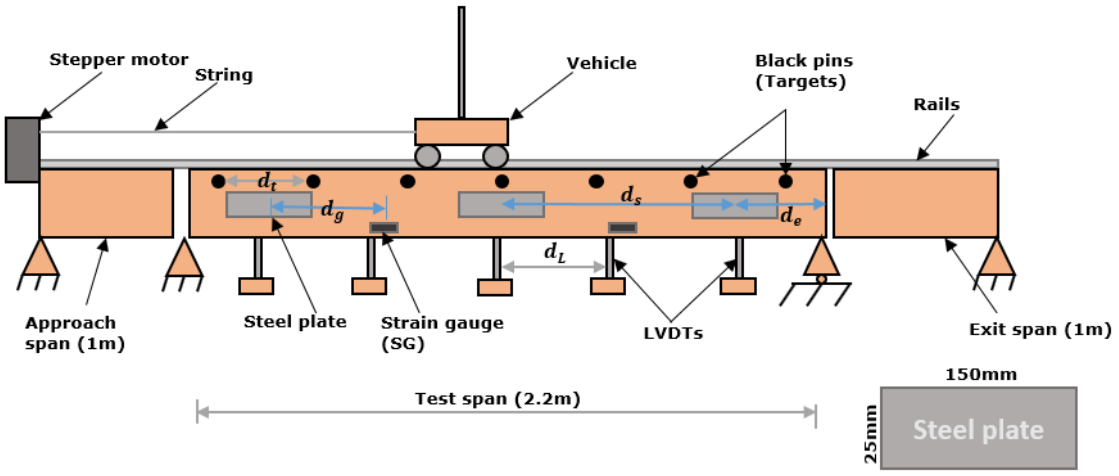

Figure 4-14: Laboratory test bed schematic. d_t, d_g, d_L, d_s, d_e = distance between: targets(120mm), steel plates and strain gauge (475mmc/c), LVDT's (225mmc/c), steel plates (950mm c/c), support and steel plate (150mmc/c); respectively.

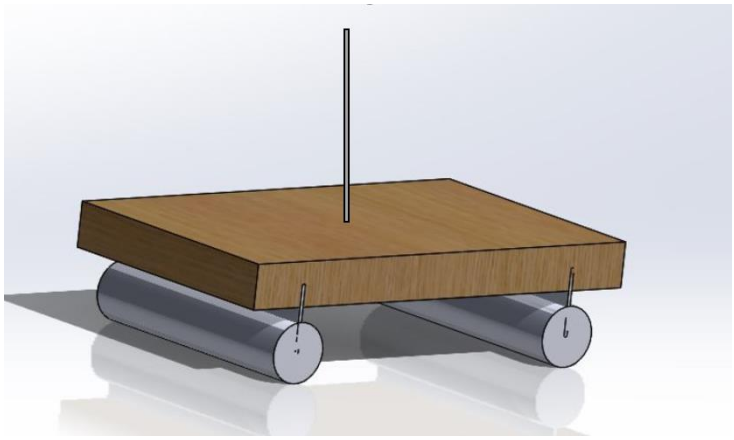

Figure 4-15: Moving load platform schematic

4.2.2 Damage simulation and loading combinations

Three 1mm steel plates ($E_1, E_2,$ and E_3) are attached to the platform at intervals for the purpose of damage simulation. When screwed firmly in place the beam is assumed to be in healthy condition. When loosened slightly and the plates no longer act as composite part of the structure, the beam is assumed damaged at the point of loosening. This loosening action represents approximately 20% stiffness loss in the cross-section. A damage scenario (D) is the loosening of any of $E_1, E_2, or\ E_3$, or a combination of any (see Figure 4-16 for metal plate). Three vehicle load severities are investigated – 5kg, 10kg, and 20kg. For each load severity, Table 4-5 lists damage scenarios investigated.

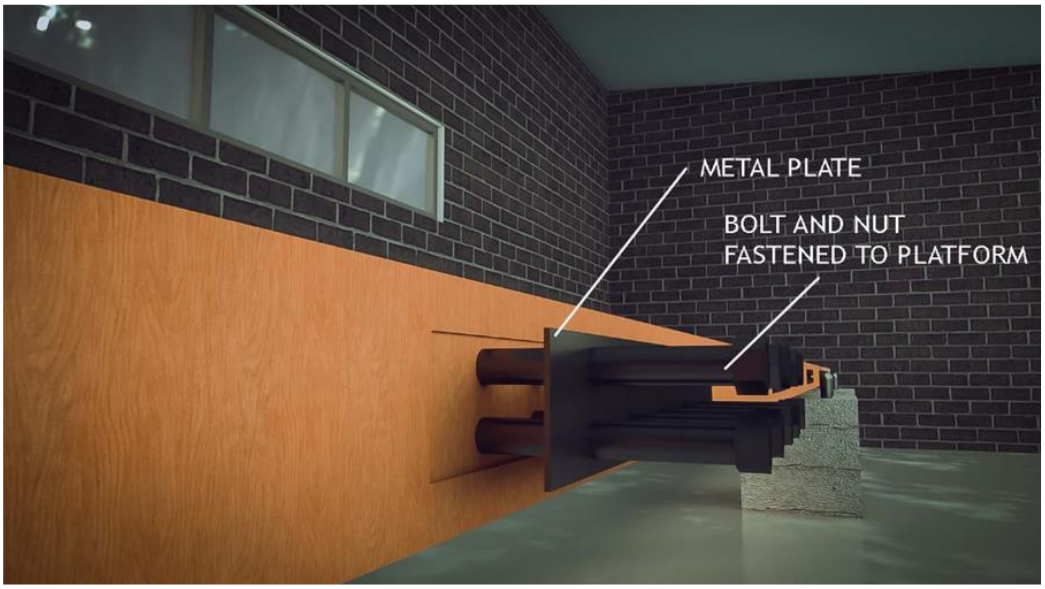

Figure 4-16: 1mm steel plates fastened to the structure. When unfastened they simulate damage on a bridge

Table 4-5: Laboratory test bed damage scenarios

Damage scenarios	$\boldsymbol{D_1}$	$\boldsymbol{D_2}$	$\boldsymbol{D_3}$	$\boldsymbol{D_4}$	$\boldsymbol{D_5}$
Steel plate(s) removed	E_1	E_2	E_3	E_1, E_2	E_1, E_3

4.2.3 Instrumentation, sensors, and their calibration

Table 4-6 gives all technical information about instrumentation. As seen in Figure 4-14, the test rig is instrumented with LVDTs and strain gauges. The LVDT and strain gauges are used to monitor displacement and strain respectively, to set them in comparison with computer vision-derived response. On the structure, black and distinct ball head pins 120mm apart, and each with a diameter of 38mm are set as targets. As illustrated in Figure 4-14, the targets are labelled from left to right for top targets, and also from left to right for bottom targets. To decrease background noise, a stationary target is placed directly below the platform's mid span on a steady white background behind the test platform. Altogether there are two strain gauges – $SG_1$and SG_2; five LVDTs – L_1 to L_5; and circular targets – T_1 to T_n 120mm from each other.

Table 4-6: Instrumentation and technical specifications

Instrument	Specifications	Positional information
Image acquisition device 1: GoPro Hero 5 with attached optical zoom lens	GoPro: Max Video Resolution 3840 x 2160, 12 megapixels; wide, medium, and narrow angle lens options available (14mm,21mm, and 28mm focal lengths respectively); Lens:	1m from test structure. Focus on two targets to validate LVDT and strain gauges.
Image acquisition device 2: iPhone 8	Max Video Resolution up to 4K, 12 megapixels 28mm wide angle lens camera	1m from beam. Captures a 1.7m central length of the beam's main span.
LVDTs		5 LVDTs positioned 225mm between each other, underneath platform.
Strain gauges		2 strain gauges positioned at front elevation of platform, midway between steel plates.
Laptop PC	64-bit, 8GB RAM, 11th Generation Intel Core i7 Processor (2.8 GHz up to 4.70 GHz)	

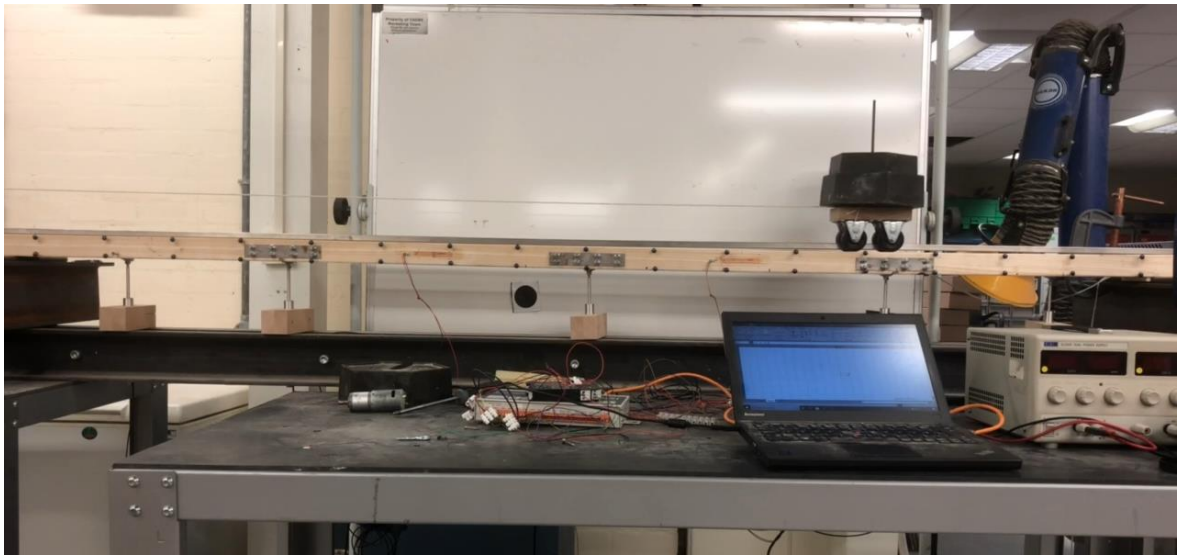

Figure 4-17: Picture of test span with load vehicle carrying 15kg load

Figure 4-18: Zoomed in picture showing attached 1mm steel plate, LVDTs, and targets

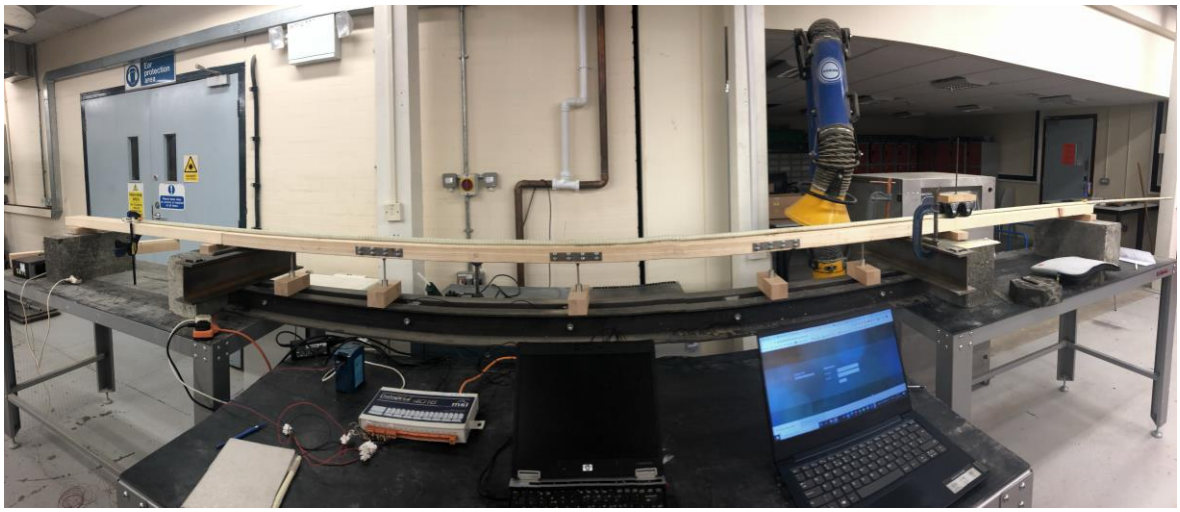

Figure 4-19: Full panoramic image of test rig including approach, test, and exit spans

4.2.4 Measurement collection

A CV-based monitoring system simply consists of a fixed image acquisition device(s) and image processing software. The set-up stage begins with setting up a tripod in a remote and stable location within clear view of the structure and mounting the image acquisition device.

Table 4-6 contains technical parameters for both image acquisition devices, i.e., GoPro Hero 5 and iPhone 8. Both gadgets are virtually identical in terms of specifications.

The cameras are used during the measurement collection event to capture image frames of the test platform subjected to known loads from the robotic vehicle. Both cameras were configured to record 4K footage at a frame rate of 30 fps. The iPhone 8 was positioned one metre away from the structure and without any attached lens so that the full FOV was captured. The GoPro was zoomed in such that it could focus only on two targets on either side of SG1. This was done to obtain very high accuracy strain measurements to compare them to measurements from the strain gauge. Hypothetically this should be realisable; for example, with a FOV no more than 0.5m (which yields a scale factor of 0.13) and a pixel resolution (from image processing algorithm) of $1/50$ pixels, a maximum of $\frac{2.5\times10^{-5}mm}{240mm}\times 10^{6} = 10\mu$ measurement error can be expected. The iPhone 8 camera with 12MP and 4K (3840 x 2160 maximum video mode) at 60fps is used to capture a 1.7m length of the structure, which yields a horizontal scale factor of ≈0.44mm/px, and with known vertical dimensions, a vertical resolution of 0.51mm/px is found. And with an achieved $1/10$ subpixel resolution in image processing, a measurement resolution (η) of 0.05mm/px is derived using Equations 4.2 and 4.3 for the experiment.

$$\eta = SF \cdot PR \tag{4.5}$$

$$SF = \frac{D}{d} \tag{4.6}$$

Videos/photos are collected during the loading event, and then analysed using image processing techniques to obtain structural response for each target. Then, using the techniques proposed in Section 3.3, absolute maximum response values from each target's measurement histories are extracted to form the bridge response profile. These can be stored, and in each new measurement collection event, bridge response obtained is compared to baseline response for condition assessment.

4.2.5 Image processing algorithms

The image processing stage typically begins after the images have been collected from the measurement event. The primary purpose of image processing in CV-SHM is to extract structural information from collected image frames by tracking a target or area of the

structure. A thorough review of the image processing phase including their classification, techniques and algorithms has been done in the Literature Review section (CHAPTER 3). Image processing encompasses a very wide range of feature detection, template matching, and target tracking methods, including digital image correlation (DIC) feature point matching, optical flow estimation, and shape-based tracking, among others. Object tracking in particular, in any of the numerous fields in which it is currently being employed, is dependent on the ability of a structure's features to be detected by the tracking algorithm. Feature point matching is one of the most popular target tracking techniques in CV-SHM. It works by detecting special or key points in two or more images independently using a feature descriptor and then determining their point correspondences based on their local image frame appearance. Key points, such as building corners, connection bolts, or other patches with attractive forms, must be robust, distinct, and invariant to image transformation and illumination variations (Harris and Stephens, 1988). The Hamming distance is typically used to match these descriptors (Calonder et al., 2010), and outliers are removed using RANDOM Sample Consensus (RANSAC) (Martin A. Fischler and Bolles, 1981). Numerous these strategies are available (see (Xu and Brownjohn, 2018)), and a comprehensive evaluation of these techniques and their applications to CV-SHM is provided in Chapter 3, but also in (Brownjohn et al., 2017; Dong and Catbas, 2020a). Several of these have been integrated into software such as Video GaugeTM (Imetrum, 2020) or open source software such as QUBDIsp (Lydon et al., 2019) and DeforMonit (Kromanis and Al-Habaibeh, 2017)).

4.2.6 Camera calibration and lens distortion correction

Lens distortion correction is necessary in particular for wide angle lens cameras, which usually has substantial distortion around the photo's edges. On the iPhone camera, a complete 3D laboratory calibration was performed to determine its intrinsic, extrinsic, and lens distortion characteristics. Figure 4-20 shows the mean reprojection errors (in pixels) acquired from each photo utilised in the calibration process. An overall mean reprojection error of 0.29 pixels was found. Additional analysis, similar to that described in Ji, Miao and Kromanis, (2020), was performed following the calibration process to demonstrate that the lens distortion effect was actually minimised. Four key points on the corners of the middle steel plate were detected in the captured photo of targets distributed along the structure. Each marker is measured for two lengths, v and h, as well as the angle α between them. The mean and standard deviations of these marker quantities along the beam were 50.1±0.2 px, 50.1±0.3 px and 90.5±0.5°. All markers had almost equal measured quantities of v, h, and α, even those near the photo's edges. This shows that the distortion had a minimal effect after rectification.

After distortion correction, the pixels are converted to real world units using the 2D planar homography. This is accomplished by generating a geometric transformation matrix from four well-defined pairs of coordinates (control points) on the object plane and then mapping them between photos. Geometric transformation matrixes are generated and applied to all target locations' measurements. Control points are employed on the vertices of the attached steel plates. 2D planar homography is helpful since it is a simple-to-use and is a robust and reliable solution, also especially useful when different cameras have been used in separate monitoring events, as measurements can be mapped to one set of control points (Kromanis and Kripakaran, 2021). However, caution should be exercised to correct lens distortion where possible.

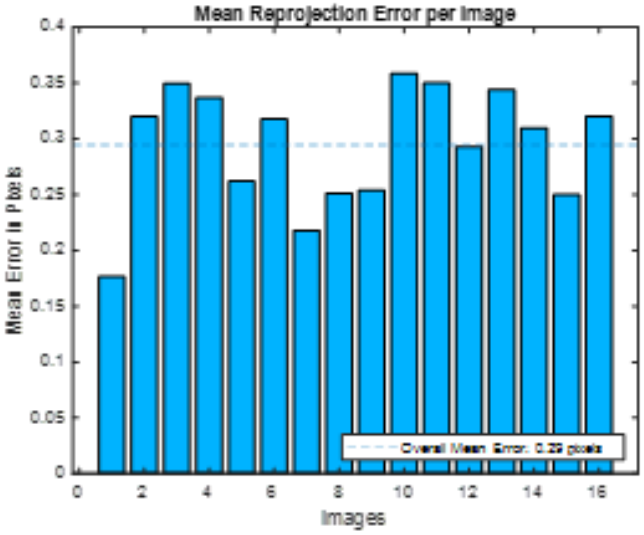

Figure 4-20: Mean reprojection errors (in pixels) from Full Projection Calibration and Lens Undistortion

4.2.7 Feature detection, Image Processing, and Measurement Extraction

The MSER blob detector is used for feature detection and is reviewed in Chapter section 2.1.5. (Literature review). It is expressly designed to locate blobs and is hence ideal for this application, as targets are circular-headed pins. To prepare the images, image pre-processing operations like rotation and histogram equalisation can be carried out. Numerous other steps can also be taken to minimize and save on use of computing resources. One of these options (used in this study) is to define and crop out a portion of interest from a whole image frame (preferably the first image) for the computer to work with. This portion would accommodate all parts of the image required to perform the image processing, which would be the areas containing the targets as well as their predicted movements. The limits of this portion of interest is then applied also to all subsequent image frames to obtain the same from them. The targets are the 18 black pins spaced evenly along the bottom of the structure, as well as a fixed target right beneath it.

The fundamental steps involved in the tracking process using MSER (and indeed most other object tracking algorithms) are:

1. Selection of reference image: A reference image, most likely the first image frame, is selected as a reference to which others are compared. As mentioned above, cropping out a portion of this image, and applying this portion to all other image frames, is advisable to save on computational resources.
2. Specification of region(s) of interest (ROI): ROIs are specified as fixed rectangular regions of known coordinates and dimensions immediately surrounding individual targets to be monitored. They are here described as 'fixed' because their coordinates and dimensions are rigidly applied to all collected image frames/videos. ROIs are specified such that they would accommodate target movements across image frames.
3. Selection/identification of object(s) of interest (OOI) within ROIs: Targets within each ROI are specified as OOIs. In object tracking, OOIs, compared to their immediate surroundings in the ROI must be robust, distinct, and invariant to image transformation and illumination variations. This is because they have to be detected as mathematical features by an appropriate feature/shape detection/tracking algorithm such MSER algorithm. The choice of tracking algorithm depends on the characteristics of the OOI (see Section 2.1.5). In this case study, ROI images are transformed to grayscale images, and then to binary via binarization — a method that assigns image pixels to one of two categories: black or white. Due to the fact that this classification is dependent on the intensity values of a pixel (I) at the coordinates (x, y) of the grayscale image, a luminance threshold (t) must be supplied to classify the image as black or white ($b\ or\ w$) (see Equation (4.4)). Automatic threshold determination is also possible using a variety of methods, one of which is the Otsu's method (Otsu, 1979) used here. This approach computes a global threshold by selecting one that minimises the intraclass variance of black and white pixels in a grayscale image that have been thresholded. Figure 4-21 (a) to (d) summarises this entire process. Objects in binarized ROI pictures are recognised and local correspondences are recorded using MSER blob detectors.

   It must be noted here that illumination must be controlled in order to use MSER blob detectors. Light reflections on targets lead to no or false target detection. False target detection could be from detecting oval or circular shaped incident light on the target. One can try to eliminate these by varying certain parameters in the algorithm, such as the step size between intensity threshold levels, minimum and maximum area or region (in pixels) to be searched, and maximum area variation between extremal regions at varying intensity thresholds. But this could be a tedious process

compounded by the fact that the same features must be automatically detected in every single frame, as sometimes parameters specified based on performance in a first frame may fail in some subsequent one, sometimes due to a change in illumination during measurement collection. One could also take an average position of detected circles, but this is suspected to lead to inaccuracies. It is therefore best to redo the measurement collection with controlled lighting, if possible, to minimise such potential challenges.

$$C(x,y) = \begin{cases} b, I(x,y) > t \\ w, I(x,y) \leq t \end{cases} \tag{4.7}$$

4. Detection and tracking of OOIs: Mathematical features of the OOIs are detected in the reference image and recorded. The tracking process involves detecting the OOIs in subsequent images and recording their positions also. This results in a displacement time series of OOI pixel positions.
5. Transformation from local to global coordinates: OOI displacements are local to the ROI, i.e., each OOI's displacement time series originates from its ROI. These must then be transformed such that the whole image frame (global) serves as new reference with origin at its bottom corner.
6. Conversion of pixel displacements to engineering units such as millimetres using either a scale factor, planar homography, or full projection matrix method.

The entire process was shown diagrammatically earlier in Figure 3-6.

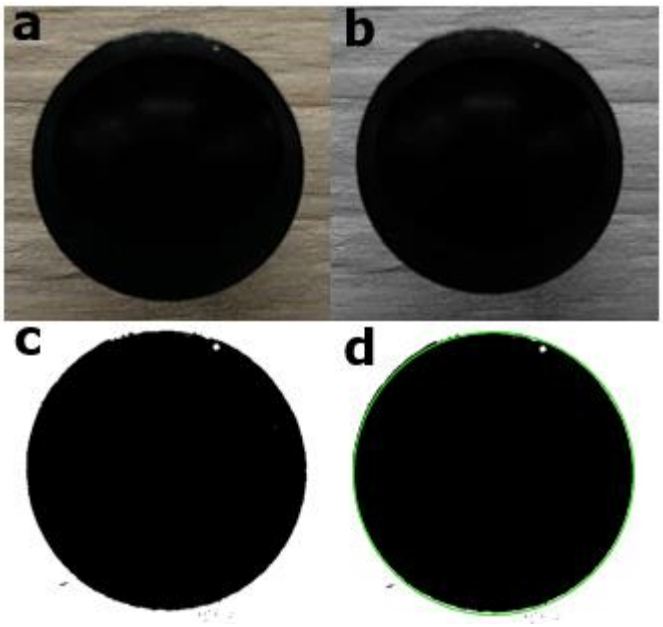

Figure 4-21: (a) Image of target, (b) Grayscale image, (c) Binary image, and (d) MSER points detected at edge of target.

4.2.8 Calibration of CV-based measurement system with contact sensing

Installed LVDT sensors were utilised to validate CV-based sensing and guarantee that the system was calibrated properly. To establish this validation, displacement time histories from both sensors at same locations are compared. In Figure 4-22, displacement time histories from the beam's midpoint with 10kg moving load are compared for both sensors – LVDT and CV-based sensing. Measurements are identical between the two sensors. The mismatch at the ends is a result of the LVDT's inability to detect even little upward movements due to insufficient stroke lengths. The remainder of the paper will concentrate on measurements from the CV-based system, as its reliability has here been established.

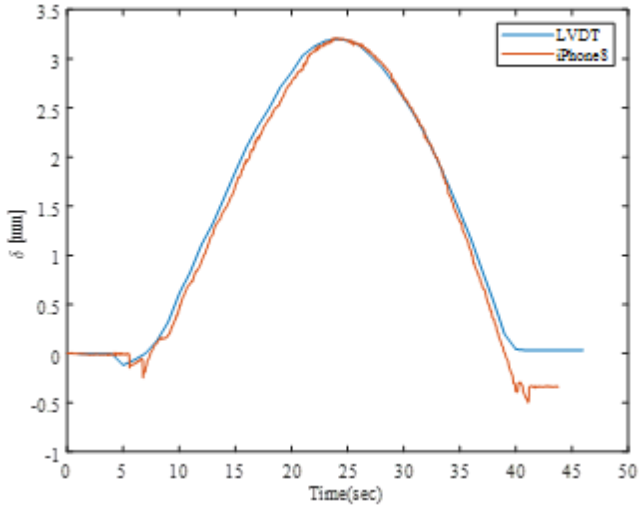

Figure 4-22: Midspan displacement time histories of LVDT and iPhone 8 camera with a 10kg moving load

4.2.9 Results

Measurement pre-processing and response time histories

Due to the noisy nature of this type of measurement response, target displacements must be pre-processed before structural response can be accurately obtained. Pre-processing of responses is structured in this study to happen in either one or two stages. In stage 1, each target's vertical and horizontal displacement time histories are smoothed using an appropriate moving average filter. A 100-point measuring window was determined to be adequate for this case study. The primary response, which has been pre-processed, is utilised to calculate the secondary responses of curvature, stresses, and inclination angles. The optional second pre-processing stage involves a second round of smoothing to deal with any residual noise in the generated secondary response. This was found to be unnecessary for this particular study. To retrieve Δr and e for damage detection, only pre-

processed data should be used. For displacement collection, measurements are retrieved at each time step from all the targets along the bottom of the girder. There were 15 targets placed on the bridge structure, and frequency of measurement collection was set at 30 frames per second using 30 to 40 second video clips, yielding between 54,000 and 72,000 data points at each retrieval event.

Figure 4-23 shows response time histories (or the influence lines) derived from a target or a set of targets (depending on the response type). The targets are at points of maximum or largest response which are around the girder's mid-span for deflections (in mm), strains (in $\mu\varepsilon$), and curvatures (unitless, thus expressed in n or 10^{-9}), and near the girder's right support for maximum inclination angles (in rad), all at the structure's baseline conditions. In other words, the target locations are selected where response is expected to be maximum. The figure displays these structural responses in their raw state (black) and after an initial pre-processing step is completed.

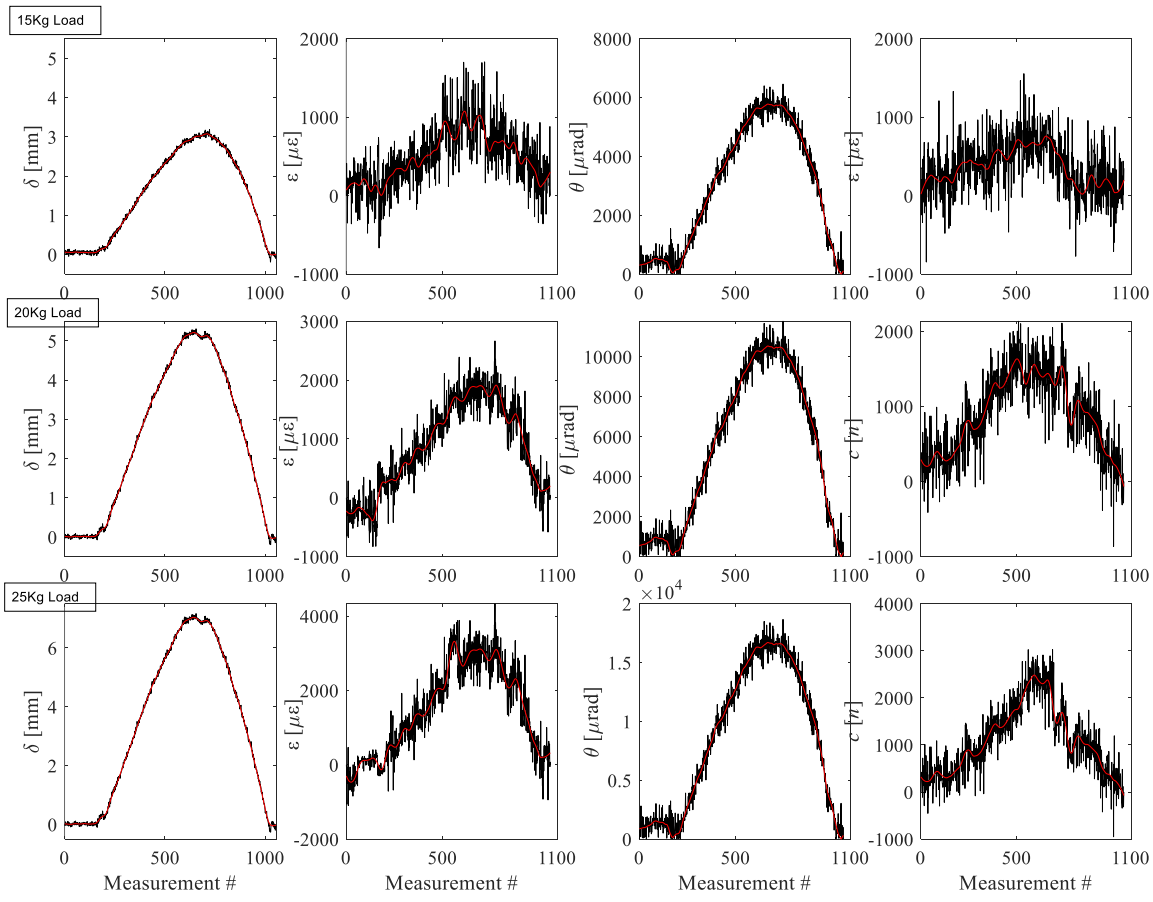

Figure 4-23: Response time histories for displacements, strains, inclination angles, and curvatures respectively. Rows 1, 2, and 3 represent 15kg, 20kg, and 25kg loadings respectively

Observations

Several observations are easily made. Consider the procedure for obtaining structural response profile as laid out in the Methodology Section 3.3.5, also diagrammatically in Figure 3-7; – i.e., for each target or set across the structure, obtain the maximum response from its response time history, and when put together gives the response profile for the structure. Therefore, merely by looking at these maximum response time histories in Figure 4-23, it is easy to see that if r_{max} is to be taken from the raw response, due to the noise contamination characterised by the unlimited spikes, their values will always be inflated. This confirms what was observed and established previously in the laboratory study of Section 4.2, which is that r_{max} from raw measurements though they generally follow the expected shape, their values are inflated or amplified. Again the reader is referred to Case study 1, Section 4.1.4 where using the strain plot in Figure 4-11 for example, if one simply traces the maximum strain values from the noisy signal, they can quite clearly see that it mirrors the shape of the smoothed data. This phenomenon is observed in every single scenario studied so far in both the numerical and laboratory tests. It can therefore be safely assumed that one main effect of noise, at least from the perspective of the technique employed in this research, is to inflate response time series values at each point, and consequently maximum response values at that point, thereby rendering them inaccurate.

4.2.10 Structural response and profile and Damage detection

Structural response is derived by first collecting the maximum response values (r_{max}) from the time histories of each target or target set's location. This is done using pre-processed data from the previous section. The structural response of the beam (r) is the r_{max} values at each target or target set (T) along the entire length of the beam. This can then be shown along beam's length by graphing r_{max} for each target or target set in a two-dimensional space.

Damage detection is performed on the structure using the techniques described in Section 3.3 with two damage scenarios presented – D1 and D3 (i.e., loosened steel plates at 0.15m and 0.19m). Damage is detected by comparing response from both scenarios to the baseline scenario. A damage threshold of 5% is set for damage detection. For each load case scenario (for example, 10kg, 15kg load case scenarios), damage detection is investigated for both damage scenarios (i.e., D1 and D2).

The sections that follow discuss and display results for each load case scenario, for all response types. Results are displayed for displacements, curvatures, inclination angles, and strains, and they include damage detection and location using the 5% threshold specified.

Deflection curve

From the calculated maximum response (r_{max}) from time histories (in Figure 4-23) for both raw and pre-processed data, the pre-processed response is selected for damage detection. The damage detection technique and equations are already described at great length in other sections of this work (see Sections 3.3, and specifically 3.3.8 for deflections), so they will not be repeated here nor in the rest of these sections describing damage detection from response. Figure 4-24 and Figure 4-24 show plots from deflection response profile (r_δ) for 15kg and 20kg loads respectively. The top row r_δ plots (L – R) represent the displacement profile of the structure due to the specified moving load (i) before introduction of damage (baseline condition), (ii) with D_1, and then (iii) with D_2, respectively. In the tests the baseline displacement response profile is measured each time before creating a damage scenario to avoid error. For example, before creating the first damage (D_1), baseline displacement response profile is measured. After D_1 is created and removed, baseline displacement profile is measured again, before introducing D_2. This activity ensures that possible small changes caused by residual strains in the structure, due to previous loadings and damage infliction are accounted for.

The columns represent damage scenarios D_1 and D_2. Δr_δ (Middle row) plots reveal a gentle, slow, undulating slope towards the damage location, as expected, going by the numerical analysis results in Section 4.1. This shape tendency (the fact that there is no sudden spike), is also the reason why damage detection is not as reliable with deflections as with secondary responses where clear spikes at damage locations are the norm. This is discussed in detail in Section 4.1.4 with supporting research evidence from literature. Hence when there is a combination of damages, it is more difficult; for example, a combination of D1 and D2 should give a slowly undulating curve that plateaus between both damage locations (see Figure 4-7).

Damage sensitive feature (e_δ) in Figure 4-25 (20kg vehicle) reveals a just above 5% threshold at damage locations due to the relatively heavy load applied. In this scenario, damage is fully detected and located even for deflection response. In Figure 4-24 (15kg vehicle), clear spikes are visible at damage locations, but they do not reach the damage threshold. This is another reason for the unreliability of deflections in damage detection – the small relative changes due to damage. A discussion is made about solving the problem of uniform damage threshold in the next chapter.

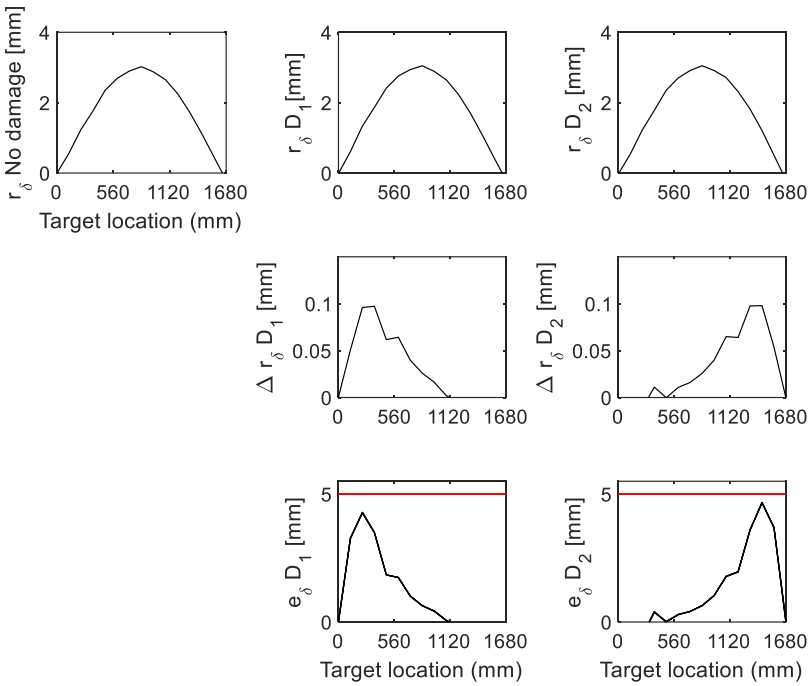

Figure 4-24: [15kg vehicle]: Top to bottom row: Deflection profile, change in deflection, and damage sensitive feature. L – R columns: No damage, with D1, and with D2

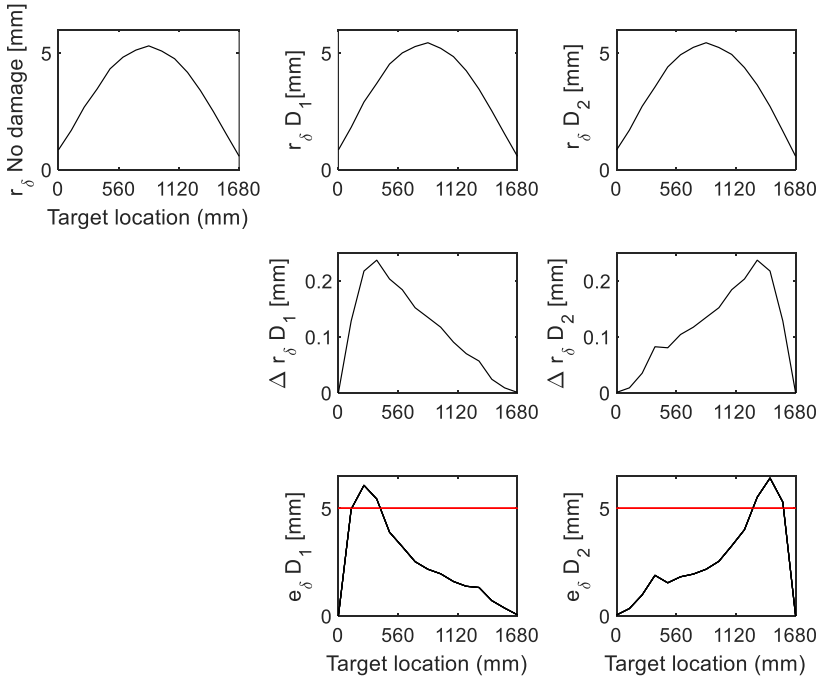

Figure 4-25: [20kg vehicle]: Top to bottom row: Deflection profile, change in deflection, and damage sensitive feature. L – R columns: No damage, with D1, and with D2

Strains

From the calculated maximum strain response (r_ε) (as shown in Figure 4-23) for both raw and pre-processed data, the pre-processed response is selected for damage detection. Figure 4-26 Figure 4-27 show strain response profile for the structure r_ε for 15kg and 20kg loads respectively. The top row r_ε plots (L – R) represent the strain profile of the structure due to the specified moving load (i) before introduction of damage (baseline condition), (ii) with D_1, and then (iii) with D_2, respectively. In the tests the baseline strain response profile is measured each time before creating a damage scenario to avoid error. For example, before creating the first damage (D_1), baseline displacement response profile is measured. After D_1 is created and removed, baseline r_ε profile is measured again, before introducing D_2. This activity ensures that possible small changes caused by residual strains in the structure, due to previous loadings and damage infliction are accounted for.

Δr_δ (Middle row) plots reveal spikes at damaged locations. These are sharper than with deflections. The bottom row shows damage sensitive feature (e_δ) which reveals clear jump in response at damage locations – 20% for 20kg, and about 12% for 15kg loads. In this scenario, damage is fully detected and located for strain response for both load scenarios.

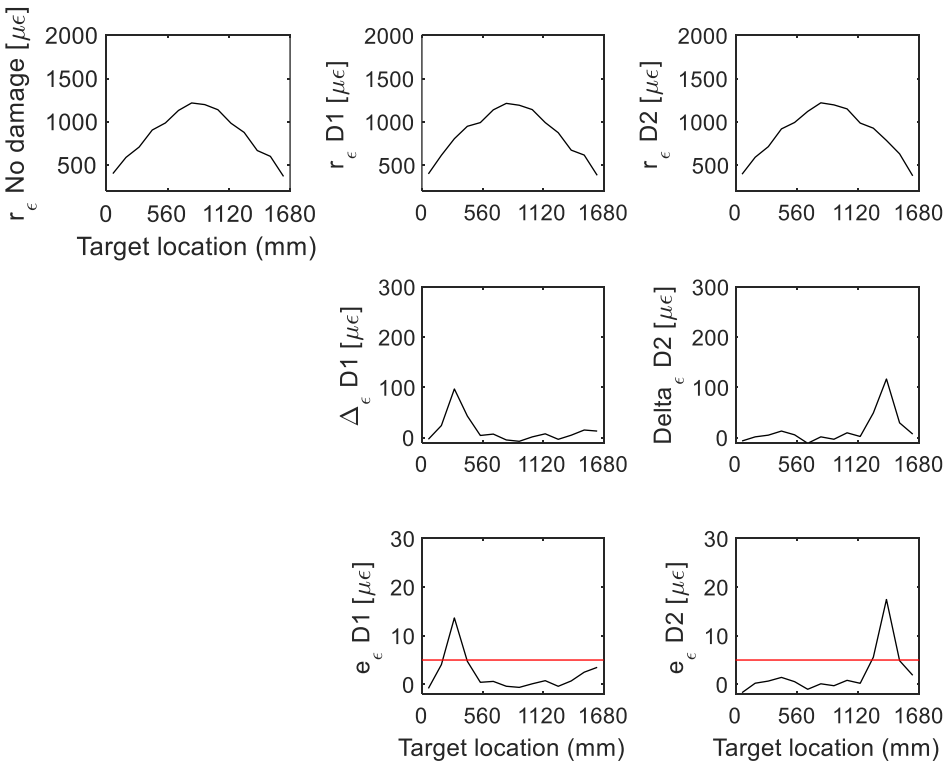

Figure 4-26: [15kg vehicle]: Top to bottom row: Strain profile, change in strain, and damage sensitive feature for strain. L – R columns: No damage, with D1, and with D2

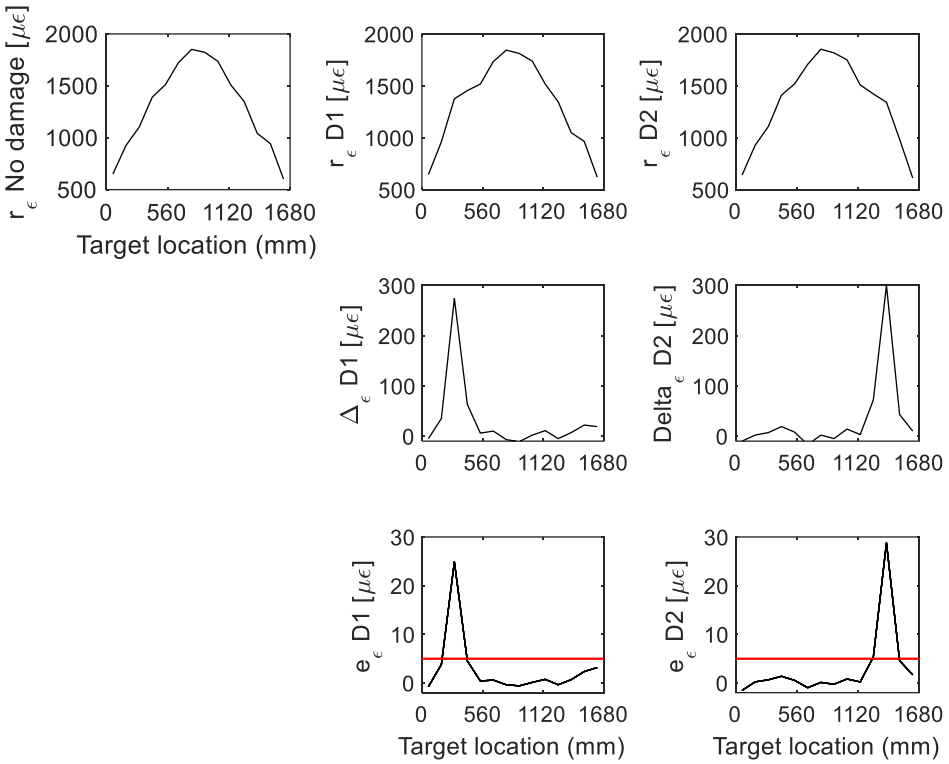

Figure 4-27: [20kg vehicle]: Top to bottom row: Strain profile, change in strain, and damage sensitive feature for strain. L – R columns: No damage, with D1, and with D2

Curvature

From the calculated maximum curvature response (r_c) (as shown in Figure 4-23) for both raw and pre-processed data, the pre-processed response is selected for damage detection. Figure 4-24 shows curvature response profile for the structure r_c. The top row r_c plots (L – R) represent the curvature profile of the structure due to the specified moving load (i) before introduction of damage (baseline condition), (ii) with D_1, and then (iii) with D_2, respectively. In the tests the baseline curvature response profile is measured each time before creating a damage scenario to avoid error. For example, before creating the first damage (D_1), baseline curvature response profile is measured. After D_1 is created and removed, baseline curvature profile is measured again, before introducing D_2. This activity ensures that possible small changes caused by residual strains in the structure, due to previous loadings and damage infliction are accounted for. Δr_c (middle row) plots reveal spikes at damaged locations. These are sharper than with deflections. The spikes are more to the ends of the structure due to the fact that three targets are chosen for curvature as opposed to two for others. The bottom row shows damage sensitive feature (e_δ) reveals clear jump in response above 15% threshold at damage locations. In this scenario, damage is fully detected and located for curvature response.

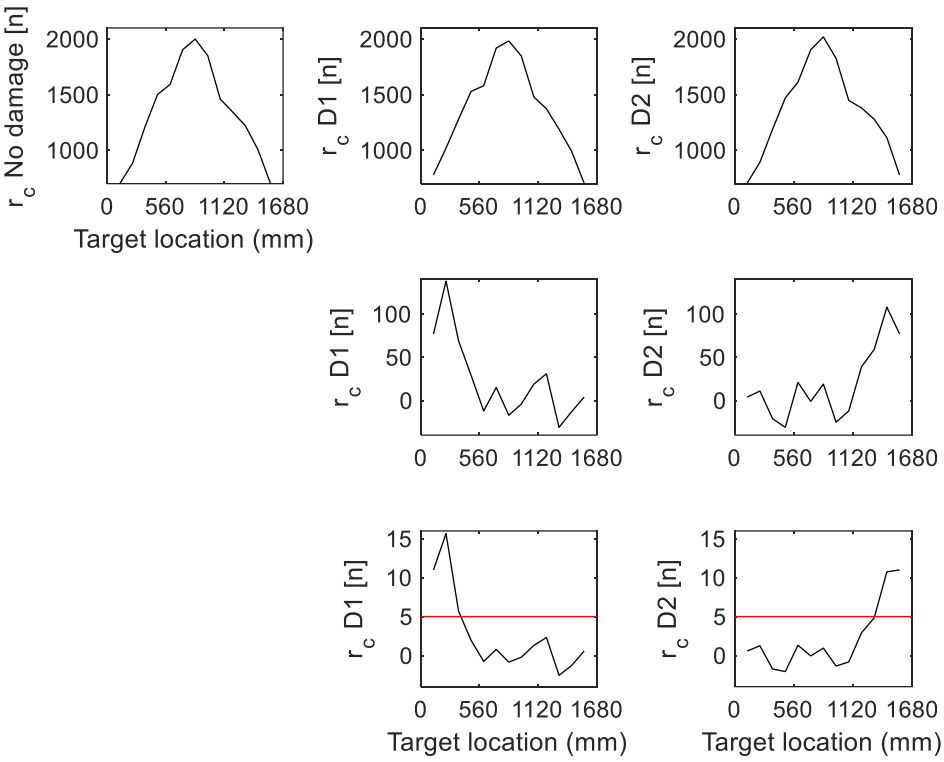

Figure 4-28: [15kg vehicle]: Top to bottom row: Curvature profile, change in curvature, and damage sensitive feature for curvature. L – R columns: No damage, with D1, and with D2

Inclination angles

From the calculated maximum inclination angle response (r_θ) (as shown in Figure 4-24) for both raw and pre-processed data, the pre-processed inclination angles response is selected for damage detection.

Figure 4-29 and Figure 4-30 show inclination angles response profile for the structure (r_θ) for 15kg and 20kg loads respectively. The top rows r_θ plots (L – R) represent the strain profile of the structure due to the specified moving load (i) before introduction of damage (baseline condition), (ii) with D_1, and then (iii) with D_2, respectively. Note here the presence of significant measurement shifts at midpoints. This phenomenon is unique to inclination angles and causes false damage detection. It has been described in detail in Section 3.3.10 as well as in Section 4.1.4 where it was described in the context of the first case study. In maintaining consistency, the baseline inclination angles profile is measured each time before creating a damage scenario to avoid error. For example, before creating the first damage (D_1), baseline inclination angles response profile is measured. After D_1 is created and removed, baseline inclination angles profile is measured again, before introducing D_2. This activity ensures that possible small changes caused by residual strains in the structure, due to previous loadings and damage infliction are accounted for.

We discover that for inclination angles damages are not detected. Δr_θ plots (second rows) show spikes at middle of the beam – where the measurement shifts occur in r_θ plots (first rows). As expected, this leads to false damage detection in damage sensitive feature (e_θ) plots (third row). The bottom rows show damage sensitive feature (e_θ) calculated using the case specific definition (see Section 3.3.10). In this case, unlike in the numerical model, damage is still not detected, instead we have a false detection. Damage detection using inclination angles has failed in this case.

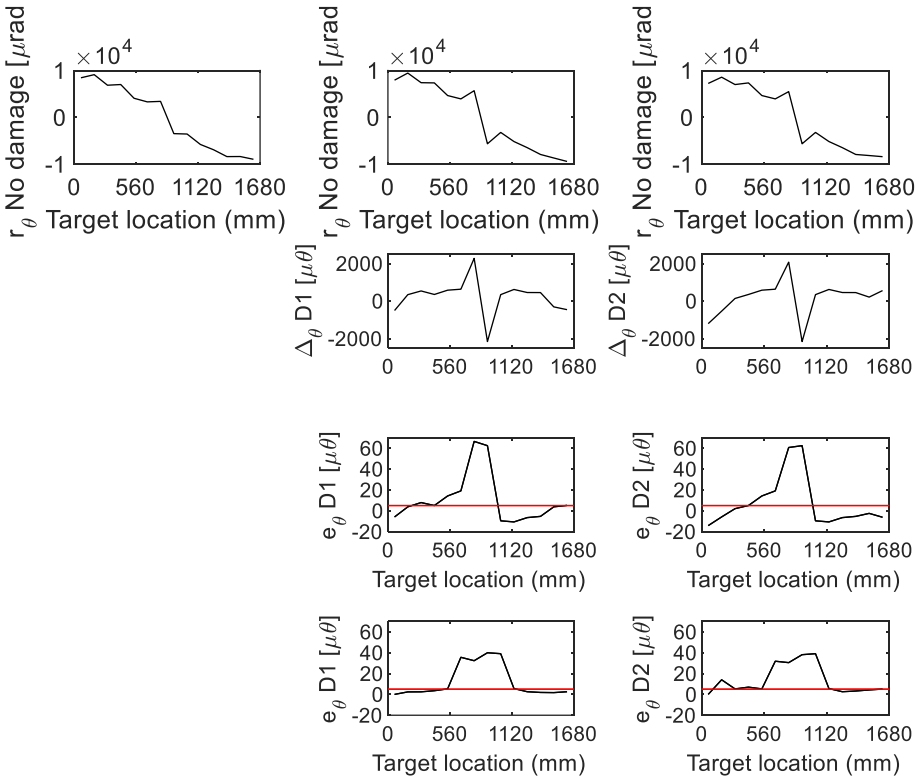

Figure 4-29: [20kg vehicle]: Top to bottom row: Inclination angle profile, change in inclination angles, and damage sensitive feature for inclination angles. L – R columns: No damage, with D1, and with D2

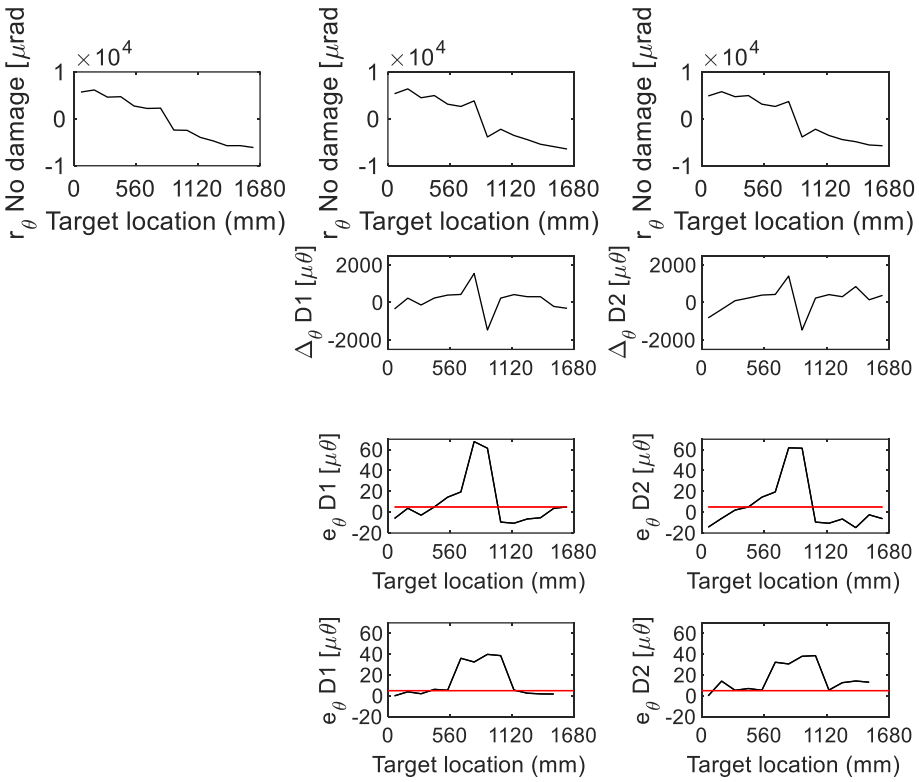

Figure 4-30: [15kg vehicle]: Top to bottom row: inclination angles profile, change in inclination angles, and damage sensitive feature for inclination angles. L – R columns: No damage, with D1, and with D2

4.2.11 Discussions

Findings from the laboratory study are discussed here. Discussions will aim to compare the performance of the laboratory structure with that of the numerical model where possible. An appraisal of practical challenges especially with regards to accuracy and measurement resolution issues is also presented.

Damage detection

The damage detection process is based on the premise of accurate obtention of target displacements from the structure. These target displacements obtained during a loading scenario (i.e., while the structure is subjected to loading) are used to compute measurement time histories. Measurement time histories are obtained from equally-spaced targets across the structure. Maximum data from each target's measurement time history are obtained and plotted to give the structure's response profile. This is done at the initial or undamaged condition of the structure which gives a baseline profile, and then at any subsequent conditions. The next stage is in the calculation of a change in response curve (Δr) which is simply the change in response profile at any damage scenarios, from the baseline profile. Damage sensitive features are a ratio of

change between baseline and current girder response profiles, also plotted along the length of the girder. Damage is then said to be detected in positions where damage sensitive features exceed the damage threshold, which in this study is set at 5%.

Damage locations are clearly discernible from damage feature plots, although they may not exceed the threshold with smaller loading. To achieve this, target displacements must be pre-processed properly, before obtention of secondary response. Without this, the measurements are unsuitable for damage detection.

Damage sensitive features computed directly from target displacements are much less sensitive to damage; they appear to change very slowly (see Δr_δ and e_δ plots in Figure 4-7 in the numerical model section 4.1.4), without clear spikes or shifts as with others, hence cannot be relied upon for damage localisation. This is supported by similar studies using the deflection curve of horizontal structures, for example in (Erdenebat et al, 2018). This statement is also true for this laboratory experiment. Though e_δ just slightly surpasses the threshold at damaged locations, one can still observe its slow change and the gentle undulating nature of its slope. e_δ only breach the threshold when damage severity or loading is high enough.

Damage-sensitive features (e_ϵ) from strains appear to be the most robust to noise. The response signal is clearest, and small damages can be detected and accurately located, with e_ϵ values at 20% at the lowest load severity (see Figure 4-27). Damage-sensitive features (e_c) from curvatures are more susceptible to noise than those from strains. Damages are detected with about 10% e_c values at damaged locations at the lowest load severity (see Figure 4-28).

Although the girder response from inclination angles seems much smoother than that of curvatures, results from Figure 4-28 show that damage-sensitive features (e_θ) from inclination angles gave false damage detection for the damage cases. This is related to the computation of e_θ from inclination angles. e_θ as obtained using the regular techniques are unable to detect shifts as opposed to spikes which is the case for inclination angles. The case-specific technique derived for inclination angles are such that measurement shifts rather than spikes in inclination angles are detected. Damage features are derived from their neighbouring measurement response values (see Equations 3.15, 3.16, 3.17). However, small values of these neighbouring responses, especially when contaminated with measurement noise, will still result in high damage feature, leading to false damage location as observed in the numerical model, as well as here again in this case study. Accurate damage detection strategy for inclination angles is therefore a recommendation from this study.

CV-based measurement accuracy and challenges

The capacity of CV-based monitoring systems to deliver accurate and cost-effective measurements/interpretations of bridge response is crucial if it must gain the trust of asset managers and the engineering community as a whole. This is important especially within the context of their prospective complementation of visual inspections of at least small to medium-scale bridges. Affordable image acquisition devices like phone cameras and open source image processing algorithms and tools makes CV-based SHM an attractive option for at least short term measurement collection and response interpretation (Dong and Catbas, 2020b; Feng and Feng, 2016). The challenge has always been to achieve accurate capture of sub-pixel movements of targets, which ensures that enough measurement resolution can be achieved especially for damage detection. Camera resolution, camera or ground motion, environmental conditions, and subpixel resolution of target tracking algorithms are some factors that can affect measurement resolution.

Unlike in the numerical model, noise in the laboratory model case is not arbitrarily added, so is controlled by the afore-mentioned factors. The iPhone 8 camera with 12MP and 4K (3840 x 2160 maximum video mode) at 60fps is used to capture a 1.7m length of the structure, which yields a horizontal scale factor of ≈0.44mm/px, and a vertical resolution of 0.51mm/px is found. And with an achieved $1/10$ subpixel resolution in image processing, a measurement resolution (η) of 0.05mm/px is derived. This, in practical terms means that 0.05mm is the least target movement that can be captured. Achieving high measurement resolution is vital as it controls the degree of target movement that can be achieved. Efforts must be increased at this stage to increase this value especially for field deployments where a higher noise ratio may be reasonably expected. Image processing algorithms have been reported in (Feng et al, 2015) to achieve pixel resolutions between $^1/_2\,px$ and $^1/_{100}\,px$, and elsewhere as high as $^1/_{500}\,px$ have been reported using a patented algorithm based on DIC (Imetrum, 2020; Potter and Setchell, 2014). Increasing pixel resolution of image processing algorithm is perhaps the most efficient and effective way to increase measurement resolution, since the other major alternative would involve hardware costs, for example expensive, high resolution devices. Also, the use of a stationary reference target in a FOV helps in reducing noise from camera motion and drift (Luo et al., 2018).

4.3 Case Study 3 - Restored Footbridge Over the Ashby Canal at Conkers Waterside Basin near Moira Furnace, Swadlincote, Derbyshire UK

4.3.1 Introduction

The final case study is set to be a real-life bridge. In selecting such bridge certain criteria were set, including a reasonable deflection (say, >1mm) so that its signal/noise ratio is high enough to guarantee trust in the results. For that purpose, a timber bridge was sought after, due to the expectation of a good deflection, and also in keeping with multiple field CV-SHM deployments and reports where timber structures have been used (Kromanis, 2021; Kromanis et al., 2019; Kromanis and Forbes, 2019; Obiechefu et al., 2021; Voordijk and Kromanis, 2022). The selected structure is shown below (Figure 4-31). It is a restored timber Footbridge Over the Ashby Canal at Conkers Waterside Basin near Moira Furnace, Swadlincote, Derbyshire UK.

Figure 4-31: Restored Footbridge Over the Ashby Canal at Conkers Waterside Basin near Moira Furnace, Swadlincote, Derbyshire UK

4.3.2 Bridge description and engineering specifications

Constructed in 2003 to span the Ashby canal at Conkers Waterside Basin, the footbridge is composed of three simply supported spans and is designed to carry a maximum load of 5kN/m^2 for pedestrian and cycle traffic. The bridge spans 29m between abutments, across the canal and adjoining areas (See Figure 4-31) and has a cross sectional span of approximately 2m (See Figure 4-32). The timber deck is braced transversely with timber beam sections thereby increasing deck stiffness. Two reinforced concrete bank seats form part of the substructure, which is supported by piles. A steel A-frame rests on these seats

and provide intermediate supports for the bridge deck. The two end spans measure 7.62 metres in length, while the centre span measures 13 metres. Figure 4-32 shows these details diagrammatically and have been obtained with permission from Leicester city council.

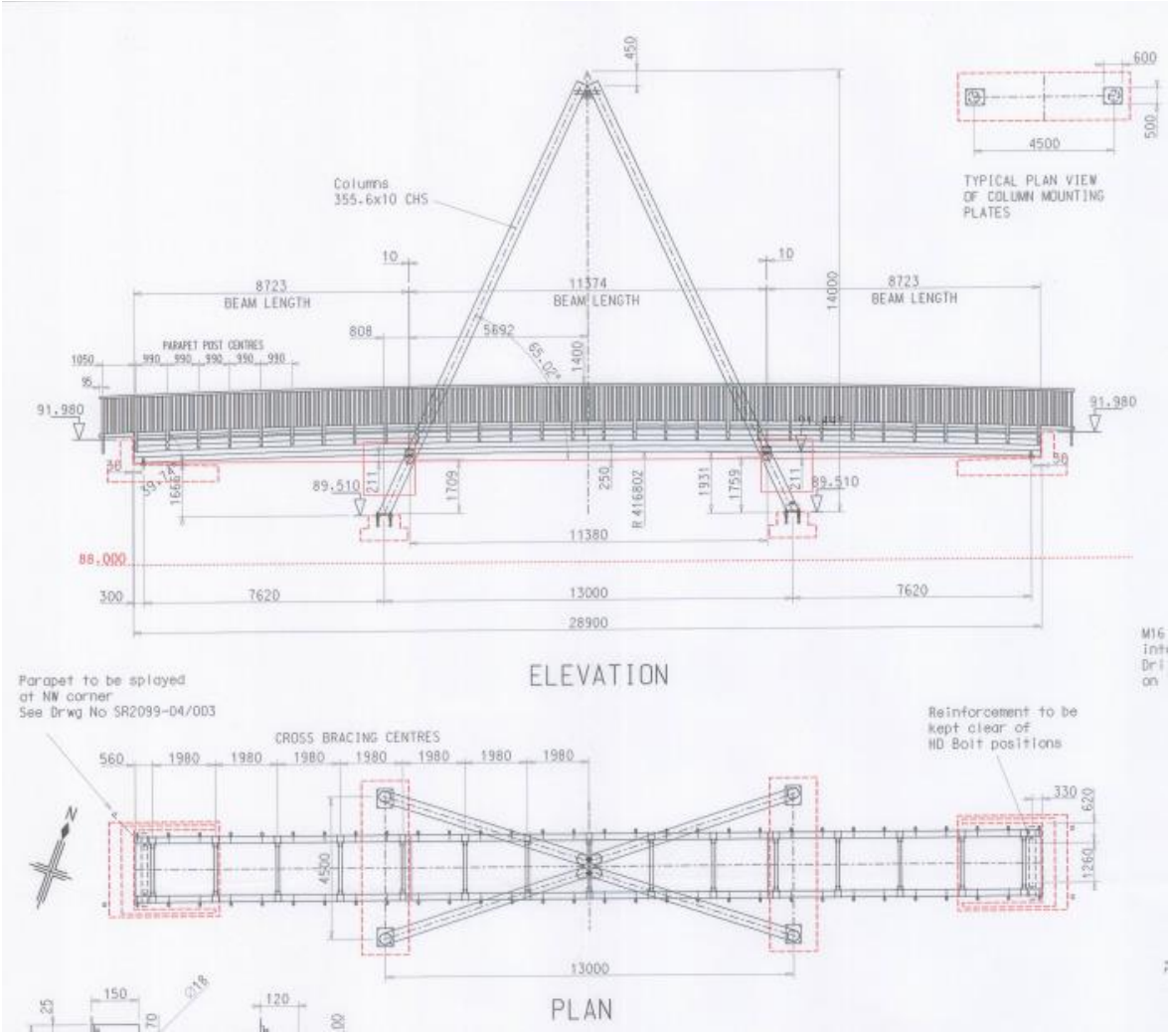

Figure 4-32: Plan and elevation of footbridge over the Ashby Canal at Conkers Waterside Basin near Moira Furnace, Swadlincote, Derbyshire UK

4.3.3 Scope and Objectives

Since damage cannot be created on a public facility, the scope of this field application becomes somewhat limited. The objectives therefore become firstly to carry out a CV-based distributed monitoring of a small (one-sixth) of the length of the middle span) section of the bridge to obtain target displacement time histories, from which curvatures, strains, and inclination angles would be calculated; and secondly to obtain their respective response profiles.

4.3.4 Monitoring and Measurement collection

A small area (1.98m) of the bridge is selected for monitoring (see Figure 4-33). This section of the structure monitored contains three targets – T_1, T_2, and T_3 selected from the top row bolts. There are altogether six (6) bolts contained in this area – two placed vertically on each of the three parapet posts as shown in Figure 4-33 and Figure 4-34. The known coordinates of the two bolts at the end parapet posts are used in planar homography for calibration and displacement estimation.

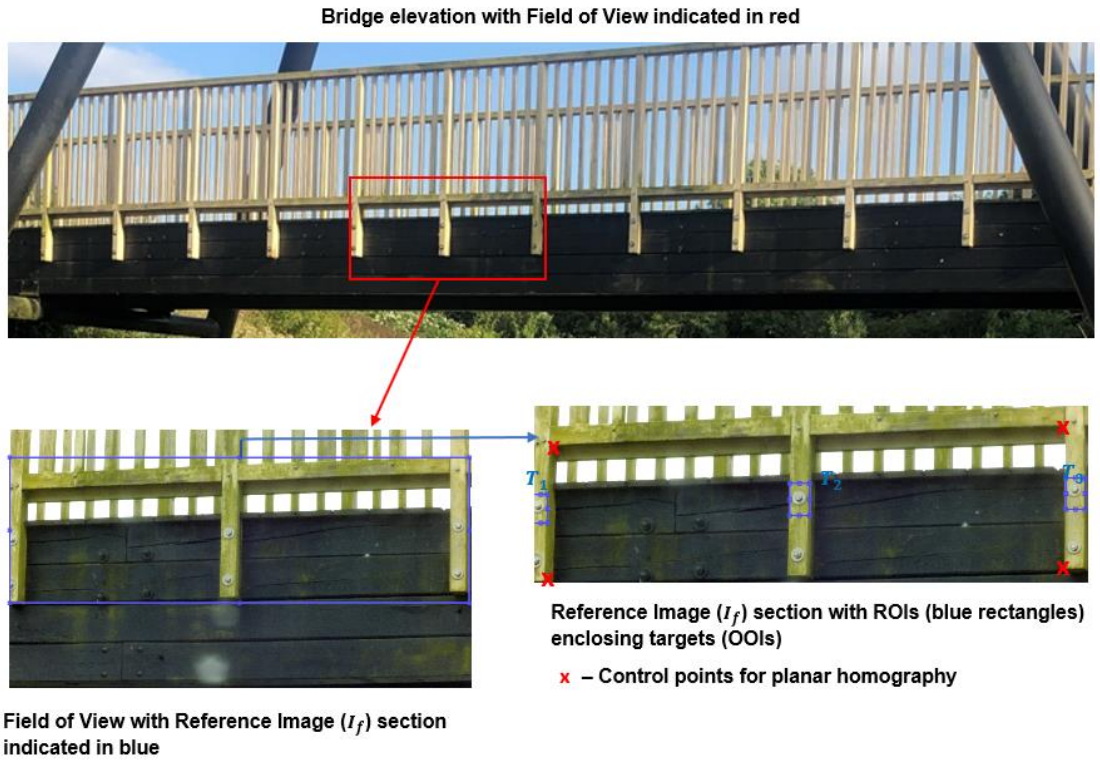

Figure 4-33: Bridge elevation showing FOV and known coordinates for planar homography

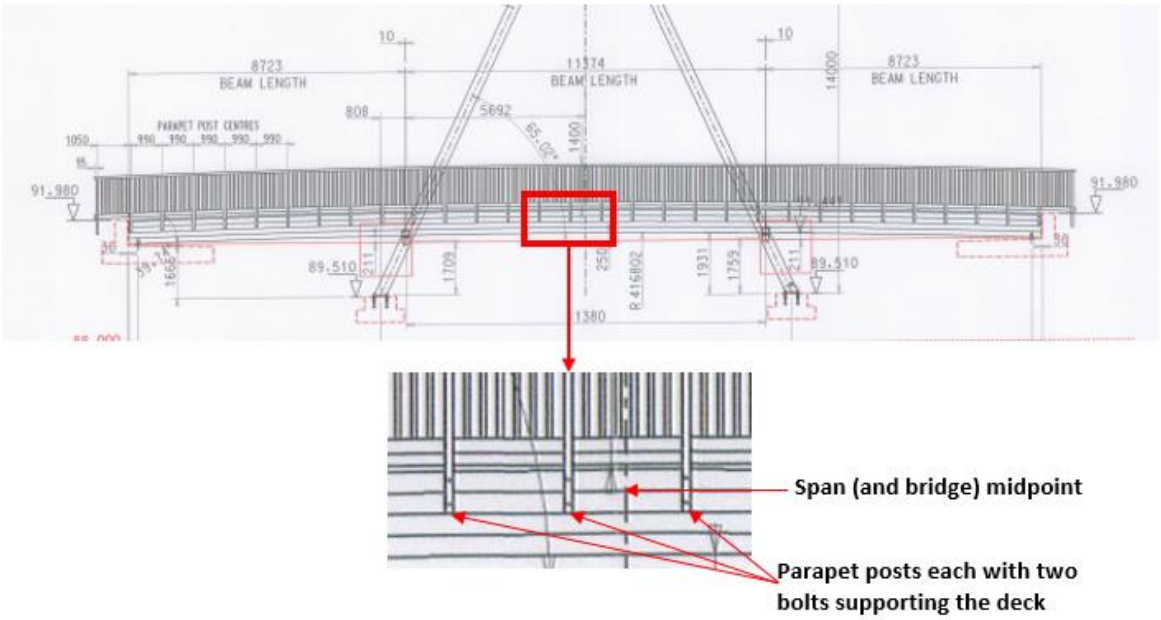

Figure 4-34: Bridge elevation drawing showing FOV and bolts

Going by the techniques discussed in CHAPTER 3, we obtain three data points for displacement, two data points (halfway between the three targets) for strains and inclination angles, and one curvature data point (since three points are required for curvature and assumed to be at the middle target).

Camera tripod was set 5m from the bridge, mounted with a GoPro Hero 5 digital camera with attached varifocal (optical) zoom lens. The GoPro specifications are: 4K, 12 MP camera (3840 x 2160 maximum video mode) at 60fps. FOV was set as a 2m length spanning the bridge's midpoint and accommodates the three columns of bolts (in the parapet posts) 990mm from each other, with the middle and right posts straddling the midpoint of the bridge (See Figure 4-34). The bolts are selected as the targets. The distribution of the parapet posts is not as symmetrical as desired since the midpoint of the bridge lies halfway between the right-end and middle posts containing targets T_2 and T_3 (See Figure 4-34). This had to be accepted as (i) at least three targets are required, (ii) there are an even number of parapet posts, and (iii) the bolts were the only easily trackable features. Each parapet post has two bolts, so that for three of them taken together there are two rows of three bolts (See Figure 4-34).

The monitoring was carried out specifically on a relatively sunny day with low winds of about 12mph to reduce noise from environmental conditions. A clickable Bluetooth remote device

was also used to start and stop the recording, this minimised the vibration/noise that would otherwise be introduced to the signal if clicking directly on the camera devices. The camera recorded and saved short (12 to 16 second) video clips of a single pedestrian cycling across the bridge several times, from which the least noisy was selected.

4.3.5 Image processing and feature detection

Videos collected during the loading event are analysed using image processing techniques to obtain structural response for each target (see Chapter 3, Sections 03.3.3 to 3.3.7 for their description). Then, using the techniques described in Chapter 3, Sections 3.3.7 to 3.3.11, absolute maximum response values from each target's measurement histories are extracted to form the structural response profile for all responses in the monitored section. These techniques are applied to this case study in an identical way to the laboratory application earlier on in this chapter (Section 4.2), They therefore need no re-introduction.

The MSER Feature/object detector algorithm is used to detect target features as it is suited best for the bolts with circular washers which are round shaped (Matas et al., 2004). Reference image is selected as the first image frame in the video file. To save on computational resources, about half the vertical length of the image – centrally positioned, is cropped out because it contains all image information required for processing, including targets and anticipated target movement, as well as control points for planar homography. This crop-out becomes the practical reference image (I_f) (see Figure 4-33). The same dimension of I_f is used to crop out subsequent images (I_s) from the rest of the image frames in the video. ROI is a small rectangular area measuring 80 by 120 pixels bounding the bolt and washer targets (which become the OOIs). OOIs, compared to their immediate surroundings in the ROI must be robust, distinct, and invariant to image transformation and illumination variations. This is because they must be detected as mathematical features by the detection/tracking algorithm. Just like in the laboratory case study, ROI images are transformed to grayscale images, and then to binary using an automatically specified luminance threshold (t) via the Otsu method (Otsu, 1979) (see Section 4.2.7 for details of this method). Binary target features (OOIs) are detected using MSER, and their coordinates recorded. Just as in Section 4.2.7 it must be noted here that illumination must be controlled in order to use MSER blob detectors. Light reflections on targets lead to no or false target detection. False target detection could be from detecting oval or circular shaped incident light on the target. One can try to eliminate these by varying certain parameters in the algorithm (Again see Section 4.2.7). OOI positions are tracked and saved across the video and obtained pixel displacements are transformed to mm using planar homography.

4.3.6 Planar homography and Deformation estimation

Pixel measurements recorded at the end of the feature detection and tracking process must be converted to engineering units using 2D planar homography (see Section 2.1.4). Here, using four (4) known 2D point correspondences on the image, a transformation matrix is generated which is used for skew correction and pixel to mm conversion. Known point correspondences were obtained from As-built drawings crosschecked on site. These are shown in Figure 4-33. The vertical parapet post pieces are at a horizontal distance of 990mm from each other, and 620mm vertical height to under of deck. The point correspondences are established first by assigning a physical/structural plane (mm) origin point (0,0) to the top left corner (see Figure 4-33). From there the following fixed points (in mm) are established – 0,0; 0,620; 990,620; 990,0 – for top left; bottom left; bottom right; and top right respectively. This is straightforward as it is in the structural plane and distances are known beforehand from As-built drawings and measured for confirmation on site. For image plane pixel coordinates (moving points) the measurement is done simply by finding the corners and recording their pixel coordinates. Therefore, two sets of control points are established – 'fixed points' in the structural plane, and their corresponding 'moving points' in the image plane.

The fixed and moving points are then input into a generic geometric transformation algorithm such as 'fitgeotrans' in MATLAB (The MathWorks Inc., 2021) which computes the specified geometric transformation matrix between the pair of points (Kromanis and Kripakaran, 2021). For every image frame, the geometric transformation matrix is then multiplied by the target's image coordinates ('moving points') to evaluate its coordinates compared to the reference coordinate plane. This procedure is done for each frame of the image. Structural deformations can then be computed from obtained coordinates.

Subpixel resolution and measurement error

From Equations 4.2 and 4.3, the horizontal measurement resolution achieved with a FOV of 2m is ~0.84mm/px, while ~0.92mm/px is achieved for the vertical direction using a scale factor. A sub-pixel resolution of $^{1}/_{15^{th}}$ is achieved using this case study. This improves the previously-stated measurement resolution to 0.056mm/px and 0.061mm/px in the horizontal and vertical directions respectively. And so, the expected strain measurement error between two targets 990mm apart can be estimated to be a maximum of $\frac{5.6\times10^{-2}mm}{990mm}\times10^{6}=62\mu\varepsilon$. If low strain values are expected due to relatively small load intensity, then they will not be expected to be reliable. Even if the distance between all three targets is combined to get 2m, the error would only be halved, which is still the best. It can already be predicted

at this stage that curvatures and inclination angles will be less reliable than strains since (i) they are likely going to have low values due to low loads, (ii) they are more affected by noise compared to strains, and (iii) they tolerate low measurement errors.

4.3.7 Results

Since damage detection cannot be carried out yet in the field, the results displayed in this section will focus on response time histories and response profiles.

Measurement Pre-processing and Displacement Time Histories

Pre-processing is done for the raw data following the steps used in Case Studies 1 and 2. Response is smoothed using a linear regression method with an 80-point size moving window. This is achieved using the 'lowess' method in the 'smoothdata' function on MATLAB (The MathWorks Inc., 2021). Linear regression model is chosen because it works best at eliminating outliers and preventing discontinuities in the displacement data. Figure 4-35 below displays displacements from the three monitored targets – T_1, T_2, and T_3 for both raw and pre-processed data, and all targets (pre-processed only).

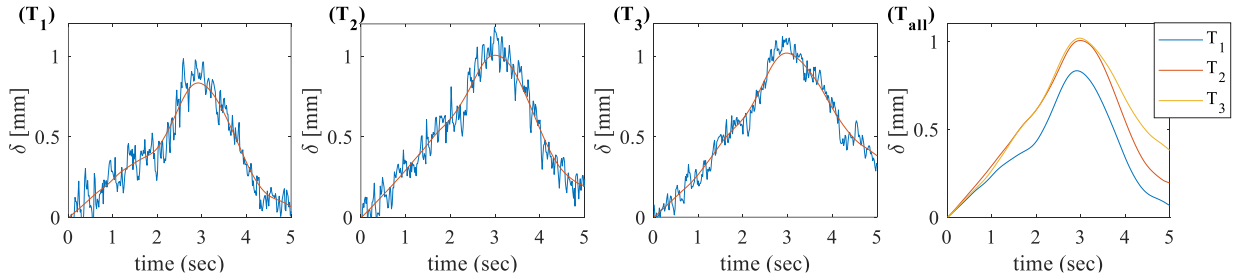

Figure 4-35: Displacement time histories (blue – raw, red – pre-processed) for targets T_1, T_2, T_3 and all targets (pre-processed only)

As expected, data from this bridge is significantly noisier than that from the laboratory (see Section 4.2 and Figure 4-23). Pre-processing is therefore much more significant. This explains why a linear regression model was selected for de-noising as opposed to quadratic model used in the laboratory case study, which was found to be less effective in removing effects of outliers and high variability noticeable in this data. All pre-processed data are shown in Figure 4-35 (T_{all}). This is now considered the displacement time history of the structure and is used to obtain secondary response histories.

Similar maximum displacements (δ_{max}) are obtained across all three targets. 0.83mm in T_1, 1.01mm in T_2, and 1.02mm in T_3. This is also expected given that we are dealing with only the middle sixth of the bridge span. Also, given the asymmetry described in Section 4.3.4, the span's midpoint lies between T_2 and T_3, while T_1 lies further to the left of T_2 (see Figure 4-33). This explains T_2 and T_3 having about the same δ_{max} (1.01mm and 1.02mm respectively), since they both straddle the span's midpoint.

Secondary Response Time Histories

Pre-processed displacement time histories are used to obtain the secondary responses of curvature, inclination angles, and strains.

With a significantly higher displacement noise ratio, secondary responses were also expected to show higher noise ratios. Figure 4-36 below displays secondary response time histories. Rows (top to bottom) display strains, tilts (Inclination angles), and curvature respectively. The columns: (L to R) represent response between targets 1 and 2 (T_1&T_2), and 3 and 4 (T_3&T_4) respectively. Raw response is shown in blue while pre-processed response is shown in red.

Strains exhibit the most robustness against noise. Its shape, including for the raw response is clear and distinct. A resolution error of $\pm 61 \mu\varepsilon$ had earlier been calculated in Section 4.3.6 using a scale factor of 0.056mm/px. An ε_{max} of $645 \mu\varepsilon$ and $730 \mu\varepsilon$ is observed for $\varepsilon_{t1,t2}$ and $\varepsilon_{t2,t3}$ respectively. The reason why the curve ends halfway and does not return to approximately zero is because the video was ended while the cyclist was at the next span and apparently still caused strains on the test span.

While visually, the noise range remains approximately the same, inclination angles and curvature responses appear relatively noisier due to the lower response values they have. For example, maximum values for $\theta_{t1,t2}$ and $\theta_{t2,t3}$ are $225 \mu rads$ and $200 \mu rads$ respectively; and for $c_{t1,t2,t3}$ is $40n$. It should be recalled here that curvature needs three data points hence one curvature response ($c_{t1,t2,t3}$). These values (θ and c) are shown to be too low in the analysis of their measurement error (i.e., using 0.056mm/px scale factor), hence their unreliability. This error analysis is done after the results are shown, since they are needed for the analysis. Inclination angles and curvatures are metrics most related to the physical curve of the structure, hence their relatively low values since there is little vertical displacement, and support conditions on the left allow for horizontal movement.

Overall, the verdict would be that only displacements and strain response can be taken as reliable given the loading and monitoring conditions. Others (inclination angles and curvatures) are too noisy, but it is expected that with increasing loading they will become less noisy and thus usable.

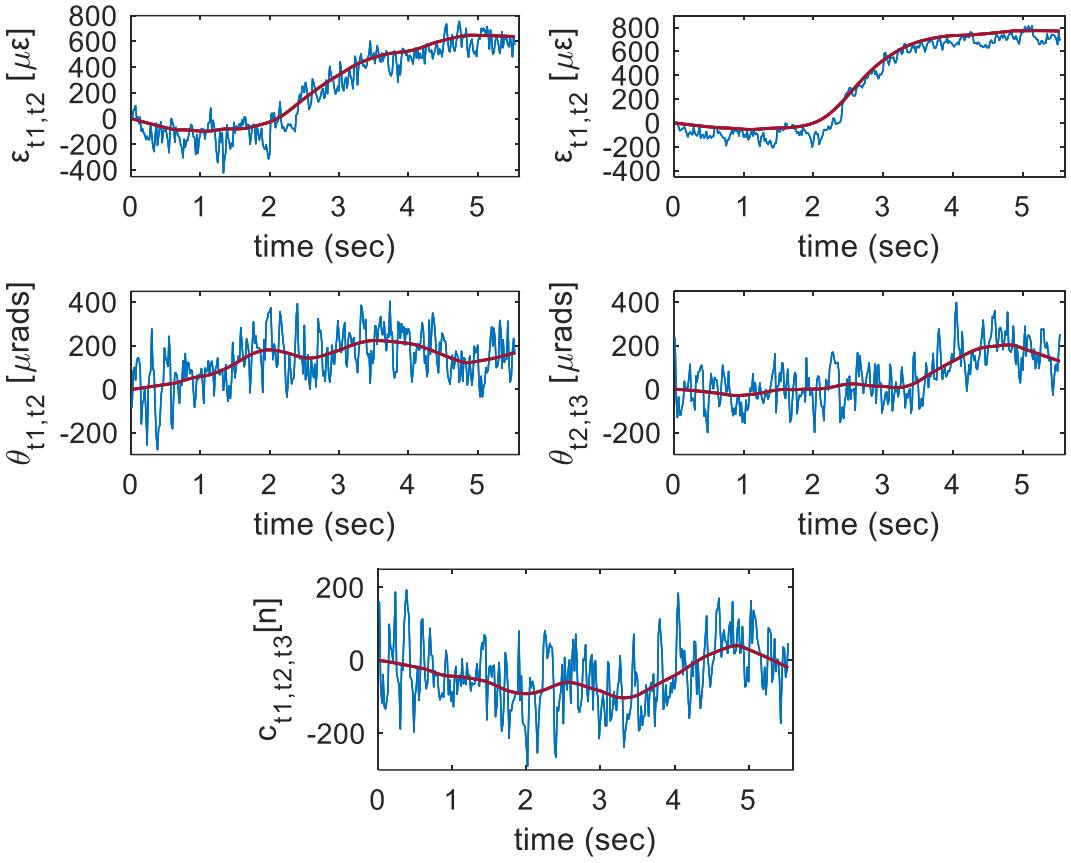

Figure 4-36: Secondary response time histories. Rows: Up to down – Strains, Tilts (Inclination angles), and Curvature. Columns: L to R – Response between targets 1 and 2 (T_1&T_2), and 3 and 4 (T_3&T_4). Raw response shown in blue; Pre-processed response shown in red.

Structural response profiles

Structural response profiles are formed by taking maximum response for all target histories (for displacements), or target-set histories (for secondary responses). From Figure 4-37(a, b, and c) below, structural response profiles are indeed achievable for real life structures. From the entire structure, an FOV at the middle of the bridge is monitored. Response from this monitoring is given in (b) and (c).

In (b), target displacement profile (r_δ) is shown in blue, the markers beneath each target represents the maximum displacements from their time histories. Strain profile (r_ε) is shown in red. The red markers between targets (i.e., a target set (T)) represent the maximum strain from their time histories and assumed to be exactly halfway between target set.

In (c), inclination angles profile (r_δ) is shown in blue. The blue markers between target sets represent the maximum inclination angle from their time histories and assumed to be exactly halfway between each target set. Curvature profile (r_c) is shown in red. Only one red marker is shown as one quadratic curvature requires coordinates of the tree targets. Therefore, the

red marker represents the maximum curvature from their time histories and assumed to be exactly at the mid target.

For r_δ in (b) a symmetrical positive parabola/curve is expected (theoretically) if this monitored section is truly central. This is not strictly the case here. However, from the much smaller maximum deflection (r_δ) ratio between T_2(1.01mm) and T_3(1.02mm) a parabolic shape that must tend upwards is discerned. This might indicate a slight structural response (moment, shear, etc) asymmetry that could be explained by the asymmetric location of the targets described earlier in Section 4.3.4, or by studying the support conditions (maybe using theoretical structural models), and/or by structural design calculations – which lie outside the scope of this thesis.

Ultimately, the structural response profiles here would not mean much as only a small section of the bridge is monitored (see Figure 4-37). These results are therefore only a demonstration of applicability. To get fuller context, a wider section must be monitored. Discussions on this is next after this section and is expanded in the next chapter.

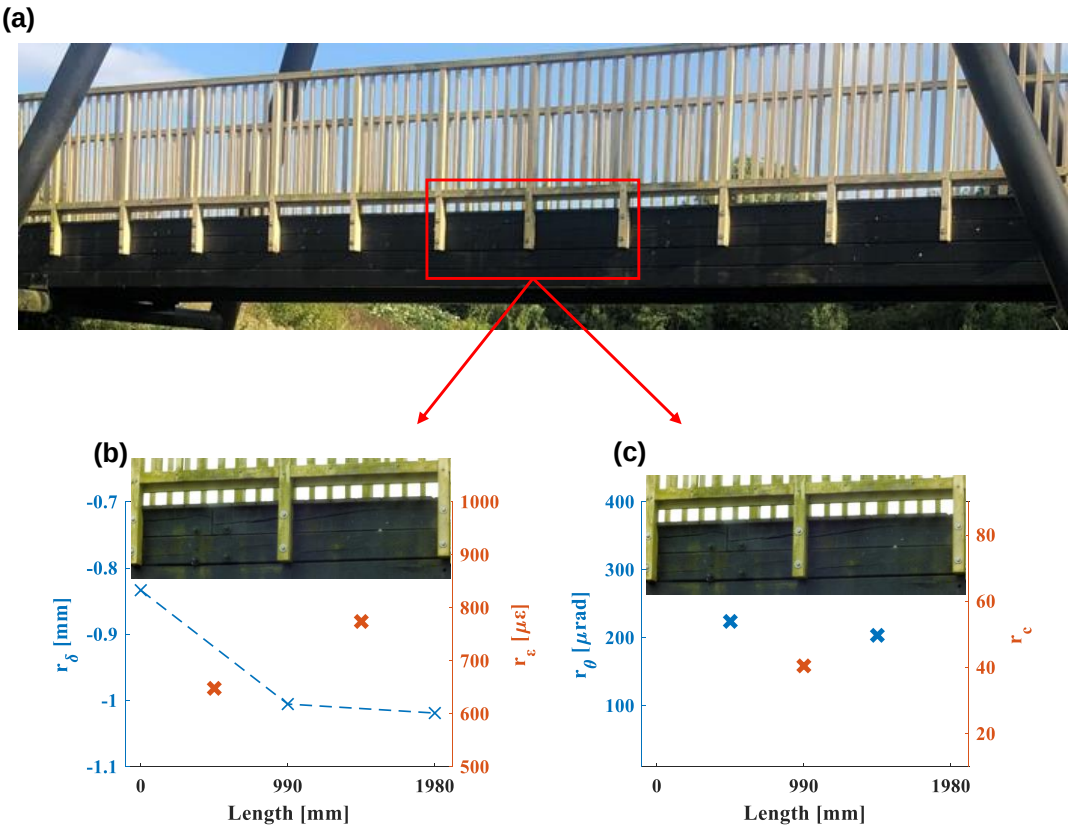

Figure 4-37: (a) Bridge span showing the monitored section. (b) Blue, Red: Maximum Displacement (response profile r_δ) for each target, Maximum Strain (response profile r_ε) for

each target set. (c) Blue, Red: Maximum Inclination angles (response profile r_θ) for each target set, Maximum Curvature (response profile r_c) for the target set (three targets for curvature).

Discussion on the measurement accuracy for curvature and inclination angles

As described in the Methodology Chapter Section 3.3.9, the curvature (c) at an i^{th} time step is the residual of quadratic coefficients (a) between a first and an i^{th} time step (see Equation 3.6). Now recall that the greater the value of a, the narrower the curve, and vice versa. Figure 4-38 below shows two polynomial curves plotted on an x – axis representing the length of the monitored bridge section, using quadratic equations with all three coefficients a, b, and c:

1. Plot 1 (blue): ${a_{max}}^2 + b_{a_{max}} x + c_{a_{max}}$, and
2. Plot 2 (red): ${a_{min}}^2 + b_{a_{min}} x + c_{a_{min}}$

a_{max} is the maximum a value in the curvature time history, and $b_{a_{max}}$ and $c_{a_{max}}$ are the corresponding linear coefficient and Y-intercept respectively for a_{max}. Similarly, a_{min} is the minimum a value in the curvature time history, and $b_{a_{min}}$ and $c_{a_{min}}$ are the corresponding linear coefficient and Y-intercept respectively for a_{min}. Plot 2 is inverted since a_{min} has a negative value. These polynomial curves represent the shape of the bridge length at maximum and minimum curvatures. The aim is to show the meaning of curvature values into the familiar context of deflection in mm. For example, Figure 4-38 simply shows that at curvature = a_{max}, the middle target (T_2) deflects about 0.04mm lower than T_1 and T_3. At a_{max} the curve has a vertical peak of -0.04mm, and at a_{min} it is 0.1mm. One can see that these values are too close to the 0.061mm/px vertical measurement resolution or error for reliability. In fact, a_{max} is less than the value of the measurement error – $a_{max} < measurement\ error$.

As described in the Methodology Chapter Section 3.3.10, inclination angles at a time step (θ_i) is the residual of the tangent relationship (α) between two targets at an i^{th} time step, with reference to α at the first image frame (see Equation 3.12). The logic applies in the same way to inclination angles. Since α depends on vertical and horizontal distances between targets, any changes in them must be reasonably higher than measurement error to have reliability.

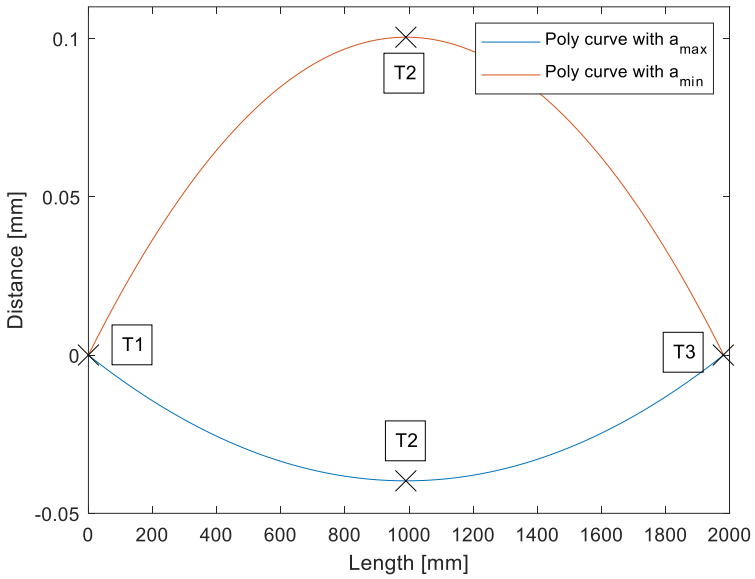

Figure 4-38: Polynomial curves for maximum quadratic coefficient (a_{max}) (in blue), and minimum quadratic coefficient (a_{min}) (in red). The plot is a diagrammatical display of the extents (in mm) of the curve between the three monitored targets at a_{max} and a_{min}. The aim is to translate curvature values into familiar context of deflection in mm. For example, this plot simply shows that at curvature = a_{max}, the middle target (T_2) deflects about 0.04mm lower than T_1 and T_3

4.3.8 Discussions

Findings from the field case study are discussed here. Firstly, structural response profiles are indeed achievable for real life structures. The discussions here therefore are mainly an appraisal of the results, and then practical field deployment challenges and a conceptualisation of possible solutions especially with regards to accuracy and measurement resolution.

In this case study, response time histories are obtained using the same procedures as in previous case studies. Target displacements are the primary response obtained from the image processing phase. Secondary responses of strains, inclination angles, and curvatures are obtained from manipulating target displacements. Maximum values from measurement time histories are obtained and plotted to give the structure's response profile, from which damage sensitive features, which is a ratio of change between baseline and current ridge response, is derived. With field deployments damage cannot be created, so it is enough at this stage to obtain and characterise response. This case study shows that this is possible, but with limitations.

Only a small section of the structure was selected as FOV and monitored. This is because the camera must be zoomed in enough to capture a relatively small length of the structure, so as to achieve a desirable measurement resolution, given by the scale factor i.e. –

physical distance/pixel distance. The smaller this ratio the better the measurement accuracy, as the same number of pixels covering a wider physical length is made to cover a smaller one. FOVs must be limited to achieve this desirable measurement resolution especially for damage detection.

Target displacement time histories, as in previous case studies, again proved that it is reliable and robust to noise. Maximum displacements can be reliably obtained since noise ratio is small (see Figure 4-35). For secondary responses strains can be deemed reliable, due to visibly low noise effects, because of their relatively higher values (see Figure 4-36). Inclination angles and curvatures are the response types most related to the physical curve of the structure. They appear the noisiest in this case study due to their relatively low values. This can be attributed to little vertical displacement due to small load and support conditions on the left allowing for horizontal movement, thereby minimising physical curvature.

Given the localised FOV containing only three targets, the structural response profiles obtained here would not mean much in the global structural or damage detection perspective. They cannot represent a true, global, response profile for the bridge. The question that then arises from here is how to monitor a larger bridge profile for a truly robust distributed/multi target monitoring. The answer to this is a multi-camera or a robotic camera approach, proposed in (Obiechefu and Kromanis, 2021). A robotic camera approach was recommended in (Kromanis and Forbes, 2019) and is discussed in the next chapter. Capturing response of a full bridge span requires multiple cameras, also discussed in the next chapter. When bridge dynamic response is collected, than cameras have to be time-synchronised (Lydon et al., 2018). The technique proposed in this paper does not require time synchronisation. Besides cameras do not need being placed in the same positions at each measurement event.

In this study, a $1/15$ pixel resolution is achieved, however, what remains clear is the need for increased sub pixelling for accurate response obtention. This can only be achieved with more research which needs to go into effective and efficient ways to achieve critical subpixel accuracy for feature detection algorithms to be employed in multipoint deformation monitoring. More on these in the next Chapter.

CHAPTER 5 – DISCUSSIONS AND CHALLENGES

5.1 Accurate response obtention

The damage detection process is based on the premise of accurate obtention of target displacements from the structure during a loading scenario which are used to compute measurement time histories. Maximum data from each target's measurement time history are obtained and plotted to give the structure's response profile, from which damage sensitive features – a ratio of change between baseline and current girder response, is also derived. Accurate response obtention is dependent on both measurement resolution achievable, and elimination of noise; in addition to these, damage detection depends further on intensity of loading, and severity of damage. All else being equal, achieving a high measurement resolution is most important. The obvious ways to achieve this are:

1. Employing expensive high-resolution cameras
2. Increasing subpixel accuracy

We know that accuracy is traded off as more targets or larger area of the structure are fit into the same device's FoV to obtain a response profile of a wider length of the structure (Busca et al., 2014). Granted, higher-resolution devices automatically increase measurement accuracy by packing more pixels for any given area, but they will be at the expense of the cardinal aim of this research – i.e., affordability. In a situation where multiple devices are required, an exponential increase in cost ensues. Therefore, increasing subpixel accuracy is the more efficient and perhaps more effective way of achieving higher measurement resolution, since the other major alternative would involve hardware costs. Increasing subpixel accuracy simply means the ability to obtain measurements from further divisions of a pixel. For example, if 1px equals 1mm length of a deck, without any sub-pixel accuracy, the response measurements will be graduated in 1mm intervals; on the other hand, a 1/10 sub-pixel accuracy would mean response graduations in $1/10^{th}$ of 1mm, i.e., 0.1mm.

Perhaps it is important to note here that using an optical zoom lens can achieve higher accuracies easily by just zooming in, but as discussed earlier in Section 2.1.3, the larger FoVs essential for multipoint monitoring must be sacrificed for this increase, and which in turn means that structural response profiles cannot be obtained. Optical zoom lens therefore can be used, and is indeed used in this thesis, but only to a fraction of its potential, as the image can only be zoomed enough to cover a reasonable FoV – for example the 2m used in the footbridge. An optical zoom is almost always preferred because a digital zoom

– commonly found in consumer-grade devices, zooms by cropping an image down to the desired or focus area with the same aspect ratio as the original image, and scaling the cropped image up to the size of the original. Hence the camera's optics are not adjusted, as it is accomplished electronically, and so no optical resolution is gained. An optical zoom gains optical resolution as the image is cropped.

Several high subpixel resolution values have been reported in literature, e.g. between $\frac{1}{2}$ and $\frac{1}{100}px$ (Feng et al, 2015), and $\frac{1}{500}px$ resolution (Imetrum, 2020; Potter and Setchell, 2014), mostly using digital image correlation. Digital image correlation is computationally-expensive, and one can observe that they have been applied mostly to cases of single target/point monitoring for example in (Caetano et al., 2010; Chang and Xiao, 2010; Chu et al., 2019; D. Feng et al., 2015a; Guo and Zhu, 2016; Ji et al., 2020; Mahal et al., 2015; Pan et al., 2009b). For a multipoint deformation monitoring case, much work must still be done to reduce its computational and time requirements. In the case studies of this thesis, subpixel resolution has been increased by scaling the images to the extent that they can, and increasing pixels to avoid losing information (akin to using a zoom lens), achieving $1/15$ sub-pixel resolution. These have been discussed in Sections 3.4 in the Methodology, and 4.1 for the numerical model. However, what remains clear is the need for increased sub pixelling for accurate response obtention. This can only be achieved with more research which needs to go into effective and efficient ways to achieve critical subpixel accuracy for feature detection algorithms to be employed in multipoint deformation monitoring.

The capacity of CV-based monitoring systems to deliver accurate and cost-effective measurements/interpretations of bridge response is crucial if it must gain the trust of asset managers and the engineering community as a whole. This is important especially within the context of their prospective complementation of visual inspections of at least small to medium-scale bridges. Affordable image acquisition devices like phone cameras and open source image processing algorithms and tools makes CV-based SHM an attractive option for at least short term measurement collection and response interpretation (Dong and Catbas, 2020b; Feng and Feng, 2016).

5.2 Multi-camera approach for more comprehensive distributed sensing

In Case Study 3 (Section 4.3), only a small section of the structure was selected as FOV (monitored). This is because the camera must be zoomed in enough to capture a relatively small length of the structure, so as to achieve a desirable measurement resolution given by the scale factor i.e. – physical distance/pixel distance. The smaller this ratio the better the measurement accuracy, as the same number of pixels covering a wider physical length is

made to cover a shorter one. Fields of view must be limited to achieve this desirable measurement resolutions especially for damage detection. The question that arises from here therefore is how to monitor a larger bridge profile for a truly robust distributed/multi target monitoring.

A multi-camera approach has been hypothetically considered in the methodology chapter, Section 3.4.2. It is further discussed here with general conditions and parameters encountered particularly in the field case study, but also from the numerical model. The approach simply involves setting up multiple cameras to cover and monitor pre-set fields of view across the span of interest in the structure. Fields of view may then be reconciled exactly with each other using for example image stitching software, or any other methods. Image stitching has been used relatively recently in CV-SHM; for example in (Aliakbar et al., 2016) an unmanned aerial vehicle provides real-time images with the aid of a SURF-based image stitching algorithm for inspection of tall structures; also in (Wang et al., 2021) it aids in crack visualization. Its performance in this approach looks promising going by successful implementations in related areas but remains to be seen.

From Equations 4.2 and 4.3, the horizontal measurement resolution achieved with a FOV of 2m is ~0.84mm/px, while ~0.92mm/px is achieved for the vertical direction using a scale factor. A sub-pixel resolution of $^{1}/_{15^{th}}$ is achieved using this case study. This improves the previously-stated measurement resolution to 0.056mm/px and 0.061mm/px in the horizontal and vertical directions respectively.

We know that accuracy is traded off as FOV increases. As an example, let us consider for a 13m bridge central span, an initial measurement resolution of ~0.34mm/px achieved given certain camera specifications, and a FOV of 1.3m. Factored with $\frac{1}{10}mm/px$ sub-pixel resolution, we get a final measurement resolution of 0.034mm/px. This practically means that 10 cameras of same specifications and final measurement resolution are required to monitor the 13m bridge central span. This cannot be considered practicable as equipment could become bulky and require much more space. With a $\frac{1}{25}mm/px$ resolution we can increase FOV by 200% to 3.3m, and with $\frac{1}{50}mm/px$ a 500% increase to 6.5m. This would allow a drastic reduction in required equipment to four cameras in the former, and two cameras in the latter. Figure 5-1 shows an exponential relationship between subpixel accuracy and achievable FOV, for monitoring a 13m bridge span, assuming an initial measurement resolution (without sub-pixelling) of 0.34mm/px. Figure 5-2 shows the number

of cameras for each sub-pixel resolution required to monitor a 13m bridge span given for an initial measurement resolution (without sub-pixelling) of 0.34mm/px.

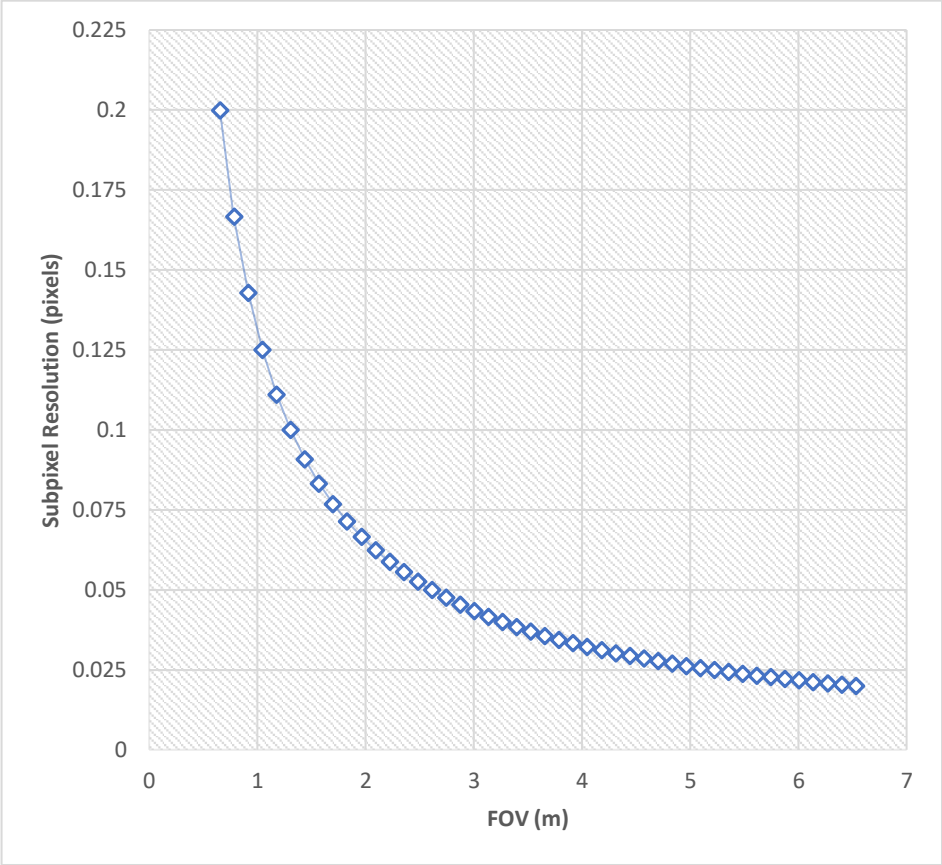

Figure 5-1: Achievable FOV for a 13m span given sub-pixel resolution for an initial measurement resolution (without sub-pixelling) of 0.34mm/px

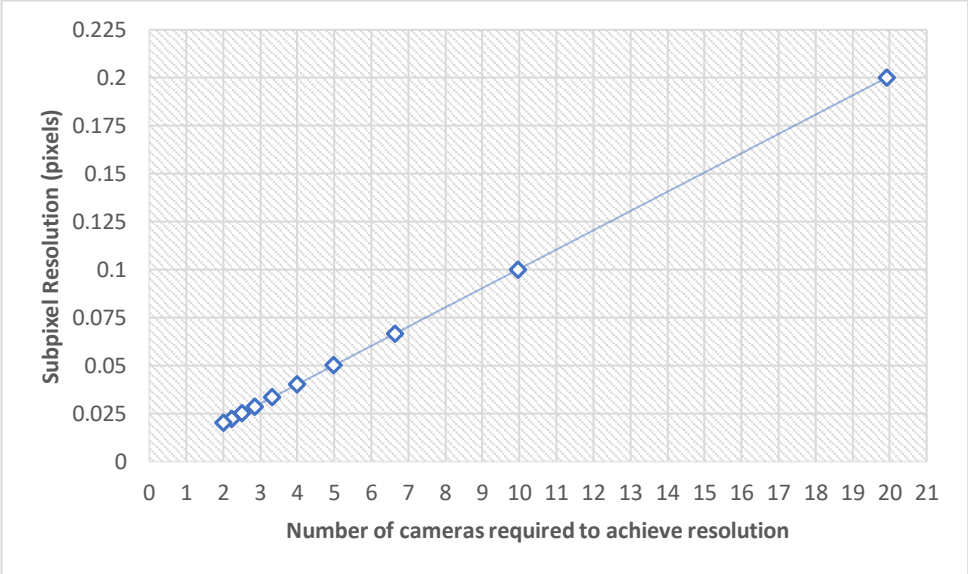

Figure 5-2: Number of cameras required for monitoring a 13m span given sub-pixel resolution for an initial measurement resolution (without sub-pixelling) of 0.34mm/px

Therefore, it can be concluded without a doubt that the key to accurate and affordable CV-SHM lies in achieving high subpixel accuracy with minimal computational resource requirements, such that multiple targets in distributed sensing can be accurately captured and analysed rapidly.

A robotic camera system that can be programmed to capture pre-set FOVs at multiple truck crossings can be considered to achieve this (Kromanis and Forbes, 2019). The robotic camera captures multiple images and is set to rotate to a new pre-set FOV after each image capturing, until the end. With this system, FOV can be kept small for increased accuracy. But challenges start to mount when moving loads are considered, outside laboratory conditions where the same truck is not expected to cross multiple times. This is because the robotic camera cannot capture the entire structure at once, it relies on capturing pre-set fields of view successively from one end to another to aid accuracy. Therefore, if the same truck does not run multiple times its use becomes limited. For response profile from distributed sensing, all parts must be captured at the same time throughout the moving loading sequence.

In a multi-camera approach, when bridge dynamic response is collected, then cameras have to be time-synchronised (Lydon et al., 2018). But the approach proposed in this thesis does not require this, and cameras do not need being placed in the same positions at each measurement event since a simple position-independent approach is available (Kromanis and Liang, 2018).

5.3 Condition assessment events as reliable SHM campaign

Having proposed a multi-camera accurate and affordable CV-SHM approach, we may, at this stage have an outlook at what it would look like, as well as potential challenges when more fully developed. By definition, a CV-SHM system must have the capacity to detect anomalous behaviour in the structure which it is monitoring hence why damage detection is essential for a SHM system.

In Section 2.2.2, a discussion on the distinction between SHM and condition assessment was made. SHM most times is used to express continuous monitoring over an extended period, and condition assessment used mostly for discrete measurement collection events. To an extent this depends on how data is collected – continuous monitoring over an extended period, or discrete monitoring with measurement collection events at scheduled intervals. However, neither of these terms is definite, and they are often used interchangeably in practise. Traditionally, most long term SHM campaigns make use of sensors that continually acquire enormous amounts of data that must be processed

afterwards, which is why signal analysis and numerical techniques for anomaly detection are so widespread (Feng and Feng, 2018; Xu and Brownjohn, 2018). Structural behaviour can be modelled from data, and even predictions made

However, there is some grey area that is up to interpretation. Discrete measurement collection events can also be analysed using signal and numerical analysis. For instance, the approach of this thesis – which is essentially a sensor collecting bridge response from a vehicular crossing and analysing the signal afterwards. The next question then becomes: how can discrete measurement collection events be organised into a reliable SHM campaign? And the answer is: - by scheduling regular measurement collection events over an extended period. Weekly, or monthly events over a year or more provides enough data to learn about the structural performance of any structure. Data collected could be shared with asset managers and city councils and in that way complement their visual inspections routine.

One obvious challenge associated with discrete events is establishing a reference condition for anomaly detection. One way of solving this issue is by using theoretical models (Erdenebat et al., 2019, 2018; Erdenebat and Waldmann, 2020) (also see Section 2.2.3), another more practical way introduced in this thesis is by using response from a first inspection to establish baseline conditions. Therefore, a continuous CV-SHM campaign for any small to medium-scale structure can be established and can go on for as long as required. A closely related consideration in long-term monitoring is the mapping process between structural response from different measurement collection events, which most likely, will not have been taken from the exact same camera positions. In other words, the methodology of this thesis must be position-independent to allow for accurate structural condition assessments. The solution to this has been specifically detailed for this exact situation in Kromanis and Liang, (2018) (also see Section 2.2.3, page 41); it is a simple application of a transformation matrix (or planar homography, (also see Section 2.1.4 for its theory, and Section 4.3.6 for its application on the restored footbridge case study)). But in this instance, target positions from a first inspection can be used to generate a transformation matrix and consequently a reference coordinate system to which the same targets' positions from subsequent inspections are transformed, establishing a reference from which deformations can be estimated. Therefore, it is important to set the reference coordinate system to the device used in a first inspection.

In summary, this section discusses the possibility in the near future to have a reliable, accurate, affordable, and easy long-term CV-SHM program that can complement visual inspections for small to medium-scale bridges. Issues that must be solved before this is a reality have been laid out earlier in this chapter, but none of them is too enormous a task or

particularly challenging, that it cannot be solved in the short to medium term, given sufficient research efforts.

CHAPTER 6 CONCLUSION AND FURTHER WORK

6.1 Conclusion

This thesis proposes an affordable CV-SHM approach and framework using consumer-grade hardware and data-driven response analysis/damage detection techniques. Computer vision is nothing new in SHM, but in this thesis, their suitability for multi target damage detection is explored.

Firstly, the thesis proposes an affordable CV-SHM framework for small to medium scale bridges where structural responses from scheduled measurement collection events are analysed for anomalies and stored in a data bank; and in which responses obtained from a first measurement collection event (baseline response) are compared to those from subsequent events to determine the relative state of the bridge, and advice interventions if necessary. Secondly, the thesis defines and describes the obtention of four structural responses for use in the afore-mentioned framework namely – displacements, strains, inclination angles, and curvatures. The response obtention process is such that there is no need for contact with the structure, or knowledge of any other information about the structure, thus ensuring a data-driven and flexible approach compared to what is obtainable. Thirdly, a damage detection and localisation technique is proposed for comparing baseline and subsequent responses and locating possible damages.

In the three case studies, the damage detection techniques were shown to be reliable, but with limitations, especially for full scale field deployments where measurement noise and other environmental challenges are much more severe. The numerical model explored the extents of affordable CV-based damage detection with all responses – i.e., displacements, strains, curvatures, and inclination angles. This exploration took into consideration the most important variables that determine measurement resolution including field of view, camera resolution, and achievable sub-pixel resolution. In the laboratory model, damage is a 20% stiffness loss. Damage is detected in all cases except for inclination angles as FoV was limited to 1.7m and using the same camera characteristics assumed for the theoretical model simulation. The FoV was 2m in the field demonstration to contain at least three targets. A $^{1}/_{15^{th}}$ sub-pixel resolution was achieved. Damage detection was not possible since it could not be created on a public facility. Response time histories, as well as their profiles were accurately obtained and displayed. A discussion of challenges for a full scale, long term field deployment has been given in the previous chapter. This would involve a multi-camera approach and must be the focus of future research in this domain. The success of the field demonstration proves that full-scale field deployments can be

envisioned in the near future. Generally, what matters most for multi-target field monitoring is the balance between achieving maximum sub pixel measurement accuracy and the demand for resources. This is important as the focus is on using consumer grade hardware and achieving multi target monitoring.

- The thesis has demonstrated the possibility of a truly data-driven and affordable CV-SHM framework for small and medium scale bridges. This framework is based on periodic measurement collection events with consumer grade hardware, secure and accessible measurements' storage, response analysis/damage detection techniques for condition assessment, and a communications channel with asset owners for communicating the relative condition of bridges and advising interventions if needed.

- The thesis has demonstrated the practicality of a wholly data-driven structural response obtention where response can be calculated without the requirement for prior information about the bridge being monitored.

- High measurement resolution is crucial for CV-SHM of bridges. Damages as little as 2% stiffness loss can be detected in a theoretical model in the absence of measurement noise, but this is not the case in real world applications. In the presence of real-world measurement noise, experimental models indicate that for as little as 20% stiffness loss, we can expect to detect damages if a measurement resolution of $5 \times 10^{-2} mm/px$ can be achieved. This is realisable with a regular iPhone or GoPro with 4k and 12MP frame, a pixel resolution of at least $^{1}/_{15^{th}}\, px$, and with FoV not more than 2m.

- The proposed damage detection technique is also flexible in such a way that it does not require a time synchronized measurement collection even if multiple cameras are employed, since only absolute maximum response values, which are extracted from target measurement series, are needed to derive bridge response.

- Damage sensitive features derived from strains perform better than other structural response types in all case studies. At high enough measurement resolutions small damages can be detected. Strains are unitless and calculated from movements of two targets, therefore requiring no scale factor, and thus making them a good option for field applications, provided that high measurement resolution is attained. Curvatures can be used for damage detection at measurement resolutions higher than that for strains, since they are more susceptible to noise. Inclination angles are not well suited to detect damages due to the measurement shift present in its profile. Displacements time series are easy to obtain since they

are the primary response, however, they change very slowly, without clear spikes or shifts as with others, and hence cannot be relied upon for damage localisation.

- Given the need for adequate measurement resolution, the FoV from consumer grade cameras can only cover a small part of most bridges, the thesis therefore proposed a multi camera approach to cover entire bridges and obtain response. This is only practicable for small to medium sized bridges. It is shown that if a moderately high measurement resolution can be achieved, for example $5 \times 10^{-2} mm/px$, then less cameras are required to cover a structure and obtain accurate response. Conversely, less measurement resolution will mean that more cameras are needed since FoV must also reduce, if an adequate measurement resolution is to be achieved.
- The thesis made a case for why periodic bridge measurement collection over a long period, especially for small to medium scale bridges not dominated by dynamic effects, can be considered as continuous monitoring. Measurement collection events over time provide enough data such that even little deviations not amounting to damage can be obtained and studied.
- The success of the field demonstration proves that full-scale field deployments can be envisioned in the near future. This would involve the proposed multi-camera approach, but must first be the focus of future research in this domain.

6.2 Further work

Firstly, more work must be done to achieve higher sub-pixel accuracies with programs that are not computationally expensive, so that, with consumer grade phones, and laptops with image processing software, a full-scale monitoring and analysis can be performed on a small to medium scale bridge. With digital image processing, several techniques are already available to achieve sub-pixelling (D. Feng et al., 2015; Imetrum, 2020; Potter and Setchell, 2014). However, these must be made computationally inexpensive so that they can be used with multiple targets at the same time. Other feature matching algorithms are already less computationally expensive, so become a very realisable task in the short term. A computationally inexpensive $\frac{1}{50} px$ sup-pixel resolution algorithm is excellent and can be an ideal to work towards.

Secondly, image stitching technology must be exploited more for stitching together several high-resolution images accurately to the sub pixel level. Image stitching of overlapping images, as discussed in the previous chapter has been used relatively recently in CV-SHM;

for example in providing real-time images with an unmanned aerial vehicle for inspection of tall structures (Aliakbar et al., 2016); also in in crack visualization (Wang et al., 2021). Future research must test its performance in the approach proposed in this thesis. Since the same key point/feature detection techniques and algorithms are applied in image stitching technology as in CV-SHM, it seems feasible to account for sub-pixel inaccuracies that may be introduced at edges of stitching between slightly overlapping images, and also those from 2D projection transformation (planar homography) of multiple stitched images. Again, the prospects look promising going by successful implementations in related area, and is relatively achievable in the short term, at least under laboratory conditions.

The next stage logically becomes an attempt at a short to medium term monitoring campaign of selected structures. This stage surely would have many challenges. Many factors such as wind and other environmental conditions that could affect data must be kept as constant as possible. One way could be by having the events in relatively good weather. Another way could be by using equipment, for example windshields. Perhaps structural identification would be required at this stage. Also, it may become easier to establish damage thresholds for damage detection if done over sufficiently long time.

6.3 Publications

6.3.1 Journal Articles

Obiechefu, C.B., Kromanis, R., 2021. Damage detection techniques for structural health monitoring of bridges from computer vision derived parameters. Struct. Monit. Maint. 8, 91–110. https://doi.org/10.12989/smm.2021.8.1.091

6.3.2 Conference Papers

Obiechefu, C.B., Kromanis, R., Mohammad, F., Arab, Z., 2021. CV-based damage detection using inclination angles and curvature, in: The 8th Workshop on Civil Structural Health Monitoring. Lecture Notes in Civil Engineering.

Obiechefu, C. B., Mohammad, F., Arab, Z., & Kromanis, R. (2020). Vision-based bridge monitoring using displacement curvatures. *Joint International Resilience Conference 2020 Interconnected: Resilience Innovations for Sustainable Development Goals*, 120–123.

REFERENCES

Abdo, M.A.B., 2012. Parametric study of using only static response in structural damage detection. Eng. Struct. 34, 124–131. https://doi.org/10.1016/j.engstruct.2011.09.027

Alahi, A., Ortiz, R., Vandergheynst, P., 2012. FREAK: Fast retina keypoint, in: Proceedings of the IEEE Computer Society Conference on Computer Vision and Pattern Recognition. pp. 510–517. https://doi.org/10.1109/CVPR.2012.6247715

Aliakbar, M., Qidwai, U., Jahanshahi, M.R., Masri, S., Shen, W.M., 2016. Progressive image stitching algorithm for vision based automated inspection. Proc. - Int. Conf. Mach. Learn. Cybern. 1, 337–343. https://doi.org/10.1109/ICMLC.2016.7860924

ANSYS, 2018. ANSYS Mechanical APDL Element Reference, in: Help System. pp. 1377–1390. https://doi.org/www.ansys.com

Atherton, T.J., Kerbyson, D.J., 1999. Size invariant circle detection. Image Vis. Comput. https://doi.org/10.1016/S0262-8856(98)00160-7

Baker, S., Matthews, I., 2004. Lucas-Kanade 20 Years On: A Unifying Framework, International Journal of Computer Vision.

Bakht, B., G. Jaeger, L., 1990. Bridge Testing—A Surprise Every Time. J. Struct. Eng. 116. https://doi.org/10.1061/(ASCE)0733-9445(1990)116:5(1370)

Bakhtiari-Nejad, F., Rahai, A., Esfandiari, A., 2005. A structural damage detection method using static noisy data. Eng. Struct. 27, 1784–1793. https://doi.org/10.1016/J.ENGSTRUCT.2005.04.019

Bay, H., Ess, A., Tuytelaars, T., Van Gool, L., 2008. Speeded-Up Robust Features (SURF). Comput. Vis. Image Underst. 110, 346–359. https://doi.org/10.1016/j.cviu.2007.09.014

Beauchemin, S.S., Barron, J.L., 1995. The computation of optical flow. ACM Comput. Surv. 27, 433–466. https://doi.org/10.1145/212094.212141

Bradsky, G., Kaehler, A., 2008. Learning OpenCV: Computer Vision with the OpenCV Library - Gary Bradski, Adrian Kaehler - Google Books. O'Reilly Media, Sebastopol.

Bremer, K., Wollweber, M., Weigand, F., Rahlves, M., Kuhne, M., Helbig, R., Roth, B., 2016. Fibre Optic Sensors for the Structural Health Monitoring of Building Structures. Procedia Technol. 26, 524–529. https://doi.org/10.1016/j.protcy.2016.08.065

Brownlie, E. (2017) 'Queensferry Crossing, Scotland', *Shuttershock.com*.

Brownjohn, J.M.W., 2007. Structural health monitoring of civil infrastructure. Philos. Trans. R. Soc. A Math. Phys. Eng. Sci. 365, 589–622. https://doi.org/10.1098/rsta.2006.1925

Brownjohn, J.M.W., Bocciolone, M., Curami, A., Falco, M., Zasso, A., 1994. Humber bridge full-scale measurement campaigns 1990-1991. J. Wind Eng. Ind. Aerodyn. 52, 185–218. https://doi.org/10.1016/0167-6105(94)90047-7

Brownjohn, J.M.W., Koo, K.-Y., De Battista, N., 2014. Sensing solutions for assessing and monitoring bridges. Sens. Technol. Civ. Infrastructures 207–233. https://doi.org/10.1533/9781782422433.2.207

Brownjohn, J.M.W., Xu, Y., Hester, D., 2017. CV-based Bridge Deformation Monitoring. Front. Built Environ. 3. https://doi.org/10.3389/fbuil.2017.00023

Brownlie, E. (2017) 'Queensferry Crossing, Scotland', *Shuttershock.com*.

Bruck, H.A., McNeill, S.R., Sutton, M.A., Peters, W.H., 1989. Digital image correlation using Newton-Raphson method of partial differential correction. Exp. Mech. https://doi.org/10.1007/BF02321405

Bryan, M.A., 2000. Method and apparatus including accelerometer and tilt sensor for detecting railway anomalies. 6,044,698.

Busca, G., Cigada, A., Mazzoleni, P., Zappa, E., 2014. Vibration Monitoring of Multiple Bridge Points by Means of a Unique CV-based Measuring System. Exp. Mech. 54, 255–271. https://doi.org/10.1007/s11340-013-9784-8

Caetano, E., Silva, S., Bateira, J., 2011. A vision system for vibration monitoring of civil engineering structures. Exp. Tech. https://doi.org/10.1111/j.1747-1567.2010.00653.x

Caetano, E., Silva, S., Bateira, J., 2010. A VISION SYSTEM FOR VIBRATION MONITORING OF CIVIL ENGINEERING STRUCTURES. Exp. Tech 32, 74–82. https://doi.org/10.1111/j.1747-1567.2010.00653.x

Calonder, M., Lepetit, V., Strecha, C., Fua, P., 2010. BRIEF: Binary robust independent elementary features, in: Lecture Notes in Computer Science (Including Subseries Lecture Notes in Artificial Intelligence and Lecture Notes in Bioinformatics). Springer Verlag, pp. 778–792. https://doi.org/10.1007/978-3-642-15561-1_56

Carden, E.P., Fanning, P., 2004. Vibration Based Condition Monitoring: A Review. Struct. Heal. Monit. 3, 355–377. https://doi.org/10.1177/1475921704047500

Catbas, N., Brown, D., Aktan, A., 2006. Use of Modal Flexibility for Damage Detection and Condition Assessment: Case Studies and Demonstrations on Large Structures. J.

Struct. Eng. 132. https://doi.org/10.1061/(ASCE)0733-9445(2006)132:11(1699)

Chang, C.C., Ji, Y.F., 2007. Flexible Videogrammetric Technique for Three-Dimensional Structural Vibration Measurement. J. Eng. Mech. 133. https://doi.org/10.1061/ASCE0733-93992007133:6656

Chang, C.C., Sun, Z., 2005. Structural damage localization using spatial wavelet packet signature. Smart Struct. Syst. 1, 29–46. https://doi.org/10.12989/sss.2005.1.1.029

Chang, C.C., Xiao, X.H., 2010. Three-Dimensional Structural Translation and Rotation Measurement Using Monocular Videogrammetry. J. Eng. Mech. 136, 840–848. https://doi.org/10.1061/(asce)em.1943-7889.0000127

Chang, C.C., Xiao, X.H., Asce, M., Xiao, X.H., 2010. Three-Dimensional Structural Translation and Rotation Measurement Using Monocular Videogrammetry. J. Eng. Mech. 136. https://doi.org/10.1061/(ASCE)EM.1943-7889.0000127

Chen, C.-C., Wu, W.-H., Tseng, H.-Z., Chen, C.-H., Lai, G., 2015. Application of digital photogrammetry techniques in identifying the mode shape ratios of stay cables with multiple camcorders 75, 134–146. https://doi.org/10.1016/j.measurement.2015.07.037

Chen, J.G., Davis, A., Wadhwa, ; Neal, Durand, F., Freeman, W.T., Büyüköztürk, O., 2017. Video Camera-Based Vibration Measurement for Civil Infrastructure Applications. J. Infrastruct. Syst. 23. https://doi.org/10.1061/(ASCE)

Chen, J.G., Wadhwa, N., Cha, Y.-J., Durand, F., Freeman, W.T., 2015. Modal identification of simple structures with high-speed video using motion magnification. J. Sound Vib. 345, 58–71. https://doi.org/10.1016/j.jsv.2015.01.024

Chen, X., Hong-ping, Z., Chuan-yao, C., 2005. Structural damage identification using test static data based on grey system theory. J. Zhejiang Univ. A 6, 790–796. https://doi.org/10.1631/jzus.2005.A0790

Choi, H.-S., Cheung, J.-H., Kim, S.-H., Ahn, J.-H., 2011. Structural dynamic displacement vision system using digital image processing. NDT E Int. 44, 597–608. https://doi.org/10.1016/j.ndteint.2011.06.003

Choi, I., Kim, J., Kim, D., 2016. A Target-Less CV-based Displacement Sensor Based on Image Convex Hull Optimization for Measuring the Dynamic Response of Building Structures. Sensors. https://doi.org/10.3390/s16122085

Chu, X., Zhou, Z., Deng, G., Duan, X., Jiang, X., 2019. An overall deformation monitoring method of structure based on tracking deformation contour. Appl. Sci. https://doi.org/10.3390/app9214532

Davies, E.R., 2012. Computer and Machine Vision: Theory, Algorithms, Practicalities, Academic Press. https://doi.org/10.1007/978-1-84882-935-0

Design Manual for Roads and Bridges, 2007. Inspection of Highway Structures. Des. Manaul Road Bridg. 3 Section.

Diamond, D.H., Heyns, P.S., Oberholster, A.J., 2017. Accuracy evaluation of sub-pixel structural vibration measurements through optical flow analysis of a video sequence. Measurement 95, 166–172. https://doi.org/10.1016/j.measurement.2016.10.021

Dong, C.-Z., Catbas, F.N., 2020a. A review of computer vision–based structural health monitoring at local and global levels. Struct. Heal. Monit. 147592172093558. https://doi.org/10.1177/1475921720935585

Dong, C.-Z., Catbas, F.N., 2020b. A review of computer CV-based structural health monitoring at local and global levels. Struct. Heal. Monit. 1. https://doi.org/10.1177/1475921720935585

Dong, L., Wang, H., Wang, G., Qiu, W., 2018. A wireless multifunctional monitoring system of tower body running state based on MEMS acceleration sensor, in: 2018 19th International Symposium on Quality Electronic Design (ISQED). Santa Clara, CA, USA.

Duda, R.O., Hart, P.E., 1972. Use of the Hough transformation to detect lines and curves in pictures. Commun. ACM. https://doi.org/10.1145/361237.361242

Dworakowski, Z., Kohut, P., Gallina, A., Holak, K., Uhl, T., 2015. CV-based algorithms for damage detection and localization in structural health monitoring. Struct. Control Heal. Monit. 23, 35–50. https://doi.org/10.1002/stc.1755

Ehrhart, M., Lienhart, W., 2015. Monitoring of Civil Engineering Structures using a State-of-the-art Image Assisted Total Station. J. Appl. Geod. 9, 174–182. https://doi.org/10.1515/jag-2015-0005

Elber, W., 1971. the Significance of Fatigue Crack Closure, in: Damage-Tolerance in Aircraft Structures, ASTM STP 486.

Erdenebat, D., Waldmann, D., 2020. Application of the DAD method for damage localisation on an existing bridge structure using close-range UAV photogrammetry. Eng. Struct. 218, 110727. https://doi.org/10.1016/j.engstruct.2020.110727

Erdenebat, D., Waldmann, D., Scherbaum, F., Teferle, N., 2018. The Deformation Area Difference (DAD) method for condition assessment of reinforced structures. Eng. Struct. 155, 315–329. https://doi.org/10.1016/j.engstruct.2017.11.034

Erdenebat, D., Waldmann, D., Teferle, N., 2019. Curvature based DAD-method for damage localisation under consideration of measurement noise minimisation. Eng. Struct. 181, 293–309. https://doi.org/10.1016/j.engstruct.2018.12.017

Farquharson, F.B., Vincent, G.S., 1949. Aerodynamic stability of suspension bridges with special reference to the Tacoma Narrows Bridge. University of Washington Press, Seattle :

Farrar, C.R., Worden, K., 2007. An introduction to structural health monitoring An introduction to structural health monitoring. Math. Phys. Eng. Sci. 303–315. https://doi.org/10.1098/rsta.2006.1928

Favaro, A., De Salvio, A., Crew, H., 1954. Galileo, Galilei, Dialogues Concerning Two New Sciences. Online Libr. Lib.

Feng, D., Feng, M., Ozer, E., Fukuda, Y., 2015. A CV-based Sensor for Noncontact Structural Displacement Measurement. Sensors 15, 16557–16575. https://doi.org/10.3390/s150716557

Feng, D., Feng, M.Q., 2018. Computer vision for SHM of civil infrastructure: From dynamic response measurement to damage detection – A review. Eng. Struct. https://doi.org/10.1016/j.engstruct.2017.11.018

Feng, D., Feng, M.Q., 2017a. Identification of structural stiffness and excitation forces in time domain using noncontact CV-based displacement measurement. J. Sound Vib. https://doi.org/10.1016/j.jsv.2017.06.008

Feng, D., Feng, M.Q., 2017b. Experimental validation of cost-effective CV-based structural health monitoring. Mech. Syst. Signal Process. 88, 199–211. https://doi.org/10.1016/j.ymssp.2016.11.021

Feng, D., Feng, M.Q., 2016. Output-only damage detection using vehicle-induced displacement response and mode shape curvature index. Struct. Control Heal. Monit. 23, 1088–1107. https://doi.org/10.1002/stc.1829

Feng, D., Feng, M.Q., Ozer, E., Fukuda, Y., 2015b. A CV-based sensor for noncontact structural displacement measurement. Sensors (Switzerland). https://doi.org/10.3390/s150716557

Feng, D., Feng, M.Q., Ozer, E., Fukuda, Y., 2015c. A CV-based Sensor for Noncontact Structural Displacement Measurement. Sensors 15, 16557–16575. https://doi.org/10.3390/s150716557

Feng, D., Feng, M.Q., Ozer, E., Fukuda, Y., 2015d. CV-based multipoint displacement

measurement for structural health monitoring. Sensors 15, 16557–16575. https://doi.org/10.1002/stc.1819

Feng, D., Feng, M.Q., Ozer, E., Fukuda, Y., 2015e. A CV-based sensor for noncontact structural displacement measurement. Sensors (Switzerland) 15, 16557–16575. https://doi.org/10.3390/s150716557

Feng, M., Fukuda, Y., Mizuta, M., Ozer, E., Feng, M., Fukuda, Y., Mizuta, M., Ozer, E., 2015. Citizen Sensors for SHM: Use of Accelerometer Data from Smartphones. Sensors 15, 2980–2998. https://doi.org/10.3390/s150202980

Ferrer, B., Acevedo, P., Espinosa, J., Mas, D., 2015. Targetless image-based method for measuring displacements and strains on concrete surfaces with a consumer camera. Constr. Build. Mater. https://doi.org/10.1016/j.conbuildmat.2014.11.019

Fischler, Martin A., Bolles, R.C., 1981. Random sample consensus: A Paradigm for Model Fitting with Applications to Image Analysis and Automated Cartography. Commun. ACM 24, 381–395. https://doi.org/10.1145/358669.358692

Fischler, Martin A, Bolles, R.C., 1981. Random Sample Consensus: A Paradigm for Model Fitting with Apphcatlons to Image Analysis and Automated Cartography. Commun. ACM 24, 381–395.

Fleet, D.J., Jepson, A.D., 1990. Computation of component image velocity from local phase information. Int. J. Comput. Vis. 5, 77–104. https://doi.org/10.1007/BF00056772

Fukuda, Y., Feng, M.Q., Narita, Y., Kaneko, S., Tanaka, T., 2013. CV-based displacement sensor for monitoring dynamic response using robust object search algorithm. IEEE Sens. J. 13, 4725–4732. https://doi.org/10.1109/JSEN.2013.2273309

Fukuda, Y., Feng, M.Q., Shinozuka, M., 2010. Cost-effective CV-based system for monitoring dynamic response of civil engineering structures. Struct. Control Heal. Monit. https://doi.org/10.1002/stc.360

Gary, B., Kaehler, A., 2009. Learning OpenCV---Computer Vision with the OpenCV Library (Bradski, G.R. et al.; 2008)[On the Shelf]. IEEE Robot. Autom. Mag. https://doi.org/10.1109/MRA.2009.933612

Gauthier, J.F., Whalen, T.M., Liu, J., 2008. Experimental validation of the higher-order derivative discontinuity method for damage identification. Struct. Control Heal. Monit. 15, 143–161. https://doi.org/10.1002/stc.210

Gucunski, N., Romero, F., Kruschwitz, S., Feldmann, R., Abu-Hawash, A., Dunn, M., 2010. Multiple Complementary Nondestructive Evaluation Technologies for Condition

Assessment of Concrete Bridge Decks. Transp. Res. Rec. J. Transp. Res. Board 2201, 34–44. https://doi.org/10.3141/2201-05

Güemes, A., Fernández-López, A., Díaz-Maroto, P.F., Lozano, A., Sierra-Perez, J., 2018. Structural health monitoring in composite structures by fiber-optic sensors. Sensors (Switzerland) 18. https://doi.org/10.3390/s18041094

Guo, J., Zhu, C., 2016. Dynamic displacement measurement of large-scale structures based on the Lucas-Kanade template tracking algorithm. Mech. Syst. Signal Process. 66–67, 425–436. https://doi.org/10.1016/j.ymssp.2015.06.004

Harlow, T., 2018. The Drive: In memoir, survivor recounts I-35W bridge collapse [WWW Document]. StarTribune.com. URL http://www.startribune.com/the-drive-in-memoir-survivor-recounts-i-35w-bridge-collapse/489462371/ (accessed 8.28.18).

Harris, C., Stephens, M., 1988. A Combined Corner and Edge Detector, in: Procedings of the Alvey Vision Conference 1988. pp. 23.1-23.6. https://doi.org/10.5244/c.2.23

Hartley, R., Zisserman, A., 2003. Multiple View Geometry in Computer Vision, Second Edition. Cambridge University Press, Cambridge.

Helfrick, M.N., Niezrecki, C., Avitabile, P., 2009. Curvature methods of damage detection using digital image correlation, in: Proc. SPIE 7295, Health Monitoring of Structural and Biological Systems 2009. p. 72950D. https://doi.org/10.1117/12.815511

Hjelmstad, K.D., Shin, S., 1997. Damage Detection and Assessment of Structures from Static Response. J. Eng. Mech. 123, 568–576. https://doi.org/10.1061/(ASCE)0733-9399(1997)123:6(568)

Ho, Y.-T., Huang, A.-B., Ma, J., Zhang, B., 2005. Ground movement monitoring using an optic fiber Bragg grating sensored system, in: 17th International Conference on Optical Fibre Sensors. SPIE, p. 1020. https://doi.org/10.1117/12.623596

Hong, C.Y., Zhang, Y.F., Zhang, M.X., Leung, L.M.G., Liu, L.Q., 2016. Application of FBG sensors for geotechnical health monitoring, a review of sensor design, implementation methods and packaging techniques. Sensors Actuators, A Phys. https://doi.org/10.1016/j.sna.2016.04.033

Hong, W., Wu, Z., Yang, C., Wu, G., Zhang, Y., 2015. Finite element model updating of flexural structures based on modal parameters extracted from dynamic distributed macro-strain responses. J. Intell. Mater. Syst. Struct. 26, 201–218. https://doi.org/10.1177/1045389X14523856

Imetrum, 2020. Digital Image Correlation [WWW Document].

Jáuregui, D. V., White, K.R., Woodward, C.B., Leitch, K.R., 2003. Noncontact Photogrammetric Measurement of Vertical Bridge Deflection. J. Bridg. Eng. 8, 212–222. https://doi.org/10.1061/(ASCE)1084-0702(2003)8:4(212)

JFTS, 2019. JFTS commissions structural health monitoring solution on Scotland's landmark Queensferry Crossing [WWW Document]. URL http://www.jftesting-services.com/media/case-studies/jfts-commissions-structural-health-monitoring-solution-scotlands-landmark-queensferry-crossing/ (accessed 9.10.19).

Ji, X., Miao, Z., Kromanis, R., 2020. CV-based measurements of deformations and cracks for RC structure tests. Eng. Struct. 212, 110508. https://doi.org/10.1016/j.engstruct.2020.110508

Ji, Y.F., Chang, C.C., 2008. Nontarget Stereo Vision Technique for Spatiotemporal Response Measurement of Line-Like Structures. J. Eng. Mech. 134. https://doi.org/10.1061/ASCE0733-93992008134:6466

Jiang, R., Jáuregui, D. V., White, K.R., 2008. Close-range photogrammetry applications in bridge measurement: Literature review. Meas. J. Int. Meas. Confed. https://doi.org/10.1016/j.measurement.2007.12.005

Ju Lee, B., Hoon Shin, D., Won Seo, J., Deuk Jung, J., Yeong Lee, J., 2011. Intelligent Bridge Inspection Using Remote Controlled Robot and Image Processing Technique.

Khuc, T., Catbas, F.N., 2017a. Computer CV-based displacement and vibration monitoring without using physical target on structures. Struct. Infrastruct. Eng. 13, 505–516. https://doi.org/10.1080/15732479.2016.1164729

Khuc, T., Catbas, F.N., 2017b. Completely contactless structural health monitoring of real-life structures using cameras and computer vision. Struct. Control Heal. Monit. 24, e1852. https://doi.org/10.1002/stc.1852

Khuc, T., Catbas, F.N., 2016. Completely contactless structural health monitoring of real-life structures using cameras and computer vision. Struct. Control Heal. Monit. 24. https://doi.org/10.1002/stc.1852

Kim, S.-W., Jeon, B.-G., Cheung, J.-H., Kim, S.-D., Park, J.-B., 2016. Stay cable tension estimation using a CV-based monitoring system under various weather conditions. Civ. Struct. Heal. Monit. 7, 343–357. https://doi.org/10.1007/s13349-017-0226-7

Kim, S.-W., Kim, N.-S., 2013. Dynamic characteristics of suspension bridge hanger cables using digital image processing. NDT&E Int. 59, 25–33. https://doi.org/10.1016/j.ndteint.2013.05.002

Kim, S.C., Kim, H.K., Lee, C.G., Kim, S.B., 2006. A vision system for identifying structural vibration in civil engineering constructions, in: 2006 SICE-ICASE International Joint Conference. https://doi.org/10.1109/SICE.2006.315227

Kim, S.W., Kim, N.S., 2011. Multi-point displacement response measurement of civil infrastructures using digital image processing, in: Procedia Engineering. https://doi.org/10.1016/j.proeng.2011.07.023

Kong, Q., Allen, R.M., Kohler, M.D., Heaton, T.H., Bunn, J., 2018. Structural Health Monitoring of Buildings Using Smartphone Sensors. Seismol. Res. Lett. 89, 594–602. https://doi.org/10.1785/0220170111

Kromanis, R., 2021. Characterizing Footbridge Response from Cyclist Crossings with Computer CV-based Monitoring, in: Lecture Notes in Civil Engineering. Springer, Cham, pp. 83–95. https://doi.org/10.1007/978-3-030-74258-4_5

Kromanis, R., 2020. Health monitoring of bridges, in: Start-Up Creation. Elsevier, pp. 369–389. https://doi.org/10.1016/b978-0-12-819946-6.00014-x

Kromanis, R., Al-Habaibeh, A., 2017. Low cost CV-based systems using smartphones for measuring deformation in structures for condition monitoring and asset management, in: The 8th International Conference on Structural Health Monitoring of Intelligent Infrastructure.

Kromanis, R., Forbes, C., 2019. A Low-Cost Robotic Camera System for Accurate Collection of Structural Response. Invent. 2019, Vol. 4, Page 47 4, 47. https://doi.org/10.3390/INVENTIONS4030047

Kromanis, R., Kripakaran, P., 2021. A multiple camera position approach for accurate displacement measurement using computer vision. J. Civ. Struct. Heal. Monit. 1–18. https://doi.org/10.1007/s13349-021-00473-0

Kromanis, R., Kripakaran, P., 2014. Predicting thermal response of bridges using regression models derived from measurement histories. Comput. Struct. https://doi.org/10.1016/j.compstruc.2014.01.026

Kromanis, R., Liang, H., 2018. Condition assessment of structures using smartphones : a position independent multi-epoch imaging approach . 9th Eur. Work. Struct. Heal. Monit. July 10-13, 2018, Manchester, UK 1–10.

Kromanis, R., Xu, Y., Lydon, D., Martinez del Rincon, J., Al-Habaibeh, A., 2019. Measuring Structural Deformations in the Laboratory Environment Using Smartphones. Front. Built Environ. 5, 44. https://doi.org/10.3389/fbuil.2019.00044

Lages Martins, L.L., Rebordão, J.M., Silva Ribeiro, A.S., 2015. Structural observation of long-span suspension bridges for safety assessment: Implementation of an optical displacement measurement system, in: Journal of Physics: Conference Series. https://doi.org/10.1088/1742-6596/588/1/012004

Lau, S.L., David, K., 2010. Movement recognition using the accelerometer in smartphones, in: Future Network and Mobile Summit 2010.

Lee, E.-T., Eun, H.-C., 2008. Damage detection of damaged beam by constrained displacement curvature. J. Mech. Sci. Technol. 22, 1111–1120. https://doi.org/10.1007/s12206-008-0310-3

Lee, J.H., Cho, S., Sim, S.H., 2015. Monocular CV-based displacement measurement system robust to angle and distance using homography, in: International Conference on Advances in Experimental Structural Engineering. 6 th International Conference on Advances in Experimental Structural Engineering.

Lee, J.J., Cho, S., Shinozuka, M., 2006. Evaluation of Bridge Load Carrying Capacity Based on Dynamic Displacement Measurement Using Real-time Image Processing Techniques. Steel Struct.

Lee, J.J., Shinozuka, M., 2006. A CV-based system for remote sensing of bridge displacement. NDT&E Int. 39, 425–431. https://doi.org/10.1016/j.ndteint.2005.12.003

Li, Y.Y., 2010. Hypersensitivity of strain-based indicators for structural damage identification: A review. Mech. Syst. Signal Process. https://doi.org/10.1016/j.ymssp.2009.11.002

Liew, K.M., Wang, Q., 1998. Application of Wavelet Theory for Crack Identification in Structures. J. Eng. Mech. 124, 152–157. https://doi.org/10.1061/(ASCE)0733-9399(1998)124:2(152)

Lowe, D.G., 2004. Distinctive image features from scale-invariant keypoints. Int. J. Comput. Vis. 60, 91–110. https://doi.org/10.1023/B:VISI.0000029664.99615.94

Lowe, D.G., 1999. Object recognition from local scale-invariant features, in: Proceedings of the Seventh IEEE International Conference on Computer Vision. https://doi.org/10.1109/ICCV.1999.790410

Lucas, B.D., Kanade, T., 1981. An iterative image registration technique with an application to stereo vision. Int. Jt. Conf. Artif. Intell. https://doi.org/Doi 10.1145/358669.358692

Luo, L., Feng, M.Q., Wu, Z.Y., 2018. Robust vision sensor for multi-point displacement monitoring of bridges in the field. Eng. Struct.

https://doi.org/10.1016/j.engstruct.2018.02.014

Lydon, D., Lydon, M., Del Rincon, J.M., Taylor, S.E., Robinson, D., O'Brien, E., Catbas, F.N., 2018. Development and field testing of a time-synchronized system for multi-point displacement calculation using low-cost wireless CV-based sensors. IEEE Sens. J. 18, 9744–9754. https://doi.org/10.1109/JSEN.2018.2853646

Lydon, D., Lydon, M., Taylor, S., Del Rincon, J.M., Hester, D., Brownjohn, J., 2019. Development and field testing of a CV-based displacement system using a low cost wireless action camera. Mech. Syst. Signal Process. 121, 343–358. https://doi.org/10.1016/j.ymssp.2018.11.015

Macdonald, J.H.G., Dagless, E.L., Thomas, B.T., Taylor, C.A., 1997. Dynamic Measurements of the Second Severn Crossing. Proc. Inst. Civ. Eng. - Transp. 123, 241–248. https://doi.org/10.1680/itran.1997.29978

Mahal, M., Blanksvärd, T., Täljsten, B., Sas, G., 2015. Using digital image correlation to evaluate fatigue behavior of strengthened reinforced concrete beams. Eng. Struct. 105, 277–288. https://doi.org/10.1016/j.engstruct.2015.10.017

Marecos, J., Castanheta, M., Trigo, J.T., 1969. Field Observation of Tagus River Suspension Bridge. J. Struct. Div. 95, 555–583.

Mark, J., Brownjohn, W., Moyo, P., Omenzetter, ; Piotr, Lu, Y., 2001. Assessment of Highway Bridge Upgrading by Dynamic Testing and Finite-Element Model Updating. J. Bridg. Eng. 8. https://doi.org/10.1061/ASCE1084-070220038:3162

Matas, J., Chum, O., Urban, M., Pajdla, T., 2004. Robust wide-baseline stereo from maximally stable extremal regions, in: Image and Vision Computing. https://doi.org/10.1016/j.imavis.2004.02.006

MathWorks, 2018. Computer Vision System Toolbox: User's Guide (R2018b) [WWW Document]. URL https://uk.mathworks.com/help/images/ref/imfindcircles.html#bti4sim (accessed 10.9.18).

Morgan, B.J., Oesterle, R.G., 1994. On-site modal analysis - a new powerful inspectoin technique, in: 2nd International Bridge Conference. Pittsburg, Pennysylvania, pp. 108–114.

Morgenthal, G., Höpfner, H., 2012. The application of smartphones to measuring transient structural displacements. Civ. Struct. Heal. Monit. 2, 149–161. https://doi.org/10.1007/s13349-012-0025-0

Obiechefu, C.B., Kromanis, R., 2021. Damage detection techniques for structural health

monitoring of bridges from computer vision derived parameters. Struct. Monit. Maint. 8, 91–110. https://doi.org/10.12989/smm.2021.8.1.091

Obiechefu, C.B., Kromanis, R., Mohammad, F., Arab, Z., 2021. CV-based damage detection using inclination angles and curvature, in: The 8th Workshop on Civil Structural Health Monitoring. Lecture Notes in Civil Engineering.

Oh, B.K., Hwang, J.W., Kim, Y., Cho, T., Park, H.S., 2015. CV-based system identification technique for building structures using a motion capture system. J. Sound Vib. 356, 72–85. https://doi.org/10.1016/j.jsv.2015.07.011

Oraczewski, T., Staszewski, W.J., Uhl, T., 2016. Nonlinear acoustics for structural health monitoring using mobile, wireless and smartphone-based transducer platform. J. Intell. Mater. Syst. Struct. 27, 786–796. https://doi.org/10.1177/1045389X15585902

Osborne, S., 2018. CCTV footage shows Genoa bridge collapse [WWW Document]. Indep. URL https://www.independent.co.uk/news/world/europe/genoa-bridge-collapse-video-cctv-footage-italy-a8500606.html (accessed 8.28.18).

Pan, B., Qian, K., Xie, H., Asundi, A., 2009a. Two-dimensional digital image correlation for in-plane displacement and strain measurement: A review. Meas. Sci. Technol. https://doi.org/10.1088/0957-0233/20/6/062001

Pan, B., Qian, K., Xie, H., Asundi, A., 2009b. Two-dimensional digital image correlation for in-plane displacement and strain measurement: a review. Meas. Sci. Technol. 20. https://doi.org/10.1088/0957-0233/20/6/062001

Pandey, A.K., Biswas, M., Samman, M.M., 1991. Damage detection from changes in curvature mode shapes. J. Sound Vib. 145, 321–332. https://doi.org/10.1016/0022-460X(91)90595-B

Park, C., Ho, H.-N., Jo, B.-W., Lee, J.-J., Lee, -J, 2014. An Efficient CV-based Three-Dimensional Motion Measurement System for Civil Infra-Structures. https://doi.org/10.1007/s40799-016-006

Park, S.W., Park, H.S., Kim, J.H., Adeli, H., 2015. 3D displacement measurement model for health monitoring of structures using a motion capture system. Meas. J. Int. Meas. Confed. 59, 352–362. https://doi.org/10.1016/j.measurement.2014.09.063

Pastor, M., Binda, M., Harčarik, T., 2012. Modal Assurance Criterion. Procedia Eng. 48, 543–548. https://doi.org/10.1016/J.PROENG.2012.09.551

Patterson, T., 2010. Is this the “safest bridge in America?” [WWW Document]. CNN.com. URL

http://edition.cnn.com/2010/TECH/innovation/07/30/minneapolis.bridge.sensors/index.html (accessed 8.28.18).

Pei, H., Cui, P., Yin, J., Zhu, H., Chen, X., Pei, L., Xu, D., 2011. Monitoring and warning of landslides and debris flows using an optical fiber sensor technology. J. Mt. Sci. 8, 728–738. https://doi.org/10.1007/s11629-011-2038-2

Peng, B.-J., Zhao, Yong, Zhao, Yan, Yang, J., 2006. Tilt Sensor With FBG Technology and Matched FBG Demodulating Method. IEEE Sens. J. 6, 63. https://doi.org/10.1109/JSEN.2005.845198

Potter, K.D., Setchell, C., 2014. Positional measurement of a feature within an image. US 8,718,403 B2.

RAC Foundation, 2020. Bridge maintenance backlog remains static [WWW Document]. RAC Found. URL https://www.racfoundation.org/research/economy/number-of-substandard-road-bridges (accessed 11.21.20).

RAC Foundation, 2017. Substandard road bridges [WWW Document]. URL https://www.racfoundation.org/research/economy/substandard-road-bridges-foi-2017 (accessed 7.25.18).

Ren, P., Zhou, Z., 2013. A Review on Strain Based Damage Detection Strategies for Structural Health Monitoring. Pac. Sci. Rev 15, 1–7.

Ribeiro, D., Calçada, R., Ferreira, J., Martins, T., 2014. Non-contact measurement of the dynamic displacement of railway bridges using an advanced video-based system. Eng. Struct. https://doi.org/10.1016/j.engstruct.2014.04.051

Rosten, E., Drummond, T., 2006. Machine Learning for High Speed Corner Detection. Comput. Vis. -- ECCV 2006. https://doi.org/10.1007/11744023_34

Rousseeuw, P.J., 1984. Least Median of Squares Regression. J. Am. Stat. Assoc. 79, 871–880. https://doi.org/10.1080/01621459.1984.10477105

Rublee, E., Rabaud, V., Konolige, K., Bradski, G., 2011. ORB: An efficient alternative to SIFT or SURF, in: Proceedings of the IEEE International Conference on Computer Vision. pp. 2564–2571. https://doi.org/10.1109/ICCV.2011.6126544

Salgado, R., Cruz, P.J.., Ramos, L.., Lourenco, P.., 2006. Comparison between damage detection methods applied to beam structures, in: CRUZ, Paulo J. S. FRANFOPOL, D.M., Neves, Luis, C. (Eds.), Bridge Mainetance, Safety, Management, Life-Cycle, Performance and Cost : Proceedings of the International Conference on Bridge Maintenance, Safety and Management. Porto.

Sansalone, M., Carino, N.J., 1986. Impact-Echo: a method for flaw detection in concrete using transient stress waves. NBSIR 86-3452, Natl. Bur. Stand. Sept. 222. https://doi.org/NBSIR 86-3452

Saul, E., 2017. Scotland's new Queensferry Crossing reveals how smart technologies monitor and maintain the health of bridges [WWW Document]. Conversat. URL https://theconversation.com/scotlands-new-queensferry-crossing-reveals-how-smart-technologies-monitor-and-maintain-the-health-of-bridges-85867 (accessed 8.28.18).

Shan, B., Zheng, S., Ou, J., 2015. Free vibration monitoring experiment of a stayed-cable model based on stereovision. Measurement 76, 228–239.

Shi, J., Tomasi, C., 1994. Good Features to Track, in: IEEE Conference on Computer and Pattern Recognition. IEEE Computer Society Press, Seattle, pp. 593–600.

Shokouhi, P., Gukunski, N., Maher, A., 2006. Time–frequency techniques for the impact-echo data analysis and interpretations, in: Proceedings of the 9th European NDT Conference (ECNDT). Berlin.

Shrestha, A., Dang, J., Wang, X., 2018. Development of a smart-device-based vibration-measurement system: Effectiveness examination and application cases to existing structure. Struct. Control Heal. Monit. 25. https://doi.org/10.1002/stc.2120

Sładek, J., Ostrowska, K., Kohut, P., Holak, K., Ga ˛ Ska B, A., Uhl, T., Gaska, A., Uhl, T., 2013. Development of a vision based deflection measurement system and its accuracy assessment. Measurement 46, 1237–1249. https://doi.org/10.1016/j.measurement.2012.10.021

Song, Y.-Z., Bowen, C.R., Kim, A.H., Nassehi, A., Padget, J., Gathercole, N., 2014. Virtual visual sensors and their application in structural health monitoring. Struct. Heal. Monit. 13, 251–264. https://doi.org/10.1177/1475921714522841

Sony, S., Laventure, S., Sadhu, A., 2019. A literature review of next-generation smart sensing technology in structural health monitoring. Struct Control Heal. Monit 26, 2321. https://doi.org/10.1002/stc.2321

Stephen, G.A., Brownjohn, J.M.W., Taylor, C.A., 1993. Measurements of static and dynamic displacement from visual monitoring of the Humber Bridge, Engineering Structures. https://doi.org/10.1016/0141-0296(93)90054-8

Stubbs, N., Kim, J.-T., Farrar, C., 1995. Field Verification of a Nondestructive Damage Localization and Severity Estimation Algorithm.

Sun, Z., Nagayama, T., Nishio, | Mayuko, Fujino, Y., 2017. Investigation on a curvature-

based damage detection method using displacement under moving vehicle. https://doi.org/10.1002/stc.2044

Sutton, M.A., Orteu, J.J., Schreier, H.W., 2009. Image Correlation for Shape, Motion and Deformation Measurements- Basic Concepts, Theory and Applications. Image Rochester NY. https://doi.org/10.1007/978-0-387-78747-3

Szeliski, R., 2011. Computer vision: algorithms and applications. Springer Science & Business Media, London.

The Mathworks Inc., 2016. MATLAB - MathWorks [WWW Document]. www.mathworks.com/products/matlab. https://doi.org/2016-11-26

The MathWorks Inc., 2021. MATLAB.

The MathWorks Inc., 2013. Computer Vision System Toolbox. (Mathworks) http://www.mathworks.com/products/computer-vision/. https://doi.org/10.1111/j.1365-2958.2006.05098.x

Tomasi, C., Kanade, T., 1991. Detection and Tracking of Point Features. Sch. Comput. Sci. Carnegie Mellon Univ. https://doi.org/10.1016/S0031-3203(03)00234-6

Transport for London, 2011. Hammersmith flyover to remain closed next week - Transport for London [WWW Document]. URL https://tfl.gov.uk/info-for/media/press-releases/2011/december/hammersmith-flyover-to-remain-closed-next-week (accessed 8.3.18).

Voordijk, H., Kromanis, R., 2022. Technological mediation and civil structure condition assessment: the case of CV-based systems. Civ. Eng. Environ. Syst. https://doi.org/10.1080/10286608.2022.2030318

Wahbeh, A.M., Caffrey, J.P., Masri, S.F., 2003. A CV-based approach for the direct measurement of displacements in vibrating systems. Smart Mater. Struct. 12, 785–794. https://doi.org/10.1088/0964-1726/12/5/016

Wang, L., Spencer, B.F., Li, J., Hu, P., 2021. A fast image-stitching algorithm for characterization of cracks in large-scale structures. Smart Struct. Syst. 27, 593–605. https://doi.org/10.12989/SSS.2021.27.4.593

Wang, Y.L., Shi, B., Zhang, T.L., Zhu, H.H., Jie, Q., Sun, Q., 2015. Introduction to an FBG-based inclinometer and its application to landslide monitoring. J. Civ. Struct. Heal. Monit. 5, 645–653. https://doi.org/10.1007/s13349-015-0129-4

Wong, K., Lau, C.K., Flint, A.R., 2000. Planning and implementation of the structural health

monitoring system for cable-supported bridges in Hong Kong, in: Aktan, A.E., Gosselin, S.R. (Eds.), . International Society for Optics and Photonics, pp. 266–275. https://doi.org/10.1117/12.387819

Wu, L.-J., Casciati, F., Casciati, S., 2014. Dynamic testing of a laboratory model via CV-based sensing. Eng. Struct. 60, 113–125. https://doi.org/10.1016/j.engstruct.2013.12.002

Xiao, F., Hulsey, J.L., Balasubramanian, R., 2017. Fiber optic health monitoring and temperature behavior of bridge in cold region. Struct. Control Heal. Monit. 24, 2020. https://doi.org/10.1002/stc.2020

Xu, Y., Brownjohn, J., Hester, D., Koo, K.Y., 2016. Dynamic displacement measurement of a long span bridge using CV-based system, in: 8th European Workshop On Structural Health Monitoring (EWSHM 2016), 5-8 July 2016, Spain, Bilbao.

Xu, Yan, Brownjohn, J., Kong, D., 2018. A non-contact CV-based system for multipoint displacement monitoring in a cable-stayed footbridge. https://doi.org/10.1002/stc.2155

Xu, Y., Brownjohn, J.M.W., 2018. Review of machine-vision based methodologies for displacement measurement in civil structures. J. Civ. Struct. Heal. Monit. 8, 91–110. https://doi.org/10.1007/s13349-017-0261-4

Xu, Yang, Li, S., Zhang, D., Jin, Y., Zhang, F., Li, N., Li, H., 2018. Identification framework for cracks on a steel structure surface by a restricted Boltzmann machines algorithm based on consumer-grade camera images. Struct Control Heal. Monit 25, 2075. https://doi.org/10.1002/stc.2075

Yang, Y., Dorn, C., Mancini, T., Talken, Z., Kenyon, G., Farrar, C., Mascareñas, D., 2017. Blind identification of full-field vibration modes from video measurements with phase-based video motion magnification. Mech. Syst. Signal Process. https://doi.org/10.1016/j.ymssp.2016.08.041

Ye, X.W., Ni, Y.Q., Wai, T.T., Wong, K.Y., Zhang, X.M., Xu, F., 2013. A CV-based system for dynamic displacement measurement of long-span bridges: Algorithm and verification. Smart Struct. Syst. https://doi.org/10.12989/sss.2013.12.3-4.363

Yoneyama, S., Kitagawa, A., Iwata, S., Tani, K., Kikuta, H., 2007. Bridge deflection measurement using digital image correlation. Exp. Tech. https://doi.org/10.1111/j.1747-1567.2006.00132.x

Yoneyama, S., Ueda, H., 2012. Bridge deflection measurement using digital image correlation with camera movement correction, in: Materials Transactions. pp. 285–290.

https://doi.org/10.2320/matertrans.I-M2011843

Yoon, H., Elanwar, H., Choi, H., Golparvar-Fard, M., Spencer, B.F., 2016. Target-free approach for CV-based structural system identification using consumer-grade cameras. Struct. Control Heal. Monit. 23, 1405–1416. https://doi.org/10.1002/stc.1850

Yuen, H., Princen, J., Illingworth, J., Kittler, J., 1990. Comparative study of Hough Transform methods for circle finding. Image Vis. Comput. https://doi.org/10.1016/0262-8856(90)90059-E

Zasso, A., Vergani, M., Bocciolone, M., Evans, R., 1993. Use of a newly designed optometric instrument for long-term, long distance monitoring of structures, with an example of its application on the Humber Bridge, in: Second International Conference on Bridge Management. University of Surrey, UK., pp. 18–21.

Zaurin, R., Catbas, F.N., 2010. Integration of computer imaging and sensor data for structural health monitoring of bridges. Smart Mater. Struct. https://doi.org/10.1088/0964-1726/19/1/015019

Zhang, J.K., Yan, W., Cui, D.M., 2016. Concrete condition assessment using impact-echo method and extreme learning machines. Sensors (Switzerland) 16. https://doi.org/10.3390/s16040447

Zhang, Z., 2000a. A flexible new technique for camera calibration. IEEE Trans. Pattern Anal. Mach. Intell. https://doi.org/10.1109/34.888718

Zhang, Z., 2000b. A Flexible New Technique for Camera Calibration. IEEE Trans. Pattern Anal. Mach. Intell. 22, 1330–1334.

Zhao, X., Han, R., Ding, Y., Yu, Y., Guan, Q., Hu, W., Li, M., Ou, J., 2015. Portable and convenient cable force measurement using smartphone. J. Civ. Struct. Heal. Monit. 5, 481–491. https://doi.org/10.1007/s13349-015-0132-9

Zhao, X., Han, R., Yu, Y., Hu, W., Jiao, D., Mao, X., Li, M., Ou, J., 2016a. Smartphone-Based Mobile Testing Technique for Quick Bridge Cable-Force Measurement. https://doi.org/10.1061/(ASCE)

Zhao, X., Liu, H., Yu, Y., Zhu, Q., Hu, W., Li, M., Ou, J., 2016b. Displacement monitoring technique using a smartphone based on the laser projection-sensing method. Sensors and Actuators 246, 35–47. https://doi.org/10.1016/j.sna.2016.05.012

Zhao, X., Zhao, Q., Yu, Y., Chen, Y., Liu, H., Li, M., Ou, J., 2017. Distributed Displacement Response Investigation Technique for Bridge Structures Using Smartphones. J. Perform. Constr. Facil. 31. https://doi.org/10.1061/(ASCE)CF.1943-5509.0001025

Zhu, H.P., He, B., Chen, X.Q., 2005. Detection of structural damage through changes in frequency. Wuhan Univ. J. Nat. Sci. 10, 1069–1073. https://doi.org/10.1007/BF02832469

APPENDICES

Appendix A: Numerical model script (Ansys Parametric Design Language (APDL) Program written on txt file)

Notes: Here is a copy of the main computer script used for the numerical model validation. It is written on a text file using APDL language. Brief comments are given for relevant commands, indicated by the '!' sign.

Within this script one other supporting script, as well as some files are called using the '/input' command. The supporting script is named 'LoadsMovingTest3**',** it is also an APDL script which specifies and controls the tram loading action. It is provided as Appendix A2 just after this.

Supporting files are excel sheets (.xls files) in which the geometry of the girder, including the variants simulating various damage scenarios, are specified using nodes and elements. These supporting files are not reproduced here due to volume

*** *** *** *** *** *** *** *** *** *** *** ***

```
! Static bridge moving vehicle test
! Brendan Obiechefu!
UNITS:N,mm,MPa!*************************************************************************!*****************************************************************
!       1.
INITIALIZATION!*************************************************************************
FINISH
/CLEAR,all
/TITLE,Static beam test
/UNITS,USER,1E-3
/NERR,,99999999
/GRAPHICS,FULL              ! To turn on Full Model display
```

```
!*****************************************************************************
!       2. PREPROCESSOR
FINISH/PREP7SELTOL,1E-8                                 !Entity selection tolerance
!*****************************************************************************
!       2.1 Parameters
Ex_RC =     35*1000             !Mpa        !Elastic Modulus of Concrete
Ex_damage = 28000  !31500 !21000 !MPa damaged       !Damaged elements
        !*****************************************************************************
!       2.2 Material
!*****************************************************************************
!Material type 1 -> for concrete element     MAT, 1
            MP,EX,1,Ex_RC !MPa                          !Young's modulus
        MP,NUXY,1,0.15                              !Poisson ratio
        MP,DENS,1,2.4E-6                        !Density
MP,ALPX,1,                                  !Thermal expansion - in all directions
        MP,ALPY,1,  MP,ALPZ,1,  MP,REFT,1,10
        ! Reference temperature!Material type 2 -> for concrete element
MAT, 2
MP,EX,2,Ex_damage !MPa
!Young's modulus
MP,NUXY,2,0.15                              !Poisson ratio  MP,DENS,2,2.4E-6
        !Density
MP,ALPX,2,                                  !Thermal expansion - in all directions
        MP,ALPY,2,  MP,ALPZ,2,  MP,REFT,2,10
        !*****************************************************************************
!       2.3                                 Element                             type
        !*****************************************************************************
!Element 1 [timber]
```

```
ET,1,PLANE183      !,,,3,,,1,1 (could be used instead of keyopt)  !      2D      8-NODE
STRUCTURAL SOLID

keyopt,1,3,3                    ! Keyoption for element thickness. Keyopt, Number, KNum
(Element behaviour - 3), Value (3 for plane stress with thickness)   !keyopt,1,6,1
        ! sets the element for using mixed formulation        THK = 400                    !
Thickness      R,1,THK                              ! R (defines element real constatnts),
NSET   (ID   number   -   1),   Real   constants   (keyopt   =   3,   so   =   THK)
        !*************************************************************************


!       2.4 Geometry!*************************************************************************
        !       2.4.1 Nodes and elements
        !************************************************************************
        /input,Nodes,txt                ! Nodes
        /input,ElementsDamage1&2&3,txt              ! Elements
!************************************************************************


!                       2.5                       Boundary                       conditions
        !************************************************************************
        AllSEL,all

D,1,UX,,,,,UY  ! Pinned support at left end

D,101,UY,,,    ! Roller support at right end

ALLSEL,ALL/eshape,1EPLOTFINISH

 /SOLU

!************************************************************************

!       Static!*************************************************************************
ANTYPE,STATIC               ! Analysis type

OUTRES, ALL,ALL             ! Controls the solution data written !F,1551,FY,-83000
        ! Point load at midpoint!NSEL,S,NODE,,51   !ACEL,0,9.81

! Acceleration

ACEL, ACEL_X, ACEL_Y, ACEL_Z!NSEL, ALL              !  Activate  all  nodes!ESEL,
ALL!SOLVE!ENDDOACEL,,9.81,0             ! Acceleration
```

```
ACEL, ACEL_X, ACEL_Y, ACEL_Z

!*****************************************************************

AXEL1ON = 1AXEL2ON = 30 AXEL3ON = 41INCR = 1ALLNODES = 101!101STEPSALL
= ALLNODES + AXEL3ON          ! THESE ARE ALL LOAD STEPSAXLE1OFF =
STEPSALL-AXEL3ON OFF02 = ALLNODES + AXEL2ON  !STEPSALL-
AXEL2ONAXLE3OFF                    =                    STEPSALL
!*****************************************************************

/input,LoadsMovingTest3,txt          !Nodes FINISH

!*****************************************************************

/POST1INRES,ALL                      ! Identifies the data to be retrieved from the results file

!

*GET,DISP,NODE,0,COUNT!              X and Y disps for array 1 (nodes 1 to 18)

*dim,datay,array,STEPSALL,18         !19 is max no of cols allowable in ansys

*dim,datax,array,STEPSALL,18

*DO,I,1,STEPSALL,1 SET,I

*DO,K,1,18,1

*GET,DISPL,NODE,1+(K-1),U,Y          ! Get Z displacement from specified nodes
        DATAY(I,K-0) = DISPL

*ENDDO

*ENDDO


*DO,I,1,STEPSALL/INCR,1   SET,I

*DO,K,1,18,1

*GET,DISPL,NODE,1+(K-1),U,X          ! Get Z displacement from specified nodes
        DATAX(I,K-0) = DISPL

*ENDDO

*ENDDO        !        X and Y disps for array 2 (nodes 19 to 36)

*dim,DATA2y,array,STEPSALL/INCR,18
```

```
*dim,DATA2x,array,STEPSALL/INCR,18

*DO,I,1,STEPSALL/INCR,1    SET,I

*DO,K,19,36,1

*GET,DISPL,NODE,1+(K-1),U,Y       ! Get Z displacement from specified nodes
        DATA2Y(I,K-18) = DISPL

*ENDDO

*ENDDO

*DO,I,1,STEPSALL/INCR,1    SET,I

*DO,K,19,36,1

*GET,DISPL,NODE,1+(K-1),U,X       ! Get Z displacement from specified nodes
        DATA2X(I,K-18) = DISPL

*ENDDO

*ENDDO        !        X and Y disps for array 3 (nodes 37 to 54)

*dim,data3y,array,STEPSALL/INCR,18

*dim,data3x,array,STEPSALL/INCR,18

*DO,I,1,STEPSALL/INCR,1    SET,I

*DO,K,37,54,1

*GET,DISPL,NODE,1+(K-1),U,Y       ! Get Z displacement from specified nodes
        DATA3Y(I,K-36) = DISPL

*ENDDO

*ENDDO

*DO,I,1,STEPSALL/INCR,1    SET,I

*DO,K,37,54,1

*GET,DISPL,NODE,1+(K-1),U,X       ! Get Z displacement from specified nodes
        DATA3X(I,K-36) = DISPL

*ENDDO

*ENDDO!        X and Y disps for array 4 (nodes 55 to 72)

*dim,data4y,array,STEPSALL/INCR,18
```

```
*dim,data4x,array,STEPSALL/INCR,18

*DO,I,1,STEPSALL/INCR,1    SET,I

*DO,K,55,72,1

*GET,DISPL,NODE,1+(K-1),U,Y       ! Get Z displacement from specified nodes
        DATA4Y(I,K-54) = DISPL

*ENDDO

*ENDDO

*DO,I,1,STEPSALL/INCR,1    SET,I

*DO,K,55,72,1

*GET,DISPL,NODE,1+(K-1),U,X       ! Get Z displacement from specified nodes
        DATA4X(I,K-54) = DISPL

*ENDDO

*ENDDO!        X and Y disps for array 5 (nodes 73 to 90)

*dim,data5y,array,STEPSALL/INCR,18

*dim,data5x,array,STEPSALL/INCR,18

*DO,I,1,STEPSALL/INCR,1    SET,I

*DO,K,73,90,1

*GET,DISPL,NODE,1+(K-1),U,Y       ! Get Z displacement from specified nodes
        DATA5Y(I,K-72) = DISPL                *ENDDO        *ENDDO

*DO,I,1,STEPSALL/INCR,1    SET,I

*DO,K,73,90,1

*GET,DISPL,NODE,1+(K-1),U,X       ! Get Z displacement from specified nodes
        DATA5X(I,K-72) = DISPL

*ENDDO

*ENDDO!        X and Y disps for array 6 (nodes 91 to 101)

*dim,data6y,array,STEPSALL/INCR,11

*dim,data6x,array,STEPSALL/INCR,11

*DO,I,1,STEPSALL/INCR,1    SET,I
```

```
*DO,K,91,101,1

*GET,DISPL,NODE,1+(K-1),U,Y       ! Get Z displacement from specified nodes
        DATA6Y(I,K-90) = DISPL

*ENDDO

*ENDDO

*DO,I,1,STEPSALL/INCR,1   SET,I

*DO,K,91,101,1

*GET,DISPL,NODE,1+(K-1),U,X       ! Get Z displacement from specified nodes
        DATA6X(I,K-90) = DISPL

*ENDDO

*ENDDO

!Ydisplacements

/OUTPUT,bridgeDisplacementsY,dat,,*vwrite,datay(1,1),datay(1,2),datay(1,3),datay(1,4),d
atay(1,5),datay(1,6),datay(1,7),datay(1,8),datay(1,9),datay(1,10),datay(1,11),datay(1,12),d
atay(1,13),datay(1,14),datay(1,15),datay(1,16),datay(1,17),datay(1,18)(e16.8,1x,e16.8,1x,
e16.8,1x,e16.8,1x,e16.8,1x,e16.8,1x,e16.8,1x,e16.8,1x,e16.8,1x,e16.8,1x,e16.8,1x,e16.8,
1x,e16.8,1x,e16.8,1x,e16.8,1x,e16.8,1x,e16.8,1x,e16.8)/output/OUTPUT,bridgeDisplacem
ents2y,dat,,*vwrite,data2y(1,1),data2y(1,2),data2y(1,3),data2y(1,4),data2y(1,5),data2y(1,6
),data2y(1,7),data2y(1,8),data2y(1,9),data2y(1,10),data2y(1,11),data2y(1,12),data2y(1,13)
,data2y(1,14),data2y(1,15),data2y(1,16),data2y(1,17),data2y(1,18)(e16.8,1x,e16.8,1x,e16
.8,1x,e16.8,1x,e16.8,1x,e16.8,1x,e16.8,1x,e16.8,1x,e16.8,1x,e16.8,1x,e16.8,1x,e16.8,1x,
e16.8,1x,e16.8,1x,e16.8,1x,e16.8,1x,e16.8,1x,e16.8)/output/OUTPUT,bridgeDisplacemen
ts3y,dat,,*vwrite,data3y(1,1),data3y(1,2),data3y(1,3),data3y(1,4),data3y(1,5),data3y(1,6),d
ata3y(1,7),data3y(1,8),data3y(1,9),data3y(1,10),data3y(1,11),data3y(1,12),data3y(1,13),d
ata3y(1,14),data3y(1,15),data3y(1,16),data3y(1,17),data3y(1,18)(e16.8,1x,e16.8,1x,e16.8
,1x,e16.8,1x,e16.8,1x,e16.8,1x,e16.8,1x,e16.8,1x,e16.8,1x,e16.8,1x,e16.8,1x,e16.8,1x,e1
6.8,1x,e16.8,1x,e16.8,1x,e16.8,1x,e16.8,1x,e16.8)/output/OUTPUT,bridgeDisplacements4
y,dat,,*vwrite,data4y(1,1),data4y(1,2),data4y(1,3),data4y(1,4),data4y(1,5),data4y(1,6),dat
a4y(1,7),data4y(1,8),data4y(1,9),data4y(1,10),data4y(1,11),data4y(1,12),data4y(1,13),dat
a4y(1,14),data4y(1,15),data4y(1,16),data4y(1,17),data4y(1,18)(e16.8,1x,e16.8,1x,e16.8,1
x,e16.8,1x,e16.8,1x,e16.8,1x,e16.8,1x,e16.8,1x,e16.8,1x,e16.8,1x,e16.8,1x,e16.8,1x,e16.
8,1x,e16.8,1x,e16.8,1x,e16.8,1x,e16.8,1x,e16.8)/output/OUTPUT,bridgeDisplacements5y,
dat,,*vwrite,data5y(1,1),data5y(1,2),data5y(1,3),data5y(1,4),data5y(1,5),data5y(1,6),data5
```

y(1,7),data5y(1,8),data5y(1,9),data5y(1,10),data5y(1,11),data5y(1,12),data5y(1,13),data5y(1,14),data5y(1,15),data5y(1,16),data5y(1,17),data5y(1,18)(e16.8,1x,e16.8,1x,e16.8,1x,e16.8,1x,e16.8,1x,e16.8,1x,e16.8,1x,e16.8,1x,e16.8,1x,e16.8,1x,e16.8,1x,e16.8,1x,e16.8,1x,e16.8,1x,e16.8,1x,e16.8,1x,e16.8,1x,e16.8,1x,e16.8)/output/OUTPUT,bridgeDisplacements6y,dat,,*vwrite,data6y(1,1),data6y(1,2),data6y(1,3),data6y(1,4),data6y(1,5),data6y(1,6),data6y(1,7),data6y(1,8),data6y(1,9),data6y(1,10),data6y(1,11)!,data6y(1,12),data6y(1,13),data6y(1,14),data6y(1,15),data6y(1,16),data6y(1,17),data6y(1,18)(e16.8,1x,e16.8,1x,e16.8,1x,e16.8,1x,e16.8,1x,e16.8,1x,e16.8,1x,e16.8,1x,e16.8,1x,e16.8,1x,e16.8,1x,e16.8,1x,e16.8,1x,e16.8,1x,e16.8,1x,e16.8,1x,e16.8,1x,e16.8,1x,e16.8,1x,e16.8)!,1x,e16.8,1x,e16.8,1x,e16.8,1x,e16.8,1x,e16.8,1x,e16.8,1x,e16.8,1x,e16.8,1x,e16.8)/output

!Xdisplacements

/OUTPUT,bridgeDisplacementsX,dat,,*vwrite,datax(1,1),datax(1,2),datax(1,3),datax(1,4),datax(1,5),datax(1,6),datax(1,7),datax(1,8),datax(1,9),datax(1,10),datax(1,11),datax(1,12),datax(1,13),datax(1,14),datax(1,15),datax(1,16),datax(1,17),datax(1,18)(e16.8,1x,e16.8,1x,e16.8,1x,e16.8,1x,e16.8,1x,e16.8,1x,e16.8,1x,e16.8,1x,e16.8,1x,e16.8,1x,e16.8,1x,e16.8,1x,e16.8,1x,e16.8,1x,e16.8,1x,e16.8,1x,e16.8,1x,e16.8,1x,e16.8)/output/OUTPUT,bridgeDisplacements2x,dat,,*vwrite,data2x(1,1),data2x(1,2),data2x(1,3),data2x(1,4),data2x(1,5),data2x(1,6),data2x(1,7),data2x(1,8),data2x(1,9),data2x(1,10),data2x(1,11),data2x(1,12),data2x(1,13),data2x(1,14),data2x(1,15),data2x(1,16),data2x(1,17),data2x(1,18)(e16.8,1x,e16.8,1x,e16.8,1x,e16.8,1x,e16.8,1x,e16.8,1x,e16.8,1x,e16.8,1x,e16.8,1x,e16.8,1x,e16.8,1x,e16.8,1x,e16.8,1x,e16.8,1x,e16.8,1x,e16.8,1x,e16.8,1x,e16.8,1x,e16.8)/output/OUTPUT,bridgeDisplacements3x,dat,,*vwrite,data3x(1,1),data3x(1,2),data3x(1,3),data3x(1,4),data3x(1,5),data3x(1,6),data3x(1,7),data3x(1,8),data3x(1,9),data3x(1,10),data3x(1,11),data3x(1,12),data3x(1,13),data3x(1,14),data3x(1,15),data3x(1,16),data3x(1,17),data3x(1,18)(e16.8,1x,e16.8,1x,e16.8,1x,e16.8,1x,e16.8,1x,e16.8,1x,e16.8,1x,e16.8,1x,e16.8,1x,e16.8,1x,e16.8,1x,e16.8,1x,e16.8,1x,e16.8,1x,e16.8,1x,e16.8,1x,e16.8,1x,e16.8,1x,e16.8)/output/OUTPUT,bridgeDisplacements4x,dat,,*vwrite,data4x(1,1),data4x(1,2),data4x(1,3),data4x(1,4),data4x(1,5),data4x(1,6),data4x(1,7),data4x(1,8),data4x(1,9),data4x(1,10),data4x(1,11),data4x(1,12),data4x(1,13),data4x(1,14),data4x(1,15),data4x(1,16),data4x(1,17),data4x(1,18)(e16.8,1x,e16.8,1x,e16.8,1x,e16.8,1x,e16.8,1x,e16.8,1x,e16.8,1x,e16.8,1x,e16.8,1x,e16.8,1x,e16.8,1x,e16.8,1x,e16.8,1x,e16.8,1x,e16.8,1x,e16.8,1x,e16.8,1x,e16.8,1x,e16.8)/output/OUTPUT,bridgeDisplacements5x,dat,,*vwrite,data5x(1,1),data5x(1,2),data5x(1,3),data5x(1,4),data5x(1,5),data5x(1,6),data5x(1,7),data5x(1,8),data5x(1,9),data5x(1,10),data5x(1,11),data5x(1,12),data5x(1,13),data5x(1,14),data5x(1,15),data5x(1,16),data5x(1,17),data5x(1,18)(e16.8,1x,e16.8,1x,e16.8,1x,e16.8,1x,e16.8,1x,e16.8,1x,e16.8,1x,e16.8,1x,e16.8,1x,e16.8,1x,e16.8,1x,e16.8,1x,e16.8,1x,e16.8,1x,e16.8,1x,e16.8,1x,e16.8,1x,e16.8,1x,e16.8)/output/OUTPUT,bridgeDisplacements6x,dat,,*vwrite,data6x(1,1),data6x(1,2),data6x(1,3),data6x(1,4),data6x(1,5),data6x(1,6),data6x(1

,7),data6x(1,8),data6x(1,9),data6x(1,10),data6x(1,11)!,data6x(1,12),data6x(1,13),data6x(1,14),data6x(1,15),data6x(1,16),data6x(1,17),data6x(1,18)(e16.8,1x,e16.8,1x,e16.8,1x,e16.8,1x,e16.8,1x,e16.8,1x,e16.8,1x,e16.8,1x,e16.8,1x,e16.8,1x,e16.8,1x,e16.8)!,1x,e16.8,1x,e16.8,1x,e16.8,1x,e16.8,1x,e16.8,1x,e16.8,1x,e16.8,1x,e16.8)

/output

Appendix A2: Load modelling and control script

Notes: Truck Load Modelling for Numerical Model (APDL Program written on a txt file). Brief comments are given for relevant commands, indicated by the '!' sign.

```
*DO,TM,AXEL1ON,AXLE3OFF,INCR TIME, TM *IF,TM,LT,AXEL2ON,THEN
FDELE,ALL NSEL,S,NODE,,1201+TM
!NSEL,A,NODE,,2801+TM !NSEL,A,NODE,,2001+TM
!NSEL,A,NODE,,1201+TM F,1201+TM,FY,-26700
*ELSEIF,TM,LT,AXEL3ON !TM,GT,AXLE20N,AND,TM,LT,AXEL3ON
FDELE,ALL NSEL,S,NODE,,1201+TM F,1201+TM,FY,-26700
!NSEL,A,NODE,,2801+TM !NSEL,A,NODE,,2001+TM
!NSEL,A,NODE,,1201+TM ! Include axel two
NSEL,A,NODE,,1201+TM - AXEL2ON !NSEL,A,NODE,,2801+TM -
AXEL2ON !NSEL,A,NODE,,2001+TM - AXEL2ON
!NSEL,A,NODE,,1201+TM - AXEL2ON F,1201+TM-AXEL2ON,FY,-
30000 *ELSEIF,TM,LT,AXLE1OFF FDELE,ALL
NSEL,S,NODE,,1201+TM F,1201+TM,FY,-26700
!NSEL,A,NODE,,2801+TM !NSEL,A,NODE,,2001+TM
!NSEL,A,NODE,,1201+TM ! Include axel two
NSEL,A,NODE,,1201+TM - AXEL2ON !NSEL,A,NODE,,2801+TM -
AXEL2ON !NSEL,A,NODE,,2001+TM - AXEL2ON
!NSEL,A,NODE,,1201+TM - AXEL2ON F,1201+TM - AXEL2ON,FY,-
30000 ! Include axel three NSEL,A,NODE,,1201+TM - AXEL3ON
!NSEL,A,NODE,,2801+TM - AXEL2ON !NSEL,A,NODE,,2001+TM -
AXEL2ON !NSEL,A,NODE,,1201+TM - AXEL2ON F,1201+TM -
AXEL3ON,FY,-30000 *ELSEIF,TM,LT,OFF02 FDELE,ALL
!include axel 2 NSEL,S,NODE,,1201+TM-AXEL2ON
!NSEL,A,NODE,,2801+TM - AXEL2ON !NSEL,A,NODE,,2001+TM -
AXEL2ON !NSEL,A,NODE,,1201+TM - AXEL2ON F,1201+TM -
```

AXEL2ON,FY,-30000 ! Include axel three NSEL,A,NODE,,1201+TM - AXEL3ON !NSEL,A,NODE,,2801+TM - AXEL2ON !NSEL,A,NODE,,2001+TM - AXEL2ON !NSEL,A,NODE,,1201+TM - AXEL2ON F,1201+TM - AXEL3ON,FY,-30000 *ELSE FDELE,ALL ! Include axel three NSEL,S,NODE,,1201+TM - AXEL3ON !NSEL,A,NODE,,2801+TM - AXEL2ON !NSEL,A,NODE,,2001+TM - AXEL2ON !NSEL,A,NODE,,1201+TM - AXEL2ON F,1201+TM - AXEL3ON,FY,-30000 *ENDIF NSEL, ALL ! Activate all nodes ESEL, ALL ACEL,,9.81,0 SOLVE *ENDDO

Appendix B: Image Processing and Deformation Estimation Script

Notes: Here is a copy of the main computer script used for image processing, and deformation estimation. It is a MATLAB script. Brief comments are given for relevant commands, indicated by the '%' sign.

An accompanying script for secondary response estimation, and damage detection and localisation is given in B2.

```
%% Using Machine Learning to obtain structural response measurements
clear;
clc
close all;
format compact; format longg

%% Calibration images
v = VideoReader('GOPR6536.MP4'); % read video file

%% Read image
% video can be split into as many parts as possible (or some parts cut
out if too long.
%Basically any edits)due to size and limited computing resources.

 numbofparts = 1; % how many parts we splitting the video
 numbframes = v.NumFrames;% number of frames for video

%% Read image frames
 Startingframe = 1; % specify starting frame.]
for n = Startingframe:numbframes/numbofparts;
  images{n-(Startingframe-1)} = read(v,[n]);%read and convert all image
frames to grayscale
end
% save('images','images','-v7.3'); %save and delete to save memory for
second part


%% Indexes
startAt = 1;
```

```
finishWith = size(images,2);

%% Crop out required region in first image
I = read(v,1);
imshow(I)
J = imrect;
Jcoords(1,:) = round(getPosition(J));
Icropped = imcrop(I,Jcoords(1,:));
save ('Jcoords','Jcoords');

%% show first image frame with cropped image superimposed to check
imshow(I)
hold on
imshow(Icropped); %cropped image
% close;

%% crop other images as well %% (continue here from part 2) %%
for i = startAt:finishWith;
  images_cropped{1,i} = imcrop(images{1,i},Jcoords(1,:)); %crop other
images
  %using coords of first crop in baseline image
end

%% scale and select ROIs
scale = 1;
I = imresize(Icropped,scale);

ROIs = 3; % regions of interest these should include the anticipated
movement of the arucos

imshow(I);

%% Select ROIs %% Ignore from part 2 %%
lObjectRegion = [];
for i = 1:ROIs
lObjectSel = imrect;
lObjectRegion(i,:) = round(getPosition(lObjectSel));
end
save('lObjectRegion','lObjectRegion');

%% Feature detection and tracking using MSER blob detector
regions = {};
for i = 1:ROIs
  croppedImage = imcrop(I,lObjectRegion(i,:));
  % OOI
  croppedImage = rgb2gray(croppedImage);
  T = 0.7%graythresh(croppedImage);
  croppedImage = im2bw(croppedImage,T);
close all
  imshow(croppedImage,[],'InitialMagnification', 'fit')

  objectSel = imrect;
  objectRegion(i,:) = round(getPosition(objectSel));
  close all

  regions{i} =
detectMSERFeatures((croppedImage),'ROI',objectRegion(i,:),'MaxAreaVariati
on',0.8); % You can slightly change the number of MinQuality if too few
or many features are detected
```

```
% regions{i} =
detectMinEigenFeatures((croppedImage),'ROI',objectRegion(i,:),'MinQuality
',0.2); % You can slightly change the number of MinQuality if too few or
many features are detected
end

%% Plot detected features
close all
for i = 1:ROIs
  figure(i)
  imshow(imcrop(I,lObjectRegion(i,:)),[],'InitialMagnification', 'fit')
  hold on
  plot(regions{i})
end
hold off

%% This is the feature tracking code -> a new image is loaded in which

% targets are located based on the 'taught' info
coords = [];
for j = 1:ROIs
  tracker = vision.PointTracker('MaxBidirectionalError',1);
  initialize(tracker,regions{j}.Location,imcrop(I,lObjectRegion(j,:)));
  for i = startAt:finishWith
% frame = images{startAt+i-startAt}; %
    frame = imresize(images_cropped{startAt+i-startAt},scale); %
    croppedImage = imcrop(frame,lObjectRegion(j,:));
    [pointsD,validity] = tracker(croppedImage);
    coords(i-startAt+1,:,j) = double(mean(pointsD));
%     disp([j i])
  end
end

%% Global coordinates
% Transform from local ROI to global (full image) coordinates
coordsG2 = [];
for i = 1:size(coords,1)
  for j = 1:size(coords,2)
    for k = 1:size(coords,3)
    coordsG2(i,j,k) = coords(i,j,k)+lObjectRegion(k,j);
    end
  end
end
%% Scale - provide four known points

II = imresize(images_cropped{1},scale); %rescale rest of image frames

imshow(II); %load first image frame
sH = impoly; % draw a poly line (start top left) with four points and
adjust it

%% Provide coords of fixed/reference points
% fixedPoints = [0 0; 0 25; 150 25; 150 0]; % GoPro
% fixedPoints = [0 0; 0 500; 930 500; 930 0];
fixedPoints = [0 0; 0 620; 990 620; 990 0];
movingPts = sH.getPosition;
% movingPts = load('movingPts2');% moving points coords have been saved
from first vid
% movingPts = movingPts.movingPts;
%
% save ('movingPts2','movingPts');
```

```
%% Perform matrix transformation
coordsT = []; % transformed coordiantes

tform = fitgeotrans(movingPts,fixedPoints,'projective');
for i = 1:size(coordsG2,1);
  for j = 1:size(coordsG2,2);
    for k = 1:ROIs
    coordsT(i,j,k) =
transformPointsForward(tform,coordsG2(i,j,k),coordsG2(i,j,k));
%     coordsT(i,2,j) =
transformPointsForward(tform,coordsG(i,1,j),coordsG(i,2,j));
    end
  end
end

%% plots (as you like, whichever you want)
plot(coordsT(:,2,1)-coordsT(1,2,1), 'Color','b');
hold on
plot(coordsT(:,2,2)-coordsT(1,2,2), 'Color','r');
hold on
plot(coordsT(:,2,3)-coordsT(1,2,3), 'Color','k');
```

Appendix B2: Secondary Response Obtention and Damage Detection (MATLAB Script)

Notes: Here is a copy of the main computer script used for secondary response estimation, and damage detection and localisation. It is a MATLAB script. Brief comments are given for relevant commands, indicated by the '%' sign.

```
%% Using Machine Learning to obtain structural response measurements
clear;
clc
close all;
format compact; format 172ord

%% Import and rename disp data here
%coordsT =
%% Zero and smooth data
% zero raw data
for I = 1:size(coordsT,3);
  coordsT(:,1,i) = (coordsT(:,1,i)-coordsT(1,1,i));
  coordsT(:,2,i) = (coordsT(:,2,i)-coordsT(1,2,i));
end

%smooth raw data
for I = 1:size(coordsT,3);
  coordsTS(:,1,i) = smoothdata(coordsT(:,1,i),'lowess',80);
  coordsTS(:,2,i) = smoothdata(coordsT(:,2,i),'lowess',80);
end
%% check plots
% plot(coordsT(:,2,3));
% hold on
plot(coordsTS(:,2,3));
hold on
plot(coordsTS(:,2,2));
```

```
hold on
plot(coordsTS(:,2,1));

%% Zero raw data and smoothdata based on zeroed smoothdata
for I = 1:size(coordsT,3);
  coordsT(:,1,i) = (coordsT(:,1,i)-coordsTS(1,1,i));
  coordsT(:,2,i) = (coordsT(:,2,i)-coordsTS(1,2,i));

  coordsTS(:,1,i) = (coordsTS(:,1,i)-coordsTS(1,1,i));
  coordsTS(:,2,i) = (coordsTS(:,2,i)-coordsTS(1,2,i));
end

%% Start computing curvature: Distribute data points horizontally across
the beam
%   m = 0;
  for I = 1:size(coordsTS,3)
     for j = 1:size(coordsTS,4)
%         m = 0;
      n = i-1;
      o = 990*n; %990 is dist btw targets
        coordsTS(:,1,I,j) = coordsTS(:,1,I,j)+o;
        coordsT(:,1,I,j) = coordsT(:,1,I,j)+o; %just to do for the
unsmoothed data
     end
  end
% coordsTS(:,2,😊) = coordsTS(:,2,😊*-1;

%% Rearrange data to the required form i.e(Nodes,x&y,time/load
steps,damage scenarios)
for I = 1:size(coordsTS,3);
  for j = 1:size(coordsTS,2);
    for k = 1:size(coordsTS,1);
       for l = 1:size(coordsTS,4);
        Beam_disp(I,j,k,l) = coordsTS(k,j,I,l);
       end
    end
  end
end
%% DEFINE moving windows (this creates an array for each slide of the
moving window)
windowsize = 3; %number of nodes to be used for curvature analysis
for I = 1:size(Beam_disp,1) - windowsize+1
 for j=1:windowsize
   for k = 1:size(Beam_disp,3)
     for l =1:size(Beam_disp,4)
      Mov_window(j,1,I,k,l)=Beam_disp(i+j-1,1,k,l);
      Mov_window(j,2,I,k,l)=Beam_disp(i+j-1,2,k,l);
     end
   end
 end
end

%% Normalise nodal displacements in Moving window
%to normalise the points in X and Y axis, find min values for x and y in
each window
%(St_response.max is used for Y because most values are negative so this
gives the closest to 0).
Mov_window2 = Mov_window;
%normalise Y by subtracting smallest value
for I = 1:size(Mov_window,3);
  for j = 1:size(Mov_window,4);
```

```
    for k = 1:size(Mov_window,5);

      Mov_window2(:,2,I,j,k) = Mov_window(:,2,I,j,k) -
Mov_window(1,2,I,j,k);
    end
  end
end

%transpose to have X and Y in rows, that's how the rotation thingy works
for I = 1:size(Mov_window,3);
  for j= 1:size(Mov_window,4);
    for k = 1:size(Mov_window,5);
      Trans_Mov_window(:,:,I,j,k) = transpose(Mov_window2(:,:,I,j,k));
    end
  end
end

%% Set center of rotation at 0,0 by normalising all the x - 174ords,
their values will be added back after rotation
% curves that tilt from L-R are normalised at left end. Reverse
conversely
for I = 1:size(Trans_Mov_window,3);
  for j = 1:size(Trans_Mov_window,4);
    for k = 1:size(Trans_Mov_window,5);
      Norm_Mov_window(1,:,I,j,k) = Trans_Mov_window(1,:,I,j,k) -
Trans_Mov_window(1,1,I,j,k);
  end
  end
end

Norm_Mov_window(2,:,:,😊) = Trans_Mov_window(2,:,:,😊); %Y-axis remains
the same as its been normalised already

%% Define rotation matrix for each curve
% matlab measures angles from right to left, so there is need to check
% If points are in the third quadrant, angle to be rotated = 360 - theta
% If points are in the fourth quadrant, angle to be rotated = theta

%First find angle theta for all curves.
For I = 1:size(Trans_Mov_window,3)
  for j = 1:size(Trans_Mov_window,4)
    for k = 1:size(Trans_Mov_window,5)
     theta(I,k,j) =
abs(Norm_Mov_window(2,3,I,j,k)/(Norm_Mov_window(1,3,I,j,k)));
    end
  end
end

thetaDeg = atand(theta); % convert from rads to degrees

%% Get Rotation matrix

% First get rotation angle
for I = 1:size(Trans_Mov_window,3);
  for j = 1:size(Trans_Mov_window,4);
    for k = 1:size(Trans_Mov_window,5);
    thetaRot(I,k,j) = thetaDeg(I,k,j);
    end
  end
end
```

```
%Then rotation matrix
for I = 1:size(Trans_Mov_window,3);
   for j = 1:size(Trans_Mov_window,4)
     for k = 1:size(Trans_Mov_window,5)
       if Norm_Mov_window(2,3,I,j,k)>0; % points in Quadrant 1 and 2
theta = 360-theta
      R(:,:,I,j,k) = [cosd(360-thetaRot(I,k,j)) -sind(360-
thetaRot(I,k,j)); sind(360-thetaRot(I,k,j)) cosd(360-thetaRot(I,k,j))];
       else
         R(:,:,I,j,k) = [cosd(thetaRot(I,k,j)) -sind(thetaRot(I,k,j));
sind(thetaRot(I,k,j)) cosd(thetaRot(I,k,j))];
      end
   end
end
end
%R(:,:,4) = 1 %for no rotation
%% Multiply Smoothdisp points by rotation matrix

for I = 1:size(Trans_Mov_window,3);
   for j = 1:size(Trans_Mov_window,4)
     for k = 1:size(Trans_Mov_window,5)
    RotatedPoints(:,:,I,j,k) = R(:,:,I,j,k)*Norm_Mov_window(:,:,I,j,k);
     end
   end
end

%add back values subtracted during rotation to restore graph to original
position
for I = 1:size(Trans_Mov_window,3);
   for j = 1:size(Trans_Mov_window,4)
     for k = 1:size(Trans_Mov_window,5)
      RotatedPoints(1,:,I,j,k) = RotatedPoints(1,:,I,j,k) +
Trans_Mov_window(1,1,I,j,k); %add subtracted
      %value to restore graph to original position
   end
end
end

for I = 1:size(Trans_Mov_window,3);
   for j = 1:size(Trans_Mov_window,4)
     for k = 1:size(Trans_Mov_window,5)
      Norm_Mov_window(1,:,I,j,k) = Norm_Mov_window(1,:,I,j,k) +
Trans_Mov_window(1,1,I,j,k);%add subtracted
  %value to restore graph to original position
  %value to restore graph to original position
     end
   end
end
%% Curve fitting
tic
coefficients = [];
for I = 1:size(Trans_Mov_window,3);
   for j = 1:size(Trans_Mov_window,4);
     for k = 1:size(Trans_Mov_window,5)
  fitcurve1 =
fit(transpose(RotatedPoints(1,:,I,j,k)),transpose(RotatedPoints(2,:,I,j,k
)),'poly2');
  coefficients(I,:,j,k) = coeffvalues(fitcurve1);
     end
   end
```

```
   %fprintf('iteration %d time %4.2f\n',I,toc)
end

% Obtain 'a' coefficients of quadratic Equation
for I = 1:size(coefficients,3)
  for j = 1:size(coefficients,4)
    Curvdata(:,i,j) = (coefficients(:,1,i,j))*1;
  end
end

%%       TILTS

% ********************************************************************** %%

% Tilts using (mm/mm) = rads, and absolute values
% Beam_disp=abs(Beam_disp);
for I = 1:size(Beam_disp,1)-1;
  for j = 1:size(Beam_disp,3);
    for k = 1:size(Beam_disp,4);
     Tilt(I,:,j,k) = ((Beam_disp(i+1,2,j,k) -
Beam_disp(I,2,j,k))/((Beam_disp(i+1,1,j,k) - Beam_disp(I,1,j,k)))); %
    end
  end
end

% change to an m x n matrix so as to copy to excel
for I = 1:size(Tilt,3);
  for j = 1:size(Tilt,4);
  Tiltdata(:,i,j) =(Tilt(:,1,i,j))*1;%0^6;
  end
end

%% STRAIN METHOD

%%%%%%%%%%%%%%%%%%%%%%%%%%%%%%%%%%%%%%%%%%%%%%%%%%%%%%%%%%%%%%%%%%%%%%%%%%%%%%%

  for I = 1:size(Beam_disp,1)-1;
    for j = 1:size(Beam_disp,3);
     for k = 1:size(Beam_disp,4);
      Edist(I,1,j,k) = (Beam_disp(i+1,1,j,k)-Beam_disp(1,1,j,k));
      Edist(I,2,j,k)= (Beam_disp(i+1,2,j,k)-Beam_disp(1,2,j,k));
     end
    end
  end

% Edist(:, = (Edist).^2;

Edist = (Edist).^2;

for I = 1:size(Edist,1);
  for j = 1:size(Beam_disp,3);
   for k = 1:size(Beam_disp,4);
    Edistance(i,1,j,k) = (Edist(i,1,j,k))+(Edist(i,2,j,k));
    Edistance_square = sqrt(Edistance);
   end
  end
 end
originallength1 = Edistance_square(1,1,1);
originallength2 = Edistance_square(2,1,1);
```

```
Strain(1,1,😊) = (Edistance_square(1,1,😊) -
Edistance_square(1,1,1))/originallength1;
Strain(2,1,😊) = (Edistance_square(2,1,😊) -
Edistance_square(2,1,1))/originallength2;

  for I = 1:size(Strain,3);
    for j = 1:size(Strain,4);
    Straindata(:,I,j) = Strain(:,1,I,j)*1;%0^6;
    end
  end


%% DAMAGE DETECTION %%
load('all.mat'); % here is the struct where all data has been prev saved
% First, disps. Here we extracting ydisps only
for I = 1:size(all.timehist.fifteen.fdisp.dispall,1);
  for j = 1:size(all.timehist.fifteen.fdisp.dispall,4);
%numb_of_scenarios;
    for k = 1:size(all.timehist.fifteen.fdisp.dispall,3);
      ydisps(k,1,I,j) = all.timehist.fifteen.fdisp.dispall(I,2,k,j);
    end
  end
end
%
for I = 1:size(ydisps,3); %numb_of_scenarios;
  for j = 1:size(ydisps,1);
    for k = 1:size(ydisps,4);
      ydisplacements(I,j,k) = ydisps(j,1,I,k);
    end
  end
end
%
%Obtain St_response.maximum displacement response
for I = 1:size(ydisplacements,3)
  for j = 1:size(ydisplacements,4)
    maximum_y = max(ydisplacements,[],1);
    maxydisp(I,:,j) = maximum_y(:,:,I,j);
  end
end

all.max.fifteen.fdisp.maxdisp =(maxydisp);

% max ydisp diff
for I = 1:size(all.max.fifteen.fdisp.maxdisp,1)-1;
  for j = 1:size(all.max.fifteen.fdisp.maxdisp,3); %third dim is useful
when there are damage severities
    all.max.fifteen.fdisp.diffdisp(I,:,j) =
all.max.fifteen.fdisp.maxdisp(i+1,:,j) -
all.max.fifteen.fdisp.maxdisp(1,:,j);
  end
end
%
% e calculation
for I = 1:size(all.max.fifteen.fdisp.diffdisp,1);
  for j = 1:size(all.max.fifteen.fdisp.diffdisp,2);
    for k = 1:size(all.max.fifteen.fdisp.diffdisp,3);
      all.max.fifteen.fdisp.edisp(I,j,k) =
((all.max.fifteen.fdisp.diffdisp(I,j,k)/all.max.fifteen.fdisp.maxdisp(1,j
,k))*100);
    end
  end
```

```
end

%% MAX curvature
for I = 1:size(all.timehist.fifteen.fcurv.curvall,3);
  for j = 1:size(all.timehist.fifteen.fcurv.curvall,4);
    all.max.fifteen.fcurv.maxcurv(:,I,j) =
max(all.timehist.fifteen.fcurv.curvall(:,:,I,j),[],2);
  end
end
% Stresponse.fifteenkgmaxcurv_d2 = maxcurv;

%% Curv diff
%St_response.maxcurv_diff
for I = 1:size(all.max.fifteen.fcurv.maxcurv,2)-1
  for j = 1:size(all.max.fifteen.fcurv.maxcurv,3)
    all.max.fifteen.fcurv.diffcurv(:,I,j) =
all.max.fifteen.fcurv.maxcurv(:,i+1,j) -
all.max.fifteen.fcurv.maxcurv(:,1,j);
  end
end

% e calculation
for I = 1:size(all.max.fifteen.fcurv.diffcurv,2);
  for j = 1:size(all.max.fifteen.fcurv.diffcurv,1);
    for k = 1:size(all.max.fifteen.fcurv.diffcurv,3);
    all.max.fifteen.fcurv.ecurv(j,I,k) =
((all.max.fifteen.fcurv.diffcurv(j,I,k)/all.max.fifteen.fcurv.maxcurv(j,1
,k))*100);
  end
end
end

%% MAXIMUM STRAIN

for I = 1:size(all.timehist.fifteen.fstrain.strainall,3);
  for j = 1:size(all.timehist.fifteen.fstrain.strainall,4);
    all.max.fifteen.fstrain.maxstrain(:,I,j) =
max(all.timehist.fifteen.fstrain.strainall(:,:,I,j),[],2);
  end
end
% Max strain diff
%St_response.maxstrain = abs(St_response.maxstrain);
for I = 1:size(all.max.fifteen.fstrain.maxstrain,2)-1
  for j = 1:size(all.max.fifteen.fstrain.maxstrain,3)
    all.max.fifteen.fstrain.maxstraindiff(:,I,j) =
all.max.fifteen.fstrain.maxstrain(:,i+1,j) -
all.max.fifteen.fstrain.maxstrain(:,1,j);
  end
end

% e calculation
for I = 1:size(all.max.fifteen.fstrain.maxstraindiff,2);
  for j = 1:size(all.max.fifteen.fstrain.maxstraindiff,1);
    for k = 1:size(all.max.fifteen.fstrain.maxstraindiff,3);
    all.max.fifteen.fstrain.estrain(j,I,k) =
((all.max.fifteen.fstrain.maxstraindiff(j,I,k)/all.max.fifteen.fstrain.ma
xstrain(j,1,k))*100);
  end
end
end
```

```
%% MAX TILT
for I = 1:size(all.timehist.fifteen.ftilt.tiltall,3);
  for j = 1:size(all.timehist.fifteen.ftilt.tiltall,4);
  all.max.fifteen.ftilt.maxmin_tilt(:,I,1) =
(max(all.timehist.fifteen.ftilt.tiltall(:,:,I,j),[],2));
  all.max.fifteen.ftilt.maxmin_tilt(:,I,2) =
(min(all.timehist.fifteen.ftilt.tiltall(:,:,I,j),[],2));
  end
end

for n = 1:size(all.timehist.fifteen.ftilt.tiltall,1);
  for I = 1:size(all.timehist.fifteen.ftilt.tiltall,3);
    if all.timehist.fifteen.ftilt.maxmin_tilt(n,I,1) >
abs(all.timehist.fifteen.ftilt.maxmin_tilt(n,I,2))
       all.timehist.fifteen.ftilt.maxtilt(n,I,1) =
all.timehist.fifteen.ftilt.maxmin_tilt(n,I,1);
    elseif all.timehist.fifteen.ftilt.maxmin_tilt(n,I,1) ==
abs(all.timehist.fifteen.ftilt.maxmin_tilt(n,I,2))
       all.timehist.fifteen.ftilt.maxtilt(n,I,1) = 0;
    else
       all.timehist.fifteen.ftilt.maxtilt(n,I,1) =
all.timehist.fifteen.ftilt.maxmin_tilt(n,I,2);
    end
  end
end
%
% Stresponse.fifteenkgmaxtilt_d2 = maxtilt;

% max tilt diff

for I = 1:size(all.timehist.fifteen.ftilt.maxtilt,2)-1
  for j = 1:size(all.timehist.fifteen.ftilt.maxtilt,3)
    all.max.fifteen.ftilt.maxtiltdiff(:,I,j) =
all.timehist.fifteen.ftilt.maxtilt(:,i+1,j) -
all.timehist.fifteen.ftilt.maxtilt(:,1,j);
  end
end
% e calculation
for I = 1:size(all.timehist.fifteen.ftilt.maxtiltdiff,2);
  for j = 1:size(all.timehist.fifteen.ftilt.maxtiltdiff,1);
    for k = 1:size(all.timehist.fifteen.ftilt.maxtiltdiff,3);
      all.max.fifteen.ftilt.etilt(j,I,k) =
((all.timehist.fifteen.ftilt.maxtiltdiff(j,I,k)/all.timehist.fifteen.ftil
t.maxtilt(j,1,k))*100);
    end
  end
end

%% mistake, so put them in the right place
all.max.fifteen.ftilt.maxtilt = all.timehist.fifteen.ftilt.maxtilt;
all.max.fifteen.ftilt.maxtiltdiff =
all.timehist.fifteen.ftilt.maxtiltdiff;

% e tilts method 2

mW = 3; % Moving window for tilt odd
f = (mW-1)/2; % number of neighboring points
% dsIn = [3 6 1]; % damage scenarios in
% sIn = [1 2 1]; %severity in
% x = 12/50/2:12/50:12-12/50/2; % X-ticks for strains (do not start at 0
and finish at 12)
```

```
for I = 1:size(all.max.fifteen.ftilt.maxtiltdiff_l,2);
  aa(:,i) = all.max.fifteen.ftilt.maxtiltdiff_l(:,I,😊; % tilt
difference
  bb(:,i) = all.max.fifteen.ftilt.maxtilt_l(:,i+1,😊; % max tilt
%   eTheta = [];
  for j = 1:size(all.max.fifteen.ftilt.maxtiltdiff_l,1)-mW+1;
    eTheta20(j+f,i) = range(abs(aa(j:j+mW-1,i)))/mean(abs(bb(j:j+mW-
1,i)))*100; % range/mean for the midpoint
%     eTheta(j) = range(abs(a(j:j+mW)))/abs(mean(b(j:j+mW)))*100; %
range/mean
  end
%   plot(12/size(a,1):12/size(a,1):12-
12/(size(a,1))*f,eTheta,'Color',colourIn(I,😊,'LineWidth', 1); % x needs
to be manually adjusted
end
```

Appendix C: Sample of LVDT and Strain Gauge Readings From Contact Sensors Used to Validate CV-based Readings (For 10kg Load)

Notes: Here is a sample of LVDT and strain gauge readings. This is the data set used to validate CV-based deformations in Section 4.2. The rest are not reproduced here for brevity.

LVDT2	LVDT3	LVDT4	LVDT5	strain1	strain2	strain3	T9
0.1178	0.0451	-0.0734	-0.2964	0.1424	0.1106	-0.0336	99
0.1182	0.0446	-0.0738	-0.2977	0.0339	0.0394	-0.0348	99
0.1189	0.0441	-0.076	-0.2999	-0.0687	-0.0513	-0.0342	99
0.1177	0.0444	-0.0745	-0.2974	-0.1633	-0.1306	-0.0344	99
0.1169	0.0446	-0.0753	-0.3003	-0.1682	-0.1368	-0.034	99
0.1174	0.043	-0.0754	-0.3026	-0.1012	-0.087	-0.0348	99
0.1191	0.0441	-0.0769	-0.3007	-0.0258	-0.0291	-0.0339	99
0.1181	0.0434	-0.0728	-0.3014	0.0823	0.0509	-0.0339	99
0.0235	-0.0732	-0.1441	-0.3267	0.137	0.1217	-0.0334	99
0.0772	-0.019	-0.1138	-0.3203	0.1664	0.1439	-0.0335	99
0.1444	0.0465	-0.0929	-0.3279	0.1541	0.1412	-0.0336	99
0.2442	0.1734	-0.0144	-0.2916	0.1148	0.0858	-0.0333	99
0.3978	0.3643	0.0993	-0.2436	0.0332	0.0284	-0.0338	99
0.643	0.6559	0.2682	-0.18	-0.0485	-0.0344	-0.0342	99
0.8235	0.8826	0.4088	-0.1195	-0.1177	-0.0999	-0.0344	99
1.0443	1.1564	0.5693	-0.0541	-0.1619	-0.1482	-0.0341	99
1.2107	1.3689	0.6995	-0.0021	-0.1648	-0.1518	-0.0342	99
1.4049	1.6305	0.86	0.0593	-0.1357	-0.1266	-0.0341	99
1.6009	1.8963	1.0209	0.1211	-0.0942	-0.1016	-0.0342	99
1.7602	2.1481	1.1838	0.1971	-0.0379	-0.0522	-0.0333	99
1.8896	2.3596	1.313	0.2463	0.0167	-0.0187	-0.0336	99
1.9757	2.5392	1.4323	0.2986	0.0616	0.0419	-0.0337	99
2.0825	2.7554	1.5761	0.3586	0.1071	0.0773	-0.0335	99
2.133	2.9059	1.6928	0.4148	0.1317	0.1231	-0.0335	99
2.189	3.0787	1.8197	0.4687	0.148	0.1348	-0.0337	99
2.1903	3.1684	1.9104	0.5123	0.1632	0.1373	-0.0333	99
2.191	3.2258	1.966	0.5333	0.1491	0.1107	-0.0335	99
2.1612	3.2459	2.0275	0.5693	0.0882	0.0809	-0.0339	99
2.1138	3.2326	2.0732	0.6021	0.044	0.0174	-0.0337	99
2.0569	3.1857	2.0942	0.6192	-0.02	-0.0221	-0.0338	99
1.9697	3.0807	2.0894	0.6354	-0.0772	-0.0801	-0.0338	99
1.8789	2.967	2.0691	0.6371	-0.1348	-0.1121	-0.0345	99
1.7674	2.8166	2.0341	0.6672	-0.1848	-0.1655	-0.0337	99
1.6522	2.6458	1.9554	0.6334	-0.187	-0.1666	-0.0338	99
1.5334	2.465	1.87	0.6159	-0.1588	-0.1356	-0.0339	99
1.3875	2.2548	1.7754	0.616	-0.1087	-0.0926	-0.0342	99
1.2285	2.0135	1.6264	0.5766	-0.0297	-0.0562	-0.0333	99
1.0419	1.755	1.4786	0.5678	0.0327	0.0129	-0.0334	99
0.8753	1.4856	1.2796	0.5091	0.0917	0.0908	-0.0334	99
0.6862	1.2085	1.0826	0.4472	0.1437	0.1285	-0.0337	99
0.4912	0.8871	0.8164	0.3375	0.1541	0.1392	-0.0333	99
0.2956	0.5801	0.5795	0.2328	0.125	0.1089	-0.0336	99
0.0942	0.2413	0.2943	0.0973	0.0579	0.0351	-0.0339	99

BO1 2kg | BO1 5kg | BO1 10kg | BO2 2kg